



**MONASH** University

---

**THREE-BEAM ELECTRON DIFFRACTION  
FOR STRUCTURAL INVESTIGATIONS**

---

**Yueming Guo**

A thesis submitted for the degree of

Doctor of Philosophy

Department of Materials Science and Engineering

Monash University

Victoria, Australia

November 2016

*To my dear parents,*

*Ms. Yuan Fan and Dr. Ran Guo,*

*who have always been my greatest supporters.*

## **Copyright notice**

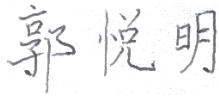
© Yueming Guo, 2016. Except as provided in the Copyright Act 1968, this thesis may not be reproduced in any form without the written permission of the author.

I certify that I have made all reasonable efforts to secure copyright permissions for third-party content included in this thesis and have not knowingly added copyright content to my work without the owner's permission.

## Declarations

I, Yueming Guo, hereby certify that this thesis is my own work and contains no material which has been accepted previously for the award of any other degree or diploma in any university or any institution and, to the best of my knowledge, this thesis does not contain any material previously published or written by another person, except where due reference is made in the text of the thesis.

Signature:



Name:

Yueming Guo

Date:

03/11/2016

## Acknowledgements

First of all, I would like to express my gratitude and appreciation to my principal supervisor, Prof. Joanne Etheridge, for her continuous support of my research and writing this thesis. Her motivation, immense knowledge and patience have made my PhD journey over the past three years and eight months an invaluable and wonderful experience. I would also like to thank my co-supervisor, A/Prof. Philip Nakashima, for his great efforts in the weekly meetings and in helping me correct this thesis. His passion for research, teaching and socialising inspires me to become an open-minded scholar.

Besides my supervisors, I would like to thank Dr. Christopher Rossouw, Dr. Changlin Zheng, Dr. Ye Zhu, A/Prof. Matthew Weyland, Dr. Timothy Peterson and Prof. Alexander Moodie for their insightful discussions and friendly advices.

All of the experimental work described in this thesis has been carried out in the Monash Centre for Electron Microscopy (MCEM). Without the support from the staffs in MCEM, this work cannot be possible. In particular, I am grateful for having the great training sessions from A/Prof. Laure Bourgeois, Dr. Amelia Liu, Dr. Timothy Williams and Dr. Emily Chen.

I would also like to thank my friends, Yu Zhang, Tianyu Liu, Ding Peng, Dan Nguyen, Fujia Luo, Xuan Cheng and Zezhong Zhang, who have always been very supportive and helpful.

Finally, I would like to thank my parents for their love and support. My mother has always encouraged me to live a healthy and happy life. My father has always been my greatest mentor.



## Contents

|   |             |
|---|-------------|
| <b>Acknowledgement .....</b>  | <b>III</b>  |
| <b>List of tables .....</b>   | <b>VII</b>  |
| <b>List of figures.....</b>   | <b>IX</b>   |
| <b>Terminology, symbols and conventions used in this thesis .....</b>               | <b>XIII</b> |
| <b>Abstract .....</b>   | <b>XVII</b> |
| <b>Chapter 1. Introduction .....</b>  | <b>1</b>    |
| <b>Chapter 2. Crystallography and electron diffraction theories.....</b>            | <b>5</b>    |
| 2.1 Introduction to crystallography and the phase problem .....                     | 6           |
| 2.2 Dynamical theory of electron diffraction .....                                  | 16          |
| 2.3 Convergent-beam electron diffraction (CBED) .....                               | 30          |
| 2.4 Three-beam electron diffraction.....  | 36          |
| <b>Chapter 3. Determination of three-phase invariants</b>                           |             |
| <b>by observation: theory .....</b>   | <b>55</b>   |
| 3.1 Closed-form solutions to three-beam electron diffraction .....                  | 55          |
| 3.2 Approach to determine the sign of $\sin\phi$ .....                              | 59          |
| 3.3 Determination of whether $ V_{\mathbf{h}-\mathbf{g}} \cos\phi$ is zero .....    | 72          |
| 3.4 Approach to determine the sign of $\cos\phi$ .....                              | 74          |
| 3.5 Valid range of thickness for direct observation of the sign of $\sin\phi$ ..... | 81          |
| 3.6 The three-beam theories in crystal structure determination .....                | 87          |
| 3.7 Summary .....   | 96          |

|  |            |
|--|------------|
| <b>Chapter 4. Determination of three-phase invariants</b>                                      |            |
| <b>by observation: experiment.....</b>   | <b>99</b>  |
| 4.1 Large-angle rocking beam electron diffraction (LARBED) .....                               | 99         |
| 4.2 Three-beam electron diffraction in selected area diffraction .....                         | 113        |
| 4.3 On automatic collection of diffraction patterns with low doses.....                        | 115        |
| <b>Chapter 5. A three-beam CBED approach for</b>   |            |
| <b>local composition measurement in <math>\text{In}_x\text{Ga}_{1-x}\text{As}</math> .....</b> | <b>117</b> |
| 5.1 Compositional characterisation in TEM .....  | 118        |
| 5.2 The diffraction condition and the theoretical basis .....                                  | 121        |
| 5.3 Experimental demonstration of the composition measurement .....                            | 127        |
| 5.4. Testing the independence of the measurements .....  | 132        |
| 5.5 The effect of strain relaxation on the composition measurement .....                       | 140        |
| 5.6 Discussions.....   | 148        |
| <b>Chapter 6. Conclusions .....</b>  | <b>151</b> |
| 6.1 Determination of three-phase invariants by observation: theory .....                       | 151        |
| 6.2 Determination of three-phase invariants by observation: experiment .....                   | 152        |
| 6.3 Composition measurement in $\text{In}_x\text{Ga}_{1-x}\text{As}$ .....                     | 152        |
| 6.4 Recommended future work .....  | 153        |
| <b>References .....</b>  | <b>155</b> |



## List of tables

| Table | The title of each table   | Page |
|-------|---|------|
| 3.1   | Summary of the criteria for extracting the phase information  | 87   |
| 3.2   | Table for estimating the triplet phase  | 88   |
| 3.3   | Summary of simulations for testing three-beam electron diffraction in some crystal structures that are not trivial to solve | 94   |
| 4.1   | Summary of the main results in Section 4.1.3  | 111  |
| 5.1   | Elastic constants and lattice constants used for the simulation by finite element method                                    | 142  |



## List of figures

| Figure | The summary of each figure  | Page |
|--------|---|------|
| 2.1    | Ewald sphere construction.  | 7    |
| 2.2    | Construction of the wave vectors in dynamic electron diffraction.   | 20   |
| 2.3    | Three-dimensional crystals are treated as slices of two-dimensional potentials in multislice.   | 25   |
| 2.4    | Schematic of CBED pattern formation.  | 32   |
| 2.5    | Schematics of (a) Bragg line and (b) Kikuchi line formation in CBED patterns.   | 33   |
| 2.6    | Geometries of on-zone (a, c) and off-zone (b, d) CBED.  | 34   |
| 2.7    | Schematic of the diffraction geometry of (a) (non-systematic) three-beam CBED and (b) an example of (non-systematic) three-beam CBED pattern.               | 37   |
| 2.8    | The multiple scattering diagram for the second-order Born approximation to three-beam dynamic diffraction.  | 41   |
| 2.9    | Intensity profiles along the Bragg line of reflection $g$ at different three-phase invariants (for the kinematical approximation).                          | 43   |
| 2.10   | Intensity profiles along the Bragg line of reflection $g$ at different thicknesses (for the kinematical approximation).                                     | 43   |
| 2.11   | Intensity profiles along the Bragg line of reflection $g$ at different thicknesses (for the Bethe's approximation).   | 47   |
| 2.12   | Validity regions of the incident beam directions for the (a) Bethe's and (b) Kambe's approximations.  | 50   |
| 3.1    | A plot of dispersion surfaces in three-beam electron diffraction.   | 57   |
| 3.2    | Illustrations of equations (3.11a, b).  | 61   |
| 3.3    | Illustration of criterion I with simulated three-beam CBED patterns of alpha-quartz (space group $P3_121$ ) near $[\bar{1} \ \bar{3} \ \bar{7}]$ at 200 kV. | 64   |
| 3.4    | Illustrations of criterion II in simulated CBED patterns of alpha-quartz (space group $P3_121$ ) near $[\bar{1} \ \bar{3} \ \bar{7}]$ at 200 kV.            | 65   |

| Figure | The summary of each figure  | Page |
|--------|---|------|
| 3.5    | Simulated three-beam CBED patterns near $[\bar{1} \ \bar{3} \ \bar{7}]$ of two different types of alpha-quartz (which form a chiral pair): the two structures are in space groups (a, b) $P3_221$ and (c, d) $P3_121$ .                 | 66   |
| 3.6    | Intensity profiles along the Bragg line of reflection $\bar{2} \ 3 \ \bar{1}$ in alpha-quartz $P3_221$ .  | 68   |
| 3.7    | A simulated CBED pattern of bismuth trioxide, $\text{Bi}_{12}\text{SiO}_{24}$ , (space group $I23$ ) at a three-beam condition near $[3 \ 10 \ 0]$ .  | 71   |
| 3.8    | A simulated CBED pattern of GaAs $[1 \ 0 \ 9]$ .  | 73   |
| 3.9    | A simulated CBED pattern of Si $[6 \ 3 \ 1]$ .  | 73   |
| 3.10   | Plots of the three polynomials in equations (3.5a-c) along the Bragg line of reflection $g$ .   | 76   |
| 3.11   | The gaps of the three dispersion surfaces, $\mu_i$ , along the Bragg line of $g$ .  | 76   |
| 3.12   | A plot comparing different approximations in three-beam electron diffraction.   | 78   |
| 3.13   | Simulated CBED patterns of ZnS $[1 \ 3 \ 7]$ near a three-beam condition which is located in the centre of each disc.   | 79   |
| 3.14   | Plots of (a) the polynomials $C_{i\oplus 1}C_{i\oplus 2}$ from equation (3.10) and (b) the gaps of the dispersion surfaces, $\mu_i$ , versus the excitation error $\zeta_h$ along the locus, $\zeta_g = \zeta_h$ (the horizontal axis). | 85   |
| 3.15   | Plots of the intensity of the central beam (in orange) and the intensity difference between a Friedel pair, $g$ and $\bar{g}$ , (in blue) along the locus $\zeta_g = \zeta_h$ (the horizontal axis).                                    | 86   |
| 3.16   | Simulated CBED patterns of alpha-quartz (space group $P3_121$ ) in zone axes $[7 \ 2 \ \bar{1}]$ (in column a) and $[1 \ 3 \ 5]$ (in column b) are used as two examples for demonstrating the phase determination.                      | 89   |
| 3.17   | Simulated CBED patterns of $\text{CsNbWO}_{14}$ .   | 95   |
| 3.18   | Simulated CBED patterns of $\text{Fe}_2\text{Si}_3\text{O}_9$ .   | 95   |
| 3.19   | A flow chart for the determination of the three-phase invariant, $\phi$ , by direct observations of three-beam CBED patterns.   | 97   |

| Figure | The summary of each figure   | page |
|--------|--|------|
| 4.1    | A schematic illustration of LARBED with a convergent beam under the special experimental setup.  | 102  |
| 4.2    | A schematic illustration of LACBED reconstruction by using the code developed in this PhD work.  | 103  |
| 4.3    | An integrated CBED pattern (a) and reconstructed LACBED patterns (b), both from a data stack of 121 CBED patterns from Si near [1 1 8] at 200kV.   | 105  |
| 4.4    | Reconstructed LACBED patterns from GaAs [5 1 0] at 200 kV.   | 108  |
| 4.5    | Reconstructed LACBED patterns of GaAs [9 1 $\bar{2}$ ] at 200 kV.  | 110  |
| 4.6    | A selected area diffraction pattern of GaAs [11 0 1] taken from a FEI Tecnai G <sup>2</sup> T20 with LaB <sub>6</sub> gun at 200 kV.   | 115  |
| 5.1    | Illustration for the diffraction condition.  | 121  |
| 5.2    | The intensity ratio for the composition measurement is defined in (a) and calculated for different compositions (b-d) as a function of thickness.  | 126  |
| 5.3    | Illustration of locating the three-beam condition inside each reflection of the Bijvoet pair and subtracting the linear background from the integrated peak intensities.                     | 129  |
| 5.4    | Illustration of composition measurement from an experimental CBED pattern  | 131  |
| 5.5    | The influence of the uncertainties in compositions and lattice constants on the thickness measurements.  | 134  |
| 5.6    | The influence of the uncertainties in lattice constant on the composition measurement.   | 137  |
| 5.7    | The influence of the composition on the measurement of lattice constants by using HOLZ patterns.   | 139  |
| 5.8    | Distribution of the normal strain component in the [1 0 0] direction, $e_{11} = \frac{a_{[1\ 0\ 0]} - a_{\text{GaAs}}}{a_{\text{GaAs}}}$ , which is calculated by the finite element method. | 143  |
| 5.9    | Simulated CBED patterns for (a) the strained QW specimen (the probe position is shown in Figure 5.8) and (b) bulk, unstrained In <sub>0.2</sub> Ga <sub>0.8</sub> As.                        | 145  |

| Figure | The summary of each figure   | page |
|--------|--|------|
| 5.10   | Composition profiles across two $\text{In}_{0.2}\text{Ga}_{0.8}\text{As}/\text{GaAs}$ interfaces in the middle of the QW specimen shown in Fig. 5.8. | 147  |

## Terminology, symbols and conventions used in this thesis

### Terminology

“Reflections” or “Bragg reflections” refer to the regularly spaced spots in X-ray or selected area electron diffraction (SAED or SAD) patterns as well as the discs in convergent-beam electron diffraction (CBED) patterns. “Strong reflections” refer to the reflections which have large structure factor magnitudes although strong reflections can have weak intensities at certain thicknesses in a dynamic diffraction pattern. Similarly, “weak” reflections have small structure factor magnitudes.

“Three-beam conditions” refer to the orientations where two and only two reflections satisfy their Bragg conditions simultaneously, and this can be achieved in some orientations experimentally. “Three-beam electron diffraction” is an approximation in the dynamic diffraction of electrons which provides a qualitative description of the diffraction patterns that are recorded in and near the three-beam conditions.

The thickness of a specimen refers to the thickness in the probed region of a TEM specimen. Various expressions for describing the thickness, i.e. “very thin”, “thin or not thick”, “thick” and “very thick”, have been used in this thesis and they refer to different ranges of thickness. The classification is based on the valid ranges for different approximations and methods in three-beam electron diffraction. The perturbed kinematical approximation described in Section 2.4.3 is only valid for a “very thin” specimen but can fail even for a specimen that is “thin or not thick”. The direct observation of the sign of three-phase invariants is valid for a specimen that is “thin or not thick” but it fails for a thick specimen. For a very thick specimen, none of the approximations or methods in this thesis can work and the thickness for a very thick specimen is often larger than 200 nm.

### Symbols

Bragg reflection:  $g$  (or  $h$ ) =  $h\ k\ l$

Reciprocal lattice vector:  $\mathbf{g} = h, k, l$

Crystal lattice plane:  $(h\ k\ l)$

A family of the symmetrically equivalent crystal planes:  $\{h\ k\ l\}$

The wavelength:  $\lambda$

The wave vector for the incident beam:  $\mathbf{K}_0$

The wave vector for the diffracted beam:  $\mathbf{K}$

The structure factor used in X-ray diffraction:  $F_{\mathbf{g}}$

The intensity of reflection  $\mathbf{g}$ :  $I_{\mathbf{g}}$

The thickness of the specimen:  $z$

The structure factor used in electron microscopy and diffraction, which is the  $\mathbf{g}^{\text{th}}$  Fourier coefficient of the crystal potential:  $V_{\mathbf{g}}$  (or  $V_{h, k, l}$ , for  $\mathbf{g} = h, k, l$ )

The phase of the structure factor:  $\phi_{\mathbf{g}}$

The three-phase invariant:  $\phi = \phi_{\mathbf{g}} + \phi_{\mathbf{h}-\mathbf{g}} + \phi_{-\mathbf{h}}$

The excitation error for reflection  $\mathbf{g}$ :  $\zeta_{\mathbf{g}}$

The interaction constant:  $\sigma = \frac{2\pi m e \lambda}{h^2}$ , where  $m$  is the relativistic mass of an electron

The structure factor used in dynamical theory of electron diffraction:  $U_{\mathbf{g}}$

$$\text{and } U_{\mathbf{g}} = \frac{K\sigma V_{\mathbf{g}}}{\pi}$$

The projection of the wave vector of the incident beam onto the zero-order Laue zone (ZOLZ) plane:  $K_t$

The extinction distance for two-beam dynamic diffraction:  $\xi$

A three-beam condition:  $0 / \mathbf{g} / \mathbf{h}$

A Friedel pair of reflections:  $\mathbf{g}$  and  $\bar{\mathbf{g}}$

A pair of centrosymmetrically related three-beam conditions:  $0 / \mathbf{g} / \mathbf{h}$  and  $0 / \bar{\mathbf{g}} / \bar{\mathbf{h}}$

The three-beam extinction distance:  $\xi_{3\text{-beam}}$

The extinction distance in the pseudo-two-beam regions:  $\xi_{\text{pseudo-2beam}}$

The eigenvalue for the  $i^{\text{th}}$  Bloch wave in dynamic diffraction:  $\gamma^i$  or  $\lambda_i$ , where



$$\frac{K}{\pi} \lambda_i = \gamma^i$$

Note: The notation for the eigen values,  $\lambda_i$ , should not be confused with the notation for the wavelength,  $\lambda$ .

The difference between two eigen values:  $\Delta\gamma$  or  $\mu$

## Conventions

This thesis has chosen  $\exp(+2\pi i \mathbf{K} \cdot \mathbf{r})$  to represent a plane wave propagating in the direction specified by the wave vector  $\mathbf{K}$ . Based on this notation, the Fourier transform of a three-dimensional potential function  $V(\mathbf{r})$  is defined as

$$V_{\mathbf{g}} = \int_{-\infty}^{+\infty} V(\mathbf{r}) \exp(-2\pi i \mathbf{g} \cdot \mathbf{r}),$$

and the inverse Fourier transform is defined as

$$V(\mathbf{r}) = \int_{-\infty}^{+\infty} V_{\mathbf{g}} \exp(2\pi i \mathbf{g} \cdot \mathbf{r}).$$

The crystallographic convention for defining the quantities in reciprocal space has been adopted:

- 1) the magnitude of wave vector  $\mathbf{K}$  is defined as  $|\mathbf{K}| = 1/\lambda$  ;
- 2) the basis vectors for reciprocal space are defined as

$$\mathbf{a}^* = \frac{\mathbf{b} \times \mathbf{c}}{\mathbf{a} \cdot (\mathbf{b} \times \mathbf{c})}, \mathbf{b}^* = \frac{\mathbf{c} \times \mathbf{a}}{\mathbf{b} \cdot (\mathbf{c} \times \mathbf{a})}, \mathbf{c}^* = \frac{\mathbf{a} \times \mathbf{b}}{\mathbf{c} \cdot (\mathbf{a} \times \mathbf{b})}.$$

The three-phase invariant,  $\phi \equiv \varphi_{\mathbf{g}} + \varphi_{\mathbf{h}-\mathbf{g}} + \varphi_{-\mathbf{h}}$ , is defined in the following direction: and the reciprocal lattice vectors,  $\mathbf{g}$ ,  $\mathbf{h}-\mathbf{g}$ ,  $-\mathbf{h}$  form a closed loop in the anticlockwise direction. This gives the sign convention for three-phase invariants in this thesis. If the three-phase invariant is defined in the clockwise direction such that  $\phi \equiv \varphi_{\mathbf{h}} + \varphi_{\mathbf{g}-\mathbf{h}} + \varphi_{-\mathbf{g}}$ , then the sign of  $\phi$  will be flipped.



## Abstract

Transmission electron microscopy and diffraction can provide structural information of materials at high spatial resolutions. Due to the strong interaction between electrons and matter, the phase information of structure factors, which is lost in kinematic diffraction, is preserved in dynamic electron diffraction. Nevertheless, it is still difficult to use dynamically diffracted intensities to solve an unknown crystal structure [1].

This work has developed a method for the measurement of the three-phase invariant, which is the summation of three structure factors phases ( $\phi = \varphi_{\mathbf{g}} + \varphi_{-\mathbf{h}} + \varphi_{\mathbf{h}-\mathbf{g}}$ ), in noncentrosymmetric crystals from convergent-beam electron diffraction (CBED) patterns. CBED patterns are taken in special crystal orientations known as three-beam conditions, where two reflections,  $\mathbf{g}$  and  $\mathbf{h}$ , satisfy their Bragg conditions simultaneously. Unlike direct methods, which derive probability distributions of the cosine phase invariants from kinematically diffracted intensities [2], three-beam CBED allows for physical measurements of three-phase invariants (including the signs) from dynamically diffracted intensities. It has been shown that replacements of the randomly assigned values of three-phase invariants with the measured ones as input to the direct methods can greatly improve phasing [3]. Therefore, it may be expected that three-beam electron diffraction may play a significant role in solving a crystal structure.

The research on three-beam electron diffraction was initiated several decades ago [4-19]. However, there are still some fundamental problems that need to be tackled. In the case of centrosymmetric crystals (where  $\phi = 0$  or  $\pi$ ), a simple inversion of three-beam dynamic diffraction has been completed [10, 11, 20], which enables the determination of the three-phase invariants by just inspection of the three-beam CBED patterns [17, 18, 21]. In the case of noncentrosymmetric crystals (where  $\phi$  can be any value between 0 and  $2\pi$ ), previous analytical theories of three-beam electron diffraction have included some approximations, which are based on perturbing kinematic [14] or two-beam dynamic diffraction [6, 15, 22], for inverting three-phase invariants. Due to the limitations of these approximations, phase measurements are limited by the applicable range of these approximations. Based on reduction of the exact solution to three-beam electron diffraction, the current work has developed a new method which allows for the determination of three-phase invariants to within  $45^\circ$  only by inspection of the three-beam CBED patterns without the necessity of knowing the specimen thickness or the structure factor magnitudes. This thesis has also implemented large-angle

rocking beam electron diffraction (LARBED) [23] to demonstrate the experiments for the new method.

In addition, an analytical theory of three-beam electron diffraction given here (which is developed from [24]) has inspired a novel approach for local composition measurement in a technically important semiconductor,  $\text{In}_x\text{Ga}_{1-x}\text{As}$ . This approach can provide simultaneous yet independent measurements of composition, thickness and possibly strain from three different parts of a single CBED pattern which is recorded in a specific three-beam condition. The composition measurement does not require any sophisticated procedures like refining the intensities in CBED but needs only a simple comparison of a certain intensity ratio in the CBED pattern to a pre-calculated look-up table based on Bloch wave calculations of many-beam diffraction. The composition measurement is not only simple but also has the potential to be very accurate and precise when compared to existing methods of composition measurement. Further simulations which contain the finite element method and multislice calculations of CBED have suggested that the current approach can be used in practical specimens, such as cross-sectional specimen of  $\text{In}_x\text{Ga}_{1-x}\text{As}/\text{GaAs}$  quantum wells.

## Chapter 1. Introduction

Crystallography is the science that examines the three-dimensional arrangement of atom positions in crystalline solids and is fundamental to many fields of research. For example, in designing a new functional or structural material, the understanding of crystal structures is an important prerequisite for understanding the properties of the material. As another example, pharmaceutical designs require the knowledge of crystal structures in both the drugs and the target proteins so that the therapeutic mechanisms can be better understood.

The determination of crystal structures employs radiation of short wavelength that is comparable to or shorter than the size of an atom ( $\sim 10^{-10}$  m) and the commonly used sources of radiation are X-rays, electrons and neutrons. Among the three types of radiation, X-rays are the most commonly used for crystal structure determination. When X-rays strike a single crystal, most of the waves are scattered in well-defined directions with respect to the crystal orientation (according to Bragg's law), resulting in a pattern of spots, a "diffraction pattern". The intensity of each spot is used for the determination of the crystal structure. However, according to the single scattering theory (also known as the kinematical theory of diffraction), measurements of the intensities in X-ray diffraction cannot provide sufficient information for defining a crystal structure (by the inverse Fourier transform). One set of parameters, called the "phase" of each scattered beam, which represents how much the waves in the different diffracted beams are displaced relative to each other, is missing from the measurements due to the nature of the kinematic diffraction. Without the knowledge of the phases, it is impossible to determine a crystal structure unequivocally. This is called "the phase problem" in X-ray crystallography.

In 1985, Karle and Hauptman were awarded the Nobel Prize in Chemistry for their work on "direct methods", which provides methods to retrieve the phases. The "direct" here means that no further knowledge about the structure except the intensities in the X-ray diffraction patterns are needed as input to the phase retrieval program. The principle behind direct methods is that atoms can be treated as discrete points and such a treatment limits the possible relationships between the phases and the intensities to a range of probabilities [25]. The application of direct methods in X-ray diffraction have shown to be very successful in *ab initio* structure determination for small-molecule structures and have contributed to most of the crystal structures that have been determined so far. These days, the crystal structure of a small-

molecule structure can be determined routinely within seconds provided that X-ray diffraction data of good quality is available. The fundamental impediment to crystal structure determination by X-ray diffraction is the growth of high quality single crystals. For some materials, growing single crystals to sizes that are usable for X-ray diffraction (from several to a few tens of micrometres in size) can be extremely difficult. In these situations, electron diffraction can be applied as it allows for the use of submicron- to nanometre-sized crystals.

Since electrons are negatively charged particles and can be strongly scattered by atoms (and the intensity of electrons scattered by an atom is typically a billion times higher than that of X-rays) [26], multiple scattering is inevitable and the kinematical theory breaks down even in a thin specimen for a transmission electron microscope (TEM). Direct methods require the intensities (as input to the programs) to be kinematic (in the fashion of single scattering). However, the intensities in electron diffraction are strongly affected by multiple scattering. Thus, electron diffraction is intrinsically not suitable for direct methods and that is why most structures have been solved by X-ray diffraction. Nevertheless, a TEM based technique called precession electron diffraction (PED) has been developed in the past few decades, which can mitigate the effect of multiple scattering in the recorded diffraction patterns. By precessing the incident electron beam around the optic axis, a PED pattern is formed by integration over the incident beam directions and has been shown to be usable in structure determinations by direct methods [27]. However, in comparison to the structure solutions by X-ray diffraction, the structures determined from PED can have relatively large errors because the dynamical effect (in other words, the effect of multiple scattering) is still present.

Every sword has two edges, so does the dynamical effect. The phase problem present in kinematic diffraction can be solved by dynamic diffraction in principle because, as will be discussed in Chapter 2 of this thesis, the intensities in dynamic electron diffraction (involving more than two diffracted beams) preserve the phase information. The phase information should be obtainable from inversion of the intensities in dynamic electron diffraction patterns (as long as the diffraction condition involves three or more beams). However, due to the complexity in the mathematical relationships between the phases and the intensities in dynamic diffraction, such an inversion is not easy to derive; and even if it is derived, it may not be feasible to implement this inversion experimentally.

This thesis has made some progress in developing a TEM method, called three-beam electron diffraction, for measuring phase information in the form of the three-phase invariants

from dynamic electron diffraction patterns recorded in special crystal orientations called three-beam conditions. In addition to its application in crystal structure determination, the study in three-beam electron diffraction has resulted in a new method for composition measurements in some zinc-blende semiconductors such as  $\text{In}_x\text{Ga}_{1-x}\text{As}$ .

This thesis is set out as follows. Chapter 2 will start with the research background for this thesis, the content of which includes the phase problem in crystallography, dynamical theories of electron diffraction and convergent-beam electron diffraction (CBED). The last section of Chapter 2 will be dedicated to a brief review of the existing analytical theories of three-beam electron diffraction. To overcome the limitations of the existing theories, Chapter 3 will present the newly developed theories in three-beam electron diffraction, which result in a simple method for the measurement of three-phase invariants from three-beam CBED patterns. Chapter 4 will illustrate the new method for measuring three-phase invariants with large-angle rocking beam electron diffraction (LARBED) [23]. Chapter 5 will present the new method for composition measurement in  $\text{In}_x\text{Ga}_{1-x}\text{As}$ . The conclusions of this thesis and proposed future work will be given in Chapter 6.





## Chapter 2. Crystallography and electron diffraction theories

This chapter will review the literatures on crystal structure determination and electron diffraction theories, which gives the research background for this thesis.

(Section 2.1) In a diffraction experiment, only intensities are recorded. The inability to measure the phase of the complex scattering amplitudes leads to the loss of information for crystal structure determination, which is known as the phase problem in crystallography. Although crystallographers have overcome the phase problem by indirect means of deducing the phases from statistics of the intensities, physical measurements of the phases would still benefit crystal structure determination. The physical measurement is based on multiple scattering of the radiation (X-rays, electrons, or neutrons), which is described by the dynamical theory of diffraction. (Section 2.2) In dynamic diffraction of electrons, several formulations have been proposed for different purposes. The theories can be used to interpret electron diffraction patterns and images formed in a transmission electron microscope (TEM). (Section 2.3) In TEM, the incident electron beams can be focused by the magnetic lenses onto a nanometre-sized region of the specimen of crystals, which results in a convergent-beam electron diffraction pattern that consists of round discs. Convergent-beam electron diffraction (CBED) patterns enable the identification of space groups of crystals based on the symmetry information contained in dynamic diffraction patterns. CBED also allows for quantitative measurements of structural properties including the phases through refinements. Nevertheless, it is still difficult to measure the phases from dynamic diffraction patterns without *a priori* knowledge of the crystal structure. (Section 2.4) However, the complexity of the phase measurement using CBED patterns can be greatly reduced when the crystal is oriented in specific directions in which two crystal planes satisfy Bragg's law simultaneously. Such a diffraction condition is called a three-beam condition, which gives the simplest form of dynamic diffraction that preserves the phases. Over the last several decades, several forms of analytical solutions to three-beam electron diffraction have been derived, which allow the phases to be measured in all centrosymmetric crystals. However, in terms of the phase measurement in noncentrosymmetric crystals, more efforts in both analytical inversion of three-beam dynamic diffraction and the experiments are needed.

## 2.1 Introduction to crystallography and the phase problem

### 2.1.1 Kinematic diffraction

In a crystalline solid, the constituents such as atoms, ions or molecules are orderly arranged in three dimensions. The smallest repeating unit of the crystalline solid is called a unit cell. In crystallography, the arrangement of the atoms in a unit cell is described by the crystal structure, which can be denoted by a set of numbers  $\{Z_i, \mathbf{r}_i\}$ , where  $Z_i$  is the atomic number of the  $i^{\text{th}}$  atom and  $\mathbf{r}_i = x_i \mathbf{a} + y_i \mathbf{b} + z_i \mathbf{c}$  is the atomic position in the unit cell (where  $\mathbf{a}, \mathbf{b}, \mathbf{c}$  are the basis vectors of the unit cell). The atomic positions are found at the local maxima of the electrostatic potential  $V(\mathbf{r})$  or the electron density  $\rho(\mathbf{r})$  of the unit cell. Without considering inelastic scattering (which applies to the whole section unless mentioned), the crystal potential function  $V(\mathbf{r})$  is a real function. Crystal structure determination, which involves the determination of  $V(\mathbf{r})$  or  $\rho(\mathbf{r})$ , is usually achieved by performing diffraction experiments.

#### a. Diffraction geometry

In X-ray and neutron diffraction experiments, the diffraction geometry is described by the Ewald sphere construction shown in Fig. 2.1. The Ewald sphere intuitively describes how a diffraction pattern of regularly spaced spots, known as “reflections” (denoted as  $\mathbf{g}, h, \dots$ ), is produced: when an incident wave with a wave vector  $\mathbf{K}_0$  (where  $|\mathbf{K}_0| = 1/\lambda$ ) is diffracted by a single crystal in the direction  $\mathbf{K}$  that satisfies the Laue condition for a family of crystal planes with the miller indexes  $(h \ k \ l)$ :

$$\mathbf{K} = \mathbf{K}_0 + \mathbf{g}, \quad (2.1a)$$

$$\mathbf{g} = h \mathbf{a}^* + k \mathbf{b}^* + l \mathbf{c}^*, \quad (2.1b)$$

where  $\mathbf{a}^*, \mathbf{b}^*, \mathbf{c}^*$  are the basis vectors in reciprocal space. For a transmission case, the Laue condition is equivalent to Bragg’s law.

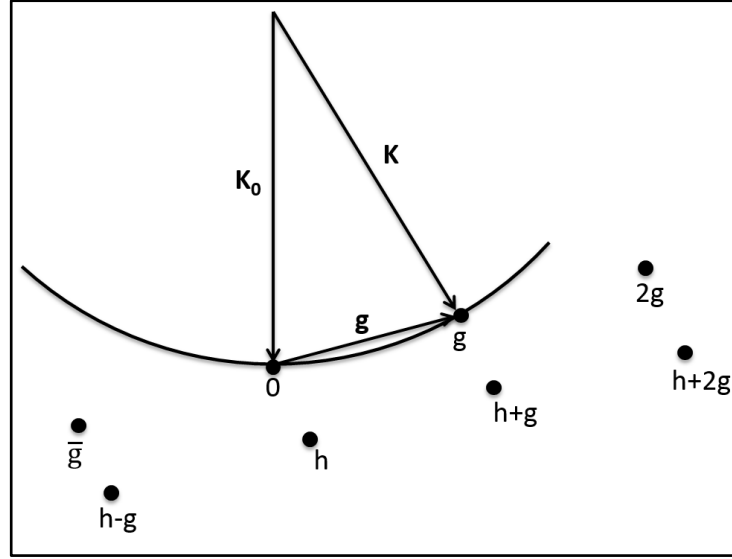


**Figure 2.1. Ewald sphere construction:** a geometric construction used in X-ray, electron and neutron diffraction to describe the connection between the reciprocal lattice of crystals and the wave vectors of incident and diffracted beams. The wave vector for the incident wave,  $\mathbf{K}_0$  (where  $|\mathbf{K}_0|=1/\lambda$  and where  $\lambda$  is the wavelength), points to the origin of reciprocal lattice. When the Laue condition (or equivalently Bragg's law) is satisfied for a set of plane which correspond to a reciprocal lattice vector  $\mathbf{g}$ , the diffracted wave vector  $\mathbf{K}$  points to the reciprocal lattice spot  $\mathbf{g}$ , giving rise to a spot of peak intensity in the diffraction pattern.

### b. The Kinematical theory of diffraction

In X-ray and neutron diffraction, the diffracted intensities can be described by the kinematical theory of diffraction.

The incident plane wave,  $\exp(+2\pi i \mathbf{K}_0 \cdot \mathbf{r})$  is weakly scattered by a single crystal in the direction  $\mathbf{K} = \mathbf{K}_0 + \mathbf{g}$  and the (complex) amplitude scattered by a unit cell at a unit distance is the superposition of the atomic scattering amplitudes of all the atoms in the unit cell, i.e.

$$F_{\mathbf{g}} = \sum_i f_i(\mathbf{g}) \exp(-2\pi i \mathbf{g} \cdot \mathbf{r}_i) , \quad (2.2)$$

where the atomic scattering amplitude  $f_i(\mathbf{g})$  is given by the first order Born approximation [26]:

$$f_i(\mathbf{K} - \mathbf{K}_0) = \frac{2\pi m|e|}{h^2} \int_{-\infty}^{+\infty} V_i(\mathbf{r}) \exp(-2\pi i (\mathbf{K} - \mathbf{K}_0) \cdot \mathbf{r}) d\mathbf{r} , \quad (2.3)$$

where  $V_i(\mathbf{r})$  is the atomic potential for the  $i^{\text{th}}$  atom in the unit cell, and  $\mathbf{K} - \mathbf{K}_0$  defines the scattering vector (which is not necessarily equal to the reciprocal lattice vector,  $\mathbf{g}$ ). The atomic scattering factor  $f_i(\mathbf{K} - \mathbf{K}_0)$  can also be denoted by  $f_i(\theta)$ , where  $\theta$  is the scattering angle and  $\sin \theta = |\mathbf{K} - \mathbf{K}_0|/2|\mathbf{K}|$ .

If only elastic scattering is considered, the atomic scattering amplitudes  $f_i(\mathbf{K} - \mathbf{K}_0)$  are real, but the amplitude scattered by the unit cell,  $F_{\mathbf{g}}$ , which is called the structure factor in crystallography, is a complex function of the reciprocal lattice vector  $\mathbf{g}$  in general (unless in centrosymmetric crystals, where  $V(\mathbf{r}) = V(-\mathbf{r})$ , the structure factors can be real when the origin of coordinates is placed at the centre of inversion). The complex structure factor for a reciprocal lattice vector  $\mathbf{g}$  has both a magnitude  $|F_{\mathbf{g}}|$  and a phase  $\varphi_{\mathbf{g}}$ . The structure factor magnitude gives the diffracted intensity as will be discussed next, the structure factor phase gives the phase of the scattered wave.

**Friedel's law:** from equation (2.1), the structure factors for a pair of reciprocal lattice vectors with the opposite directions,  $\mathbf{g}$  and  $-\mathbf{g}$ , are complex conjugates to each other:

$$F_{\mathbf{g}} = F_{-\mathbf{g}}^* , \quad (2.4a)$$

$$|F_{\mathbf{g}}| = |F_{-\mathbf{g}}| , \quad (2.4b)$$

$$\varphi_{\mathbf{g}} = -\varphi_{-\mathbf{g}} . \quad (2.4c)$$

The amplitude scattered by a single crystal in the direction  $\mathbf{K} = \mathbf{K}_0 + \mathbf{g}$  is a superposition of the amplitudes scattered by all the unit cells, which depends on the structure factor  $F_{\mathbf{g}}$ , the size of the unit cell  $V_{\text{cell}}$ , and the dimensions of the crystal. This amplitude is still complex. However, what can be recorded by the detectors are the intensities, which are real instead of complex. For the transmission of a thin-plate specimen of a single crystal with a thickness of  $z$ , the diffracted intensity of reflection  $\mathbf{g}$  is:

$$I_{\mathbf{g}} = \frac{|F_{\mathbf{g}}|^2}{K^2 V_{\text{cell}}^2 \cos^2 \theta} \frac{\sin^2(\pi z \zeta_{\mathbf{g}})}{(\pi \zeta_{\mathbf{g}})^2}, \quad (2.5)$$

where  $\zeta_{\mathbf{g}}$  is the deviation of the reciprocal lattice point  $\mathbf{g}$  from the Ewald sphere and is called excitation error, which specifies the exact crystal orientation with respect to the direction of the incident beam (the details about the excitation error will be discussed in Section 2.2.1).

Therefore, only the magnitude  $|F_{\mathbf{g}}|$  can be measured from the diffraction patterns and the phase  $\varphi_{\mathbf{g}}$  is lost.

### 2.1.2 The phase problem

In principle, both the magnitudes and the phases of the structure factors for all reflections are needed to derive the potential  $V(\mathbf{r})$  of the unit cell (and to derive the atomic positions) because the structure factors and the electrostatic potential  $V(\mathbf{r})$  of the unit cell are simply connected by an inverse Fourier transform:

$$V(\mathbf{r}) = \frac{h^2}{2\pi m |e|} \sum_{\mathbf{g}} F_{\mathbf{g}} \exp(2\pi i \mathbf{g} \cdot \mathbf{r}). \quad (2.6a)$$

In the community of electron microscopy, the structure factor is often denoted

by  $V_{\mathbf{g}}$ , where  $V_{\mathbf{g}} = \frac{h^2}{2\pi m |e|} F_{\mathbf{g}}$ . Then, the inverse Fourier transform becomes

$$V(\mathbf{r}) = \sum_{\mathbf{g}} V_{\mathbf{g}} \exp(2\pi i \mathbf{g} \cdot \mathbf{r}). \quad (2.6b)$$

Due to the loss of structure factor phases in the measurement, it is impossible to derive a unique crystal potential  $V(\mathbf{r})$  by equation (2.6b), which causes a fundamental problem, known as “the phase problem”, in crystal structure determination. The phases have to be found to determine crystal structures (and the procedure of finding the phases is often termed as “phasing”). Furthermore, the phases play a more important role than the magnitudes in confining atomic positions: studies in Fourier synthesis (inverse Fourier transform) have shown

that the atomic positions or the local maxima in  $V(\mathbf{r})$  are very sensitive to variations of phases but fairly insensitive to variations of the magnitudes [28]. The phase problem was once believed unsolvable in principle.

However, thanks to the development in solutions to the phase problem, hundreds of thousands of crystal structures have been solved and more than 800,000 crystal structures have been entered into the Cambridge structural database (CSD) [29] up to date.

### 2.1.3 Direct methods

According to the kinematical theory of diffraction, the structure factor phases cannot be measured from diffraction patterns experimentally. Nevertheless, it is still possible to derive probability distributions of the phases from the structure factor magnitudes and to deduce the atomic positions by a family of phasing methods called direct methods.

#### 2.1.3.1 Normalised structure factor and confinement of atomic positions

Even though the atomic positions in a unit cell (reconstructed by inverse Fourier transform) are not sensitive to the structure factor magnitudes, the magnitudes do vary with the atomic positions. One can realise this fact by taking the modulus square of both sides of equation (2.2) and applying the Euler's Formula for complex numbers to make the right hand side of the equation real:

$$|F_{\mathbf{g}}|^2 = \sum_i f_i(\mathbf{g})^2 + 2 \sum_{i \neq j} f_i(\mathbf{g}) f_j(\mathbf{g}) \cos(-2\pi i \mathbf{g} \cdot (\mathbf{r}_i - \mathbf{r}_j)) , \quad (2.7)$$

where  $|\mathbf{r}_i - \mathbf{r}_j|$  is the distance between  $i^{\text{th}}$  and  $j^{\text{th}}$  atom in the unit cell.

If : 1) all the atoms in a unit cell are assumed to be non-vibrating point scatterers, i.e., the atomic potential in (2.2) is replaced by a delta function,  $V_i(\mathbf{r}) = Z_i \delta(\mathbf{r})$ , and 2) the potential in the unit cell is positive everywhere, then the equation (2.7) will become

$$|E_{\mathbf{g}}|^2 = 1 + \frac{2 \sum_{ij} Z_i Z_j \cos(-2\pi i \mathbf{g} \cdot (\mathbf{r}_i - \mathbf{r}_j))}{\sum_i Z_i^2} , \quad (2.8a)$$

where  $E_{\mathbf{g}}$  is called the normalised structure factor which has the same phase as  $F_{\mathbf{g}}$ . The magnitude of the normalised structure factor is:

$$|E_{\mathbf{g}}|^2 = \frac{|F_{\mathbf{g}}|^2}{\sum_i f_i(\mathbf{g})^2} , \quad (2.8b)$$

which can be determined approximately from  $|F_{\mathbf{g}}|^2$  if the atomic numbers and the composition is known. Otherwise, an approximation needs to be made, for example

$$\sum_i f_i(\mathbf{g})^2 = \langle |F_{\mathbf{g}}|^2 \rangle , \quad (2.8c)$$

where  $\langle |F_{\mathbf{g}}|^2 \rangle$  is the mean value of  $|F_{\mathbf{g}}|^2$  over all the reflections within a range of scattering angles which is centred at the Bragg angle of reflection  $\mathbf{g}$ ,  $\theta_{\mathbf{g}}$ . The approximation was proposed by Wilson (1942) [30], which can also be derived from equation (2.7).

Equation (2.8a) represents a family of equations for all different reflections, which connect the measurable quantities,  $|E_{\mathbf{g}}|$ , with the interatomic distances  $|\mathbf{r}_i - \mathbf{r}_j|$ . In general, the number of the unknowns,  $|\mathbf{r}_i - \mathbf{r}_j|$ , is overwhelmed by the number of the equations which have the form of (2.8a). Therefore, the phase problem is reduced to solving a finite number of unknowns in an overdetermined system and it becomes possible to solve the atomic positions from the structure factor magnitudes once the origin of the unit cell is fixed [25].

### 2.1.3.2 Phase invariants

The choice of origin of the crystal potential function  $V(\mathbf{r})$  affects structure factor phases. If the origin is translated by  $\mathbf{r}_0$ , the crystal potential will become

$$V(\mathbf{r} - \mathbf{r}_0) = \sum_{\mathbf{g}} |V_{\mathbf{g}}| \exp(2\pi i \mathbf{g} \cdot \mathbf{r}) \exp(i\varphi_{\mathbf{g}} + 2\pi i \mathbf{g} \cdot \mathbf{r}_0) . \quad (2.9a)$$

The structure factor in the new coordinate system is:

$$V'_g = |V_g| \exp(i\varphi_g + 2\pi i \mathbf{g} \cdot \mathbf{r}_0), \quad (2.9b)$$

so the phase depends on  $\mathbf{r}_0$ , which can be arbitrary.

However, the product of structure factors for the reciprocal vectors that form a closed loop is invariant. For example, the product of three structure factors:

$$\begin{aligned} V'_g V'_{h-g} V'_{-h} &= |V_g| |V_{h-g}| |V_{-h}| \exp\{i(\varphi_g + \varphi_{h-g} + \varphi_{-h}) \\ &\quad + 2\pi i(\mathbf{g} + \mathbf{h} - \mathbf{g} - \mathbf{h}) \cdot \mathbf{r}_0\} \end{aligned} \quad (2.10a)$$

$$V'_g V'_{h-g} V'_{-h} = V_g V_{h-g} V_{-h}. \quad (2.10b)$$

In equation (2.10a), the summation of the three structure factor phases,

$$\phi = \varphi_g + \varphi_{h-g} + \varphi_{-h}, \quad (2.11)$$

is invariant with respect to translations of the origin and is a property of the crystal structure. Thus, it is termed as **three-phase invariant**<sup>1</sup>

### 2.1.3.3 The statistical phasing method

Direct methods are based on probabilistic relationships between the normalised structure factors magnitudes and cosine phase invariants (not limited to three-phase invariants) to deduce the phases of structure factors [25]. By eliminating the atomic position vectors, conditional probability distribution of phase invariants can be associated with the normalised structure factor magnitudes (since the phase invariants are unknown, they are treated as random variables). For example, the conditional probability distribution of three-phase invariants,  $P(\phi \mid |E_g|, |E_h|, |E_{h-g}|)$ , tends to give a mean value of  $\phi$  at  $\phi = 0$  with small variances (high

---

<sup>1</sup> It is also termed as “three-phase structure invariant” or “triplet phase”.



probability) when  $|E_g|, |E_h|, |E_{h-g}|$  are all large [31]. A consequence of this statistical theorem is the most commonly used tangent formula [2]:

$$\langle \tan \varphi_g \rangle = \frac{\sum_h |E_h| |E_{h-g}| \sin(\varphi_{h-g} + \varphi_{-h})}{\sum_h |E_h| |E_{h-g}| \cos(\varphi_{h-g} + \varphi_{-h})}, \quad (2.12)$$

where a series of reciprocal lattice vectors,  $\mathbf{h}$ , are chosen so that both  $|E_h|$  and  $|E_{h-g}|$  are large.

#### 2.1.3.4 The enantiomorph problem

Two structures which are related to each other by a centre of inversion, i.e.,  $V(\mathbf{r})$  and  $V(-\mathbf{r})$ , are said to be enantiomorphs of each other if the two structures cannot be superimposed onto each other by pure rotations. Such structures are called enantiomorphic structures or chiral structures. Equation (2.2) shows that reversing the direction of the atomic position vectors ( $\mathbf{r}_i \rightarrow -\mathbf{r}_i$ ) will change the sign of the structure factor phase ( $\varphi_g \rightarrow -\varphi_g$ ) and therefore the sign of phase invariants. Equation (2.7) shows that reversing the direction of the atomic position vectors ( $\mathbf{r}_i \rightarrow -\mathbf{r}_i$  and  $\mathbf{r}_j \rightarrow -\mathbf{r}_j$ ) does not change the structure factor magnitudes or diffracted intensities, which means that a pair of chiral structures cannot be distinguished from kinematic diffraction patterns. In direct methods, probability distributions of three-phase invariants,  $P(\phi | |E_g|, |E_h|, |E_{h-g}|)$ , show equal probability at  $+\phi$  and  $-\phi$ , which leads to the enantiomorph ambiguity [2]. The enantiomorph has to be chosen arbitrarily by fixing the signs of a phase invariant in the early stage of structure solutions (known as *ab initio* structure determination). The uncertainty of the signs of the phase invariants can cause difficulties in solving crystal structures by direct methods, which is termed as the enantiomorph problem or the sign problem [2].

#### 2.1.4 Other phasing techniques

##### 2.1.4.1 Charge flipping algorithm

In recent years, an alternative to direct methods called charge flipping algorithm (CFA) [32] which uses alternating modifications in real and reciprocal spaces with an initial set of randomly assigned structure factor phases (without invoking phase-invariants) have become

popular in structure determination. The enantiomorph problem still exist in the new method because CFA also depends on kinematic diffraction data.

#### 2.1.4.2 Anomalous scattering

When the incident X-ray waves oscillate at the same frequency as the atomic orbital frequency, resonance will occur which perturbs atomic scattering, resulting in an atomic scatter amplitude that is complex as opposed to real in normal atomic scattering. Such a deviation to the normal atomic scattering is called the anomalous scattering effects, which can make the intensities between a Friedel pair,  $I_g$  and  $I_{-g}$ , unequal and can resolve the enantiomorph ambiguity given that the elements that can be used for anomalous scattering are present in the crystal structure [33]. If the elements that can be used for anomalous scattering do not exist in the crystal, isomorphous replacements can be carried out.

#### 2.1.4.3 Isomorphous replacement

In protein crystallography, some atoms can be replaced by heavy atoms or ions through chemical reactions in heavy-atom solutions. Presumably, the space group as well as the atom positions in the newly derived structure are the same as the previous structure (or the native structure), which is called an isomorphous replacement. The process can be repeated in different heavy-atom solutions, giving multiple isomorphous replacements. The diffraction patterns from such a derivative structure will differ from those recorded from a native structure and the differences can be used to deduce the heavy atom positions from anomalous scattering or Patterson difference map [34].

#### 2.1.4.4 Multiple scattering solutions

In kinematical theory of diffraction, the amplitude scattered by a single crystal is a superposition of the amplitudes scattered by every individual atom within the crystal, and the atomic scattering amplitude is described by the first Born approximation. In this theory, the incident wave has only been scattered once by one set of crystal planes that satisfies the Bragg condition. Such a theoretical treatment works for X-ray diffraction because:

- 1) The interaction between the waves and the crystal is weak.
- 2) Real single crystals used in X-ray diffraction experiments usually have a size of few to a few dozen  $\mu\text{m}$ . They are not perfect themselves but are seen as mosaics of perfect

crystals (or so-called mosaic blocks) with 100 nm in size for each dimension, which are mis-oriented to each other by less than  $0.02^\circ$  (in reality about  $0.2^\circ$ ). Since the interference can only occur for the waves scattered from the same mosaic block and waves diffracted from different mosaic blocks are incoherent, kinematical theory of diffraction can be applied to X-ray diffraction of real single crystals [35].

However, if a single crystal is perfect (low in mosaicity) and large in size (tens of  $\mu\text{m}$ ), the kinematical theory of diffraction which assumes single scattering will fail and multiple scattering effects will arise: the incident wave is diffracted more than once and by more than one family of crystal planes. The reflection intensity depends on the relative phase of complex amplitudes scattered by different crystal planes and the relative phase is just equal to the phase invariants (which will be discussed in Section 2.4). The phase invariants of structure factors are now preserved in the diffraction patterns and therefore can be measured in principle, which can solve the phase problem as well as the enantiomorph ambiguity in a more direct and reliable fashion.

A number of practices in multiple scattering of X-rays have shown encouraging results in measuring three phase-invariants from organic crystals to small protein crystals (for a review see [36-38]). However, the requirement for growing single crystals with low mosaicity has presented huge impediments to the development of multiple scattering solutions to the phase problem [39]. Also, the interpretation of dynamic diffraction patterns for crystals with large unit cells are challenging as the inverse problem for dynamic diffraction is difficult to solve. Thirdly, the speed of data collection is usually very slow in an X-ray diffractometer.

Electron diffraction can be a good way to overcome these limitations:

1) Due to the strong Coulomb interaction (the atomic scattering amplitude of electrons is  $10^4 \sim 10^5$  times higher than that of X-rays [26]), crystals of just a few nanometres thick can result in strong multiple scattering effects. Therefore, the growth of crystals is no longer a problem.

2) Data collection can be more efficient because more instrumental flexibility is available in an electron microscope. For example, both the incident electron beam and the specimen can be tilted in a TEM while only the specimen can be tilted in a synchrotron X-ray diffractometer.

3) With advancements in computation and algorithms, difficulties in data analyses may become solvable.

A challenge for applying electron diffraction is the beam damage due to the high energies of electron and their strong interactions with crystals. However, low dose diffraction techniques can be developed to overcome such issues.

Multiple scattering effects in electron diffraction need to be accounted for by a full dynamical theory of electron diffraction.

## 2.2 Dynamical theory of electron diffraction

Starting from the time-independent Schrödinger equation, different formulations of dynamical theory of electron diffraction are reviewed.

### 2.2.1. The defining equation

For 200 KeV electrons, the speed of the electrons is about 70% of the speed of light. Special relativity needs to be taken into account. The physical law for the motion of electrons near the speed of light should be the Dirac equation, which involves a four-potential to make it a Lorentz invariant. However, in the community of electron microscopy, where characterising the structure of materials is of primary interest, it is a common practice to apply the time-independent Schrödinger equation (which is intrinsically non-relativistic since the Hamiltonian is not a Lorentz invariant) with so-called “relativistic corrections” that compensate the relativistic effect:

$$-\frac{\hbar^2}{2m}\nabla^2\Psi(\mathbf{r}) - |e|V(\mathbf{r})\Psi(\mathbf{r}) = \frac{\hbar^2\mathbf{k}_0^2}{2m}\Psi(\mathbf{r}) , \quad (2.13)$$

where  $\mathbf{k}_0$  is the wave vector <sup>2</sup> of the incident electrons such that  $\mathbf{k}_0 = 1/\lambda$ ,  $|e|$  is the charge of an electron and  $\hbar = h/2\pi$  ( $h$  is the Planck’s constant).

---

<sup>2</sup> In crystallography, the magnitude of the wave vector is the reciprocal of the wavelength rather than  $2\pi/\lambda$  as in In quantum mechanics and solid-state physics

In equation (2.13), two “relativistic corrections” are made:

- 1) The relativistically-corrected wavelength of the electrons is

$$\lambda = h[2m_0eW(1 + |e|W/2m_0c^2)]^{-1/2} , \quad (2.14)$$

where  $W$  is the accelerating voltage,  $m_0$  is the static mass of an electron,  $c$  is the speed of light.

- 2) The relativistically corrected electron mass is:

$$m = m_0 \sqrt{1 + (\hbar^2 k_0^2 / m_0^2 c^2)} . \quad (2.15)$$

The validity of such corrections has been tested by comparison to the Dirac equation [40, 41], which shows that, to a very good approximation, the effect of electron spin can be neglected so that the solution to equation (2.13) is the same as that to the Dirac equation. A breakdown of the corrections has also been found when inelastic scattering is considered [42].

By defining  $U(\mathbf{r}) = \frac{2m|e|}{\hbar^2} V(\mathbf{r})$ , equation (2.13) becomes:

$$\nabla^2 \Psi(\mathbf{r}) + \left( 4\pi^2 k_0^2 + 4\pi^2 U(\mathbf{r}) \right) \Psi(\mathbf{r}) = 0 . \quad (2.16)$$

There are several approaches to solving equation (2.16). The Bloch wave method and multislice algorithm are commonly used for finding numerical solutions of dynamic electron diffraction. Other formulations are also useful for different purposes.

### 2.2.2. Bloch wave formulation

For a periodic potential,  $V(\mathbf{r})$ , one of the solutions to equation (2.16),  $\psi^j(\mathbf{r})$ , must satisfy the Bloch theorem [22]:

$$\psi^j(\mathbf{r}) = C(\mathbf{r}) \exp(2\pi i \mathbf{k}_0^j \cdot \mathbf{r}) , \quad (2.17)$$

where  $C(\mathbf{r})$  is a periodic function and can be expanded by inverse Fourier transform, and  $\mathbf{k}_0^j$  is the wave vector for the  $j^{\text{th}}$  Bloch wave which points to the origin of reciprocal lattice.

$$C(\mathbf{r}) = \sum_{\mathbf{h}} C_{\mathbf{h}}^j \exp(2\pi i \mathbf{h} \cdot \mathbf{r}) . \quad (2.18)$$

Substituting equation (2.18) into (2.17) yields

$$\psi^j(\mathbf{r}) = \sum_{\mathbf{h}} C_{\mathbf{h}}^j \exp[2\pi i (\mathbf{k}_0^j + \mathbf{h}) \cdot \mathbf{r}] . \quad (2.19a)$$

Since  $C_{\mathbf{h}}^j$  characterises the same Bloch state as  $C_{\mathbf{k}_h}^j$ , equation (2.19 a) can also be written as:

$$\psi^j(\mathbf{r}) = \sum_{\mathbf{k}_h} C_{\mathbf{k}_h}^j \exp[2\pi i \mathbf{k}_h^j \cdot \mathbf{r}] , \quad (2.19b)$$

where  $\mathbf{k}_h^j = \mathbf{k}_0^j + \mathbf{h}$  .

Fourier transform of equation (2.16) (from  $\mathbf{r}$  to  $\mathbf{k}_h^j$  ) gives:

$$\left( \mathbf{k}_0^j{}^2 + U_0 - \mathbf{k}_h^j{}^2 \right) C_{\mathbf{h}}^j + \sum_{\mathbf{g} \neq \mathbf{h}} U_{\mathbf{h}-\mathbf{g}} C_{\mathbf{g}}^j = 0 , \quad (2.20a)$$

where  $U_{\mathbf{g}} = \frac{2m|e|}{\hbar^2} V_{\mathbf{g}}$  .

$U_0$  is the zeroth order Fourier coefficient of  $U(\mathbf{r})$  and represents the mean inner potential.

The wave vector for the incident wave is modified by including the mean inner

potential such that  $\mathbf{K}_0 = \sqrt{\mathbf{k}_0^2 + U_0} \frac{\mathbf{k}_0}{|\mathbf{k}_0|}$ . Then, equation (2.20.a) becomes:

$$[\mathbf{K}_0^2 - (\mathbf{k}_0^j + \mathbf{h})^2] C_h^j + \sum_{g \neq h} U_{h-g} C_g^j = 0 \quad (2.20b)$$

Physically, equation (2.20b) defines the wave vectors,  $\mathbf{k}_0^j$ , for Bloch waves ( $j=1,2,3\dots$ ) at a fixed total energy of the fast electrons. The geometric construction of the wave vectors involved in dynamic diffraction is depicted in Fig. 2.2.

In Fig. 2.2, we plot an Ewald sphere with a radius of  $|\mathbf{K}_0|$  ( $=|\mathbf{K}|$ ). The Ewald sphere misses the reciprocal lattice point  $\mathbf{h}$  by a distance of  $|\boldsymbol{\zeta}_h|$ . The vector  $\boldsymbol{\zeta}_h$  starts from the reciprocal lattice point  $\mathbf{h}$  and ends at the Ewald sphere. Therefore,  $\mathbf{K} \cdot \boldsymbol{\zeta}_h$  is positive when the reciprocal lattice point  $\mathbf{h}$  is inside the Ewald sphere, otherwise  $\mathbf{K} \cdot \boldsymbol{\zeta}_h$  is negative. The sign of  $\boldsymbol{\zeta}_h$  is defined to be the same as  $\mathbf{K} \cdot \boldsymbol{\zeta}_h$ . The vectors are connected by a relation, where

$$\mathbf{K} = \mathbf{K}_0 + \mathbf{h} + \boldsymbol{\zeta}_h. \quad (2.21)$$

We consider transmission of electrons through a slab sample with a thickness of  $z$ . The boundary conditions imply that the tangential components of wave vectors on both sides of the boundaries are equal (which is equivalent to Snell's law of refraction). To include the boundary condition, we draw a line that passes through the centre of the Ewald sphere and lies parallel to the surface normal vector  $\mathbf{n}$ . The origins of all of the wave vectors lie on this line so that all of the incident waves have the same tangential component. The wave vectors for Bloch wave  $\psi^j(\mathbf{r})$ ,  $\mathbf{k}_0^j$ ,  $\mathbf{k}_h^j$ ,  $\mathbf{k}_g^j \dots$  all originate from the same tie point  $L^j$ , which is separated from the centre of Ewald sphere,  $L$ , by a distance of  $|\boldsymbol{\gamma}^j|$  or  $\gamma^j$ . The eigenvalue  $\boldsymbol{\gamma}^j$  specifies the difference between the  $\mathbf{n}$  components of the wave vectors  $\mathbf{K}_0$  and  $\mathbf{k}_0^j$  and is a real number when inelastic scattering is ignored.

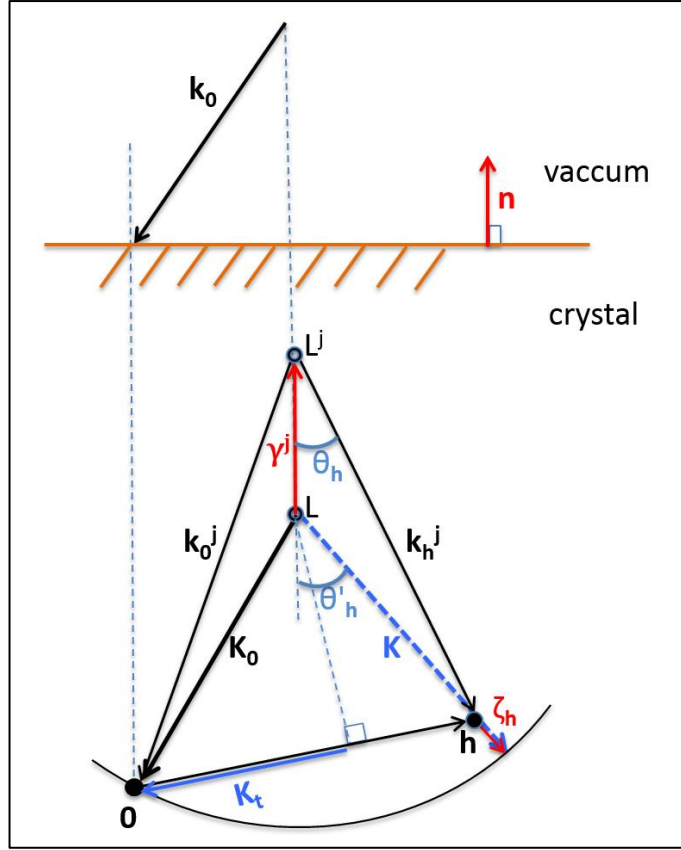


**Figure 2.2. Construction of the wave vectors in dynamic electron diffraction.** To present with a neat diagram, the wave vectors for only one Bloch state and one reciprocal lattice point are sketched. The incident wave vectors  $\mathbf{k}_0$  (in vacuum) and  $\mathbf{K}_0$  (in crystal) have equal tangential components according to Snell's law of refraction. The point L defines the centre of the Ewald sphere, and two wave vectors  $\mathbf{K}_0$  and  $\mathbf{K}$  ( $|\mathbf{K}| = |\mathbf{K}_0|$ ) origin from that point.  $\mathbf{K}_0$  points to the origin of reciprocal lattice and  $\mathbf{K}$  (in blue) passes the reciprocal lattice point h (c.f. Fig. 2.1). All the wave vectors that characterise the  $j^{\text{th}}$  Bloch state origin from the tie point,  $L^j$ , which is displaced from the point L by a vector of  $\boldsymbol{\gamma}^j$ . The excitation error of reflection h,  $\zeta_h$ , lies collinearly with the wave vector  $\mathbf{K}$ . The reciprocal vector  $\mathbf{h}$  together with other reciprocal vectors (not drawn here) can define a reciprocal plane called zero order Laue zone (ZOLZ). The projection of the incident wave vector  $\mathbf{K}_0$  in ZOLZ is denoted by  $\mathbf{K}_t$ . Since  $\mathbf{K}$  is normally three orders of magnitude higher than  $\boldsymbol{\gamma}^j$ , to a very good approximation,  $\theta'_h \approx \theta_h$  and  $\mathbf{k}_h^j + \mathbf{K} \approx 2\mathbf{K}$ .



Since we have the relation,

$$\mathbf{k}_h^j = \mathbf{K} - \boldsymbol{\zeta}_h - \boldsymbol{\gamma}^j, \quad (2.22)$$

we can express the term in (2.20b) with the newly defined terms,  $\boldsymbol{\zeta}_h$  and  $\boldsymbol{\gamma}^j$  :

$$\mathbf{K}_0^2 - \mathbf{k}_h^j{}^2 = \mathbf{K}^2 - \mathbf{k}_h^j{}^2 = (\mathbf{K} - \mathbf{k}_h^j) \cdot (\mathbf{K} + \mathbf{k}_h^j) = 2K(\boldsymbol{\zeta}_h - \boldsymbol{\gamma}^j \cos \theta_h) \quad (2.23)$$

where we have made an approximation for high energy electrons as such

$$\mathbf{k}_h^j + \mathbf{K} \approx 2\mathbf{K}. \quad (2.24)$$

Therefore, equation (2.20b) can be re-written as:

$$2K \boldsymbol{\zeta}_h \cdot \mathbf{C}_h^j + \sum_{\mathbf{g} \neq \mathbf{h}} U_{\mathbf{h}-\mathbf{g}} C_g^j = 2K \boldsymbol{\gamma}^j \cos \theta_h C_h^j. \quad (2.25a)$$

If the angle between the scattered wave and the surface normal,  $\theta_h$ , is small, i.e.  $\cos \theta_h \approx 1$ , then equation (2.25a) will become:

$$2K \boldsymbol{\zeta}_h \cdot \mathbf{C}_h^j + \sum_{\mathbf{g} \neq \mathbf{h}} U_{\mathbf{h}-\mathbf{g}} C_g^j = 2K \boldsymbol{\gamma}^j C_h^j, \quad (2.25b)$$

which can be expressed by an eigenmatrix equation such that

$$\begin{pmatrix} 0 & \sigma V_g^* & \sigma V_h^* & \sigma V_{g'}^* & \sigma V_{h'}^* & \cdots \\ \sigma V_g & 2\pi \boldsymbol{\zeta}_g & \sigma V_{h-g}^* & \sigma V_{g'-g}^* & \sigma V_{h'-g}^* & \cdots \\ \sigma V_h & \sigma V_{h-g} & 2\pi \boldsymbol{\zeta}_h & \sigma V_{g'-h}^* & \sigma V_{h'-h}^* & \cdots \\ \sigma V_{g'} & \sigma V_{g'-g} & \sigma V_{g'-h} & 2\pi \boldsymbol{\zeta}_{g'} & \sigma V_{h'-g'}^* & \cdots \\ \sigma V_{h'} & \sigma V_{h'-g} & \sigma V_{h'-h} & \sigma V_{h'-g'} & 2\pi \boldsymbol{\zeta}_{h'} & \cdots \\ \vdots & \vdots & \vdots & \vdots & \vdots & \ddots \end{pmatrix} \begin{pmatrix} C_0 \\ C_g \\ C_h \\ C_{g'} \\ C_{h'} \\ \vdots \end{pmatrix} = \lambda \begin{pmatrix} C_0 \\ C_g \\ C_h \\ C_{g'} \\ C_{h'} \\ \vdots \end{pmatrix}. \quad (2.26a)$$

The eigenmatrix can be denoted by  $\mathbf{A}$  and the eigenvector can be denoted by  $\mathbf{C}$ , thus the equation (2.26a) can also be written as:

$$\mathbf{A} \mathbf{C} = 2K_0 \gamma^j \mathbf{C} . \quad (2.26b)$$

The diagonal elements in the eigenmatrix  $\mathbf{A}$  specify the angle of incidence:

$$2K\zeta_h = -2\mathbf{K}_0 \cdot \mathbf{h} - \mathbf{h}^2 . \quad (2.27a)^3$$

The incident wave vector  $\mathbf{K}_0$  can be projected onto the plane in which the reciprocal lattice vectors  $\mathbf{h}, \mathbf{g}, \mathbf{g}-\mathbf{h}, \dots$  lie (more than two reciprocal vectors). Such a plane is known as zero-order Laue zone (ZOLZ) plane. The projected component of  $\mathbf{K}_0$  is denoted by  $\mathbf{K}_t$ , which can specify the incident beam direction alone such that

$$2K\zeta_h = -2\mathbf{K}_t \cdot \mathbf{h} - \mathbf{h}^2 . \quad (2.27b)$$

The normal vector to the ZOLZ plane, which is perpendicular to  $\mathbf{g}, \mathbf{h}, \mathbf{g}-\mathbf{h}$ , etc., is often referred to as the zone axis<sup>4</sup>. Usually, a zone axis is denoted by a real space vector  $[u \ v \ w]$ , where  $u, v$  and  $w$  are all integers.

The plot of  $\gamma^j$  versus  $\mathbf{K}_t$  (or  $(\zeta_g, \zeta_h)$ ) is called a dispersion surface, which is an important concept that will be covered in later discussions.

The exit wave function,  $\psi(\mathbf{r})$ , can be expanded in eigenstates (Bloch waves):

$$\psi(\mathbf{r}) = \sum_j \alpha^j \psi^j(\mathbf{r}) = \sum_j \alpha^j \left\{ \sum_{\mathbf{h}} C_{\mathbf{h}}^j \exp[2\pi i(\mathbf{k}_0^j + \mathbf{h}) \cdot \mathbf{r}] \right\} . \quad (2.28)$$

---

<sup>3</sup> This can be derived from (2.21) by squaring both sides of the equation and omitting the insignificant terms.

<sup>4</sup> The choice of zone axis and therefore ZOLZ plane can be arbitrary. However, it is conventional to choose an orientation near the incident beam direction where the corresponding ZOLZ plane contains many reciprocal lattice vectors.

It can be also expanded in reciprocal space:

$$\psi(\mathbf{r}) = \sum_{\mathbf{h}} \Psi_{\mathbf{h}} \exp[2\pi i (\mathbf{K}_0 + \mathbf{h}) \cdot \mathbf{r}] . \quad (2.29)$$

Since  $\gamma^j = \mathbf{K}_0 - \mathbf{k}_0^j$  , by combining equation (2.28) and (2.29), we have:

$$\Psi_{\mathbf{h}} = \sum_j \alpha^j C_{\mathbf{h}}^j \exp(-2\pi i \gamma^j z) . \quad (2.30)$$

If incident wave is a plane wave, the boundary condition at the entrance yield:

$$\alpha^j = (C^{-1})_0^j , \quad (2.31)$$

where  $(C^{-1})_0^j$  is the element of  $C^{-1}$  , which is the inverse matrix of  $C_{\mathbf{h}}^j$ .

Therefore, the intensity of reflection h is:

$$I_{\mathbf{h}} = |\Psi_{\mathbf{h}}|^2 = \left| \sum_j (C^{-1})_0^j C_{\mathbf{h}}^j \exp(-2\pi i \gamma^j z) \right|^2 . \quad (2.32)$$

### 2.2.3. Multislice

In 1957, Cowley and Moodie treated a crystal as discrete slices of two-dimensional scattering planes separated by vacuum gaps and applied wave optics to formularise the multiple scattering process [43]. The two-dimensional potential of  $n^{\text{th}}$  slice is projected from the potential between  $z_n$  and  $z_n + \Delta z$ , (shown in Fig. 2.3) viz:

$$V_n(x, y) = \int_{z_n}^{z_n + \Delta z} V(x, y, z) dz . \quad (2.33)$$

Thus the phase change produced by transmission through the  $n^{\text{th}}$  slice is:

$$q_n(x, y, \Delta z) = \exp\{i\sigma V_n(x, y)\Delta z\}, \quad (2.34)$$

where  $\sigma$  is the interaction constant and  $\sigma = \frac{2\pi me\lambda}{h^2}$ .

Then, the Huygens-Fresnel principle is applied to calculate the evolution of the wave function from one slice to the next:

$$\psi_{n+1}(x, y, z_n + \Delta z) = \{\psi_n(x, y, z_n)q_n(x, y, \Delta z)\} \otimes p(x, y, \Delta z), \quad (2.35)$$

where

$$p(x, y, \Delta z) = \frac{1}{i\lambda\Delta z} \exp\left\{\frac{i\pi(x^2 + y^2)}{\Delta z\lambda}\right\} \quad (2.36)$$

is the propagation function in the small-angle-scattering approximation and  $\otimes$  is the convolution operator.

Although multislice was originally derived from a physical optics approach, equation (2.35) can also be derived from the integral solution to equation (2.16), where backscattering is omitted and the small-angle scattering is assumed [44]. Also, the incident beam is perpendicular to the slices. To incorporate the effect of inclined illumination with a large angle, it is necessary to modify of the propagation function and the interaction constant [45].

There are two main advantages of multislice. First, the fast Fourier transform (FFT) can be included to accelerate the numerical calculation [46]. In contrast, Bloch wave method can become extremely slow when a large number of reflections are included in the eigenmatrix (as the diagonalization of a large matrix is slow). Secondly, unlike Bloch wave, the multislice calculations do not require any periodicity in the structure (but the four sides of the image for each slice must obey periodic boundary conditions to avoid wrap-around error in FFT). Therefore, the multislice method can calculate electron scattering by crystals containing defects, dislocations, interfaces, etc.

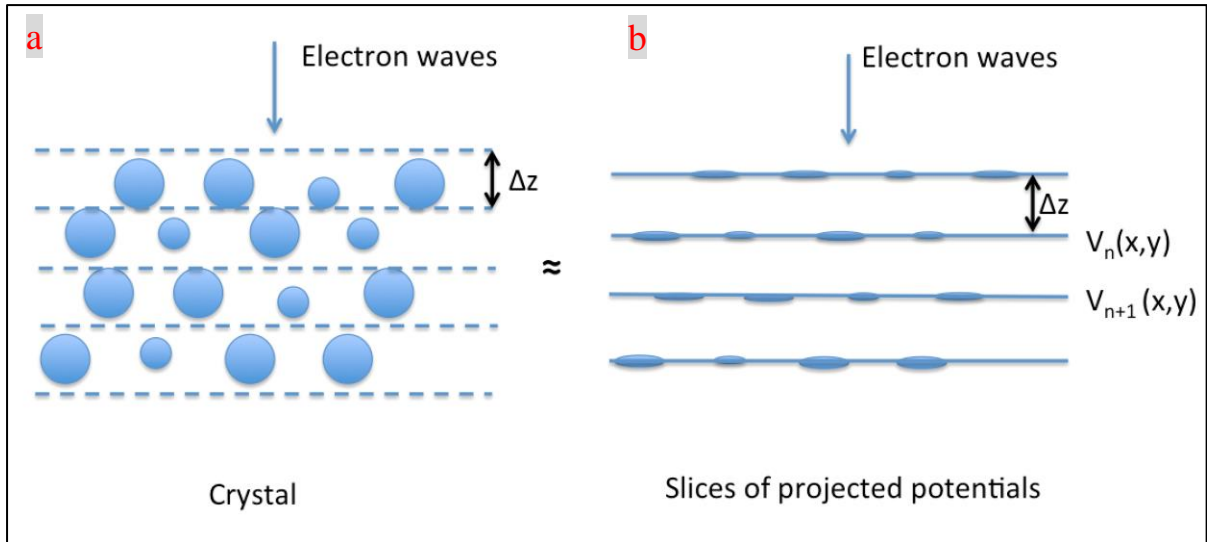


**Figure 2.3. Three-dimensional crystals are treated as slices of two-dimensional potentials in multislice.** The whole TEM specimen (a) is decomposed into slices (labelled with the dashed lines) that are perpendicular to the direction of the incident wave, and the three-dimensional potentials within each slice are projected onto two-dimensional planes, which are treated as two-dimensional phase objects (b),  $V_n(x, y)$ .

#### 2.2.4. Other formulations

This subsection will introduce three other formulations of dynamic electron diffraction. The theories involve scattering matrix, projection operators and Born series, respectively. These formulations are commonly used for analytical analyses, which will be discussed in later discussions.

##### 2.2.4.1 The scattering matrix

The scattering matrix theory can be derived from the eigenmatrix equation (2.26a), resulting in a simple matrix form:

$$\begin{pmatrix} \psi_0 \\ \psi_g \\ \psi_h \\ \psi_{g'} \\ \psi_{h'} \\ \vdots \end{pmatrix} = \exp\left(\frac{i\pi}{K} \mathbf{A} z\right) \begin{pmatrix} 1 \\ 0 \\ 0 \\ 0 \\ 0 \\ \vdots \end{pmatrix} \quad (2.37a)$$

where  $\mathbf{A}$  is the eigenmatrix in equation (2.26a) [47, 48].

If we adopt a different notation convention (to include  $\sigma V_{\mathbf{g}}$  in the off-diagonal elements, which is consistent with the literatures that will be discussed later sections) such that:

$$\mathbf{M} = \frac{\pi}{K} \mathbf{A}, \quad \mathbf{M} \mathbf{C} = \lambda_i \mathbf{C} \text{ and } \frac{K}{\pi} \lambda_i = \gamma^i.$$

Then equation (2.37a) can be re-written as:

$$\begin{pmatrix} \psi_0 \\ \psi_g \\ \psi_h \\ \psi_{g'} \\ \psi_{h'} \\ \vdots \end{pmatrix} = \exp(i \mathbf{M} z) \begin{pmatrix} 1 \\ 0 \\ 0 \\ 0 \\ 0 \\ \vdots \end{pmatrix}, \quad (2.37b)$$

which can be expressed in the Dirac notation as

$$|\psi\rangle = \mathbf{S}|0\rangle, \quad (2.37c)$$

where  $\mathbf{S} = \exp(i \mathbf{M} z)$  is the unitary scattering matrix. Thus, equations (2.37c) can be seen as rotation in Hilbert space [49].

#### 2.2.4.2 The projection operator

Furthermore, equation (2.37c) can be further developed to include projection operators:

$$|\psi\rangle = \mathbf{S}|0\rangle = \sum_i \mathbf{P}_i \exp(2\pi i \lambda_i z), \quad (2.38)$$

where the projection operator for the  $i^{\text{th}}$  Bloch wave is

$$\mathbf{P}_i = \prod_{n \neq i} \frac{(\mathbf{M} - \lambda_n \mathbf{I})}{\lambda_i - \lambda_n}, \quad (2.39)$$

and  $\mathbf{I}$  is the identity matrix [50].

These formulae provide analytical insights into dynamic diffraction and will be the bases for the theoretical treatment of three-beam electron diffraction in Chapter 3.

### 2.2.4.3 The Born series

The multislice formulation for the multiple scattering of electrons in crystals can be recast into a Born series with an increasing power of structure factors and the thickness:

$$\Psi_{hkl} = \sum_{n=1}^{\infty} \Psi_{hkl}^{(n)} = \sum_{n=1}^{\infty} E_n Z_n , \quad (2.40a)$$

and

$$E_n = \sum_l \sum_{h_1} \sum_{l_1} \sum_{k_1} \cdots \sum_{h_{n-1}} \sum_{k_{n-1}} \sum_{l_{n-1}} (\sigma V_{h_1, k_1, l_1}) \cdots$$

$$\cdots (\sigma V_{h-\sum_{r=1}^{n-1} h_r, k-\sum_{r=1}^{n-1} k_r, l-\sum_{r=1}^{n-1} l_r}) , \quad (2.40b)$$

where the total scattering amplitude,  $\Psi_{hkl}^{(n)}$ , is a summation of the complex amplitude for  $n$ -times scattering,  $\Psi_{hkl}^{(n)}$ , and  $\Psi_{hkl}^{(n)}$  is also a summation of wave functions for all the possible scattering trajectories that start from 0 0 0 and finish at reflection  $h k l$  with  $n$  steps. The first order term of the Born series,  $\Psi_{hkl}^{(1)}$ , yields the wave function for single scattering (which is the first Born approximation).  $E_n$  only depends on structure factors of the scattering vectors along the trajectories.  $Z_n$  only depends on the diffraction geometry and the thickness:

$$Z_n = \sum_{r=0}^{\infty} \frac{(-2\pi i z)^{n+r}}{(n+r)!} h_r(\zeta_{hkl}, \zeta_1, \zeta_2 \cdots \zeta_{n-1}) , \quad (2.40c)$$

where  $h_r(\zeta_{hkl}, \zeta_1, \zeta_2 \cdots \zeta_{n-1})$  is the complete homogeneous symmetric polynomials of degree  $r$  [51, 52] and the  $(\zeta_{hkl}, \zeta_1, \zeta_2 \cdots \zeta_{n-1})$  are the excitation errors for each reflection in the scattering paths, which depend on the incident beam direction and the reciprocal lattice vectors as being defined in equation (2.27b).

It has been shown that the Born series in equation (2.40a) can also be derived by using Green's function, and  $\Psi_{hkl}^{(n)}$  (which can also be denoted as  $\Psi_g^{(n)}$  where  $g = h k l$ ) corresponds to the  $n^{\text{th}}$  order Born approximation expressed in reciprocal space [53].

For weak interactions between electrons and a very thin specimens (or specimens with light atoms), the higher-order terms in the Born series is a perturbation of the lower-order terms, i.e.  $|\Psi_g^{(n+1)}| \ll |\Psi_g^{(n)}|$ . In general cases, however, the Born series converge slowly and can hardly be used in computation of dynamic diffraction.

Nevertheless, the Born series formulation is extremely useful in analytical analyses of symmetries in multiple scattering. The multiplication of structure factors in equation (2.40b) can be depicted by multiple scattering diagrams that consist of all possible scattering paths. The use of such diagrams has facilitated the identification of symmetry elements in crystal structures by electron diffraction [49, 54, 55, 56].

### 2.2.5. Two-beam dynamic diffraction

Previous subsections have introduced different formulations of dynamic diffraction in which many beams (ideally, infinite number of beams) are considered. This subsection will introduce an approximation of dynamic diffraction where only two beams, reflection 0 and  $g$ , are considered. The two-beam approximation is held when all the other reflections are far from their Bragg conditions except for reflection  $g$ . In such a case, all the excitation errors all large except the excitation error for reflection  $g$ ,  $\zeta_g$ , and equation (2.26a) can be truncated to:

$$\begin{pmatrix} 0 & U_g \\ U_{-g} & 2K\zeta_g \end{pmatrix} \begin{pmatrix} C_0^j \\ C_g^j \end{pmatrix} = 2K\gamma^j \begin{pmatrix} C_0^j \\ C_g^j \end{pmatrix}. \quad (2.41)$$

Solving the eigenvalues of the matrix equation above results in two dispersion surfaces:

$$2K\gamma^{1,2} = K\zeta_g \pm \sqrt{(K\zeta_g)^2 + |U_g|^2}. \quad (2.42)$$

The diffracted intensity of reflection  $g$  is:



$$I_g = \frac{|U_g|^2 \sin^2(\pi z \Delta\gamma)}{(K\Delta\gamma)^2}, \quad (2.43a)$$

$$I_g = \frac{|U_g|^2 \sin^2\left\{\frac{\pi z}{K} \sqrt{(K\zeta_g)^2 + |U_g|^2}\right\}}{(K\zeta_g)^2 + |U_g|^2}, \quad (2.43b)$$

$$I_0 = 1 - I_g, \quad (2.43c)$$

where  $\Delta\gamma$  is the difference between the two eigenvalues, i.e.,  $\Delta\gamma = \gamma^1 - \gamma^2$ .

Equation (2.43b) shows that the diffracted intensity,  $I_g$ , is an even function of the excitation error of reflection  $g$ , i.e.,  $I_g(\zeta_g) = I_g(-\zeta_g)$ , and thus the intensity profile of the line that is perpendicular to the Bragg condition line for reflection  $g$  has a mirror symmetry about  $\zeta_g = 0$ . This is similar to two-beam kinematic diffraction as described by equation (2.5). Another similarity to kinematic diffraction is that the intensity in two-beam dynamic diffraction intensity does not contain structure factor phases as can be seen from equation (2.43b). In contrast to kinematic diffraction, the two-beam dynamic diffraction intensity (without inelastic scattering) for any incident angle (with a certain fixed value of  $\zeta_g$ ), is a periodic function of the specimen thickness. The diffracted intensity at  $\zeta_g = 0$  drops to zero (becomes extinct) when the thickness satisfies the relations,  $\pi z \Delta\gamma = n\pi$  or  $z = n\xi$ , where  $\xi$  is called the extinction distance for two-beam dynamic diffraction, and is given by the following equation:

$$\begin{aligned} \xi &= \frac{1}{\Delta\gamma(\zeta_g = 0)} \\ &= \frac{K}{|U_g|} \end{aligned} \quad (2.44)$$

Strong reflections (or reflections having large structure factor magnitudes), have short extinction distance and the diffracted intensities near their two-beam conditions ( $\zeta_g = 0$ ) change rapidly with the thickness.

## 2.3 Convergent-beam electron diffraction (CBED)

Dynamical theory of electron diffraction has been successfully applied to interpretation of imaging and diffraction in TEM. This work focuses on one of the diffraction techniques called convergent-beam electron diffraction (CBED). This section will introduce the geometries and applications of CBED.

### 2.3.1. Geometry

#### 2.3.1.1 Formation of CBED discs and the Bragg lines

In CBED, a convergent beam of electrons is focused into a probe of about a few nanometres in diameter on a specimen of a few dozen to a few hundred nanometres thick. This results in diffraction patterns where a reflection is a disc instead of a spot. If a coordinate system is set up for every disc, a coordinate  $(K_x, K_y)$  represents a direction of the incident beam. If the probe is placed within a single crystal, a coordinate  $(K_x, K_y)$  in all of the discs corresponds to an orientation of the crystal with respect to the incident beam direction (shown in Fig. 2.4). Therefore, a CBED disc is a collection of the diffracted intensities of a reflection in different crystal orientations. The orientations in which the Bragg condition for reflection  $g$  is exactly satisfied correspond to a straight line across each disc. This locus of the exact Bragg condition is termed as the Bragg line of reflection  $g$  (Fig. 2.5), and along this line, we have:

$$\zeta_g = 0 , \quad (2.45a)$$

$$2\mathbf{K}_t \cdot \mathbf{g} = g^2 . \quad (2.45b)$$

In two-beam CBED, if the thickness is smaller than the extinction distance ( $z < \xi$ ), the Bragg line of reflection  $g$  inside the disc  $(0, 0, 0)$ , which is also known as the central disc or the bright field pattern (BFP), appears as a dark line and is called the deficiency line. The Bragg line of reflection  $g$  in the disc  $g$ , which is also known as the dark field pattern, appears as a bright line and is called the excess line. In many-beam dynamic diffraction where the Ewald sphere is close to multiple reciprocal points, Bragg lines may not appear as straight lines.

A reciprocal lattice plane that is parallel to the ZOLZ and does not pass through the origin is called a higher order Laue zone (HOLZ). The Bragg lines of HOLZ reflections (Fig. 2.6) are

called HOLZ lines. For HOLZ reflections that satisfy the Bragg conditions, the extinction distances are usually large, and the Bragg diffraction can produce a thin bright line across the disc of the HOLZ reflection (called “the excess HOLZ excess line”) and a thin dark line across the central disc (called “the deficiency HOLZ line”).

### 2.3.1.2 Formation of Kikuchi lines

Apart from the discs that mainly arise from elastic scattering, there are Kikuchi lines in the same pattern. The formation of Kikuchi lines is attributed to inelastic scattering. At certain depths within the specimen, the incident wave as well as the scattered waves can be inelastically scattered in all different directions due to thermal vibrations of atoms, excitation of photons, plasmons, etc. Some of the inelastically scattered electrons hit a crystal plane at the Bragg angle  $\theta_g$  (so they come in the directions that lie on a cone) and are then elastically diffracted (in the directions that lie on another cone), resulting in an excess bright line for  $g$  and a deficiency dark line for  $\bar{g}$  (Fig. 2.5b). The Kikuchi lines for a Friedel pair of reflections,  $g$  and  $\bar{g}$ , can form a band known as the Kikuchi band, which includes the two parallel Kikuchi lines and regions between them (the explanations for the intensity distribution within the band can be found in [44]).

Kikuchi lines or bands result from sources of illumination inside a crystal, which has a wide angular range. Therefore, Kikuchi patterns show a map of crystal orientations [57].

### 2.3.1.3 Zone-axis and off-zone CBED

When the incident beam is parallel with an orientation of high-symmetry (or is in a major zone axis), the centre of the central disc is located at an intersection of Kikuchi bands. Such CBED patterns are known as zone-axis patterns. Otherwise, they are off-zone patterns (Fig. 2.6). By definition, the origin of vector  $\mathbf{K}_t$  is at the zone axis and finishes at a point of interest ( $K_x, K_y$ ) within the central disc. For zone-axis CBED patterns, the Ewald sphere is tangent to the ZOLZ plane and the origin of vector  $\mathbf{K}_t$  is at the centre of the central disc. For off-zone CBED patterns, the Ewald sphere intersects with the ZOLZ plane (the intersection is called the Laue circle) and the origin of  $\mathbf{K}_t$ , or is the centre of the Laue circle (CLC), is away from the central disc (but always at the zone axis as defined before).

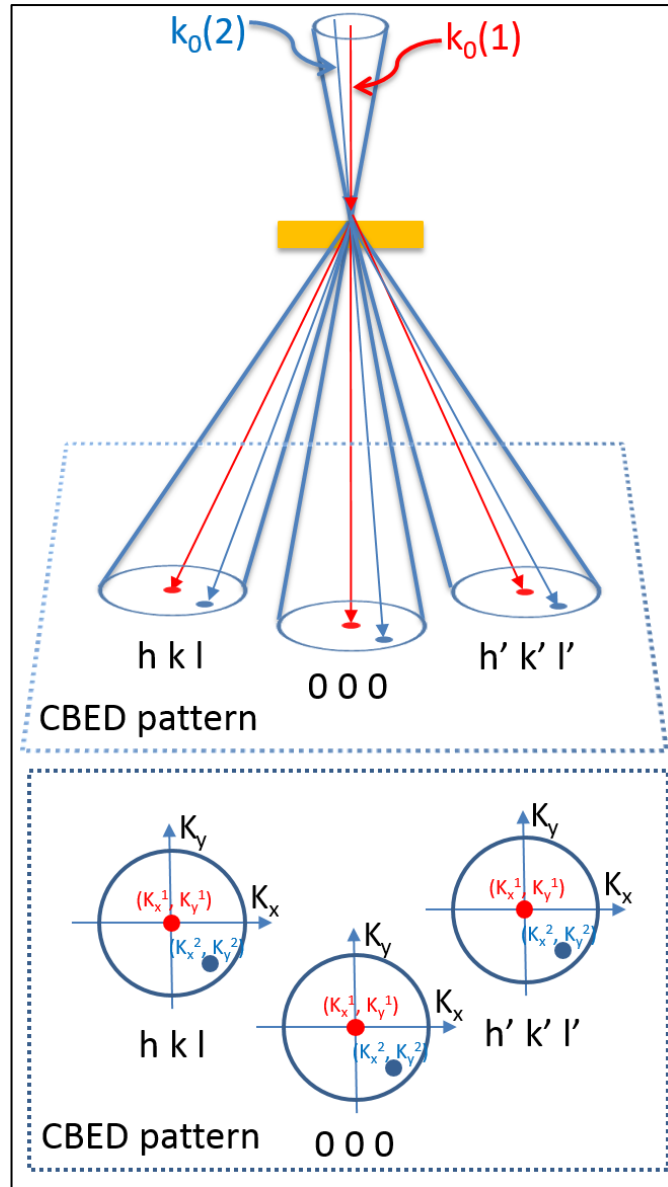


**Figure 2.4. Schematic of CBED pattern formation.** A convergent beam of illumination is focused into a nanometre-sized probe on a TEM specimen, resulting in a diffraction pattern where a reflection is a disc. Each disc is a collection of spots, and the coordinate of each spot represents a direction of the incident beam. Spots in different discs with the same coordinate correspond to the same direction of the incident beam. For example, the red spots in every disc have the same coordinate  $(K_x^1, K_y^1)$  and they correspond to the incident beam direction  $\mathbf{k}_0(1)$  while the blue spots with the coordinate  $(K_x^2, K_y^2)$  correspond to the incident beam direction  $\mathbf{k}_0(2)$ . As  $\mathbf{k}_0(1)$  and  $\mathbf{k}_0(2)$  travel in different orientations of the crystal,  $(K_x^1, K_y^1)$  and  $(K_x^2, K_y^2)$  represent two different crystal orientations.

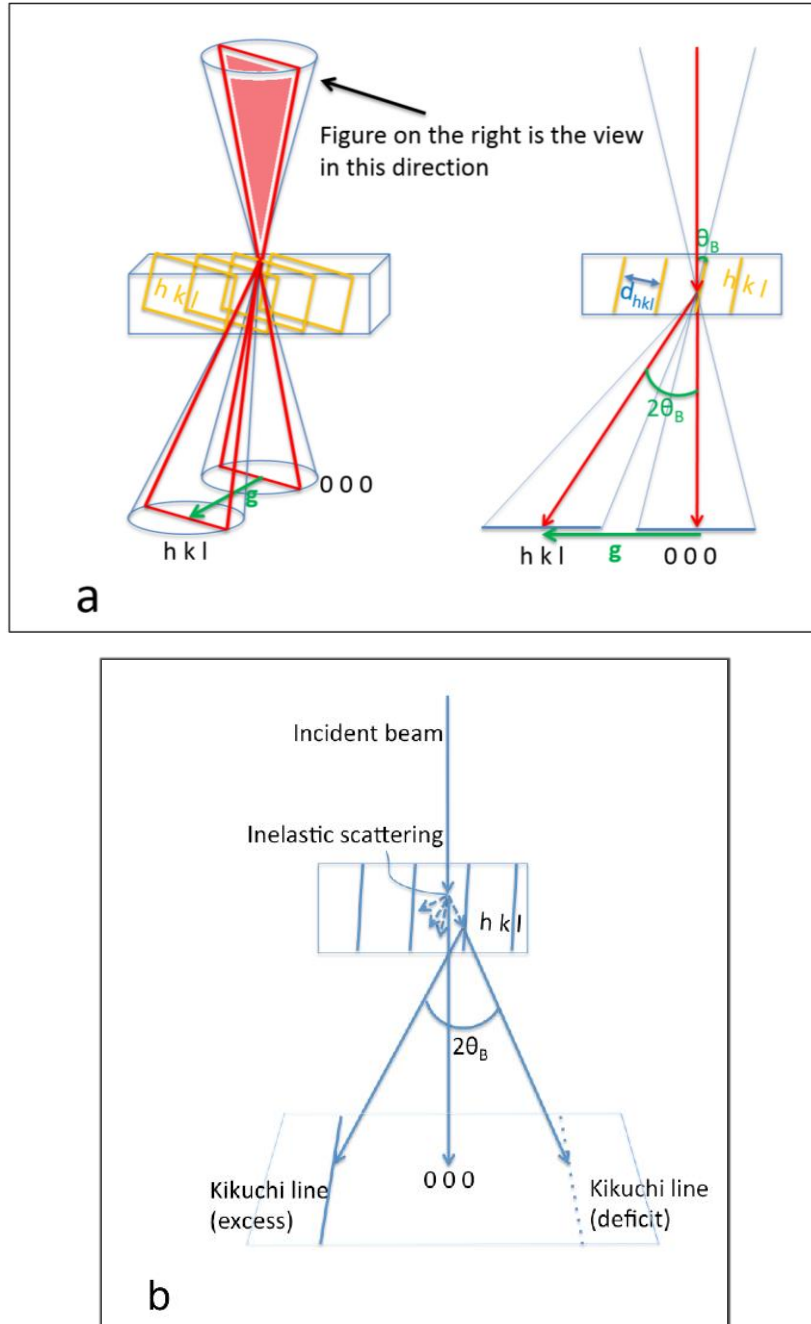


**Figure 2.5. Schematics of (a) Bragg line and (b) Kikuchi line formation in CBED patterns:**

(a) The incident-beam directions that satisfy the exact Bragg condition for reflection  $g$  (i.e.,  $2d_{hkl}\sin\theta_g = \lambda$ ) lie in a section (the red triangle) of the illumination cone. Therefore, the Bragg condition for reflection  $g$  corresponds to a straight line in each disc and the line is termed as “the Bragg line” of reflection  $g$ . The Bragg lines in the disc  $000$  and  $hkl$  are conjugated by the reciprocal lattice vector  $\mathbf{g} = h, k, l$ . (b) The inelastically scattered electrons travel in a wide range of directions. In some directions, the inelastically scattered electrons satisfy the Bragg condition for a reflection  $hkl$ , resulting in an excess and a deficiency (or deficit) Kikuchi line

in the diffraction pattern. Note: for illustration purposes, the schematics have only considered two-beam diffraction and have omitted other reflections. Many-beam diffraction can complicate the features and one may not find the Bragg lines or Kikuchi lines as straight lines.

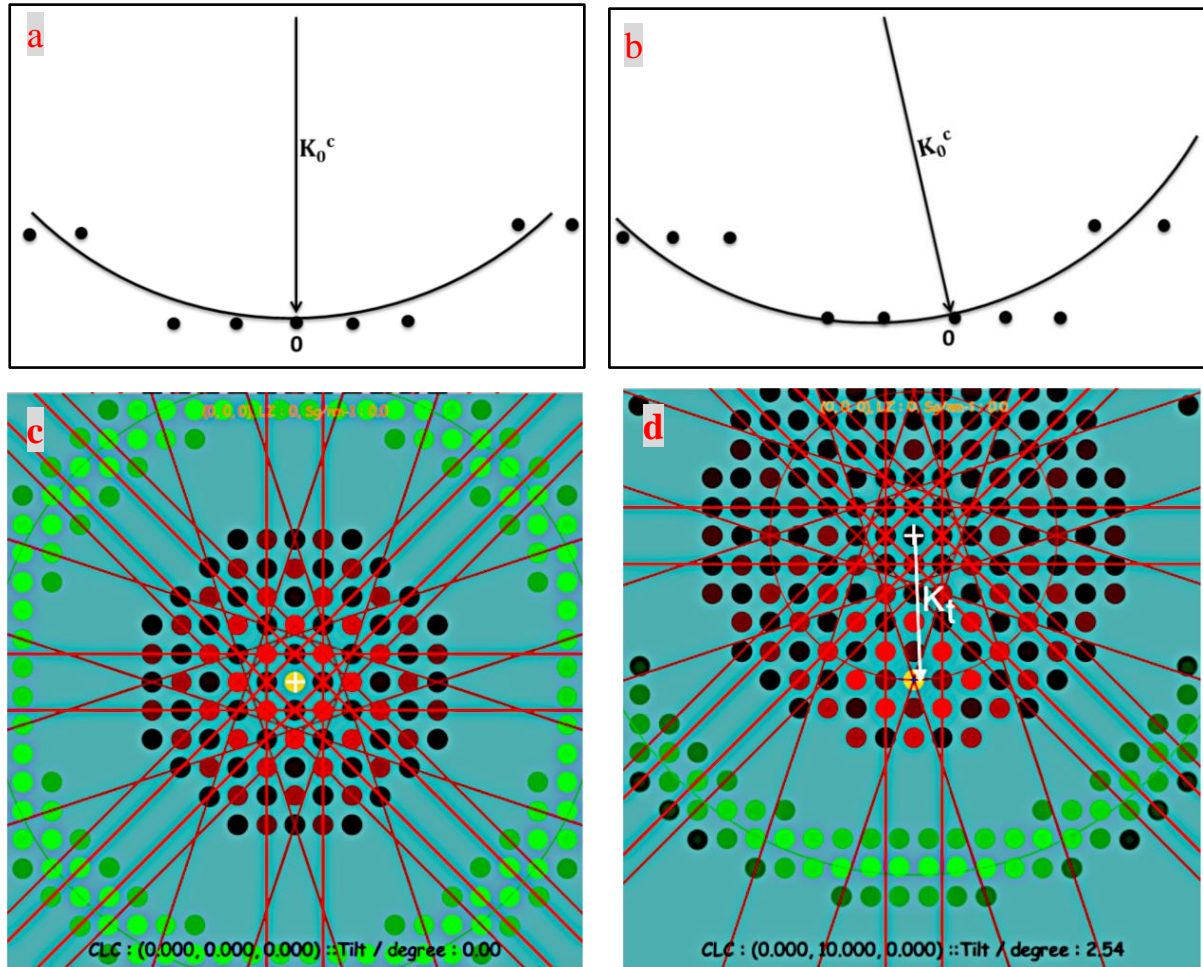


**Figure 2.6. Geometries of on-zone (a, c) and off-zone (b, d) CBED.** Ewald sphere constructions of on-zone (a) and off-zone (b) diffraction: the vector,  $K_0^c$ , represents the incident beam direction in the optic axis, which corresponds to the central point in the central disc. In schematics of on-zone (c) and off-zone (d) CBED patterns, the central discs are coloured in yellow and the Kikuchi lines are coloured in red. The red and the black discs are ZOLZ reflections, and the green discs are HOLZ reflections. The centres of Laue circles (CLCs) are labelled with white crosses (Laue circle is the intersection of Ewald sphere with the ZOLZ plane). The projection of  $K_0$  onto the ZOLZ plane is the vector  $K_t$ , which origins from the zone axis (i.e. CLC) and finishes at a point of interest (an orientation) in the central disc. The schematics in (c) and (d) are drawn by using the simulation package, JEMS [58].

### 2.3.2. Identification of symmetry elements in crystal structures

The equation (2.40b) allows for identification of glide planes or screw axes (which are translational symmetry elements within a unit cell) [54]. Besides, all the 32 Point groups can be identified by observation of symmetries (1) in the central disc, (2) in the whole patterns (3) in a reflection  $g$  which contains an exact Bragg condition within the disc (called “dark-field pattern”) and (4) between two reflections  $g$  and  $\bar{g}$  (called “ $\pm G$  dark-field pattern”) [59, 60]. Therefore, nearly all the space groups (except for enantiomorphic space groups) can be identified by observation of symmetries in CBED patterns without solving the crystal structure [61]. By contrast, X-ray diffraction patterns without anomalous scattering can identify only 11 Laue groups. The CBED method benefits from dynamic diffraction, which provides rich information about symmetry elements in crystal structures.

More recently, CBED with a scanning probe has been used to map polarizations in ferroelectric nano-domain structures. This technique is also based on symmetries in the dynamic diffraction patterns [62-64].

### 2.3.3. Refinement of lattice parameters and structure factors

Because of the long reciprocal lattice vector, the positions of the deficiency HOLZ lines in the central beam (which can be specified by  $\mathbf{K}_t$ ) are very sensitive to the variation of lattice parameters. Matching simulated HOLZ patterns (in the bright field) with experimental ones can determine the lattice constants of small crystals within an error of 0.1% [65]. An application of refining the deficiency HOLZ lines is the local strain measurement in quantum wells [66, 67].

Intensity distributions within HOLZ discs (in the dark field) can be used to determine atom positions [68-71] and order parameters in precipitates in alloys [72].

The low-order structure factors can be measured to very high accuracy by fitting the simulated CBED patterns (simulations are usually based on Bloch wave approach) to experimental ones [73]. The accurate measurement of low-order structure factors is essential in experimental determination of charge density and chemical bonds [74-76].

A variation of CBED called Large-angle CBED (LACBED) uses an under-focused (defocused) probe and a selected area aperture in the imaging plane to acquire diffraction



information from a much larger angle of incidence without overlapping discs [77]. Both CBED and LACBED can identify lattice defects such as stacking faults, dislocations [78] and twinning [79]. LACBED patterns contain information in both real and reciprocal space, which allows for a mapping of interfaces like grain and twin boundaries [80].

#### 2.3.4. The inverse problem

The calculation of diffracted intensities in CBED patterns from the known crystal structure can now be performed routinely, and the refinement of structure factors from matching calculated and experimental CBED patterns has shown to be successful. Nevertheless, if the crystal structure and the phases of structure factors are totally unknown, it is still quite challenging to determine the phases from CBED patterns. In other words, the inverse problem of dynamic diffraction, which is determining structural information from the dynamic diffraction patterns, is still difficult to solve because of the complicated mathematical relations, which can be seen from Section 2.2. Inversion of the dynamically diffracted intensities has been attempted in [81-85]. However, “a general method for solving unknown crystal structures using dynamic diffraction intensities has yet to be developed” [1].

### 2.4 Three-beam electron diffraction

#### 2.4.1 Introduction

##### 2.4.1.1 Concepts

In order to simplify the phase recovery from CBED patterns, an approximation of three-beam diffraction can be made such that only three reflections, 0, g and h, are considered for dynamic diffraction. In mathematical terms, the matrix equation (2.26a) is truncated as:

$$\begin{pmatrix} 0 & U_{-g} & U_{-h} \\ U_g & 2K\zeta_g & U_{g-h} \\ U_h & U_{h-g} & 2K\zeta_h \end{pmatrix} \begin{pmatrix} C_0^j \\ C_g^j \\ C_h^j \end{pmatrix} = 2K\gamma^j \begin{pmatrix} C_0^j \\ C_g^j \\ C_h^j \end{pmatrix}, \quad (2.46)$$

and thus



$$I_h = |\Psi_h|^2 = \left| \sum_j^3 (C^{-1})_0^j C_h^j \exp(-2\pi i \gamma^j z) \right|^2. \quad (2.47)$$

Three-beam dynamic diffraction equations, (2.46) and (2.47), provide a qualitative description of diffraction patterns that are recorded in specific orientations where two reflections  $g$  and  $h$  satisfy their Bragg conditions simultaneously (shown in Fig. 2.7a) while other reflections are far from their Bragg conditions<sup>5</sup>. Fig. 2.7b shows an example of a three-beam CBED pattern, in which two deficiency Bragg lines intersect at one point in the central disc. The point of intersection in the central disc together with the other two points that have the same coordinate in disc  $g$  and  $h$  correspond to the exact three-beam condition, where  $\zeta_g = \zeta_h = 0$ .

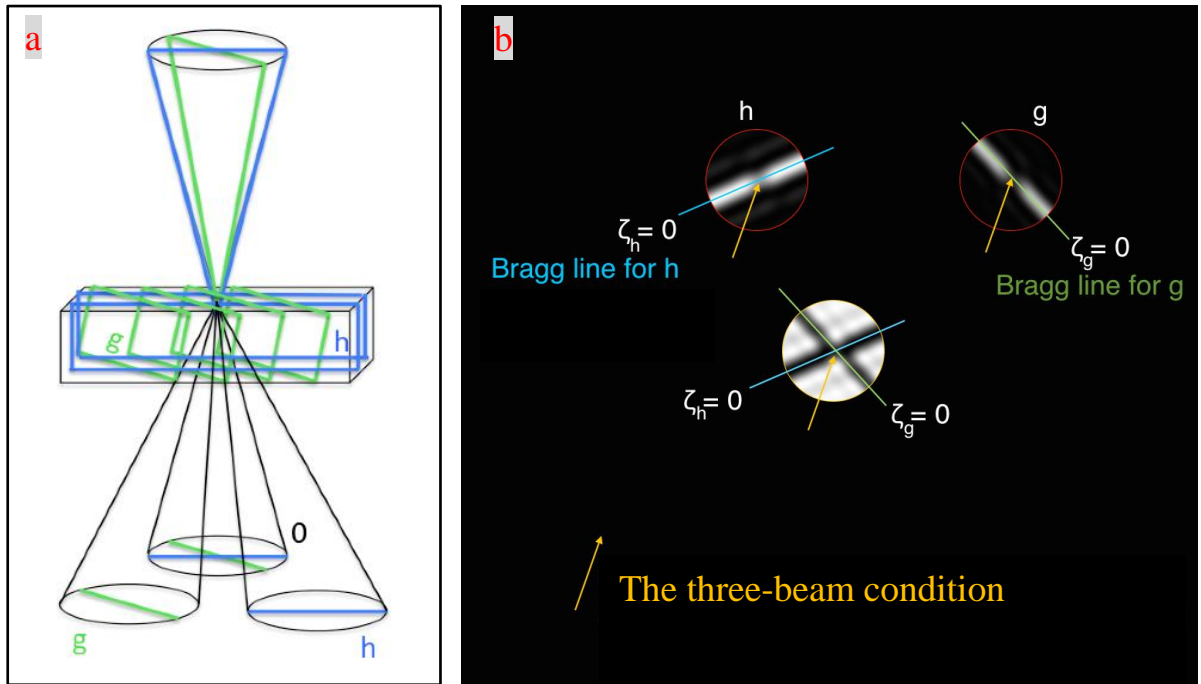


**Figure 2.7. Schematic of the diffraction geometry of (a) (non-systematic) three-beam CBED and (b) an example of (non-systematic) three-beam CBED pattern.** The diffraction geometry in three-beam condition (a) is similar to that in two-beam condition (shown in Fig.

<sup>5</sup> This is the definition of the non-systematic three-beam condition. The equations (2.46) and (2.47) can also describe systematic three-beam conditions, where reflections 0,  $g$ ,  $h$  are aligned in a row and only reflection  $g$  or  $h$  satisfies its Bragg condition exactly.

2.5a) but there is one more beam that satisfies its Bragg condition at the same time. An example of three-beam CBED patterns is given in (b). The calculation of the pattern is based on equations (2.46) and (2.47) by using JEMS [58]. Two deficiency Bragg lines intersect at a point in the central disc. The coordinate ( $K_x, K_y$ ) of the intersection correspond to the exact three-beam condition.

#### 2.4.1.2 Validity of the three-beam approximation

Three-beam dynamic diffraction defined by equations (2.46) and (2.47) can approximate many-beam diffraction in equations (2.26a) and (2.32) near a three-beam condition as long as no other reflections are strongly excited in the vicinity of the three-beam condition. In other words, when there is no other Bragg line crossing or lying next to the three-beam condition, three-beam CBED patterns, which are calculated from equations (2.46) and (2.47), will mimic many-beam CBED patterns, which are calculated from equations (2.26a) and (2.32), in the vicinity of the three-beam condition.

The orientations where the effect of three-beam diffraction dominates are common in crystal structures with small unit cells but are less accessible in structures with large unit cells where the Bragg lines are very dense and the effects of many-beam diffraction are inevitable. In other words, three-beam theory can be widely applied in small structures but become restricted in large structures. However, studies in three-beam X-ray diffraction reveal that even in some macromolecular structures, there still exist some orientations where three-beam theory can be applied [86, 87]. It could be expected that three-beam electron diffraction may also be applied to large structures. However, since the wavelength of electrons is much smaller than X-rays, the applicability of three-beam electron diffraction in large structures may be a different issue and will be further discussed in Section 3.6.3.

#### 2.4.1.3 The benefit of the three-beam approximation

The intensity distribution in the neighbourhood of a three-beam condition depends on the direction of incidence (specified by  $\zeta_g$  and  $\zeta_h$ ), specimen thickness  $z$ , three structure factor magnitudes  $|V_g|$ ,  $|V_h|$ ,  $|V_{h-g}|$  and one three-phase invariant  $\phi = \varphi_g + \varphi_{-h} + \varphi_{h-g}$ . With fewer parameters defining the diffraction equations, three-beam diffraction makes it more feasible to recover the phase information than diffraction in major zone-axes. In other words,

three-beam approximation simplifies the inverse problem of dynamic diffraction and may allow for the measurement of three-phase invariants.

Three-beam electron diffraction has been discussed in the field of diffraction physics and crystallography for several decades [4-19, 24]. However, a dedicated review of the subject has never been published. This section will serve as a brief review of three-beam electron diffraction from the perspective of analytical theories and their applications to the measurements of three-phase invariants.

### 2.4.2 Analytical expressions for the intensities

Three-beam dynamic diffraction is the simplest form of dynamic diffraction that contains the phases of structure factors in the intensity distributions. Nevertheless, it is too lengthy to express the intensity in equation (2.47) as an explicit function of  $\zeta_g$ ,  $\zeta_h$ ,  $|V_g|$ ,  $|V_h|$ ,  $|V_{h-g}|$ ,  $z$  and  $\phi$ . In order to obtain three-phase invariants from the pattern, a simple analytical expression for the diffracted intensities must be obtained.

Over decades, many efforts have been made to find such simple expressions. For simplicity of the mathematics, most of the analytical expressions do not consider inelastic scattering. Such practice is acceptable for application of three-beam diffraction in *ab initio* determination of the phases where the measured phases with low accuracy can be accepted. In such an approximation, the eigenmatrix in equation (2.46) is Hermitian, i.e.,  $U_{-g} = U_g^*$ ,  $U_{-h} = U_h^*$  and  $U_{g-h} = U_{h-g}^*$ .

In addition, most of the analytical expressions have made further approximations by involving perturbation theories or the expressions that can be recast into perturbational treatments: the derivations usually start from the exact solution to either kinematic diffraction [14, 88, 89] or two-beam dynamic diffraction [6, 15], and then involve phase dependent terms in the perturbational parts. The perturbational treatments have facilitated the interpretation the three-phase invariants from the three-beam diffraction patterns where three-beam dynamic diffraction can be regarded as a perturbation of kinematic or two-beam dynamic diffraction. For example, theories based on perturbation of kinematic diffraction have resulted in applications in three-beam dynamic X-ray diffraction where the specimens are typically 10 - 20  $\mu\text{m}$  thick [36-38]. If the crystal is thicker (to about 100  $\mu\text{m}$ ) the perturbational treatment would fail [90].

Since the atomic scattering amplitude of electrons is  $10^4 - 10^5$  times higher than that of X-rays [26], the extinction distance (defined in equation (2.4.4)) for dynamic X-ray diffraction at 1 keV is about  $10^3 - 10^4$  times higher than that of dynamic diffraction of fast electrons at 100 keV. This means that the intensity distribution in Dynamic X-ray diffraction by a crystal of 10 - 20  $\mu\text{m}$  thick is similar to that in electron diffraction by a crystal of about 10 nm thick if only elastic scattering is considered.

For electron diffraction, a typical value of the specimen thickness is about 100 nm and it is not feasible to prepare specimens of 10 nm thick. Therefore, three-beam electron diffraction requires a more strict theoretical treatment of three-beam dynamic diffraction for a specimen thicker than 10 nm, which needs to be more than just a perturbation of kinematic diffraction.

However, as stated before, the exact solution (which is referred to as the intensity expression given by equation (2.47)) to three-beam electron diffraction can be extremely lengthy if the reflection intensity is expressed explicitly in terms of the three-phase invariants, the structure factor magnitudes, excitation errors and the thickness. This means that the exact solution needs to be reduced to simpler forms. The reductions of the exact three-beam solutions have been discussed in the papers by Hurley and Moodie [10, 11, 20, 24, 91].

The following three subsections will introduce analytical theories of three-beam electron diffraction, the derivations of which are based on different approximations:

- 1) perturbation of kinematic diffraction,
- 2) perturbation of two-beam dynamic diffraction,
- 3) the exact solution to three-beam dynamic diffraction.

### **2.4.3 Perturbation of kinematic diffraction**

As discussed in Section 2.2.4, the first Born approximation gives rise to kinematic diffraction; higher-order terms in the Born series are perturbation to lower-order terms ( $|\Psi_{\mathbf{g}}^{(n-1)}| \ll |\Psi_{\mathbf{g}}^{(n)}|$ ) when the wave-matter interaction is weak. A formulation that involves the second-order term in the Born series (known as the second-order Born approximation) can be used to derive three-beam dynamic diffraction for very thin specimens or weak reflections (e.g. HOLZ reflections). This has been discussed in the papers [14, 76, 83, 88], which have

involved an iterative procedures of integration to solve the differential forms of electron and dynamic X-ray diffraction equations. Alternatively, the formulation of the Born series expressed in reciprocal space (discussed in Section 2.2.4) can be used for deriving such solutions too [89]. This has only been mentioned in [89] but without details. The details are presented here.

The amplitude of the waves scattered to reflection  $g$  is:

$$\Psi_g = \sum_n \Psi_g^{(n)} = \sum_n E_n Z_n , \quad (2.48)$$

which is a repetition of the Born series in equation (2.40a). The Born series is truncated to include only the first and second-order terms:

$$\Psi_g = \Psi_g^{(1)} + \Psi_g^{(2)} = E_1 Z_1 + E_2 Z_2, \quad (2.49)$$

where  $E_1$  and  $E_2$  are multiplications of the structure factors (shown in the multiple scattering diagram in Fig. 2.8), and  $Z_1$  and  $Z_2$  are the geometric factors:

$$Z_1 = i \exp(-\pi i \zeta_g z) \frac{\sin(\pi \zeta_g z)}{\pi \zeta_g} , \quad (2.50a)$$

$$Z_2 = \frac{i}{2\pi} \frac{\exp(-\pi i \zeta_g z)}{\zeta_g - \zeta_h} \left\{ -\exp[-\pi i (\zeta_h - \zeta_g) z] \frac{\sin(\pi \zeta_h z)}{\pi \zeta_h} + \frac{\sin(\pi \zeta_g z)}{\pi \zeta_g} \right\} , \quad (2.50b)$$

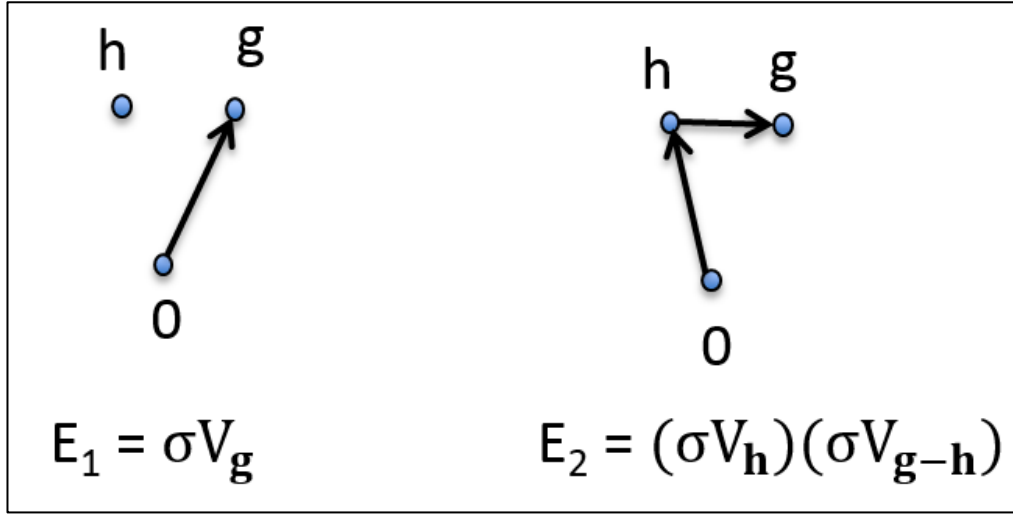


**Figure 2.8. The multiple scattering diagram for the second-order Born approximation to three-beam dynamic diffraction.** The arrows are the scattering vectors, which label the scattering paths in reciprocal space for the single scattering (left) and double scattering (right).

Therefore, the intensity of reflection  $g$  can be written as:

$$I_g = |\Psi_g^{(1)} + \Psi_g^{(2)}|^2 = (E_1 Z_1 + E_2 Z_2)(E_1 Z_1 + E_2 Z_2)^*, \quad (2.51)$$

The cross-terms in equation (2.51) contain the three-phase invariant and the intensity along the Bragg line of  $g$  (where  $\zeta_g = 0$ ) can be expressed as:

$$I_g(\zeta_h, z) = \sigma^2 |V_g|^2 z^2 + \sigma^3 |V_g| |V_h| |V_{g-h}| z^3 \left\{ \left( \frac{1}{\pi \zeta_h z} \right) \left[ \frac{\sin(2\pi \zeta_h z)}{2\pi \zeta_h z} - 1 \right] \cos \phi + \frac{\sin^2(\pi \zeta_h z)}{(\pi \zeta_h z)^2} \sin \phi \right\}, \quad (2.52)$$

where  $(E_2 Z_2)^2$  has been omitted in this expression (since the magnitude of  $(E_2 Z_2)^2$  is comparably smaller than the other terms and it is lengthy) and equation (2.52) is identical to the solution in [14] which uses an iterative scheme to solve the Howie-Whelan equation [92].

Equation (2.52) explicitly contains the three-phase invariant,  $\phi$ . By inputting different values of  $\phi$ , the intensity given by equation (2.52) is plotted in Figure 2.9 together with the exact three-beam solution given by equations (2.46) and (2.47). The plots show that the second-order Born approximation gives a similar result of intensities to the exact three-beam solution and the three-phase invariant  $\phi$  can be roughly measured from shape of the intensity profile

along the Bragg line of reflection  $g$ . The paper [14] suggests that the phase can be measured more precisely to within  $\pm 15^\circ$  by measuring the distances between the extrema and the three-beam condition point.

The limitation of this approach is also obvious. Since the formulation is based the second-order Born approximation which breaks down for the three-beam cases with large structure factor magnitudes and/or a large thickness (see Fig. 2.10), the phase measurement is only limited to the specimens where the thicknesses are only a small fraction (about less than 20% ) of the extinction distance for two-beam dynamic diffraction.

Therefore, the perturbative correction to kinematic diffraction serves as a good approximation for extracting the three-phase invariants,  $\phi$ , from weakly scattered beams such as HOLZ reflections in CBED patterns. In order to measure the phases of strong reflections, a different formulation needs to be introduced.

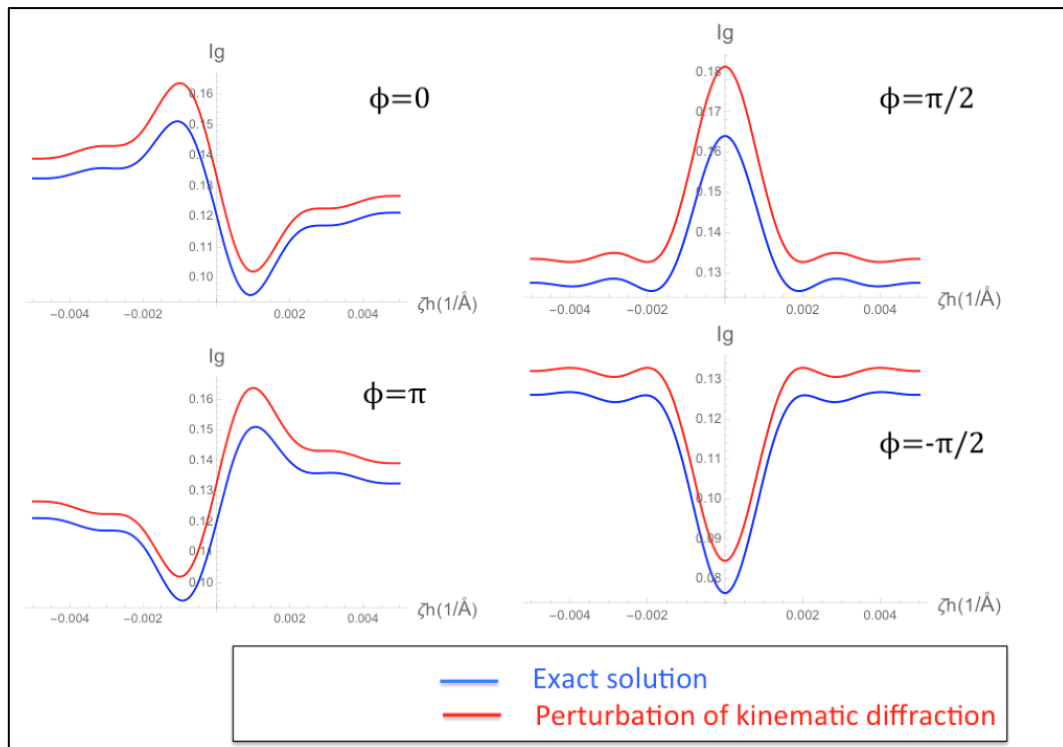


**Figure 2.9. Intensity profiles along the Bragg line of reflection  $g$  at different three-phase invariants.** An example of three-beam diffraction with  $|V_g| = |V_h| = |V_{g-h}| = 1$  V,  $z = 500$  Å is considered here. The plots are produced by using Mathematica, Version 10 [93].

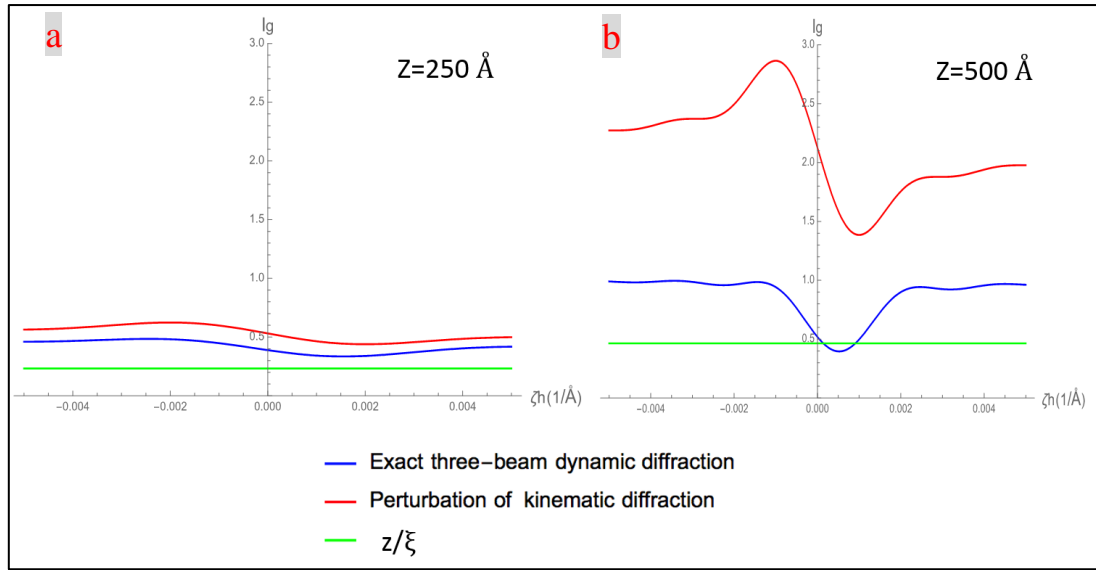


**Figure 2.10. Intensity profiles along the Bragg line of reflection  $g$  at different thicknesses.**

The three-beam diffraction with moderately large structure factor magnitudes is considered, where  $|V_g| = 4$  V,  $|V_h| = 3$  V,  $|V_{g-h}| = 2$  V,  $\phi = 0$ . (a) The thickness has to be a small fraction of the extinction distance for two-beam dynamical diffraction of reflection  $g$ , i.e.  $z/\xi$  must be small. (b) Otherwise, the perturbation approximation diverges quickly from the exact three-beam diffraction. The plots are produced by using Mathematica, Version 10 [93].

#### 2.4.4. Perturbation of two-beam dynamical diffraction

In some special conditions, the  $3 \times 3$  eigenmatrix in equation (2.46) can be treated by perturbation of a  $2 \times 2$  eigenmatrix (e.g. equation (2.41)). The intensity expressions derived from the  $2 \times 2$  matrix are asymptotic the exact three-beam solutions (equation (2.47)) in a certain range of incident angles. Both Bethe [22] and Kambe [6] formulated their solutions to three-beam dynamic diffraction in this way. The formulations were summarised in the language of perturbation theory [15]. A brief introduction to the formulations is given here, using notations from [15].

##### 2.4.4.1 Bethe's approximation [15, 22]

It is assumed that a weak reflection  $h$  is coupled to a strong reflection  $g$ , i.e.,

$$K|\zeta_h| \gg |U_g| \quad \& \quad |\zeta_h| \gg |\zeta_g|. \quad (2.53)$$



Under this approximation, the 3 x 3 matrix, denoted by  $\mathbf{A}$ , in equation (2.46) can be seen as a perturbation of the 2 x 2 matrix in equation (2.41):

$$\mathbf{A} = \mathbf{A}_0 + \mathbf{A}' , \quad (2.54a)$$

$$\mathbf{A}_0 = \begin{pmatrix} 0 & U_{-g} & 0 \\ U_g & 2K\zeta_g & 0 \\ 0 & 0 & 0 \end{pmatrix} , \quad (2.54b)$$

$$\mathbf{A}' = \begin{pmatrix} 0 & 0 & U_{-h} \\ 0 & 0 & U_{g-h} \\ U_h & U_{h-g} & 2K\zeta_h \end{pmatrix} , \quad (2.54c)$$

where the zero-order matrix  $\mathbf{A}_0$  is the 2 x 2 matrix for a two-beam dynamic diffraction in equation (2.41). From equations (2.53) and (2.42), we have the relation:

$$K|\zeta_h| \gg K|\gamma| . \quad (2.55)$$

Thus, the third row in equation (2.46) can be modified to:

$$C_h \approx - \left( \frac{U_h C_0}{2K\zeta_h} + \frac{U_{h-g} C_g}{2K\zeta_h} \right) . \quad (2.56)$$

By inserting equation (2.56) into equation (2.46), we get

$$\begin{pmatrix} -2K\gamma^{\text{eff}} & U_{-g}^{\text{eff}} \\ U_g^{\text{eff}} & 2K\zeta_g^{\text{eff}} - 2K\gamma^{\text{eff}} \end{pmatrix} \begin{pmatrix} C_0 \\ C_g \end{pmatrix} = 0 , \quad (2.57a)$$

where

$$U_g^{\text{eff}} = U_g - \frac{U_h U_{h-g}}{2K\zeta_h} , \quad (2.57b)$$

$$2K\gamma^{\text{eff}} = 2K\gamma + \frac{|U_h|^2}{2K\zeta_h} \quad (2.57c)$$

$$\text{and} \quad 2K\zeta_g^{\text{eff}} = 2K\zeta_g + \frac{|U_{h-g}|^2}{2K\zeta_h} - \frac{|U_h|^2}{2K\zeta_h} . \quad (2.57d)$$

The perturbed two-beam expression for the diffracted intensity is then

$$I_g = \frac{|U_g^{\text{eff}}|^2 \sin^2(\pi z \Delta\gamma^{\text{eff}})}{K^2 (\Delta\gamma^{\text{eff}})^2} , \quad (2.58a)$$

where

$$|U_g^{\text{eff}}|^2 = |U_g|^2 - \frac{|U_g||U_h||U_{h-g}|}{K\zeta_h} \cos\phi + \frac{|U_h|^2 |U_{h-g}|^2}{(2K\zeta_h)^2} , \quad (2.58b)$$

$$\begin{aligned} \Delta\gamma^{\text{eff}} = (1/2K) & \left\{ [2K\zeta_g + \frac{|U_h|^2 - |U_{h-g}|^2}{2K\zeta_h}]^2 \right. \\ & \left. + 4|U_g|^2 \left[ 1 - 2 \frac{|U_{h-g}||U_h|}{|U_g|2K\zeta_h} \cos\phi + \frac{|U_h|^2 |U_{h-g}|^2}{|U_g|^2 (2K\zeta_h)^2} \right] \right\} . \end{aligned} \quad (2.58c)$$

The intensity in (2.58a) as a function of the excitation error of reflection  $h$  is plotted in Figure 2.11. The expression is shown to be asymptotic to the exact three-beam solution in regions that are away from the three-beam point. This successfully describes the effect of  $\cos\phi$ : if the specimen is not too thick, the intensity on the  $\zeta_g < 0$  side is larger than that on the  $\zeta_g > 0$  side for  $\cos\phi > 0$ , (as shown in Fig. 2.11a, b), and vice versa. By comparing Fig. 2.11b and Fig. 2.10b, it can be seen that it is possible to determine the sign of  $\cos\phi$  using the formulae based on the two-beam dynamic diffraction at the thicknesses (e.g.  $z = 500 \text{ \AA}$ ) where the kinematic diffraction based formulation fails to converge to the exact three-beam solutions. However, equations (2.58a-c) fail to show the effect of the sign of  $\phi$  because the expression does not contain the sign.

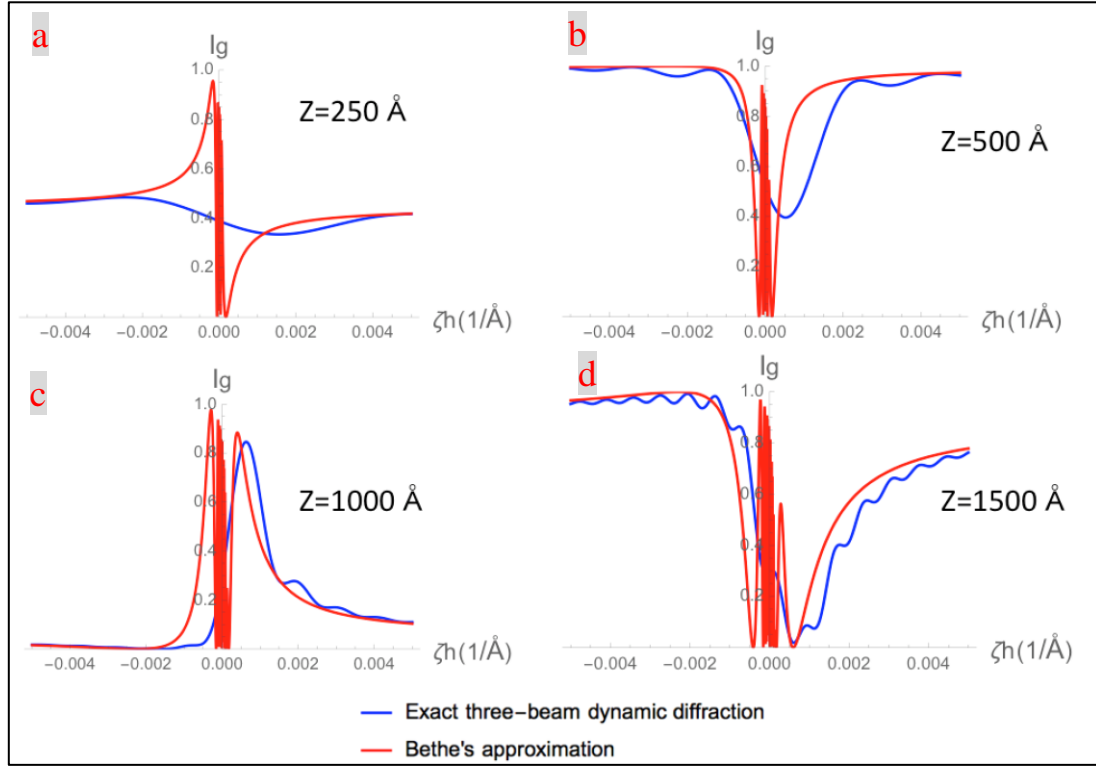


**Figure 2.11. Intensity profiles along the Bragg line of reflection  $g$  at different thicknesses.** The three-beam diffraction with moderately large structure factor magnitudes is considered, where  $|V_g| = 4$  V,  $|V_h| = 3$  V,  $|V_{g-h}| = 2$  V,  $\phi = 0$ . For all thicknesses, the formula according to Bethe's approximation [15, 22] converges to the exact three-beam solutions in the regions that are away from the three-beam condition point. However, a large deviation from the exact three-beam solutions is observed in the vicinity of the three-beam condition condition.

#### 2.4.4.2 Kambe's approximation [6, 15]

It is assumed that two weak reflections are coupled by a vector that has a large structure factor magnitude, i.e.

$$|U_{h-g}| \gg |U_g| \text{ or } |U_h|. \quad (2.59)$$

Under this approximation, the  $3 \times 3$  matrix, denoted by  $\mathbf{A}$ , in equation (2.46) can be seen as a perturbed system of another  $2 \times 2$  matrix:

$$\mathbf{A} = \mathbf{B}_0 + \mathbf{B}' , \quad (2.60a)$$

$$\mathbf{B}_0 = \begin{pmatrix} 0 & 0 & 0 \\ 0 & 2K\zeta_g & U_{g-h} \\ 0 & U_{h-g} & 2K\zeta_h \end{pmatrix} , \quad (2.60b)$$

$$\mathbf{B}' = \begin{pmatrix} 0 & U_{-g} & U_{-h} \\ U_g & 0 & 0 \\ U_h & 0 & 0 \end{pmatrix} , \quad (2.60c)$$

The Bloch waves (the eigenvectors) defined by equation (2.60b) are used as the basis functions for solving the Bloch waves defined by equation (2.46). After several manipulations (details can be found in [15]), the intensities near

two hyperbolae in the discs (shown by the dashed lines in Fig. 2.12.b) which are expressed as

$$\text{(the upper branch)} \quad \zeta_+ = \frac{1}{2} \{ \zeta_g + \zeta_h + [|U_{g-h}/K|^2 + (\zeta_g - \zeta_h)^2]^{1/2} \} = 0 \quad (2.61a)$$

$$\text{and (the lower branch)} \quad \zeta_- = \frac{1}{2} \{ \zeta_g + \zeta_h - [|U_{g-h}/K|^2 + (\zeta_g - \zeta_h)^2]^{1/2} \} = 0 , \quad (2.61b)$$

can be simplified as

$$\text{(the upper branch)} \quad I_g = \cos^2\left(\frac{\beta}{2}\right) \frac{\sin[\pi z(\zeta_+^2 + |U_+/K|^2)^{1/2}]}{1 + |\zeta_+ K/U_+|^2} \quad (2.62 a)$$

$$\text{and (the lower branch)} \quad I_g = \sin^2\left(\frac{\beta}{2}\right) \frac{\sin[\pi z(\zeta_-^2 + |U_-/K|^2)^{1/2}]}{1 + |\zeta_- K/U_-|^2} , \quad (2.62 b)$$

where

$$\begin{aligned} |U_+|^2 = |U_h|^2 \sin^2\left(\frac{\beta}{2}\right) & \left\{ \left[ 1 + \left| \frac{U_g}{U_h} \right|^2 \cot\left(\frac{\beta}{2}\right) \cos\phi \right]^2 \right. \\ & \left. + \left| \frac{U_g}{U_h} \right|^2 \cot^2\left(\frac{\beta}{2}\right) \sin^2\phi \right\} , \end{aligned} \quad (2.62c)$$

$$|U_-|^2 = |U_h|^2 \cos^2\left(\frac{\beta}{2}\right) \left\{ \left[ 1 - \left| \frac{U_g}{U_h} \right|^2 \tan\left(\frac{\beta}{2}\right) \cos\phi \right]^2 + \left| \frac{U_g}{U_h} \right|^2 \tan^2\left(\frac{\beta}{2}\right) \sin^2\phi \right\} \quad (2.62d)$$

$$\text{and} \quad \cot\beta = (\zeta_g - \zeta_h)K/|U_{gh}|. \quad (2.62e)$$

Equations (2.62a-e) suggest that (1) if  $\cos\phi > 0$  and the thickness is not very large, i.e.  $z < K/2|U_{+/-}|$ , the maximum intensity appears on the upper branch,  $\zeta_+ = 0$ ; (2) if  $\cos\phi < 0$  and the thickness is not very large, the maximum intensity appears on the lower branch,  $\zeta_- = 0$ . It should be noticed that the restriction on the thickness here is also less strict than that in the kinematic approach in Section 2.4.3.

#### 2.4.4.3 Summary of Bethe's and Kambe's approximations [6, 15, 22]

Both Bethe's [22] and Kambe's [6] formulae provide asymptotic solutions to three-beam diffraction in a certain range of incident angles labelled in Fig. 2.12. If the dispersion surfaces for this range of excitation errors (or incident angles) are plotted, there will be two branches of dispersion surfaces (each for a Bloch state) close to each other while another branch far from the other two. It is this feature of the dispersion surfaces that makes one Bloch state contributes much less than the other two states to the value of the diffracted intensities, and therefore allows for the two-beam approximations to be made in the first place, which is followed by a perturbation treatment.

Both Bethe's [22] and Kambe's [6] theories fail near the exact three-beam condition where the influences of the three Bloch waves are all significant and the 3x3 matrix can no longer be seen as a perturbation of a 2x2 matrix. Besides, the sign of  $\phi$  is lost in both formulae, which means neither formula can resolve enantiomorph ambiguity, although the effect of the sign of  $\phi$  exists in three-beam dynamic diffraction (which can be described by the previous theory in cases of weak interactions). Nevertheless, the theories based on perturbing two-beam dynamic diffraction can be applied to a wider range of thicknesses than the theories based on perturbing kinematic diffraction.

As Fig. 2.11c and Fig.2.11d suggest, the perturbed two-beam dynamic diffraction can converge to the exact three-beam solutions in the domain labelled in Fig.2.12a even at large thicknesses, it should be possible to extract the three-phase invariants from thick specimens of noncentrosymmetric crystals as well. However, this has never been discussed in the papers that proposed these formulations [6, 15, 22].

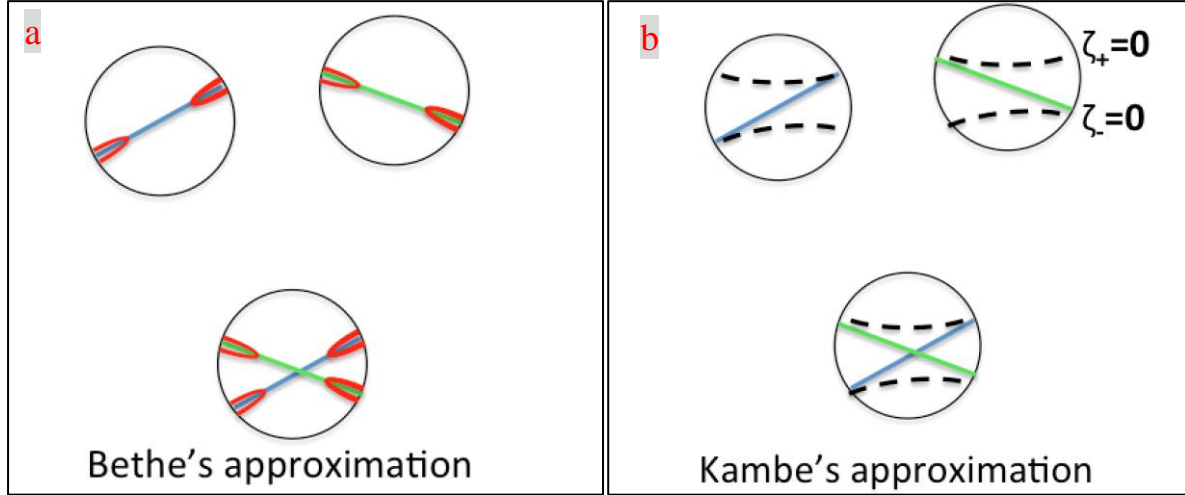


**Figure 2.12. Validity regions of the incident beam directions for (a) Bethe's [22] and (b) Kambe's [6] approximations.** Bethe's approximation [22] is valid within the enclosed region bounded by the red curves while Kambe's approximation [6] is valid near the hyperbolae (described by equations (2.61a, b)) shown by dashed lines. These schematics are fashioned after [15].

#### 2.4.5. The exact three-beam dynamical theories

A more stringent treatment of three-beam diffraction is to consider all of the three eigenvalues given by equation (2.46). To be consistent with the notations in the literatures that will be discussed below, equation (2.46) can be rewritten as:

$$\begin{pmatrix} 0 & \sigma V_g^* & \sigma V_h^* \\ \sigma V_g & 2\pi\zeta_g & \sigma V_{h-g}^* \\ \sigma V_h & \sigma V_{h-g} & 2\pi\zeta_h \end{pmatrix} \begin{pmatrix} C_0 \\ C_g \\ C_h \end{pmatrix} = \lambda_i \begin{pmatrix} C_0 \\ C_g \\ C_h \end{pmatrix}, \quad (2.63a)$$

$$\text{or} \quad \mathbf{MC} = \lambda_i \mathbf{C} , \quad (2.63b)$$

$$\text{where} \quad \mathbf{M} = \frac{\pi}{K} \mathbf{A} \quad (2.64a)$$

$$\frac{K}{\pi} \lambda_i = \gamma^i \quad (2.64b)$$

The determinant,  $|\mathbf{M} - \lambda \mathbf{I}| = 0$  , yields the cubic equation whose solutions are the three eigenvalues:

$$\lambda^3 + b\lambda^2 + c\lambda + d = 0 , \quad (2.65a)$$

$$\text{where} \quad b = -2\pi(\zeta_g + \zeta_h) , \quad (2.65b)$$

$$c = (2\pi\zeta_g)(2\pi\zeta_h) - (\sigma|V_g|)^2 - (\sigma|V_h|)^2 - (\sigma|V_{h-g}|)^2 , \quad (2.65c)$$

$$\begin{aligned} \text{and} \quad d = & (2\pi\zeta_g)(\sigma|V_h|)^2 + (2\pi\zeta_h)(\sigma|V_g|)^2 \\ & - 2(\sigma|V_g|)(\sigma|V_h|)(\sigma|V_{h-g}|)\cos\phi . \end{aligned} \quad (2.65d)$$

It is worth noticing that the eigenvalues depend on  $\cos\phi$  but not the sign of  $\phi$ .

#### 2.4.5.1 The theory by Gjønnes and Høier for centrosymmetric crystals

For centrosymmetric crystals, there is a point at which the matrix equation (2.46) has two degenerate eigenvalues (i.e.,  $\Delta\lambda = 0$  or  $\Delta\gamma = 0$ ). The point, which is referred to as the Gjønnes-Høier point, can be found at [9]:

$$\zeta_g = \sigma \frac{V_g(V_{g-h}^2 - V_h^2)}{V_h V_{h-g}} , \quad (2.66a)$$

$$\zeta_h = \sigma \frac{V_h(V_{g-h}^2 - V_g^2)}{V_g V_{h-g}}. \quad (2.66b)$$

The Gjønnes-Høier point can be found at a point of zero intensity from the split excess Bragg lines in either a Kikuchi pattern [9] or a dark-field CBED disc [15]. The location of the point of zero intensity, i.e. at which branch of the excess lines it is located, depends on whether  $\cos\phi = 1$  or  $-1$ . Actually, “the Gjønnes-Høier point has zero intensity” is an assumption, which is deduced from the assumption that “the contrast of a Kikuchi line is proportional to the width of the corresponding gap at the dispersion surface” [9].

If one inserts equations (2.66a, b) and  $\cos\phi = 1$  into equation (2.62b) or inserts equations (2.66a, b) and  $\cos\phi = -1$  into equation (2.62a), he will find that the intensities are zero. This can partially support the assumption of zero intensity “the Gjønnes-Høier point has zero intensity”. However, this assumption can only be verified for the validity range of Kambe’s approximation [6], where  $|U_{h-g}| \gg |U_g|$  or  $|U_h|$ . Beyond this range, the Gjønnes-Høier point may not have a zero intensity (not even for centrosymmetric crystals) and it may not be easy to locate such a point in a three-beam CBED pattern.

#### 2.4.5.2 The theories mainly by Hurley and Moodie for centrosymmetric crystals

More complete studies of three-beam theories for centrosymmetric crystal have been carried out mainly by Hurley and Moodie since late 1970s. The papers show that in three-beam CBED discs, there are straight lines along which two-beam-form intensity distribution can be found [10, 11, 20]. The two-beam loci naturally arise from the symmetry in the three-beam dynamic diffraction equations for centrosymmetric crystals. Unlike Bethe’s [22] and Kambe’s [6] approximations, these theories do not make any assumptions about the relative magnitudes of structure factors or validity range of incident beam directions. The positions of the two-beam loci are independent of thickness and depend only on  $|V_g|$ ,  $|V_h|$ ,  $|V_{g-h}|$  and  $\cos\phi$  ( $= 1$  or  $-1$ ). The two-beam loci can be located according to the mirror symmetry that exists in the two-beam-form intensity distribution (a computer code for locating the two-beam loci in three-beam CBED patterns has been written by the author of this thesis). The structure factor magnitudes can be determined by measuring the coordinates of (1) the centre of the one two-beam locus and the three-beam condition and (2) the intersection of two two-beam loci (which happens to



be the same as the Gjønnes-Høier point) [17, 18]. Three-phase invariants (either 0 or  $\pi$ ) can be determined from the position of the centres of the two-beam intensity distributions [17, 18] or by an inspection of the whole pattern [21]. Thus, the inversion of three-beam dynamic diffraction by centrosymmetric crystals has been completed.

In practice, due to the presence of other excited beams, an error of about 20% can be found in the measurement of structure factor magnitudes [17, 18]. Nevertheless, determination of the sign for  $\cos\phi$  is unambiguous, since  $\phi = 0$  or  $\pi$  can make a significant difference in the patterns.

#### 2.4.5.3 The theories mainly by Hurley and Moodie for noncentrosymmetric crystals

Inversion of three-beam diffraction for noncentrosymmetric crystals has also been attempted [24, 91]. No two-beam locus like in the centrosymmetric case exists, and thus inversion of three-beam dynamic diffraction for noncentrosymmetric case cannot be completed in the same way as in the centrosymmetric case. A different scheme of inversion has been proposed [24]:

An intensity difference is defined as

$$\Delta \equiv I_g(\mathbf{M}) - I_g(\mathbf{M}^T) = \frac{4\kappa[\sin\mu_1 z + \sin\mu_2 z + \sin\mu_3 z]}{\mu_1 \mu_2 \mu_3} , \quad (2.67a)$$

$$\text{where} \quad \kappa = -\sigma^3 |V_{h-g}| |V_g| |V_h| \sin\phi , \quad (2.67b)$$

$$\mu_1 = \lambda_2 - \lambda_3 , \quad (2.67c)$$

and  $\mathbf{M}^T$  is the transpose of the Hermitian matrix,  $\mathbf{M}$ , defined in equations (2.63a, b).

Although the paper [24] did not clarify how to set up an orientation so that the intensity,  $I_g(\mathbf{M}^T)$ , can be measured, a careful study of the diffraction geometry from equation (2.27b) and the symmetry of structure factors (Friedel's law) from equation (2.4a) would reveal that  $I_g(\mathbf{M}^T)$  can correspond to the intensity in the opposite reflection  $\bar{g}$  ( $g$  and  $\bar{g}$  are known as a

Friedel pair),  $I_{\bar{g}}(\mathbf{M})$ , near the three-beam condition for  $0 / \bar{g} / \bar{h}$ . ( $0$ ,  $g$ ,  $h$ ,  $\bar{g}$ , and  $\bar{h}$  all lie in the same ZOLZ plane).

If the intensity difference can be measured at different thicknesses, the value of  $\kappa$  can be determined. All three structure factors can be determined if further steps described in this paper [24] could be carried out. Experimental implementation of this inversion scheme has never been realised due to its complexity. However, equations (2.67a, b) can be investigated further to determine the sign of  $\phi$ , which is lost the Bethe's [22] or Kambe's [6] approximation.

#### 2.4.5.4 Summary for the exact three-beam dynamical theories

In summary, the exact three-beam dynamical theories involve all of the three eigenvalues, and therefore they provide a more general treatment of three-beam dynamic diffraction than the previous two theories introduced in Sections 2.4.3 and 2.4.4, which are based on perturbing the kinematic and two-beam dynamic diffraction, respectively. The theories mainly by Hurley and Moodie have resulted in a complete inversion of three-beam dynamical diffraction for centrosymmetric crystals [10, 11, 20] and some insights into the inversion for noncentrosymmetric crystals [24, 91].

#### 2.4.6 Future scope

The perturbation theories discussed in Section 2.4.3 and 2.4.4 have provided schemes to measure three-phase invariants from three-beam electron diffraction patterns (both CBED and Kikuchi patterns) in both centrosymmetric and noncentrosymmetric crystals. However, the kinematical treatment is insufficient for phase recovery in cases where strong scatterings exist (i.e. specimens are not too thin or reflections are not too weak) and the perturbation of two-beam dynamic diffraction cannot describe the effect of the sign of  $\phi$ .

The analytical theories involving exact three-beam solutions need to be further developed to measure three-phase invariants in noncentrosymmetric crystals. The analytical theory must correlate the intensity to both  $\cos\phi$  and  $\sin\phi$  in a direct fashion so that a practical experimental scheme can be developed. That will allow the determination of  $\phi$  (or at least the signs of  $\cos\phi$  and  $\sin\phi$ ) from three-beam CBED patterns in general.

## Chapter 3. Determination of three-phase invariants by observation: theory

The purpose of this chapter is to develop analytical theories of three-beam electron diffraction to identify experimental conditions that permit direct measurement of three-phase invariants in noncentrosymmetric crystals. Section 3.1 will derive the full analytical solution to three-beam electron diffraction, which is the basis for later derivations. Section 3.2 will derive a simple expression of the intensity difference between a Friedel pair of reflections (which is basically a factorised form of equations (2.67a-c)) and develop a practical scheme for the determination of the sign of three-phase invariants. The sign can be determined by a qualitative comparison between the intensities of the Friedel pair within a validity range of thicknesses. Whether the thickness is within the validity range can be judged by two criteria based purely on observations of the CBED patterns (the criteria will be explained in Section 3.5). Based on the analytical solution derived in Section 3.1, Section 3.3 will show that a centre of inversion can be found within each diffraction disc when three-phase invariants are  $\pi/2$  or  $-\pi/2$ . Section 3.4 will derive another expression from the full analytical solution, which leads to the determination of the sign of the cosine three-phase invariant by observations of the CBED patterns. Section 3.6 will combine the results from the previous sections and introduce a physical approach to the determination of three phase-invariants to within  $\pm\pi/8$  for noncentrosymmetric crystals. In conjunction with direct methods, the current approach of phase measurement can play a significant role in *ab initio* structure determination. The applicability of three-beam electron diffraction in structures with large unit cells will be illustrated with a few examples. Section 3.7 will summarise the current method for the qualitative determination of three-phase invariants with a flow chart. All of the simulations for CBED patterns have included many-beam diffraction effects in order to demonstrate the applicability of the three-beam methods derived here in real situations.

### 3.1 Closed-form solutions to three-beam electron diffraction

As stated in Section 2.4.2, it would be too lengthy to express the intensity in equation (2.47) as an explicit function of  $\zeta_g$ ,  $\zeta_h$ ,  $|V_g|$ ,  $|V_h|$ ,  $|V_{h-g}|$ ,  $z$  and  $\phi$ . However, a much shorter equation can be derived if the arguments include a mixture of eigenvalues and those parameters. Here, we derive such a closed-form solution to three-beam dynamic diffraction.

The wave function of the diffracted beam  $g$  and the central beam  $0$  can be expressed as:

$$\psi_g = \langle g | \exp(i \mathbf{M} z) | 0 \rangle \quad (3.1a)$$

and  $\psi_0 = \langle 0 | \exp(i \mathbf{M} z) | 0 \rangle$ , (3.1b)

where  $z$  is the specimen thickness,

$$|0\rangle = (1, 0, 0)^T \quad \text{and} \quad \langle g| = (0, 1, 0)$$

are the initial and final states of the scattering processes described by the Hermitian scattering matrix  $\mathbf{M}$ , and

$$\mathbf{M} = \begin{pmatrix} 0 & \sigma V_g^* & \sigma V_h^* \\ \sigma V_g & 2\pi\zeta_g & \sigma V_{h-g}^* \\ \sigma V_h & \sigma V_{h-g} & 2\pi\zeta_h \end{pmatrix}, \quad (3.2)$$

which is the eigen matrix for the equation:

$$\mathbf{M} \mathbf{C} = \lambda_i \mathbf{C}. \quad (3.3)$$

The incident beam direction is specified by the excitation errors of reflections  $g$  and  $h$ , denoted as  $\zeta_g$  and  $\zeta_h$  respectively.  $V_g^*$  is the complex conjugate of the structure factor  $V_g$  and  $\sigma$  is the interaction constant.

The 3x3 matrix  $\mathbf{M}$  has three real eigenvalues,  $\lambda_1$ ,  $\lambda_2$ ,  $\lambda_3$ , and each represents a Bloch wave.

The eigenvalues are calculated from the characteristic equation  $|\mathbf{M} - \lambda_i \mathbf{I}| = 0$ , which yields

$$\lambda^3 + b\lambda^2 + c\lambda + d = 0, \quad (3.4a)$$

$$b = -2\pi(\zeta_g + \zeta_h), \quad (3.4b)$$

$$c = (2\pi\zeta_g)(2\pi\zeta_h) - (\sigma|V_g|)^2 - (\sigma|V_h|)^2 - (\sigma|V_{h-g}|)^2 \quad (3.4c)$$

and

$$d = (2\pi\zeta_g)(\sigma|V_h|)^2 + (2\pi\zeta_h)(\sigma|V_g|)^2 - 2(\sigma|V_g|)(\sigma|V_h|)(\sigma|V_{h-g}|)\cos\phi. \quad (3.4d)$$

The real roots to this cubic equation can be expressed in trigonometric forms:

$$\lambda_1 = 2\sqrt{-Q} \cos\left(\frac{\theta}{3}\right) - \frac{b}{3}, \quad (3.5a)$$

$$\lambda_2 = 2\sqrt{-Q} \cos\left(\frac{\theta + 2\pi}{3}\right) - \frac{b}{3} \quad (3.5b)$$

and

$$\lambda_3 = 2\sqrt{-Q} \cos\left(\frac{\theta + 4\pi}{3}\right) - \frac{b}{3}, \quad (3.5c)$$

where 
$$Q = \frac{3c - b^2}{9}, \quad (3.5d)$$

$$R = \frac{9bc - 27d - 2b^3}{54} \quad (3.5e)$$

and 
$$\theta = \cos^{-1}\left(\frac{R}{\sqrt{-Q^3}}\right). \quad (3.5f)$$

Fig. 3.1. shows a plot of the three dispersion surfaces along the Bragg condition for reflection  $g$ , which lies on a line (the so-called Bragg line) where  $\zeta_g = 0$ , and  $\zeta_h$  varies continuously. Note:  $\lambda_1, \lambda_2, \lambda_3$  have been assigned in a sequence such that  $\lambda_1 \geq \lambda_2 \geq \lambda_3$ . This convention applies to the whole chapter.

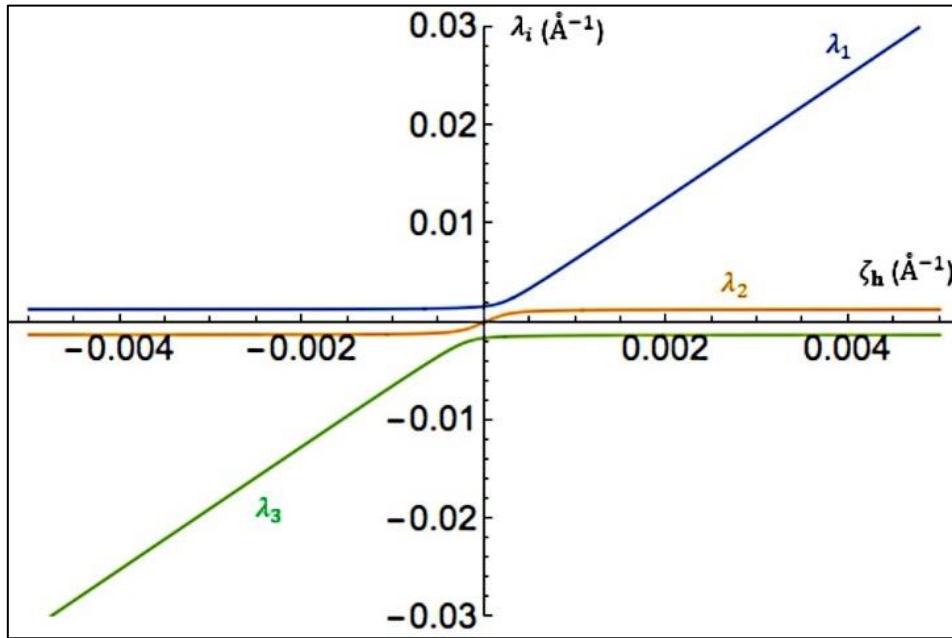


**Figure 3.1.** A plot of dispersion surfaces in three-beam electron diffraction. The three eigenvalues,  $\lambda_1, \lambda_2, \lambda_3$ , are described by equations (3.5a-c). Wolfram Mathematica 10 [93] is used for generating this plot.

Following [50], we apply the projection operator

$$\exp(i \mathbf{M} z) = \sum_{i=1}^3 P_i \exp(i \lambda_i z) \quad (3.6a)$$

and 
$$P_i = \frac{\mathbf{M} - \lambda_{i\oplus 1}}{\lambda_i - \lambda_{i\oplus 1}} \frac{\mathbf{M} - \lambda_{i\oplus 2}}{\lambda_i - \lambda_{i\oplus 2}} \quad (i = 1, 2, 3), \quad (3.6b)$$

where an operator  $\oplus$  is introduced to indicate cyclic addition:  $1\oplus 1=2$ ,  $1\oplus 2=3$ ,  $2\oplus 1=3$ ,  $2\oplus 2=1$ ,  $3\oplus 1=1$ ,  $3\oplus 2=2$ . Before moving on, we introduce some shorthand notations:

$$\begin{aligned} S_g &= 2\pi\zeta_g, \quad U_1 = \sigma|V_g|, \quad U_2 = \sigma|V_h|, \quad U_3 = \sigma|V_{h-g}|, \\ \text{and } \mu_i &= \lambda_{i\oplus 1} - \lambda_{i\oplus 2} \text{ (i.e. } \mu_1 = \lambda_2 - \lambda_3, \mu_2 = \lambda_3 - \lambda_1, \text{ and } \mu_3 = \lambda_1 - \lambda_2). \end{aligned}$$

By combining equations (3.1), (3.5a, b) and (3.6a, b), we can obtain the wave functions for reflections  $g$  and  $0$ :

$$\psi_g = -U_1 \exp(i\varphi_g) \sum_{i=1}^3 \exp(i\lambda_i z) \frac{\frac{U_2 U_3}{U_1} \exp(-i\phi) + S_g - \lambda_{i\oplus 1} - \lambda_{i\oplus 2}}{\mu_{i\oplus 1} \mu_{i\oplus 2}} \quad (3.7)$$

$$\text{and } \psi_0 = - \sum_{i=1}^3 \exp(-i\lambda_i z) \frac{\lambda_{i\oplus 1} \lambda_{i\oplus 2} + U_1^2 + U_2^2}{\mu_{i\oplus 1} \mu_{i\oplus 2}}. \quad (3.8)$$

Thus, we can derive the intensity expressions for reflections  $g$  and  $h$ :

$$\begin{aligned} I_g = \psi_g \psi_g^* &= 2U_1^2 \sum_{i=1}^3 \left\{ (\cos\mu_i z - 1) \left( \frac{|G_0|^2}{\mu_1 \mu_2 \mu_3 \mu_i} + G_{i\oplus 1} G_{i\oplus 2} \right) \right. \\ &\quad + (\cos(\mu_i z + \phi) - \cos\phi) \frac{|G_0| G_{i\oplus 1}}{\mu_i \mu_{i\oplus 1}} + \\ &\quad \left. (\cos(\mu_i z - \phi) - \cos\phi) \frac{|G_0| G_{i\oplus 2}}{\mu_i \mu_{i\oplus 2}} \right\} \end{aligned} \quad (3.9a)$$

and

$$\begin{aligned} I_h = \psi_h \psi_h^* &= 2U_2^2 \sum_i^3 \left\{ (\cos\mu_i z - 1) \left( \frac{|G_0'|^2}{\mu_1 \mu_2 \mu_3 \mu_i} + G_{i+1}' G_{i+2}' \right) \right. \\ &\quad + (\cos(\mu_i z - \phi) - \cos\phi) \frac{|G_0'| G_{i\oplus 1}'}{\mu_i \mu_{i\oplus 1}} + \\ &\quad \left. (\cos(\mu_i z + \phi) - \cos\phi) \frac{|G_0'| G_{i\oplus 2}'}{\mu_i \mu_{i\oplus 2}} \right\}, \end{aligned} \quad (3.9b)$$

$$\text{where } |G_0| = \frac{U_2 U_3}{U_1}, |G_0'| = \frac{U_1 U_3}{U_2};$$

$$\text{and } G_i = \frac{S_g - \lambda_{i\oplus 1} - \lambda_{i\oplus 2}}{\mu_{i\oplus 1} \mu_{i\oplus 2}}, \quad G_i' = \frac{S_h - \lambda_{i\oplus 1} - \lambda_{i\oplus 2}}{\mu_{i\oplus 1} \mu_{i\oplus 2}}.$$

The intensity expression for the central beam is:

$$I_0 = \psi_0 \psi_0^* = 1 + 2 \sum_{i=1}^3 C_{i\oplus 1} C_{i\oplus 2} (\cos \mu_i z - 1) , \quad (3.10)$$

where

$$C_i = \frac{\lambda_{i\oplus 1} \lambda_{i\oplus 2} + U_1^2 + U_2^2}{\mu_{i\oplus 1} \mu_{i\oplus 2}} .$$

From equations (3.9a, b) and (3.10), it can be seen that  $I_g$  and  $I_h$  depend on the three-phase invariant,  $\phi$ , and  $I_0$  depends on only its magnitude,  $|\phi|$ . Here, the three-phase invariant is defined as the summation of three structure factor phases,  $\phi \equiv \varphi_g + \varphi_{h-g} + \varphi_{-h}$ , and the reciprocal lattice vectors,  $g, h-g, -h$  form a closed loop in the anticlockwise direction, which sets up the sign convention<sup>6</sup> for three-phase invariants. This convention applies to the whole thesis.

Although the expressions for  $I_g$  and  $I_h$  in equations (3.9a, b) and (3.10) convey all the structural parameters, an inversion for the three-phase invariant,  $\phi$ , is still not straightforward. To invert the three-phase invariant,  $\phi$ , or at least the signs of  $\sin \phi$  and  $\cos \phi$ , it is necessary to reduce equation (3.9) further. To invert the sign of  $\sin \phi$ , Section 3.2 will reduce equation (3.9a) without making any approximation. To invert the sign of  $\cos \phi$  in a practical way, Section 3.4 will introduce some approximations when reducing equation (3.9a).

### 3.2 Approach to determine the sign of $\sin \phi$

It is not only possible but also practical to determine the sign of  $\sin \phi$  by simple inspection of three-beam CBED patterns. In general, it requires a Friedel pair of three-beam conditions, (i.e., the three-beam conditions  $0 / g / h$  and  $0 / \bar{g} / \bar{h}$ ) to determine the sign of the three-phase invariant,  $\phi$ . If reflections  $g$  and  $h$  happen to have equal or approximately equal structure factor magnitudes, i.e.  $|V_g| = |V_h|$  or  $|V_g| \approx |V_h|$ , only one three-beam condition,  $0 / g / h$ , is needed for the sign determination. These particular scenarios are common in most space groups that have symmetry related reflections called Bijvoet pairs, e.g.  $h k l$  and  $h \bar{k} l$  where  $V_{h, k, l} = V_{h, \bar{k}, l}^*$ .

---

<sup>6</sup> If the three-phase invariant is defined as  $\phi \equiv \varphi_h + \varphi_{g-h} + \varphi_{-g}$ , then the sign of  $\phi$  will be flipped.

### 3.2.1 General scenarios: using a centrosymmetrically related pair of three-beam conditions

#### 3.2.1.1 Derivations of the criterion for the sign determination

Commencing from equation (3.9a), one can derive a short expression for the intensity difference between a Friedel pair,  $g$  and  $\bar{g}$ . To be more specific, it is the intensity of  $g$  at a point  $(\zeta_g, \zeta_h)$  near the three-beam condition for  $0 / g / h$  (shown in Fig.3.2a i) subtracted by the intensity of  $\bar{g}$  at  $(\zeta_{\bar{g}}, \zeta_{\bar{h}}) = (\zeta_g, \zeta_h)$  near the three-beam condition for  $0 / \bar{g} / \bar{h}$  (shown in Fig.3.2a ii):

$$I_g(\zeta_g, \zeta_h, z) - I_{\bar{g}}(\zeta_{\bar{g}}, \zeta_{\bar{h}}, z) = -4 \sin\phi U_1 U_2 U_3 \sum_{i=1}^3 \frac{\sin(\mu_i z)}{\mu_1 \mu_2 \mu_3}, \quad (3.11a)$$

where  $\zeta_g$  and  $\zeta_h$  are the excitation errors for reflections  $g$  and  $h$ , and  $\zeta_{\bar{g}}$  and  $\zeta_{\bar{h}}$  are the excitation errors for reflections  $\bar{g}$  and  $\bar{h}$ .

This is identical to equation (2.67a), which is given in [24].

Since  $\mu_1 + \mu_2 + \mu_3 = 0$ , equation (3.11a) can be factorized:

$$I_g(\zeta_g, \zeta_h, z) - I_{\bar{g}}(\zeta_{\bar{g}}, \zeta_{\bar{h}}, z) = 16 \sin\phi U_1 U_2 U_3 \prod_{i=1}^3 \frac{\sin(\frac{\mu_i z}{2})}{\mu_i}. \quad (3.11b)$$

#### critterion (3.12)

At any thickness,

$$\text{if } I_g(\zeta_g, \zeta_h, z) = I_{\bar{g}}(\zeta_{\bar{g}}, \zeta_{\bar{h}}, z), \quad \text{then } \sin\phi = 0 \text{ or } |V_{h-g}| = 0. \quad (3.12)$$



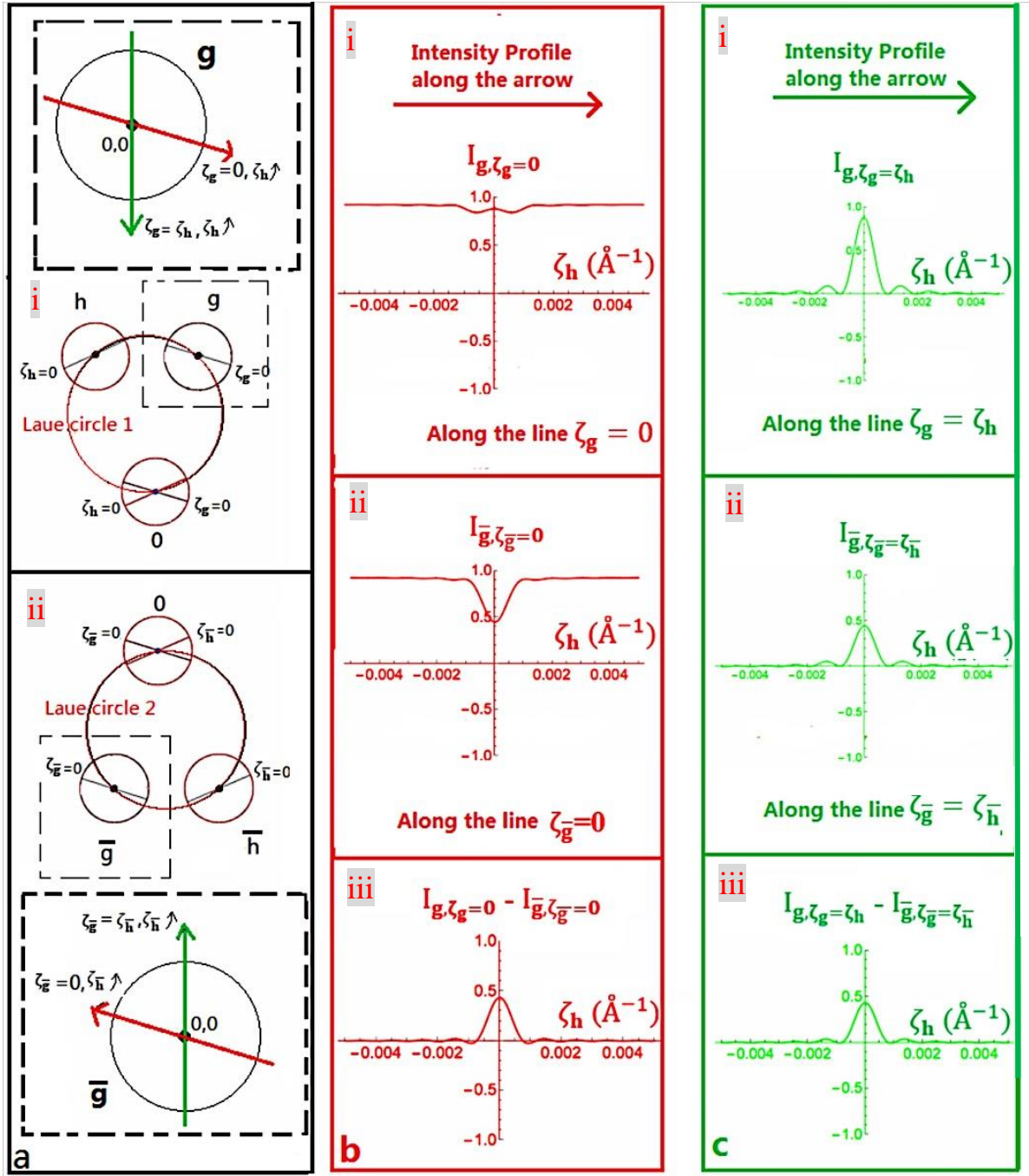


**Figure 3.2. Illustrations of equations (3.11a, b).** The columns in red (b) and green (c) show the intensity profiles along the loci that are labelled by the red and green arrows in (a). (a) shows a schematic of a pair of centrosymmetrically related three-beam CBED patterns, (i) and (ii), which share the same zone axis that is perpendicular to the vectors  $\mathbf{g}$ ,  $\mathbf{h}$ ,  $\bar{\mathbf{g}}$  and  $\bar{\mathbf{h}}$ , but have  $\mathbf{K}_t$  (projection of the wave vector  $\mathbf{K}$ , defined in equation (2.27b)) in the opposite directions. The intensity profiles in (b, c) are calculated with the following parameters:  $|V_g|=1.78$  V,  $|V_h|=1.20$  V,  $|V_{h-g}|=0.53$  V,  $\phi=90^\circ$  and  $z=1000$  Å, using Wolfram Mathematica 10 [93]. The values of three structure factor magnitudes are chosen from a three-beam condition near  $[\bar{1} \bar{3}$

$\bar{7}]$  in alpha-quartz (space group  $P3_121$ ) to represent a real situation (except that the three-phase invariant is modified).

At the exact three-beam diffraction conditions,  $(\zeta_g, \zeta_h) = (\zeta_{\bar{g}}, \zeta_{\bar{h}}) = (0,0)$ , we define a “three-beam extinction distance”,  $\xi_{3\text{-beam}}$ , where

$$\xi_{3\text{-beam}} \equiv \frac{2\pi}{|\mu_2(\zeta_g = 0, \zeta_h = 0)|} , \quad (3.13)$$

so that:

1) when  $z = \xi_{3\text{-beam}}$  ,

$$\prod_{i=1}^3 \frac{\sin(\frac{\mu_i z}{2})}{\mu_i} = 0$$

and  $I_g(\zeta_g = 0, \zeta_h = 0, z) - I_{\bar{g}}(\zeta_{\bar{g}} = 0, \zeta_{\bar{h}} = 0, z) = 0$  ;

2) when  $z < \xi_{3\text{-beam}}$  ,

since at  $(\zeta_g = 0, \zeta_h = 0)$ ,  $|\mu_2| = |\mu_1| + |\mu_3|$ , we have

$$\prod_{i=1}^3 \frac{\sin(\frac{\mu_i z}{2})}{\mu_i} > 0 .$$

Therefore,

**criterion (3.14)**

if  $z < \xi_{3\text{-beam}}$  ,      and  $I_g(\zeta_g = 0, \zeta_h = 0, z) > I_{\bar{g}}(\zeta_{\bar{g}} = 0, \zeta_{\bar{h}} = 0, z)$ ,  
then  $\sin\phi > 0$  ; (3.14a)

if  $z < \xi_{3\text{-beam}}$  ,      and  $I_g(\zeta_g = 0, \zeta_h = 0, z) < I_{\bar{g}}(\zeta_{\bar{g}} = 0, \zeta_{\bar{h}} = 0, z)$ ,  
then  $\sin\phi < 0$  . (3.14b)

This the criterion for determining the sign of  $\sin\phi$  and therefore the sign of  $\phi$ .

However, if  $z > \xi_{3\text{-beam}}$ , structure factor magnitudes and thickness are needed to get the sign of

$$\prod_{i=1}^3 \frac{\sin(\frac{\mu_i z}{2})}{\mu_i}$$

first, which complicates the determination of the sign of  $\sin\phi$ , and hence,  $\phi$ .

In summary, provided that the specimen thickness is smaller than the extinction distance ( $z < \xi_{3\text{-beam}}$ ), it is feasible to determine the sign of  $\sin\phi$ . Importantly, this condition is often realisable in practice and is easily tested, as follows.

1) The validity of the condition,  $z < \xi_{3\text{-beam}}$ , is not restricted to very thin specimens.

The three-beam extinction distance,  $\xi_{3\text{-beam}}$ , decreases with increasing structure factor magnitudes, so the range of the thickness that satisfies the condition,  $z < \xi_{3\text{-beam}}$ , becomes narrower in three-beam cases where the structure factor magnitudes are large. One may think that the specimen needs to be very thin for a three-beam case with large structure factors. However, it can be shown that even if the three-beam case involves fairly large structure factors, the three-beam extinction distance is still fairly high. For example, a three-beam case,  $000/3\bar{1}\bar{1}/31\bar{1}$ , in zinc blende ZnTe, where  $|V_{3, \bar{1}, \bar{1}}| = |V_{3, 1, \bar{1}}| = 4.2$  V and  $|V_{0, 2, 0}| = 2.5$  V, may serve as an example of three-beam cases with three fairly large structure factor magnitudes since a fairly heavy element, Te, is present in the structure and  $|V_{3, 1, \bar{1}}|$  and  $|V_{0, 2, 0}|$  are among the largest for this structure. In this case, the three-beam extinction distance,  $\xi_{3\text{-beam}}$ , at 200kV is about 650 Å, which is sufficiently large to allow specimen thicknesses less than  $\xi_{3\text{-beam}}$  to be accessed practically in TEM. In general, a typical value of the three-beam extinction distance,  $\xi_{3\text{-beam}}$ , at 200kV for inorganic crystal structures is above 1000 Å and for organic crystal structure it is above 2000 Å.

2) The validity of the condition,  $z < \xi_{3\text{-beam}}$ , can be tested by inspection.

By inspection of the Bragg lines, one can decide whether the thickness is smaller than the extinction distance according to the following two criteria (the proof of these criteria below is lengthy and will be discussed in Section 3.5):

**criterion I.** In the diffracted discs and away from the three-beam condition, the excess Bragg line has a central bright fringe that is more than 1.5 times (1.618 to be more exact) wider than the neighbouring bright fringe (which is illustrated in Fig. 3.3).

**criterion II.** In the central disc, the intensity profile along the locus  $\zeta_g = \zeta_h$  has a local minimum at or near the exact three-beam condition, i.e.,  $\frac{d^2 I_0}{d\zeta_h^2} > 0$  (which is illustrated

If only one criterion is satisfied, then the CBED pattern should still be rejected as unsuitable for the sign observation. For example, the three-beam CBED pattern in Fig. 3.4b satisfies criterion I but not II, so this CBED pattern has to be rejected. If both criteria I and II are met, (for example, the three-beam CBED pattern in Fig. 3.4a) then it can be concluded that  $z < \xi_{3\text{-beam}}$ . In other words, satisfying criteria I + II is sufficient but not necessary for having  $z < \xi_{3\text{-beam}}$ .

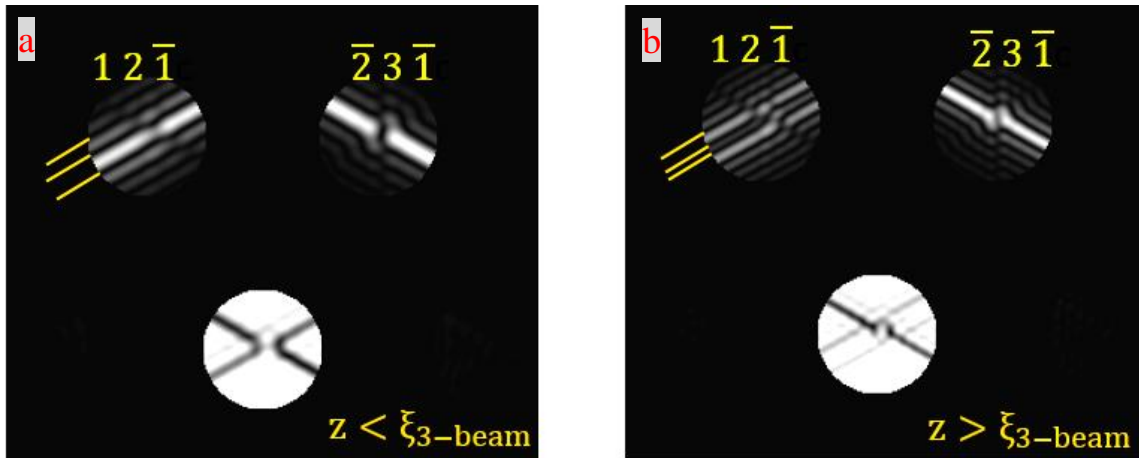


**Figure 3.3. Illustration of criterion I with simulated three-beam CBED patterns of alpha-quartz (space group  $P3_121$ ) near  $[\bar{1} \ \bar{3} \ \bar{7}]$  at 200 kV.** Criterion I is satisfied in (a) but not in (b), which can be seen by comparing the widths of the central and neighbouring bright fringes. These widths are highlighted by the orange lines which are drawn by extending the line of the corresponding dark fringes that sandwich each bright fringe. In (a) where  $z = 0.85 \xi_{3\text{-beam}}$ , it can be seen that the central fringe is much wider than the neighbouring bright fringe. By

contrast, in (b) where  $z = 1.15 \xi_{3\text{-beam}}$ , the central fringe is narrower than the second bright fringe. The CBED patterns are simulated using JEMS [58].

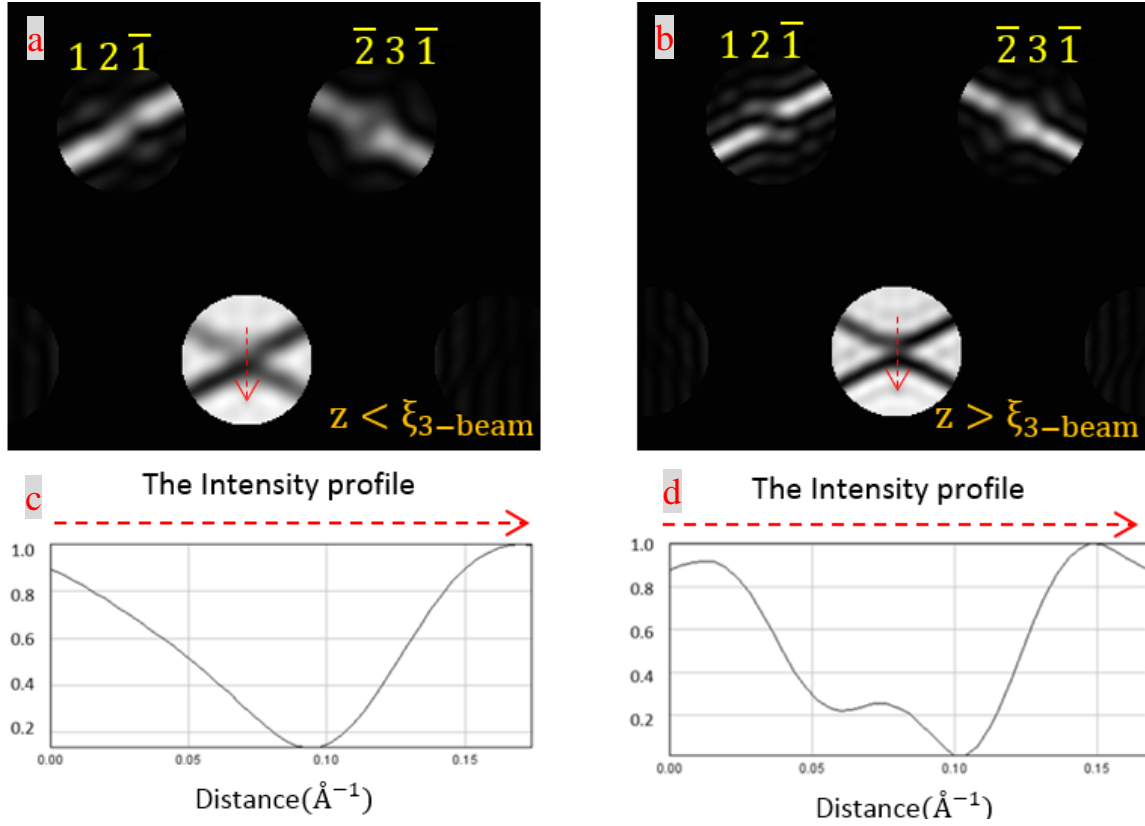


**Figure 3.4. Illustrations of criterion II in simulated CBED patterns of alpha-quartz (space group  $P3_121$ ) near  $[\bar{1} \ 3 \ \bar{7}]$  at 200 kV.**  $|V_{3, \bar{1}, 0}|$  has been increased artificially to 2.87 V (to create a three-beam case with a strong coupling reflection rather than a weak reflection as in Figure 3.3). Criterion II is satisfied in (a) but not in (b), which can be determined by inspection of the intensity profile along the locus  $z_g = z_h$  (shown by the yellow dashed line): (c) for  $z < \xi_{3\text{-beam}}$  (where  $z = 0.85 \xi_{3\text{-beam}}$  is used), the intensity profile has a local minimum near the three-beam condition, i.e.  $\frac{d^2 I_0}{dz_h^2} > 0$ ; (d) for  $z > \xi_{3\text{-beam}}$  (where  $z = 1.15 \xi_{3\text{-beam}}$ ), the intensity profile has a local maximum near the three-beam condition, i.e.  $\frac{d^2 I_0}{dz_h^2} < 0$ . The CBED patterns are simulated using JEMS [58].

### 3.2.1.2 Examples of sign determination

Once both criteria I and II are met, and thus  $z < \xi_{3\text{-beam}}$  is met, which allows criterion (3.14) to be applied for sign determination. Here, two examples for determining the sign of  $\sin\phi$  are demonstrated with simulated CBED patterns shown in Fig. 3.5, where two different structures of alpha-quartz (in different space groups) are used.

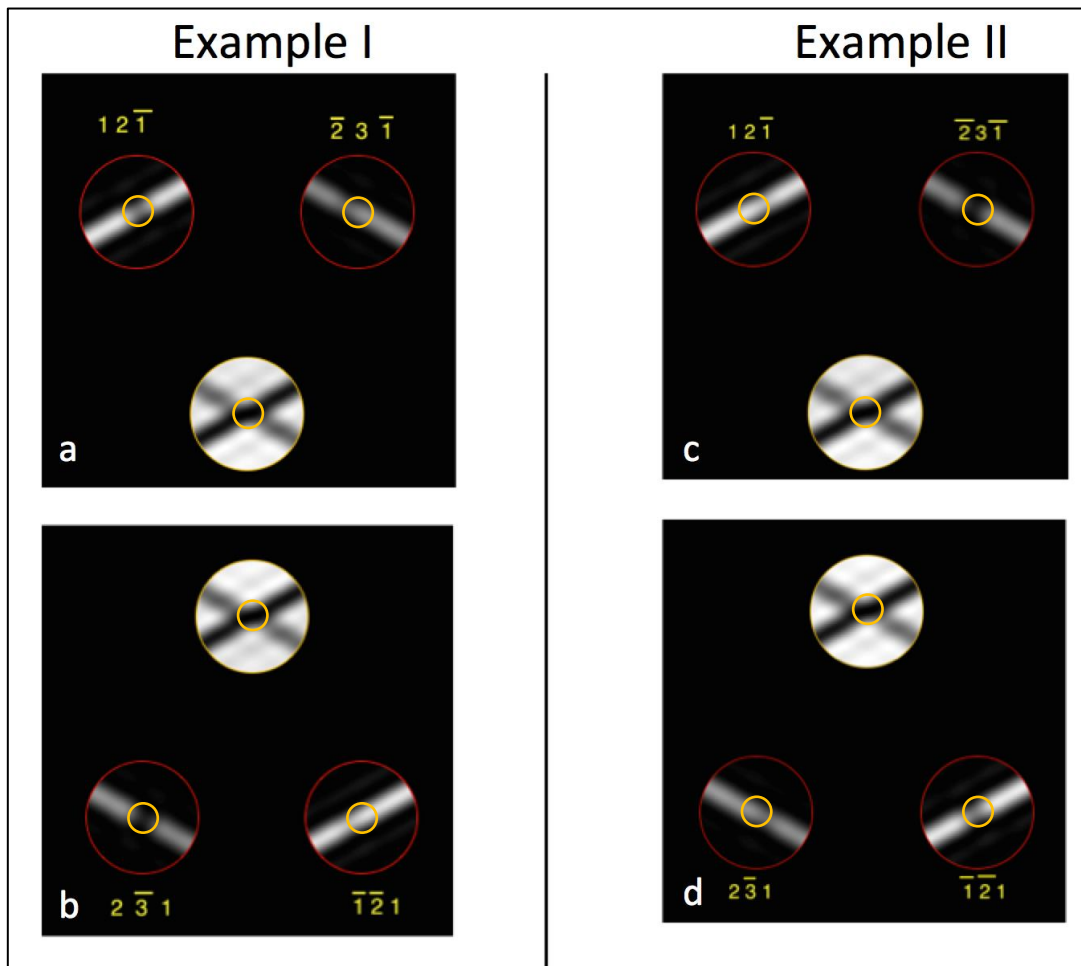


**Figure 3.5. Simulated three-beam CBED patterns near  $[\bar{1} \ \bar{3} \ \bar{7}]$  of two different types of alpha-quartz (which form a chiral pair): the two structures are in space groups (a, b)  $P3_221$  and (c, d)  $P3_121$ . In (a,b),  $\phi = \varphi_{\bar{2},3,\bar{1}} - \varphi_{1,2,\bar{1}} + \varphi_{3,\bar{1},0} = 103^\circ$ . In (c, d),  $\phi = \varphi_{\bar{2},3,\bar{1}} - \varphi_{1,2,\bar{1}} + \varphi_{3,\bar{1},0} = -103^\circ$ . The structure factor-magnitudes are  $|V_{\bar{2},3,\bar{1}}| = 1.20 \text{ V}$ ,  $|V_{1,2,\bar{1}}| = 1.78 \text{ V}$ ,  $|V_{3,\bar{1},0}| = 0.53 \text{ V}$ , the specimen thickness is  $1000 \text{ \AA}$ . The three-beam extinction distance,  $\xi_{3\text{-beam}}$ , is  $1900 \text{ \AA}$ . The CBED patterns are simulated using JEMS [58]. In the simulation, more than a hundred beams are included and inelastic scattering is accounted for by phenomenological absorption.**

**Example I.** alpha-quartz (space group  $P3_221$ ), which is shown in Fig. 3.5a, b:

1. Both criteria I and II are met, which means  $z < \xi_{3\text{-beam}}$ .
2. At (and near) the exact three-beam conditions (circled in Fig 3.5a, b),

$$I_{\bar{2}\ 3\ \bar{1}}(\zeta_g = 0, \zeta_h = 0, z) > I_{2\ \bar{3}\ 1}(\zeta_g = 0, \zeta_h = 0, z) .$$

Therefore, it can be concluded that  $\sin(\varphi_{\bar{2},3,\bar{1}} - \varphi_{1,2,\bar{1}} + \varphi_{3,\bar{1},0}) > 0$ .

**Example II.** alpha-quartz (space group  $P3_121$ ), which is shown in Fig. 3.5c, d:

1. Both criteria I and II are met, which means  $z < \xi_{3\text{-beam}}$ .
2. At (and near) the exact three-beam conditions (circled in Fig 3.5c, d),

$$I_{\bar{2}\ 3\ \bar{1}}(\zeta_g = 0, \zeta_h = 0, z) < I_{2\ \bar{3}\ 1}(\zeta_g = 0, \zeta_h = 0, z) .$$

Therefore, it can be concluded that  $\sin(\varphi_{\bar{2},3,\bar{1}} - \varphi_{1,2,\bar{1}} + \varphi_{3,\bar{1},0}) < 0$ .

### 3.2.1.3 Comparison with the kinematical approximation

In the two examples above, the thickness used in the simulations, which is 1000 Å, satisfies the condition,  $z < \xi_{3\text{-beam}}$ , and thus criterion (3.14) for the sign determination can be used. However, at such a thickness, the kinematical approximation discussed in Section 2.4.3 will fail, which can be seen from Fig. 3.6. Therefore, criterion (3.14) which has been derived from the exact solution to three-beam electron diffraction can be applied to much wider ranges of thicknesses than the kinematical theory.

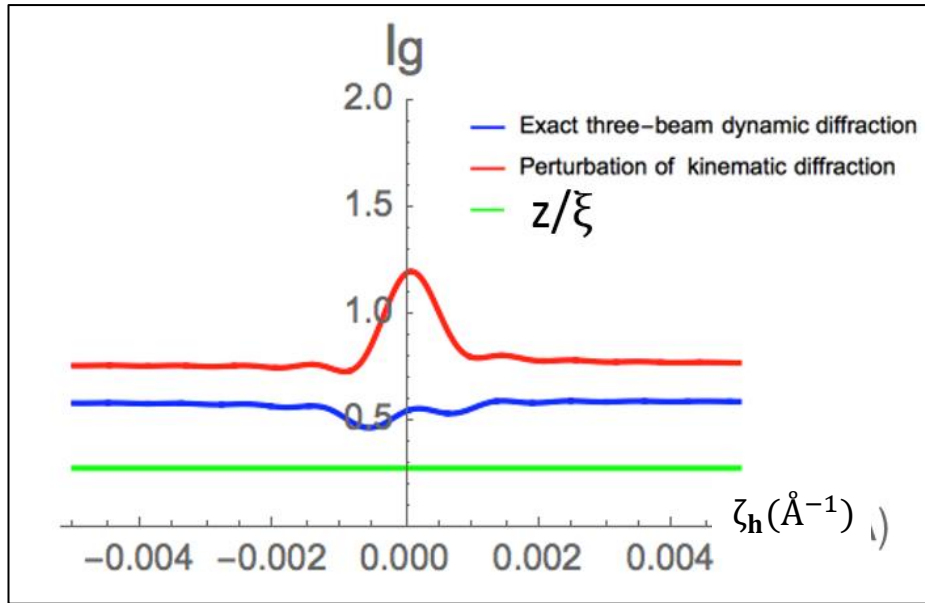


**Figure 3.6. Intensity profiles along the Bragg line of reflection  $\bar{2} \ 3 \ \bar{1}$  in alpha-quartz  $P3_21$ .** The structure factors and the thickness are the same as in Fig. 3.3. The perturbation theory fails to account for the intensity profile in this case where the thickness is more than a quarter of the two-beam extinction distance,  $\xi$ , and is nearly a half of the three-beam extinction distance,  $\xi_{3\text{-beam}}$ , or the maximum allowed thickness for the application of criterion (3.14). Wolfram Mathematica 10 [93] is used for this plot.

#### 3.2.1.4 Experimental realisation of the sign determination

Application of criterion (3.14) requires the recording of a pair of three-beam CBED patterns at the same thickness from two incident directions that are several to a few dozen mrad apart. This can be labour intensive and sometimes difficult to achieve experimentally. However, this can be realised more easily by new diffraction techniques that are based on the computer control of beam tilts and the sequential recording of diffraction patterns from different incident directions [23, 94]. Illustrations of the experiments will be given in the next chapter.

#### 3.2.2 Particular scenarios: using a single three-beam condition

Without including a centrosymmetrically related pair of three-beam conditions, it is also



possible to determine the sign of  $\sin\phi$  in special cases of three-beam conditions where  $|V_g| = |V_h|$  (for example, reflections  $\mathbf{g}$  and  $\mathbf{h}$  form a Bijvoet pair) or at least  $|V_g| \approx |V_h|$ . In these scenarios, we only need to take one three-beam CBED pattern to obtain the sign of the three-phase invariant.

For  $|V_g| = |V_h|$ , by subtracting equation (3.9b) from (3.9a), we can derive another expression for the intensity difference along the locus  $\zeta_g = \zeta_h$ :

$$I_g(\zeta_h, z) - I_h(\zeta_h, z) = 16\sin\phi U_1 U_2 U_3 \prod_{i=1}^3 \frac{\sin\left(\frac{\mu_i z}{2}\right)}{\mu_i}. \quad (3.15)$$

The sign of  $\sin\phi$  can also be determined according to criterion (3.14) using single CBED pattern. An example of the sign determination based on equation (3.15) and criterion (3.14) is given in Fig. 3.7.

For  $|V_g| \neq |V_h|$ , it is necessary to use a centrosymmetrically related pair of three-beam conditions as in the general scenarios. Otherwise, determination of the sign is not feasible, which can be seen from the following discussion. An intensity difference can be expressed as

$$\begin{aligned} \frac{I_g(\zeta_h, z)}{U_1^2} - \frac{I_h(\zeta_g, z)}{U_2^2} &= 8\sin\phi (|G_0| + |G'_0|) \prod_{i=1}^3 \frac{\sin\left(\frac{\mu_i z}{2}\right)}{\mu_i} \\ &+ T(\zeta_g, |V_g|, |V_h|, |V_{h-g}|, \cos\phi, z), \end{aligned} \quad (3.16)$$

where  $T(\zeta_g, |V_g|, |V_h|, |V_{h-g}|, \cos\phi, z)$  is a function that is independent of the sign of  $\phi$  and its sign depends on the relative magnitudes of  $|V_g|$  and  $|V_h|$ :

$$\text{when } |V_g| > |V_h|, \quad T(\zeta_h = \zeta_g = 0, |V_g|, |V_h|, |V_{h-g}|, \cos\phi, z) < 0; \quad (3.17a)$$

$$\text{when } |V_g| < |V_h|, \quad T(\zeta_h = \zeta_g = 0, |V_g|, |V_h|, |V_{h-g}|, \cos\phi, z) > 0. \quad (3.17b)$$

From equations (3.16) and (3.17a, b), it can be seen that the sign of  $\phi$  may be determined directly from the intensity difference between reflections  $g$  and  $h$ :

criterion (3.18)

$$\text{if } |V_g| > |V_h|, z < \xi_{3\text{-beam}}, \text{ and } \frac{I_g(\zeta_h = 0, z)}{I_h(\zeta_g = 0, z)} > \frac{|V_g|^2}{|V_h|^2},$$

$$\text{then } \sin\phi > 0 ; \quad (3.18a)$$

$$\text{if } |V_g| < |V_h|, z < \xi_{3\text{-beam}}, \text{ and } \frac{I_g(\zeta_h = 0, z)}{I_h(\zeta_g = 0, z)} < \frac{|V_g|^2}{|V_h|^2},$$

$$\text{then } \sin\phi < 0 . \quad (3.18b)$$

Figs. 3.5b, c show the examples to which criterion (3.18) can be applied. The application of this criterion requires *a priori* knowledge of the relative structure factor magnitudes,  $|V_g|/|V_h|$ , which is less feasible than that of criterion (3.14). However, this requires less experimental work. The reason for setting a Bijveot pair to three-beam conditions for the intensity comparison is to eliminate the term,  $T(\zeta_h, |V_g|, |V_h|, |V_{h-g}|, \cos\phi, z)$ , which results in a straightforward relation between the intensity contrast and the sign of the three-phase invariant as in criterion (3.14).

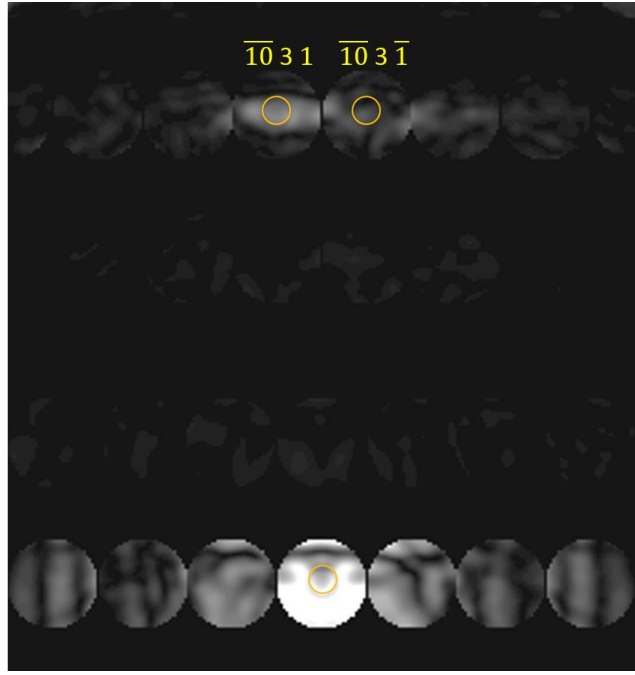


**Figure 3.7. A simulated CBED pattern of bismuth trioxide,  $\text{Bi}_{12}\text{SiO}_{24}$ , (space group I23) at a three-beam condition near  $[3\ 10\ 0]$ .** In the input parameters:  $\phi = \phi_{\overline{10}\ 3\ \overline{1}} - \phi_{\overline{10}\ 3\ 1} + \phi_{0\ 0\ 2} = -48^\circ$ ,  $z = 800\ \text{\AA}$ . More than 130 reflections (including the HOLZ reflections) were included in the simulation. The sign of the  $\phi$  can be determined by comparing the intensities at the three-beam condition (in the circled regions) within reflections  $\overline{10}\ 3\ \overline{1}$  and  $\overline{10}\ 3\ 1$ :  $I_{\overline{10}\ 3\ \overline{1}}(\zeta_g = 0, \zeta_h = 0, z) < I_{\overline{10}\ 3\ 1}(\zeta_g = 0, \zeta_h = 0, z)$ . According to criterion (3.14), the three-phase invariant,  $\phi$ , is negative, which agrees with  $\phi = -48^\circ$ . The crystal structure  $\text{Bi}_{12}\text{SiO}_{24}$  (space group I23) is used as an example for this illustration, because it is a structure that is not trivial to solve: it has 65 atom positions in the unit cell with both heavy and light atoms. The Bloch wave method in JEMS [58] was used for this simulation, including more than 300 reflections to represent real situations.

### 3.3 Determination of whether $|V_{h-g}|\cos\phi$ is zero

The last section has established a method for determining if  $\sin\phi$  is positive, zero or negative, and the derivations of criteria (3.12) and (3.14) are based on the exact three-beam solutions given in equations (3.9) and (3.10) in Section 3.1. The following two sections will establish the approach to determine if  $\cos\phi$  is positive, zero or negative. This section will be dedicated to one problem: the determination of whether  $|V_{h-g}|\cos\phi$  is zero.

By inserting  $\cos\phi = 0$  or  $|V_{h-g}| = 0$ , into equation (3.4d), we have the zeroth order coefficient for the cubic equation (3.4a):

$$d = (2\pi\zeta_g)(\sigma|V_h|)^2 + (2\pi\zeta_h)(\sigma|V_g|)^2. \quad (3.19)$$

Inserting equation (3.19) into equations (3.5 a-c), one can find that

$$\lambda_i(-\zeta_g, -\zeta_h) = -\lambda_{i\oplus 2}(\zeta_g, \zeta_h), \quad (3.20a)$$

$$\text{thus,} \quad \mu_i(-\zeta_g, -\zeta_h) = -\mu_{i\oplus 2}(\zeta_g, \zeta_h). \quad (3.20b)$$

In other words, the dispersion surfaces  $\lambda_i(\zeta_g, \zeta_h)$  are centrosymmetric about the exact three-beam condition at  $(\zeta_g = 0, \zeta_h = 0)$ , which agrees with the pioneer work of P. P. Ewald and Y. Heno [95].

By inserting equations (3.20a, b) into equations (3.9a, b) and (3.10), one will find that

$$I_g(-\zeta_g, -\zeta_h) = I_g(\zeta_g, \zeta_h), \quad (3.21a)$$

$$I_h(-\zeta_g, -\zeta_h) = I_h(\zeta_g, \zeta_h), \quad (3.21b)$$

$$\text{and} \quad I_0(-\zeta_g, -\zeta_h) = I_0(\zeta_g, \zeta_h). \quad (3.21c)$$

Conversely,

#### critterion (3.22)

at any thickness,

$$\text{if } I_g(-\zeta_g, -\zeta_h) = I_g(\zeta_g, \zeta_h),$$

$$\text{then} \quad |V_{h-g}|\cos\phi = 0. \quad (3.22)$$

Therefore, the presence of the centre of inversion at the exact three-beam condition is attributed to  $\cos\phi = 0$  (as shown in Fig. 3.8) or  $|V_{h-g}| = 0$  (as shown in Fig. 3.9).

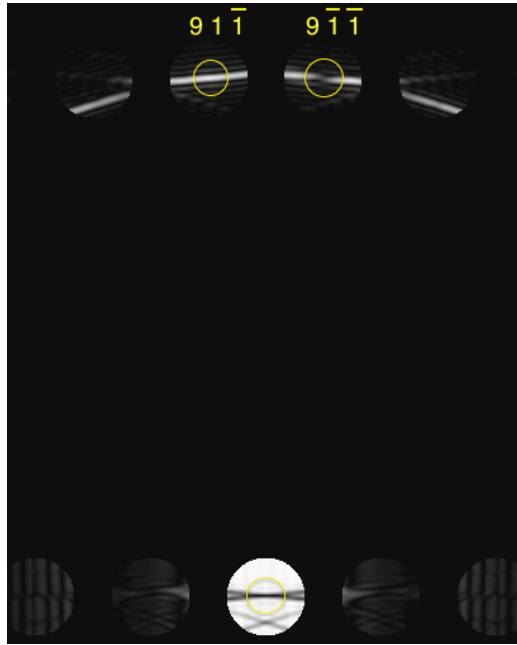


**Figure 3.8.** A simulated CBED pattern of GaAs [1 0 9]. Here,  $\phi = -92^\circ$ , i.e.  $\cos(\varphi_{9, 1, \bar{1}} - \varphi_{9, \bar{1}, \bar{1}} + \varphi_{0, 2, 0}) \approx 0$ . A centre of inversion is present at the exact three-beam condition in each reflection, which is located at the centre of each yellow circle. The simulation was carried out by using JEMS [58].

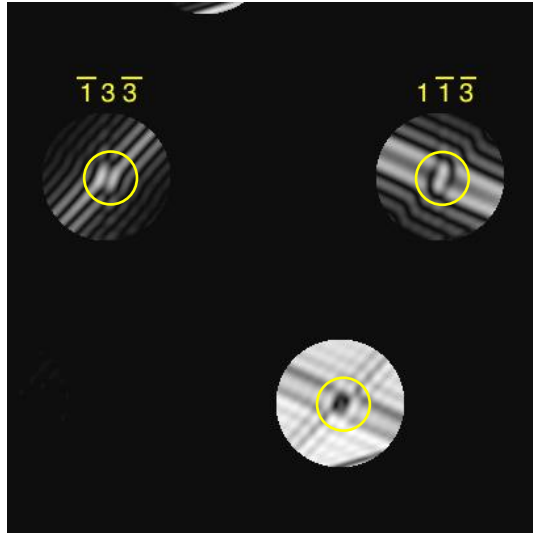


**Figure 3.9.** A simulated CBED pattern of Si [6 3 1]. Here,  $|V_{\bar{2}, 4, 0}| = 0$ , and thus a centre of inversion is present at the exact three-beam condition in each reflection, which is at the centre of each yellow circle. The simulation was carried out by using JEMS [58].

### 3.4 Approach to determine the sign of $\cos\phi$

We have shown that when  $|V_{h-g}|\cos\phi$  is zero, a centre of inversion will be present at the exact three-beam condition in CBED discs. Here, we will show that the sign of  $\cos\phi$  (when  $|V_{h-g}| > 0$ ) is directly related to the intensity asymmetry about the exact three-beam condition. The relationship between the intensity asymmetry and the sign of  $\cos\phi$  has been described by the perturbation theories of two-beam dynamic diffraction (discussed in Section 2.4.4), the formulation of which includes only two effective eigenvalues. This section will derive a new formulation from the exact three-beam solutions given by equations (3.9) and (3.10), which includes all of the three eigenvalues.

#### 3.4.1. The use of interactive plots for deriving empirical rules

Mathematica 10 [93] has been used to generate interactive plots of the analytical functions of eigenvalues, intensities, some polynomials and so on, which allows for visualisation of these functions for all possible values of the input parameters. There are five parameters in the input to these functions:  $|V_g|$ ,  $|V_h|$ ,  $|V_{h-g}|$ ,  $\phi$  and  $z$ . A wide range of possible values has been set for each parameter:  $|V_g|$ ,  $|V_h|$ ,  $|V_{h-g}| \in [0, 7]$  (in  $V$ ),  $\phi \in [-\pi, \pi]$ , and  $z \in [0, 2000]$  (in  $\text{\AA}$ ).

In some situations, it is difficult, if not impossible, to derive a mathematical relation, especially an approximate equality by using pure mathematics alone. In the current practical problem in which finding the features that relate to the sign of cosine three-phase invariants is the main concern, we allow the use of some empirical rules such as approximate equalities that are concluded from observations of the interactive plots: if an approximate equality is always found in the interactive plots where the five parameters have been finely tuned to give almost all the possible combinations of their values within their ranges, then it can be accepted as an empirical rule that such an approximate equality is held for three-beam dynamic diffraction in all cases (not limited to Bethe's [15, 22] or Kambe's approximations [6, 15]). For the purpose of deriving empirical rules, the interactive plots will be used in the current and next sections.

### 3.4.2. Derivation of the criteria for determining the sign of $\cos\phi$

In equation (3.9a) or (3.10), either  $I_g$  or  $I_0$  is a summation of three polynomials. An interactive plot is generated for the three polynomials in equation (3.9a) along the Bragg line of reflection  $g$  (an example is shown in Fig. 3.10). The interactive plots show that a certain distance<sup>7</sup>,  $|\Delta\zeta_h|^c$ , away from the exact three-beam condition,  $\zeta_h = 0$ , the intensity is mostly contributed by only one of the three polynomials. The distinct contributions of the polynomials can be explained by the terms  $1/(\mu_1\mu_2\mu_3\mu_i)$  in their expressions, which include the dispersion surface gaps  $\mu_i$  in the denominator: when  $\zeta_h < -|\Delta\zeta_h|^c$ ,  $|\mu_3| \ll |\mu_1| < |\mu_2|$ ; when  $\zeta_h > |\Delta\zeta_h|^c$ ,  $|\mu_1| \ll |\mu_3| < |\mu_2|$  (which can be seen from Fig. 3.11). Therefore, we can approximate the exact solution, which is a summation of three polynomials, by only one of the polynomials for the regions where  $|\zeta_h| > |\Delta\zeta_h|^c$ . By factorisation of the first and the third polynomial ( $i=1$  and 3), we can derive a piecewise function that is asymptotic to the exact solutions given by equations (3.9a) and (3.10) on both sides of the three-beam condition:

$$I_g \approx \begin{cases} (\cos\mu_3 z - 1) T_3, & \text{for } \zeta_h < -|\Delta\zeta_h|^c \\ (\cos\mu_1 z - 1) T_1, & \text{for } \zeta_h > |\Delta\zeta_h|^c \end{cases} \quad (3.23a)$$

$$\text{and} \quad I_0 \approx \begin{cases} 1 + 2C_1C_2(\cos\mu_3 z - 1), & \text{for } \zeta_h < -|\Delta\zeta_h|^c \\ 1 + 2C_3C_2(\cos\mu_1 z - 1), & \text{for } \zeta_h > |\Delta\zeta_h|^c \end{cases}, \quad (3.23b)$$

where the terms<sup>8</sup>,  $T_1$  and  $T_3$ , are independent of the thickness,  $z$ , and

$$T_3 = \frac{2 U_1^2}{\mu_1\mu_2\mu_3^2} \{G_0^2 - G_0(\lambda_1 + \lambda_2 + 2\lambda_3)\cos\phi + (\lambda_1 + \lambda_3)(\lambda_2 + \lambda_3)\} \quad (3.24a)$$

$$\text{and} \quad T_1 = \frac{2 U_1^2}{\mu_1^2\mu_2\mu_3} \{G_0^2 - G_0(\lambda_2 + \lambda_3 + 2\lambda_1)\cos\phi + (\lambda_2 + \lambda_1)(\lambda_1 + \lambda_3)\}. \quad (3.24b)$$

The interactive plots of  $T_1(\zeta_h)$ ,  $T_3(\zeta_h)$ ,  $C_1(\zeta_h)C_2(\zeta_h)$  and  $C_2(\zeta_h)C_3(\zeta_h)$  show that

$$T_3(-|\zeta_h|) \approx T_1(|\zeta_h|), \quad \text{for } |\zeta_h| > |\Delta\zeta_h|^c; \quad (3.25a)$$

$$\text{and} \quad C_1(-|\zeta_h|)C_2(-|\zeta_h|) \approx C_2(|\zeta_h|)C_3(|\zeta_h|), \quad \text{for } |\zeta_h| > |\Delta\zeta_h|^c. \quad (3.25b)$$

<sup>7</sup> The value of  $|\Delta\zeta_h|^c$  is very small for reflections having small structure factor magnitudes but increases with increasing structure factor magnitudes.

<sup>8</sup> A term involving  $\sin\phi$  has been ignored because its contribution in the region  $|\zeta_h| > |\Delta\zeta_h|^c$  is very small.

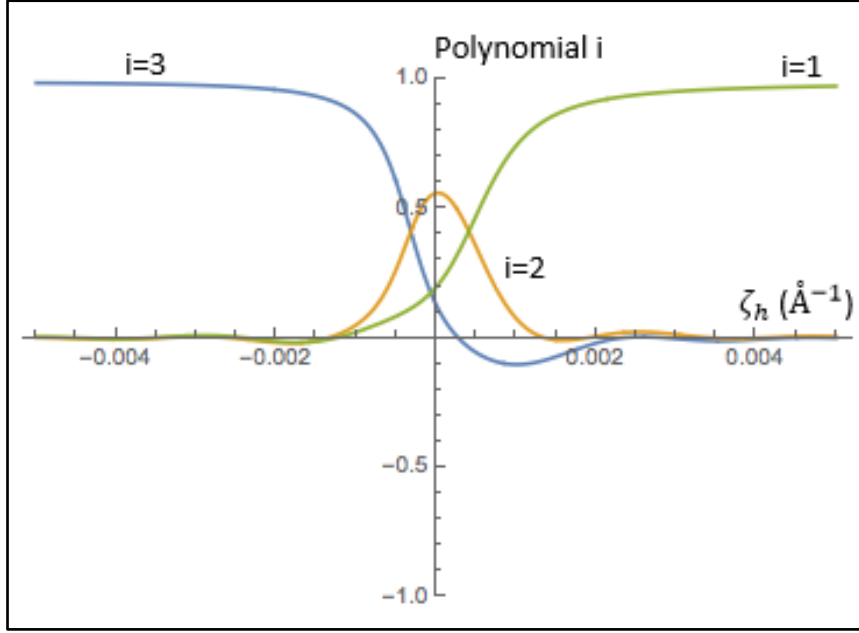


**Figure 3.10.** Plots of the three polynomials in equations (3.5a-c) along the Bragg line of reflection **g**. The summation of the three gives the intensity profile of  $I_g$  along its Bragg line. On the left hand side (say  $\zeta_h < -0.002 \text{ \AA}^{-1}$ ), the summation of the three polynomials is governed by the polynomial where  $i=3$  while on the right hand side (say  $\zeta_h > 0.002 \text{ \AA}^{-1}$ ), the summation of the three polynomials is governed by the polynomial where  $i=1$ . Wolfram Mathematica 10 [93] was used for this plot.

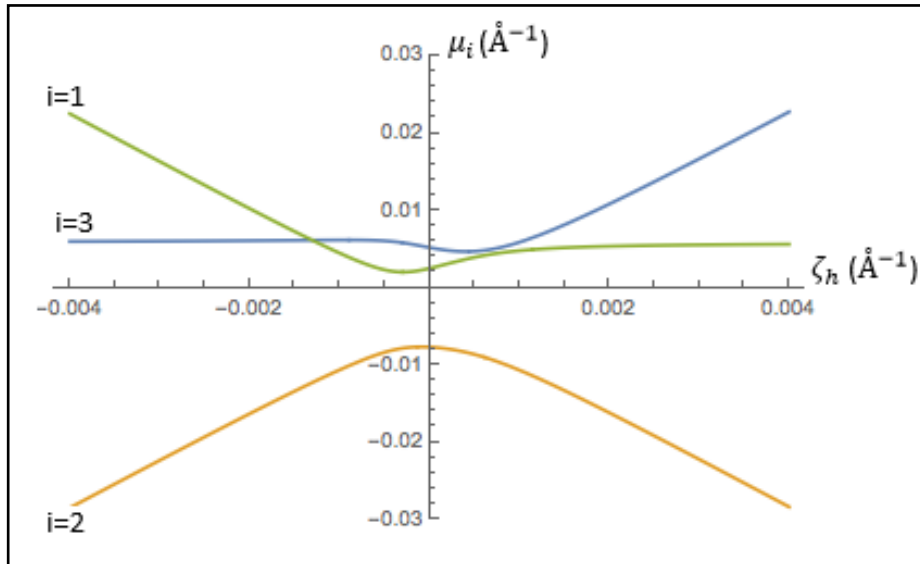


**Figure 3.11.** The gaps of the three dispersion surfaces,  $\mu_i$ , along the Bragg line of **g**. On the left hand side (say  $\zeta_h < -0.002 \text{ \AA}^{-1}$ ),  $|\mu_3| \ll |\mu_1| < |\mu_2|$ ; while on the right hand side (say  $\zeta_h > 0.002 \text{ \AA}^{-1}$ ),  $|\mu_1| \ll |\mu_3| < |\mu_2|$ . Wolfram Mathematica 10 [93] was used for this plot.



Combining equations (3.23 a) and (3.25 a), we have

$$\frac{I_g(-|\zeta_h|)}{I_g(|\zeta_h|)} \approx \frac{\sin^2(\mu_3 z/2)}{\sin^2(\mu_1 z/2)}, \quad \text{for } |\zeta_h| > |\Delta\zeta_h|^c \left( \text{except for } z \approx \frac{2\pi}{\mu_1} \right). \quad (3.26)$$

In other words, the asymmetry between  $I_g(-|\zeta_h|)$  and  $I_g(|\zeta_h|)$  as well as between  $I_0(-|\zeta_h|)$  and  $I_0(|\zeta_h|)$  is dominated by the difference between the thickness-dependent factors  $\sin^2(\mu_3 z/2)$  and  $\sin^2(\mu_1 z/2)$ .

From equations (3.5a-f), it can be proven analytically that

$$\cos\phi > 0 \Leftrightarrow \mu_3(-|\zeta_h|) > \mu_1(|\zeta_h|) \quad (3.27a)$$

$$\text{and} \quad \cos\phi < 0 \Leftrightarrow \mu_3(-|\zeta_h|) < \mu_1(|\zeta_h|). \quad (3.27b)$$

### The criterion for thin specimens

Therefore, when the specimen is not thick, such that  $z \leq \min\{\pi/\mu_3, \pi/\mu_1\}$ , the asymmetry between  $I_g(-|\zeta_h|)$  and  $I_g(|\zeta_h|)$  can reveal the sign of  $\cos\phi$  (Fig. 3.13a, b):

**criterion (3.28)**

$$I_g(-|\zeta_h|) > I_g(|\zeta_h|) \text{ or } I_0(-|\zeta_h|) < I_0(|\zeta_h|) \Rightarrow \cos\phi > 0, \quad (3.28a)$$

$$I_g(-|\zeta_h|) < I_g(|\zeta_h|) \text{ or } I_0(-|\zeta_h|) > I_0(|\zeta_h|) \Rightarrow \cos\phi < 0. \quad (3.28b)$$

### Comparison with Bethe's approximation [15, 22]

It can be noticed that the current and Bethe's approximation [15, 22] have something in common:

1) Both the current approximation given by equations (3.23a, b) and Bethe's approximation [15, 22] given by equation (2.57) are asymptotic to the exact three-beam solution given by equation (3.9a) for the regions that are away from the exact three-beam condition. Such a comparison is shown in Fig. 3.12. In other words, they have similar regions of validity.

2) In terms of the determination of the sign of  $\cos\phi$  for thin specimens, criterion (3.28) is equivalent to those derived from Bethe's approximation [15, 22] which have been discussed in Section 2.4.4.

3) In terms of mathematical structure, both are in factorised forms and have a factor like

$$\frac{\sin^2 \frac{\mu_i}{2} z}{\mu_i^2} \text{ or } \frac{\sin^2(\pi z \Delta\gamma^{\text{eff}})}{(\Delta\gamma^{\text{eff}})^2},$$

which is the characteristic of two-beam dynamic diffraction (c.f. equation (2.43a)). Therefore, in the valid regions of these approximations, the intensity distributions in both the central beam and the diffracted beams will show bright and dark fringes that run parallel to the Bragg lines, which is similar to two-beam CBED patterns. These fringes, the so called “thickness fringes”, can be seen in the regions of validity labelled by rectangles in Figs. 3.13c, d.

The differences between the current and Bethe’s approximations [15, 22] are:

- 1) The current formulation is based on the three eigenvalues of the  $3 \times 3$  scattering matrix while Bethe’s formulation [15, 22] is based on two effective eigenvalues.
- 2) The current approximation has better convergence to the exact three-beam solution than Bethe’s [15, 22] approximation, which can be seen from Fig. 3.12 (and this is true for all combinations of the five input parameters).

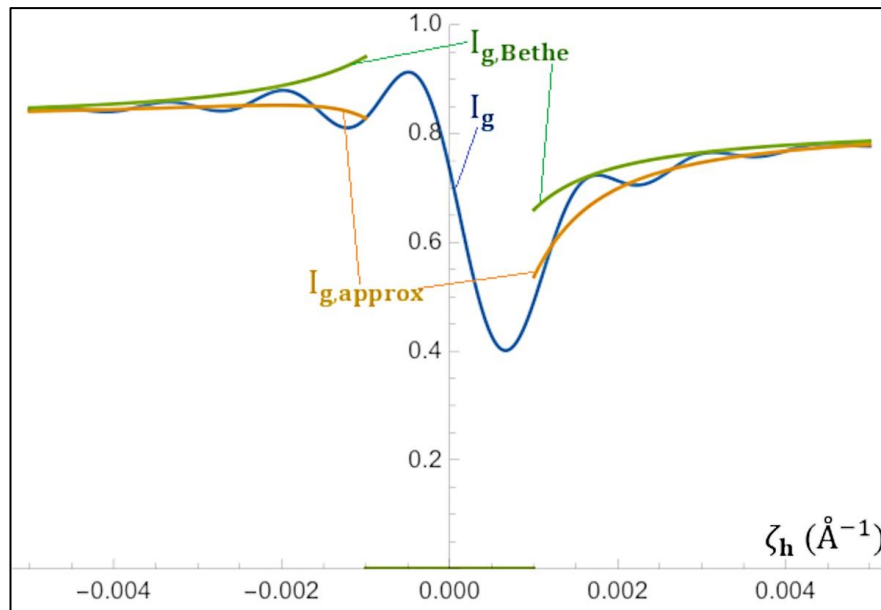


**Fig 3.12. A plot comparing different approximations in three-beam electron diffraction:** the current approximation which is given by equation (3.23a) is plotted as the orange curve, Bethe’s approximation [15, 22] which is given by equation (2.47) is plotted as the green curve, and the exact solution which is given by equation (3.9a) is plotted as the blue curve. The calculations are based on the following inputs:  $|V_g| = 2.05$  V,  $|V_h| = 1.65$  V,  $|V_{h-g}| = 2.65$  V,  $z = 756$  Å,  $\phi = 45^\circ$ . Wolfram Mathematica 10 [93] was used for this plot.

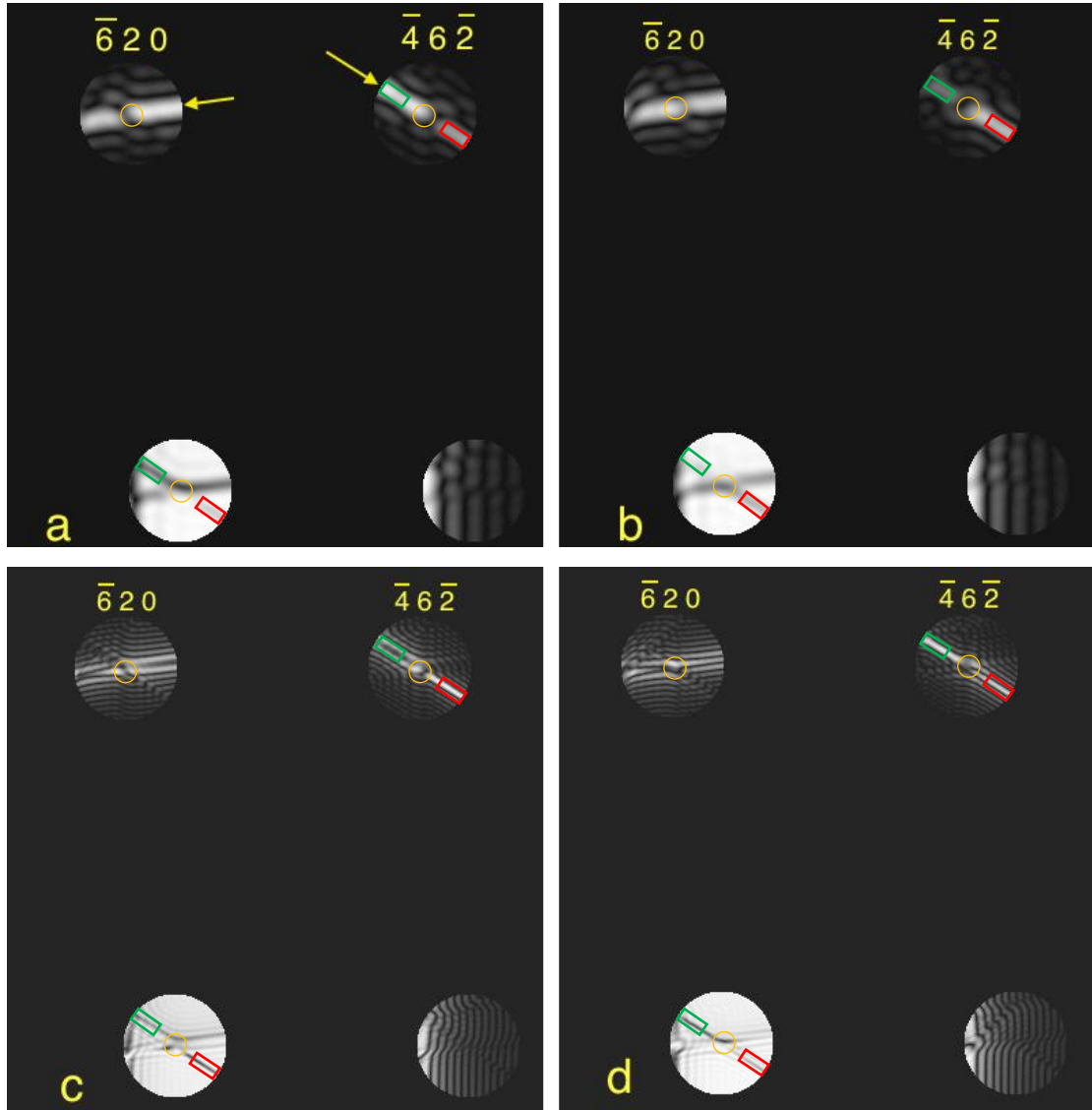


**Figure 3.13. Simulated CBED patterns of ZnS [1 3 7] near a three-beam condition which is located in the centre of each disc.** In the simulations, the three-phase invariant and the thickness are adjusted to different values: (a)  $\phi = 2.5^\circ$ ,  $z=700 \text{ \AA}$ ; (b)  $\phi = -140^\circ$ ,  $z=700 \text{ \AA}$ ; (c)  $\phi = 2.5^\circ$ ,  $z=2000$ ; (d)  $\phi = -140^\circ$ ,  $z=2000 \text{ \AA}$ . The exact positions of the three-beam condition are not required for the sign determination of  $\cos\phi$  and the orange circles roughly indicate these positions. The valid ranges of the current approximation (the pseudo-two-beam regions), equations (3.23a, b) are labelled by green rectangles for the negative side,  $\zeta_h < -|\Delta\zeta_h|^c$ , and red rectangles for the positive side,  $\zeta_h > |\Delta\zeta_h|^c$ . The arrows in (a) show the directions of increasing excitation errors, from negative to positive, for the other diffracted beam involved in the three-beam case. A Bloch wave simulation for many-beam diffraction was carried out by using JEMS [58].

### The criterion for thick specimens

When the specimen is thick, it is still possible to determine the sign of  $\cos\phi$ . However, as far as the author of this thesis is aware, this has never been discussed in the existing literatures [6, 15, 22].

As mentioned earlier, in the valid regions of the current approximation, there are bright and dark fringes that run parallel to the Bragg lines, which is similar to two-beam CBED patterns. For this reason, this valid regions are also called “pseudo-two-beam regions”. In two-beam CBED patterns, the fringe spacing, which is the distance between any two consecutive bright fringes or two consecutive dark fringes, depends on the thickness and the extinction distance  $\xi (= 1/\Delta\gamma)$ . For two-beam CBED, the extinction distance is a constant along the Bragg line. As the thickness increases from close to zero to the extinction distance,  $\xi$ , the spacing between the two dark fringes that are next to the Bragg line (or the width of the central bright fringe) will decrease to zero. The same trend applies to the “pseudo-two-beam regions” in a three-beam CBED pattern. However, in a three-beam CBED pattern, the extinction distance for the “pseudo-two-beam regions”,  $\xi_{\text{pseudo-2beam}} (= 2\pi/\mu_i)$ , is different for different sides of the three-beam condition:

$$\text{for } \zeta_h < -|\Delta\zeta_h|^c, \quad \xi_{\text{pseudo-2beam}}(-|\zeta_h|) = 2\pi/\mu_3(-|\zeta_h|); \quad (3.29a)$$

$$\text{for } \zeta_h > |\Delta\zeta_h|^c, \quad \xi_{\text{pseudo-2beam}}(|\zeta_h|) = 2\pi/\mu_1(|\zeta_h|). \quad (3.29b)$$

According to equations (3.27a, b), we have

$$\cos\phi > 0 \Leftrightarrow \xi_{\text{pseudo-2beam}}(-|\zeta_h|) < \xi_{\text{pseudo-2beam}}(|\zeta_h|), \quad (3.30a)$$

$$\cos\phi < 0 \Leftrightarrow \xi_{\text{pseudo-2beam}}(-|\zeta_h|) > \xi_{\text{pseudo-2beam}}(|\zeta_h|). \quad (3.30b)$$

In a reflection  $g$ , the fringe spacing in the region for  $\zeta_h < -|\Delta\zeta_h|^c$  and the region for  $\zeta_h > |\Delta\zeta_h|^c$  are different, and such a difference is attributed to the difference between  $\xi_{\text{pseudo-2beam}}(-|\zeta_h|)$  and  $\xi_{\text{pseudo-2beam}}(|\zeta_h|)$  which is caused by the sign of  $\cos\phi$ . Therefore, the difference in the fringe spacing can be used for determining the sign of  $\cos\phi$ .

### critterion (3.31)

Near the Bragg lines of reflection  $g$ , (which can be seen from both the central disc and the disc  $g$ ), fringes that are parallel to each other are used for inspection:

if the fringe spacing on the negative side,  $\zeta_h < -|\Delta\zeta_h|^c$ , is shorter than that on the positive side,  $\zeta_h > |\Delta\zeta_h|^c$ ,

$$\text{then, } \mu_3(-|\zeta_h|) > \mu_1(|\zeta_h|) \Rightarrow \cos\phi > 0 ; \quad (3.31a)$$

$$\text{otherwise, } \mu_3(-|\zeta_h|) < \mu_1(|\zeta_h|) \Rightarrow \cos\phi < 0 . \quad (3.31b)$$

The criterion above is held for thick specimens, where  $\min\{\pi/\mu_3, \pi/\mu_1\} < z \leq \min\{2\pi/\mu_3, 2\pi/\mu_1\}$ . The upper limit is usually larger than a specimen thickness (which is typically less than 2000 Å). Examples of criterion (3.31) are illustrated in Figs. 3.13c, d, respectively.

In summary, the sign of  $\cos\phi$  can be determined from the intensity asymmetry between the two opposite sides of three-beam condition in the CBED discs. Unlike the determination of the sign of  $\sin\phi$ , this is not restricted by the specimen thickness.

## 3.5 Valid range of thickness for direct observation of the sign of $\sin\phi$

To decide whether the thickness is smaller than the “three-beam extinction distance”,  $\xi_{3\text{-beam}}$ , inspection of the Bragg lines is needed. Two criteria have been described in Section 3.2 without explanations. The explanations will be given in this section. **Note:** the current section is on a very specific and technical topic, readers who are interested in more practical aspects can skip this section.

The intensity difference between a Friedel or Bijvoet pair is small when the thickness gets close to the three-beam extinction distance,  $\xi_{3\text{-beam}}$ . To have a contrast that is observable even by eye, the thickness has to be far from the three-beam extinction distance.

As an empirical rule, when  $z < 0.85 \xi_{3\text{-beam}}$  or  $z > 1.15 \xi_{3\text{-beam}}$  (excluding very thick specimens, which are obvious from observing the corresponding CBED patterns), then

$I_g(\zeta_g = 0, \zeta_h = 0, z) - I_{\bar{g}}(\zeta_{\bar{g}} = 0, \zeta_{\bar{h}} = 0, z) \gtrless 0.2$  of the incident beam intensity. Therefore, as long as one can distinguish the Bragg lines for  $z < 0.85 \xi_{3\text{-beam}}$  from those for  $z > 1.15 \xi_{3\text{-beam}}$ , one will be able to decide whether the thickness is smaller than the extinction

distance,  $\xi_{3\text{-beam}}$ . Here, we are able to find two criteria, I and II. The satisfaction of both criteria I and II is sufficient but not necessary for having  $z < \xi_{3\text{-beam}}$ . The two criteria are derived from two opposite situations as will be discussed below.

### 3.5.1 When $\max\{|V_g|, |V_h|\} \gtrsim |V_{h-g}|$

The curves,  $\mu_1(\zeta_h)$ ,  $\mu_3(\zeta_h)$  along the Bragg line of g (e.g. in Fig. 3.11) always have local minima near the exact three-beam conditions,  $\zeta_h = 0$ . Thus, we have

$$|\mu_1(\zeta_h = 0)| < \mu_1(\zeta_h > |\Delta\zeta_h|^c), \quad (3.32a)$$

$$|\mu_3(\zeta_h = 0)| < \mu_3(\zeta_h < -|\Delta\zeta_h|^c) \quad (3.32b)$$

$$\text{and} \quad |\mu_2(\zeta_h = 0)| < \mu_3(\zeta_h < -|\Delta\zeta_h|^c) + \mu_1(\zeta_h > |\Delta\zeta_h|^c) \quad (3.32c)$$

Without losing generality, we consider the case for  $\max\{|V_g|, |V_h|\} = |V_g|$ :

$$\begin{aligned} \text{for } \cos\phi > 0, \quad \xi_{3\text{-beam}} &= \frac{2\pi}{|\mu_2(\zeta_h = 0)|} \gtrsim \frac{1}{2} \frac{2\pi}{|\mu_3(\zeta_h < -|\Delta\zeta_h|^c)|}, \\ &\Rightarrow \xi_{3\text{-beam}} \gtrsim \frac{1}{2} \xi_{\text{pseudo-2beam}}(\zeta_h < -|\Delta\zeta_h|^c); \end{aligned} \quad (3.33a)$$

$$\begin{aligned} \text{for } \cos\phi < 0, \quad \xi_{3\text{-beam}} &= \frac{2\pi}{|\mu_2(\zeta_h = 0)|} \gtrsim \frac{1}{2} \frac{2\pi}{|\mu_1(\zeta_h > |\Delta\zeta_h|^c)|}, \\ &\Rightarrow \xi_{3\text{-beam}} \gtrsim \frac{1}{2} \xi_{\text{pseudo-2beam}}(\zeta_h > |\Delta\zeta_h|^c). \end{aligned} \quad (3.33b)$$

Here, a shorthand notation is introduced:

$$\xi_{\text{pseudo-2beam}} = \min\{\xi_{\text{pseudo-2beam}}(\zeta_h < -|\Delta\zeta_h|^c), \xi_{\text{pseudo-2beam}}(\zeta_h > |\Delta\zeta_h|^c)\}.$$

Then equations (3.33a, b) can be re-written as:

$$\xi_{3\text{-beam}} \gtrsim \frac{1}{2} \xi_{\text{pseudo-2beam}}. \quad (3.33c)$$

According to two-beam diffraction equations (2.43a, b), when  $z = \frac{1}{2} \xi$ , the central bright peak is 1.618 times as broad as the neighbouring bright peak. Therefore, when  $\max\{|V_g|, |V_h|\} \gtrsim |V_{h-g}|$ ,  $z < \frac{1}{2} \xi_{\text{pseudo-2beam}}$  is a sufficient condition for  $z \lesssim \xi_{3\text{-beam}}$  and criterion I can be stated as:

The excess Bragg line in the “pseudo two-beam region” of the stronger reflection has a central bright fringe that is at least 1.6 times wider than the second bright fringe.

Next, we consider the opposite situation.

### 3.5.2 When $\max\{|V_g|, |V_h|\} \ll |V_{h-g}|$ (where Kambe's approximation [6] applies)

The interactive plots of  $\mu_i(\zeta_h)$  along the Bragg line of reflection g,  $\zeta_g = 0$ , show that

$$|\mu_2(\zeta_h = 0)| > \mu_3(\zeta_h < -|\Delta\zeta_h|^c) + \mu_1(\zeta_h > |\Delta\zeta_h|^c). \quad (3.34)$$

In this situation, criterion I is no longer a sufficient condition for  $z < \xi_{3\text{-beam}}$ , so we need to derive a different criterion.

Fig. 3.14a shows the plot of  $C_{i\oplus 1}C_{i\oplus 2}$ , the terms in equation (3.10), along the locus  $\zeta_g = \zeta_h$ , where  $C_1C_3 \approx 0$  (an empirical rule),  $C_2C_3$  and  $C_1C_2$  show two peaks at the turning points of  $\mu_3$  and  $\mu_1$  on each side of  $\zeta_h = 0$ . These turning points are close to the exact three-beam condition,  $\zeta_h = 0$  (shown in Fig. 3.14b).

We first consider a case when  $|\phi| = \frac{\pi}{2}$ . Since  $C_1C_3 \approx 0$ , equation (3.10) becomes:

$$I_0 = 1 + 2C_2C_3(\cos\mu_1z - 1) + 2C_1C_2(\cos\mu_3z - 1). \quad (3.35)$$

Here we consider any point on the locus,  $\zeta_g = \zeta_h$ , that is close to the three-beam condition,  $\zeta_h = 0$ , from the negative side (shown by the dashed line in Figs. 3.14 & 3.15). All the arguments or functions below refer to the same point, and the coordinate,  $(\zeta_h)$ , will be omitted for short-hand notations. The derivative of  $I_0$  with respect to  $\zeta_h$  is:

$$\begin{aligned} \frac{dI_0}{d\zeta_h} = & 2 \frac{dC_2C_3}{d\zeta_h}(\cos\mu_1z - 1) + 2 \frac{dC_1C_2}{d\zeta_h}(\cos\mu_3z - 1) \\ & - 2C_2C_3\sin\mu_1z \frac{d\mu_1z}{d\zeta_h} - 2C_1C_2\sin\mu_3z \frac{d\mu_3z}{d\zeta_h}. \end{aligned} \quad (3.36a)$$

Since  $\left| \frac{dC_2C_3}{d\zeta_h} \right| \gg \left| C_2C_3 \frac{d\mu_1}{d\zeta_h} \right|,$

We have  $\frac{dI_0}{d\zeta_h} \approx 2 \frac{dC_2C_3}{d\zeta_h}(\cos\mu_1z - 1) + 2 \frac{dC_1C_2}{d\zeta_h}(\cos\mu_3z - 1).$  (3.36b)

For any thickness, we have:

$$2 \frac{dC_2C_3}{d\zeta_h}(\cos\mu_1z - 1) > 0, \quad (3.37a)$$

$$2 \frac{dC_1C_2}{d\zeta_h}(\cos\mu_3z - 1) < 0, \quad (3.37b)$$

$$\text{and } \left| \frac{dC_1C_2}{d\zeta_h} \right| < \left| \frac{dC_2C_3}{d\zeta_h} \right|. \quad (3.38)$$

For very thin specimens, where the perturbation theory of kinematic diffraction can be applied, we have

$$\frac{dI_0}{d\zeta_h} < 0, \quad (3.39a)$$

which is equivalent to

$$\frac{\left| \frac{dC_1 C_2}{d\zeta_h} \right| \left| \sin^2 \left( \frac{\mu_3 z}{2} \right) \right|}{\left| \frac{dC_2 C_3}{d\zeta_h} \right| \left| \sin^2 \left( \frac{\mu_1 z}{2} \right) \right|} > 1 \quad (3.39b)$$

In other words,  $\frac{\left| \sin^2 \left( \frac{\mu_3 z}{2} \right) \right|}{\left| \sin^2 \left( \frac{\mu_1 z}{2} \right) \right|} (>1)$  beats the multiplier  $\frac{\left| \frac{dC_1 C_2}{d\zeta_h} \right|}{\left| \frac{dC_2 C_3}{d\zeta_h} \right|} (<1)$  and results in a product of

larger than 1 for very thin specimens. When the thickness increases,  $\frac{\left| \frac{dC_1 C_2}{d\zeta_h} \right|}{\left| \frac{dC_2 C_3}{d\zeta_h} \right|}$  is constant while

$\frac{\left| \sin^2 \left( \frac{\mu_3 z}{2} \right) \right|}{\left| \sin^2 \left( \frac{\mu_1 z}{2} \right) \right|}$  will decrease from a value of larger than 1 to a value of less than 1 and the product,

and thus  $\frac{\left| \frac{dC_1 C_2}{d\zeta_h} \right| \left| \sin^2 \left( \frac{\mu_3 z}{2} \right) \right|}{\left| \frac{dC_2 C_3}{d\zeta_h} \right| \left| \sin^2 \left( \frac{\mu_1 z}{2} \right) \right|}$ , will become less than 1 and  $\frac{dI_0}{d\zeta_h}$  will become positive at a

certain stage. The sign of  $\frac{dI_0}{d\zeta_h}$  will be flipped when the thickness increases to about:

$$\frac{\mu_1 z}{2} = \frac{\pi}{2}. \quad (3.40)$$

From the interactive plots (an example of the plots is given in Fig. 3.14b), we have

$$\mu_1 \approx \frac{\mu_2(\zeta_h = 0)}{2}. \quad (3.41)$$

Therefore,

$$\begin{aligned} z \geq \xi_{3\text{-beam}} &\equiv \frac{2\pi}{\mu_2(\zeta_h = 0)} \approx \frac{\pi}{\mu_1} \\ &\Rightarrow \frac{dI_0}{d\zeta_h} > 0. \end{aligned} \quad (3.42a)$$

The converse-negative proposition is also true:

$$\frac{dI_0}{d\zeta_h} \leq 0 \Rightarrow z < \xi_{3\text{-beam}}. \quad (3.42b)$$

Now, we consider any point on the locus,  $\zeta_g = \zeta_h$ , that is close to the three-beam condition,  $\zeta_h = 0$ , from the positive side. Similarly, we have:



$$\frac{dI_0}{d\zeta_h} \geq 0 \Rightarrow z < \xi_{3\text{-beam}} . \quad (3.42c)$$

In summary, for any point that is along the locus  $\zeta_g = \zeta_h$  and near the three-beam condition, we have:

$$\frac{d^2I_0}{d\zeta_h^2} \geq 0 \Rightarrow z < \xi_{3\text{-beam}} . \quad (3.42d)$$

Similar arguments can be repeated for  $|\phi| \neq \frac{\pi}{2}$ , where the sign of  $\frac{dI_0}{d\zeta_h}$  near the point that corresponds to the intersection of  $C_2 C_3$  and  $C_1 C_2$  (rather than  $\zeta_h = 0$ ) is considered.

Therefore, we can state criterion II:

Near the exact three-beam condition in the central beam, the intensity along the locus  $\zeta_g = \zeta_h$  has a local minimum, i.e.  $\frac{d^2I_0}{d\zeta_h^2} \geq 0$ , then  $z < \xi_{3\text{-beam}}$ .

When both criteria I and II are satisfied, it is sufficient to conclude that the thickness is smaller than the three-beam extinction distance or the maximum allowed thickness for direct observation of the sign. Then, the sign of the three-phase invariants can be determined by comparing the intensity difference directly without measuring the thickness. Otherwise, without the knowledge of the thickness and the structure factor magnitudes, the diffraction pattern should be rejected as unsuitable for the direct determination of the sign by inspection.

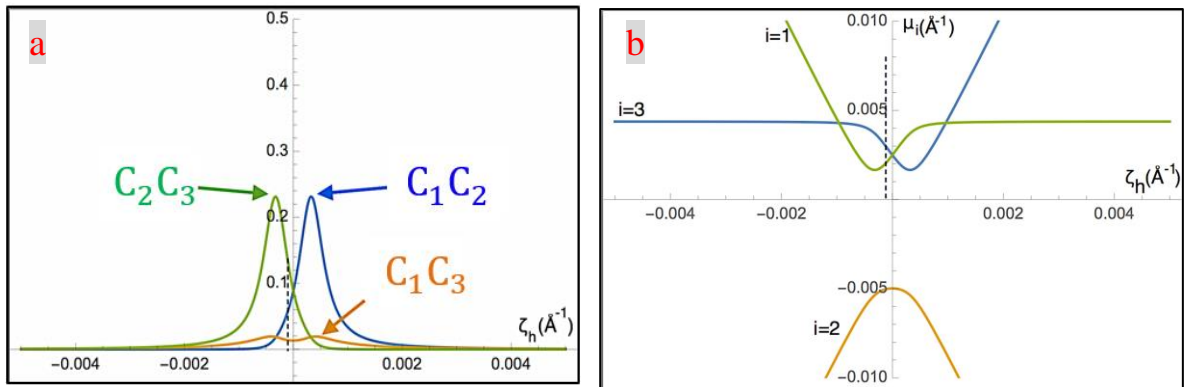


**Figure 3.14.** Plots of (a) the polynomials  $C_{i\oplus 1}C_{i\oplus 2}$  from equation (3.10) and (b) the gaps of the dispersion surfaces,  $\mu_i$ , versus the excitation error  $\zeta_h$  along the locus,  $\zeta_g = \zeta_h$  (the horizontal axis). The dashed line shows a point that can be anywhere close to the three-beam condition,  $\zeta_h = 0$ , from the positive side,  $\zeta_h < 0$ . Wolfram Mathematica 10 [93] was used for generating this plot.

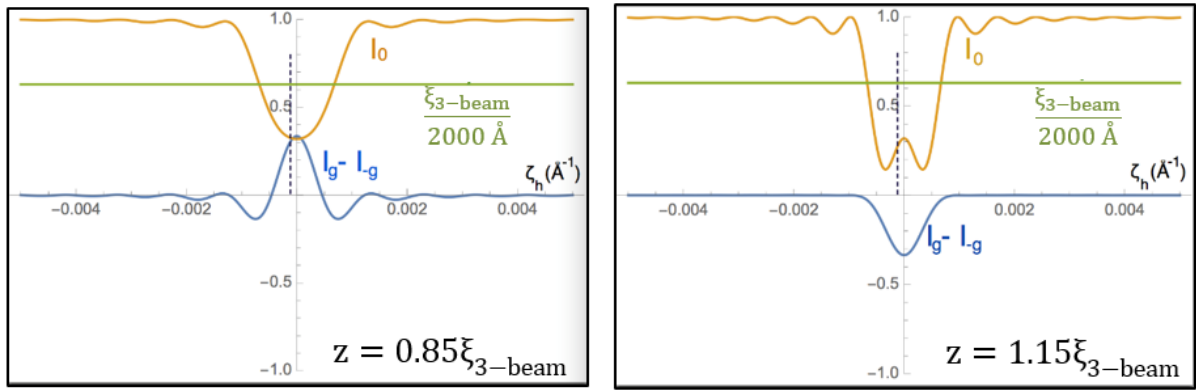


**Figure 3.15.** Plots of the intensity of the central beam (in orange) and the intensity difference between a Friedel pair,  $g$  and  $\bar{g}$ , (in blue) along the locus  $\zeta_g = \zeta_h$  (the horizontal axis). When the thickness increases from  $z < 0.85 \xi_{3\text{-beam}}$  to  $z > 1.15 \xi_{3\text{-beam}}$ , the sign of the intensity difference flips to the opposite direction and the convexity of intensity profile of the central beam,  $I_0$ , is also changed. The dashed line shows a point that can be anywhere close to the three-beam condition,  $\zeta_h = 0$ , from the positive side,  $\zeta_h < 0$ . Wolfram Mathematica 10 [93] was used for generating this plot.

Previous work by Marthinsen et al. [16] suggested it may not be possible to determine the sign by only direct observation of the intensities. It discussed a three-beam case in which  $|V_{h-g}|$  was artificially increased 10 times (to 12 V), while  $|V_h|$  and  $|V_g|$  were fixed. Ambiguity in the sign determination was claimed for simulated CBED patterns that have split Bragg lines in the central disc (like in Fig. 3.4b). The claim of ambiguity in the sign observation in their case, however, does not contradict our method for sign observation: criterion II is not satisfied in their case and the three-beam CBED pattern should be rejected as unsuitable for the direct sign observation since the thickness is too large. A calculation by the author of this thesis further shows that the thicknesses used in their simulations, 1100 Å and 2200 Å, are well above the three-beam extinction distance (or the maximum thickness for direct observation of the sign) in their case, which is 400 Å.

### 3.6 The three-beam theories in crystal structure determination

This section will first introduce the physical method for phase determination based on the criteria for determining the signs of  $\sin\phi$  and  $\cos\phi$ . Then, the application of the method for crystal structure determination will be discussed.

#### 3.6.1 A physical method for phase estimation

Several criteria for extracting the phase information from three-beam CBED patterns are derived from the exact analytical solution to three-beam dynamical diffraction of elastically scattered electrons, i.e. equations (3.9a, b) and (3.10). The criteria and the corresponding figures are summarised in Table 3.1.

**Table 3.1. Summary of the criteria for extracting the phase information**

| Numbers of the criteria | To determine whether                    | Examples in the figures |
|-------------------------|---|-------------------------|
| (3.12)                  | $ V_{h-g} \sin\phi = \text{or } \neq 0$ |                         |
| (3.14), (3.18)          | $\sin\phi > \text{or } < 0$             | Figs. 3.5 and 3.7       |
| (3.22)                  | $ V_{h-g} \cos\phi = \text{or } \neq 0$ | Figs. 3.8 and 3.9       |
| (3.28), (3.31)          | $\cos\phi > \text{or } < 0$             | Fig. 3.13               |

There are eight ways to combine “ $\sin\phi >, =, \text{ or } < 0$ ” with “ $\cos\phi >, =, \text{ or } < 0$ ”. We can divide the full range of the phase angles  $[-180^\circ, 180^\circ]$  into eight equal octants. By applying the criteria listed in Table 3.1, we can allocate the three-phase invariants into one of the octants and we can assign the middle value of that octant to the initial guessed value of  $\Phi$  according to Table 3.2.

**Table 3.2. Table for estimating the triplet phase**

| $\sin \Phi$ | $\cos \Phi$ | Initial guess of $\Phi$ |
|-------------|-------------|-------------------------|
| $\approx 0$ | $>0$        | $0^\circ$               |
| $>0$        | $>0$        | $45^\circ$              |
| $>0$        | $\approx 0$ | $90^\circ$              |
| $> 0$       | $< 0$       | $135^\circ$             |
| $\approx 0$ | $< 0$       | $180^\circ$             |
| $< 0$       | $< 0$       | $-135^\circ$            |
| $< 0$       | $\approx 0$ | $-90^\circ$             |
| $< 0$       | $> 0$       | $-45^\circ$             |

### Examples of estimating three-phase invariants by inspection

Two examples of the phase estimation are illustrated here.

**Example 1.** In Fig. 3.16a:

1.  $z < \xi_{3\text{-beam}}$  can be concluded from inspection of the Bragg lines according to the two criteria for the valid range of thickness.
2.  $I_{\bar{1}2\bar{3}}(\zeta_{\bar{1}2\bar{3}} = 0, \zeta_{\bar{1}3\bar{1}} = 0, z) < I_{1\bar{2}3}(\zeta_{\bar{1}2\bar{3}} = 0, \zeta_{\bar{1}3\bar{1}} = 0, z)$ . According to criterion (3.14)  $\sin \Phi < 0$ .
3. Within the disc of  $\bar{1}2\bar{3}$ ,  $I_{\bar{1}2\bar{3}}(-|\zeta_{\bar{1}3\bar{1}}|) > I_{\bar{1}2\bar{3}}(|\zeta_{\bar{1}3\bar{1}}|)$ . According to criterion (3.28 a),  $\cos \Phi > 0$ .
4. Following Table 3.2, an initial guess of  $\Phi = -45^\circ$  can be assigned. The actual value is  $-33^\circ$ , so the error is  $-12^\circ$ .

**Example 2.** In Fig. 3.16b:

1.  $z < \xi_{3\text{-beam}}$ .
2.  $I_{\bar{3}10}(\zeta_{\bar{2}\bar{1}1} = 0, \zeta_{\bar{3}10} = 0, z) \approx I_{3\bar{1}0}(\zeta_{\bar{2}\bar{1}1} = 0, \zeta_{\bar{3}10} = 0, z)$ . According to criterion (3.12),  $\sin \Phi \approx 0$ .
3. Within the disc of  $(\bar{2}\bar{1}1)$ ,  $I_{\bar{2}\bar{1}1}(-|\zeta_{\bar{3}10}|) > I_{\bar{2}\bar{1}1}(|\zeta_{\bar{3}10}|)$ . According to criterion (3.28 b),  $\cos \Phi < 0$ .

4. Following Table 3.2, an initial guess of  $\Phi = 180^\circ$  can be assigned. The actual value is  $161^\circ$ , so the error is  $+19^\circ$ .

One may argue that there is a subtle difference between  $I_{\bar{3}10}(\zeta_{\bar{2}\bar{1}1} = 0, \zeta_{\bar{3}10} = 0, z)$  and  $I_{\bar{3}\bar{1}0}(\zeta_{\bar{2}\bar{1}1} = 0, \zeta_{\bar{3}10} = 0, z)$ , and  $I_{\bar{3}10}(\zeta_{\bar{2}\bar{1}1} = 0, \zeta_{\bar{3}10} = 0, z) > I_{\bar{3}\bar{1}0}(\zeta_{\bar{2}\bar{1}1} = 0, \zeta_{\bar{3}10} = 0, z)$ . According to criterion (3.14a),  $\sin \Phi > 0$ . Since  $\cos \Phi < 0$  is unambiguous, another guess can be  $\Phi = 135^\circ$ . The error is  $-26^\circ$ .

As there are eight ways to combine “ $\sin \phi >, =, \text{ or } < 0$ ” with “ $\cos \phi >, =, \text{ or } < 0$ ”. The mean error of the three-phase invariants should be  $\pm 22.5^\circ$ .

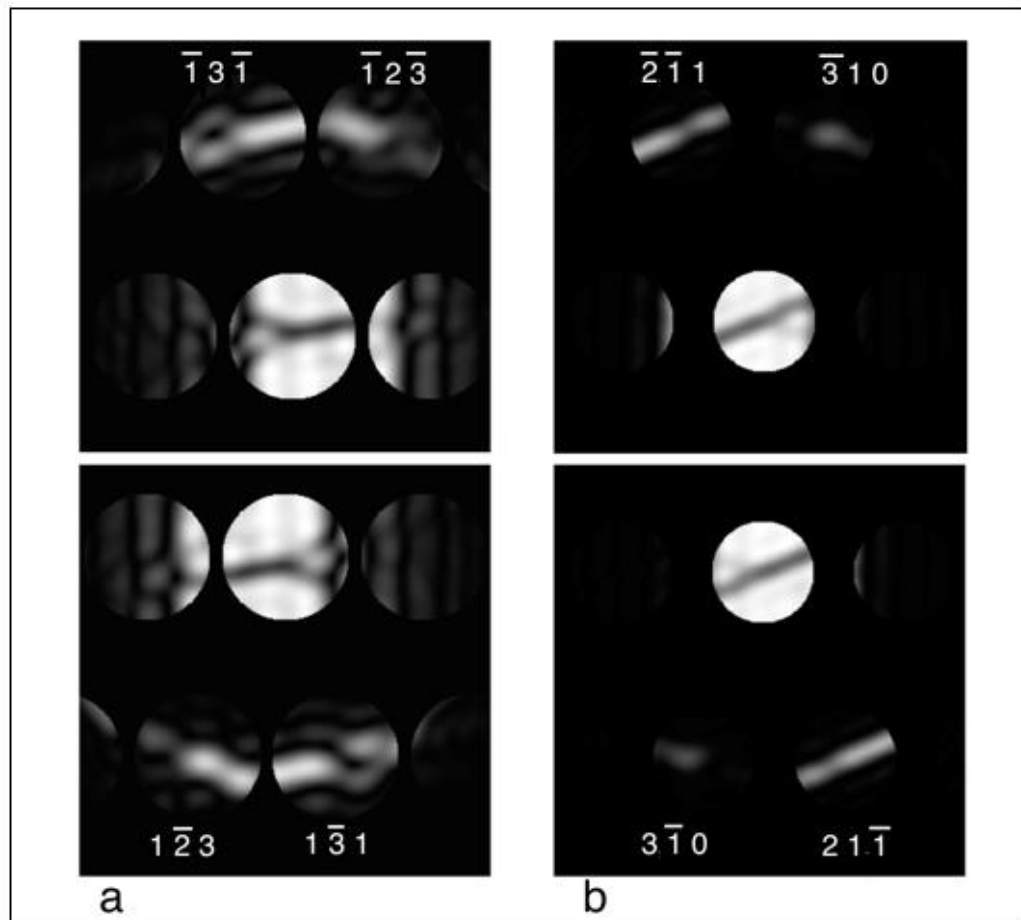


**Figure 3.16. Simulated CBED patterns of alpha-quartz (space group  $P3_121$ ) in zone axes  $[7\ 2\ \bar{1}]$  (in column a) and  $[1\ 3\ 5]$  (in column b) are used as two examples for demonstrating the phase determination.** Each column includes a pair of centrosymmetrically related three-beam conditions. The simulation has included more than 100 reflections and phenomenological absorptions to reflect the applicability of three-beam diffraction in the real experiments. The simulation was carried out using JEMS [58].

Without *a priori* knowledge of the structure or the specimen thickness, three-phase invariants can be determined to within a mean error of  $\pm 22.5^\circ$  from direct observation of three-beam CBED patterns. Therefore, the direct measurement of three-phase invariants can be in principle achieved from noncentrosymmetric crystals. This method of the phase measurement for noncentrosymmetric crystals should not be confused with those which also make use of three-beam or few-beam CBED but actually require *a priori* knowledge of the phases to start refinements [96, 97].

Without knowing the crystal structure, the procedure of finding the structure factor phases (or the phase invariants) is called phasing. Traditional phasing methods like direct methods deduce the phases from the kinematic diffraction intensities which are independent of the reflection phases. By contrast, three-beam dynamic diffraction (for both X-ray and electrons) allows for direct measurement of three-phase invariants from the intensities that are dependent on three-phase invariants. Therefore, such a method is known as the physical method of phase determination as opposed to non-physical or statistical methods like direct methods [98]. The advantage of this physical phasing method will be discussed in the next subsection.

### 3.6.2 The significance of the measured phases in *ab initio* structure determination

From the previous subsection, it has been shown that practical experimental conditions can be found for which the three-phase invariant can be determined to within an octant by inspection of three-beam CBED patterns. In this subsection, we will consider one question: how useful are the measured three-phase invariants (with an uncertainty of  $\pm 22.5^\circ$ ) in *ab initio* crystal structure determination?

The most commonly applied phasing methods are non-physical methods like direct methods. Whether direct methods can get a structure solution from the statistics of the kinematic diffraction intensities depends on the resolution<sup>9</sup> and kinematic quality of the diffraction data. If either the kinematic quality or the resolution of the diffraction data is low, direct methods may not acquire any structure solutions at all.

Coupling three-beam dynamic diffraction with direct methods can greatly improve the success rate of direct methods for obtaining a structure solution. In conjunction with direct

---

<sup>9</sup> In X-ray crystallography, resolution is the smallest distance between crystal lattice planes that is resolved in the diffraction pattern, which depends on the number of resolvable peaks of non-equivalent reflections in the diffraction pattern. Larger values of resolution (in unit of Å) mean poorer resolutions.

methods, the measured three-phase invariants have been shown to be useful for *ab initio* determination of crystal structure [3, 99]. In the work by Mo et al [3], kinematic diffraction data of a small protein, rubredoxin (the volume of its unit cell is  $19,303 \text{ \AA}^3$ ), at a resolution of  $1.5 \text{ \AA}$  was used in conjunction with the known three-phase invariants with random errors that were artificially set. With the kinematic diffraction data alone, no structure solution could be found. To get a structure solution from the phasing algorithms, a resolution of at least  $1.2 \text{ \AA}$  was required. However, the crystal structure was solved when extra information of three-phase invariants was added to the phasing algorithm. For such a small protein structure, only 45 three-phase invariants with a mean error of  $\pm 22.5^\circ$  were sufficient [3].

The study of [3] reveals that the combination of traditional phasing methods and direct measurement of three-phase invariants can greatly improve *ab initio* crystal structure determination especially when the diffraction data are incomplete. If a crystal structure of interest is less complicated than the protein structure in the example, it can be expected that even fewer three-phase invariants will be needed.

In addition, the measurement of three-phase invariants from three-beam electron diffraction patterns can be combined with the techniques based on quasi-kinematic electron diffraction (for example precession electron diffraction (PED) [100] and rotation electron diffraction (RED) [101]), where structure factor magnitudes cannot be measured as accurately as in X-ray diffraction, i.e., the kinematic quality of the diffraction data is lower than that of X-ray diffraction data. Importantly, such a combination may result in more complete and robust structure solutions for nano-sized and submicron-sized crystals which need to be studied in a TEM.

### 3.6.3 The three-beam approximation for large unit cells

So far, we have demonstrated the method of measuring three-phase invariants from three-beam CBED patterns and discussed its application to crystal structure determination with examples of simulated CBED patterns where many-beam diffraction effects have been included. The method is based on the three-beam approximation, which means that many-beam dynamic diffraction is approximated by interactions among only three reflections, 0,  $g$  and  $h$ . As mentioned in Section 2.4.1, the approximation can qualitatively describe dynamically diffracted intensities near three-beam conditions and works well for crystal structures with small unit cells. We have also mentioned in Section 2.4.1 that the three-beam approximation may be applicable to large unit cells. This subsection will discuss the applicability of three-beam electron diffraction in structures with large unit cells in more detail.

The three-beam approximation can be mathematically described as follows:

$$\begin{pmatrix} 0 & \sigma V_g^* & \sigma V_h^* & \sigma V_{g'}^* & \sigma V_{h'}^* & \cdots \\ \sigma V_g & 2\pi\zeta_g & \sigma V_{h-g}^* & \sigma V_{g'-g}^* & \sigma V_{h'-g}^* & \cdots \\ \sigma V_h & \sigma V_{h-g} & 2\pi\zeta_h & \sigma V_{g'-h}^* & \sigma V_{h'-h}^* & \cdots \\ \sigma V_{g'} & \sigma V_{g'-g} & \sigma V_{g'-h} & 2\pi\zeta_{g'} & \sigma V_{h'-g'}^* & \cdots \\ \sigma V_{h'} & \sigma V_{h'-g} & \sigma V_{h'-h} & \sigma V_{h'-g'} & 2\pi\zeta_{h'} & \cdots \\ \vdots & \vdots & \vdots & \vdots & \vdots & \ddots \end{pmatrix} \begin{pmatrix} C_0 \\ C_g \\ C_h \\ C_{g'} \\ C_{h'} \\ \vdots \end{pmatrix} = \lambda \begin{pmatrix} C_0 \\ C_g \\ C_h \\ C_{g'} \\ C_{h'} \\ \vdots \end{pmatrix}$$

$$\xrightarrow{\text{three-beam approximation}} \begin{pmatrix} 0 & \sigma V_g^* & \sigma V_h^* \\ \sigma V_g & 2\pi\zeta_g & \sigma V_{h-g}^* \\ \sigma V_h & \sigma V_{h-g} & 2\pi\zeta_h \end{pmatrix} \begin{pmatrix} C_0 \\ C_g \\ C_h \end{pmatrix} = \lambda \begin{pmatrix} C_0 \\ C_g \\ C_h \end{pmatrix}. \quad (3.43)$$

Such an approximation can be held strictly if the excitation errors of the reflections other than reflections  $g$  and  $h$  are much larger than their structure factor magnitudes, i.e.,

$$\min\{2\pi\zeta_{g'}, 2\pi\zeta_{h'} \dots\} \gg \max\{|\sigma V_{g'}|, |\sigma V_{h'}|, |\sigma V_{g'-g}|, |\sigma V_{h'-g}| \dots\}, \quad (3.44a)$$

$$\text{and thus,} \quad \max\{C_{g'}, C_{h'} \dots\} \approx 0. \quad (3.44b)$$

It is not difficult to find three-beam conditions that satisfy the requirements above in structures with small unit cells (say  $a$ ,  $b$  and  $c$  are all smaller than  $10 \text{ \AA}$ ) because the projection of reciprocal lattice is sparse and reflections  $g'$ ,  $h'$  ..., tend to be weakly excited (their excitation errors,  $\zeta_{g'}$ ,  $\zeta_{h'}$  ... tend to be large) near the three-beam condition for reflections  $g$  and  $h$ .

By contrast, the projection of reciprocal lattice for structures with large unit cells is dense and reflections  $g'$ ,  $h'$  ..., tend to be strongly excited (their excitation errors,  $\zeta_{g'}$ ,  $\zeta_{h'}$  ... tend to be small) near the three-beam condition for reflections  $g$  and  $h$ . That is why the three-beam approximation tends to fail in structures with large unit cells and the many-beam diffraction effects are inevitable. Nevertheless, if reflections  $g$  and  $h$  have much larger structure factor magnitudes than the other reflections involved in the neighbourhood of the three-beam condition, the many-beam diffraction can still be treated as perturbation of three-beam approximation. Of course, the three-beam approximation is less strict for large unit cells than small unit cells, and thus it is referred to as “pseudo three-beam diffraction” when it is applied to macromolecular crystals. An empirical criterion for a three-beam diffraction condition in macromolecular crystal is stated in a study of three-beam dynamic X-ray diffraction [36] as:

$$|F'_{g'}| |F'_{h-g'}| \lesssim 0.25 |F'_g| |F'_{h-g}|,$$



where  $F'_g$  are  $F_g$  corrected for polarization. Therefore, in macromolecular crystals, only reflections with large structure factor magnitudes can be used for three-beam diffraction [87, 102, 103]. Another study in three-beam dynamic X-ray diffraction [103] has shown that hundreds of three-phase invariants could be measured from rhombohedral insulin crystals (space group R3), which has a unit-cell volume of 20,000 Å<sup>3</sup>.

Nevertheless, it does not necessarily mean that three-beam electron diffraction can be applied to crystals with large unit cells. The Ewald sphere for electron diffraction is much flatter than that for soft X-rays due to the much shorter wavelength of electron waves (0.025 Å at 200 keV versus 1.1 Å, a typical wavelength used for three-beam X-ray diffraction [103]), and hence many more reflections are likely to be excited simultaneously. Therefore, the application of three-beam diffraction to structures with large unit cells could be more restricted with high-energy electrons.

To test the possibility of measuring three-phase invariants from crystal structures that are not trivial to solve, CBED simulations have been carried out here in three crystal structures with unit-cell volumes larger than 1000 Å<sup>3</sup>. Three inorganic structures were chosen, which cover a range of structures with distinct unit cell sizes, symmetries and atomic weights. The results are summarised in Table 3.3. Whether the orientation (a point in the CBED discs) is a three-beam condition can be judged by inspection of CBED patterns as follows:

**Criterion III.** In the central disc, the intersection of the two deficiency Bragg lines is in the shape of a cross and is isolated from any neighbouring Bragg lines. For example, in Fig. 3.17b, the intersection of two strong Bragg lines for  $1\ 2\ \bar{2}$  and  $16\ 10\ 1$  is isolated from other Bragg lines or intersections.

Sometimes, the intersection may not be easily identifiable in the central disc. For example, in Figs. 3.18, due to the crowded reciprocal lattice, the convergence angle needs to be small to avoid two neighbouring discs from overlapping, and the “cross” is not clearly visible within limited angular range (unless LARBED [23] or Digital-LACBED [94] are used, and then criterion 1 can be applied).

**Criterion IV.** In this case, one can identify the three-beam condition from the discs of diffracted beams, where only two discs in the three-beam condition have intensities while other discs are much darker (like in Figs. 3.18).

Following these criteria, three-beam electron diffraction conditions can be found in crystal structures with a unit cell volume of ~5,000 Å<sup>3</sup>. It can be expected that three-beam electron

diffraction should be applicable to other crystal structures with similar sizes of unit cells and numbers of atoms. It would be more beneficial to apply three-beam electron diffraction to organic crystal structures (say for drug design), where the measured three-phase invariants can constrain the enantiomorph and atom positions much more efficiently, if low-dose, low-temperature CBED [104] is used.

**Table 3.3. Summary of simulations for testing three-beam electron diffraction in some crystal structures that are not trivial to solve**

|  |  |   |   |
|--|--|---|---|
| Chemical formula   | $\text{Bi}_{12}\text{SiO}_{24}$                                  | $\text{CsNbWO}_{14}$  | $\text{Fe}_2\text{Si}_3\text{O}_9$  |
| Crystal system   | Cubic  | Orthorhombic  | Triclinic   |
| Space group  | I23  | Pbam  | P-1   |
| Unit cell constants  | $a=10.104 \text{ \AA}$<br><br>volume= $1031 \text{ \AA}^3$       | $a=27.145 \text{ \AA}$ ,<br>$b=21.603 \text{ \AA}$ ,<br>$c=3.946 \text{ \AA}$ ,<br>volume= $2314 \text{ \AA}^3$ | $a=22.200$ , $b=22.290$ ,<br>$c=17.835$ , $\alpha=125.03^\circ$ ,<br>$\beta=95.98^\circ$ , $\gamma=120^\circ$ ,<br>volume= $5220 \text{ \AA}^3$ |
| Number of atoms  | 65   | 193   | 335   |
| Examples of zone axes in which three-beam diffraction conditions are found | $[2 \bar{2} 5]$ ,<br>$[0 1 4]$ ,<br>$[1 12 0]$ ,<br>$[3 10 0]$ . | $[7 5 1]$ ,<br>$[9 5 1]$ ,<br>$[9 3 1]$ ,<br>$[\bar{2} 3 2]$ .  | $[7 9 2]$ ,<br>$[7 9 3]$ ,<br>$[3 9 7]$ .   |
| Figures for illustrations  | Fig. 3.7   | Fig. 3.17   | Fig. 3.18   |
| References of the structure file   | [105]  | the structure file available in JEMS [58]   | the structure file available in JEMS [58]   |

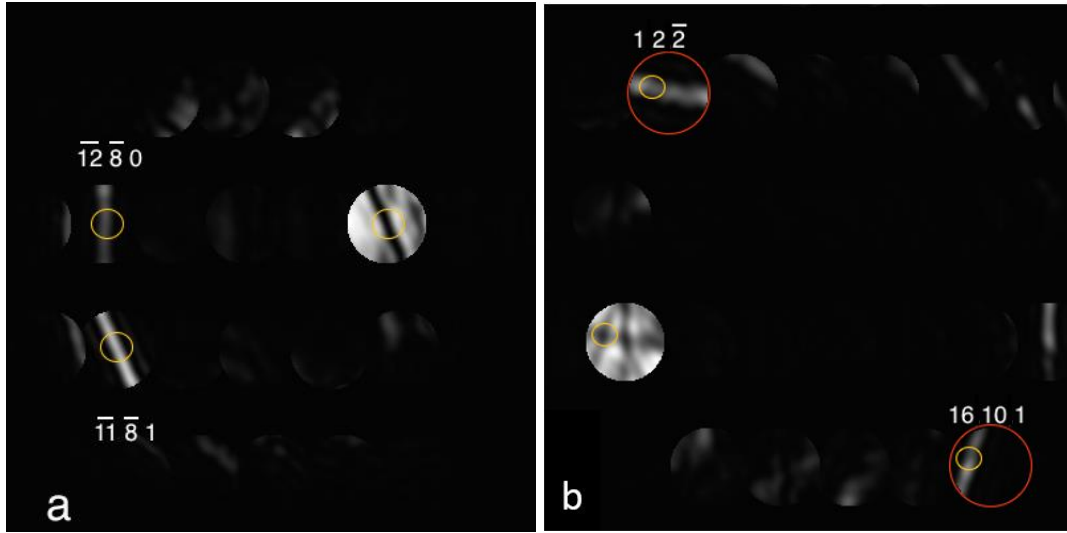


**Figure 3.17. Simulated CBED patterns of CsNbWO<sub>14</sub>.** The Bloch wave method in JEMS [58] was used, where more than 200 reflections were included. Three-beam diffraction effects (labelled with orange circles) are found in  $[\bar{2} \ 3 \ 2]$ . The phase information can be extracted: (a) According to criterion (3.22),  $|V_{1, 0, 1}| \approx 0$  V. (b) According to criterion (3.28),  $\cos(\varphi_{16, 10, 1} + \varphi_{\bar{15}, \bar{8}, \bar{3}} - \varphi_{1, 2, \bar{2}}) < 0$ . For a centrosymmetric crystal,  $\varphi_{16, 10, 1} + \varphi_{\bar{15}, \bar{8}, \bar{3}} - \varphi_{1, 2, \bar{2}} = \pi$ .

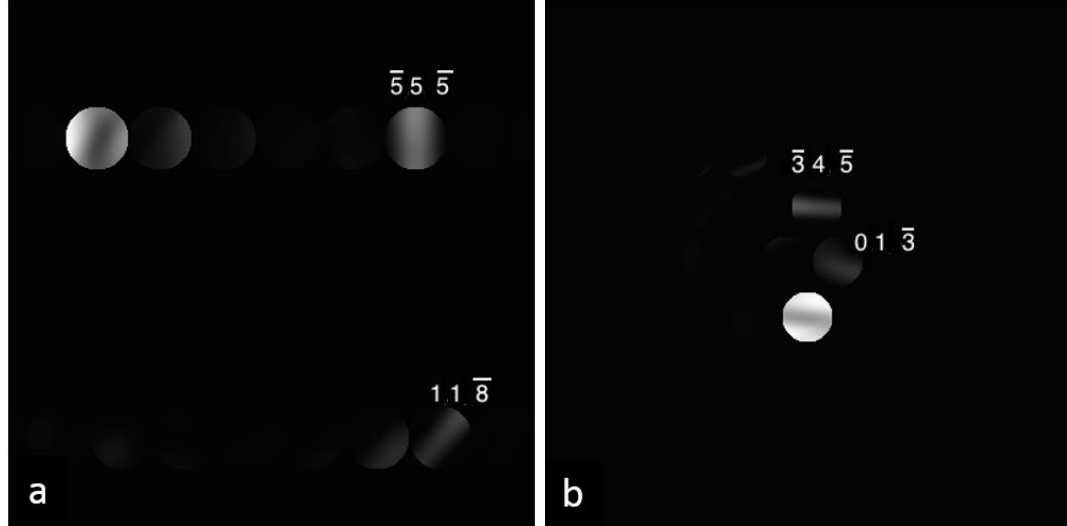


**Figure 3.18. Simulated CBED patterns of Fe<sub>2</sub>Si<sub>3</sub>O<sub>9</sub>.** The Bloch wave calculation in JEMS [58] was used, where more than 200 reflections were included. Three-beam diffraction conditions are found in (a)  $[7 \ 9 \ 2]$  and (b)  $[7 \ 9 \ 3]$ . The phase information can be extracted : (a) According to criterion (3.22),  $|V_{6, \bar{4}, \bar{3}}| \approx 0$  V. (b) According to criterion (3.28),  $\cos(\varphi_{0, 1, \bar{3}} + \varphi_{3, \bar{3}, 2} - \varphi_{\bar{3}, 4, \bar{5}}) < 0$ . For a centrosymmetric crystal,  $\varphi_{0, 1, \bar{3}} + \varphi_{3, \bar{3}, 2} - \varphi_{\bar{3}, 4, \bar{5}} = \pi$ .

### 3.7 Summary

In this chapter, we started from the exact solution to three-beam dynamic diffraction of elastically scattered electrons, equation (3.9a), and then reduced the expressions to two different formulae of factorised forms, equations (3.11b) and (3.23a). From these formulae, we derived the criteria for determining the signs of the sine and cosine three-phase invariants, i.e., criteria (3.12), (3.14), (3.18), (3.22), (3.28) and (3.31), which allow one to decide if the sine and cosine three-phase invariants are plus, minus or zero by inspection of three-beam CBED patterns. To apply criteria (3.12) and (3.14), a centrosymmetrically related pair of three-beam CBED patterns at the same thickness is often required unless the two diffracted beams in the three-beam case have the same or approximately the same values of structure factor magnitudes. The intensity contrast between a Fridel pair,  $g$  and  $\bar{g}$  (which satisfy three-beam conditions for  $0 / g / h$  and  $0 / \bar{g} / \bar{h}$ ) can be used to determine the sign of three-phase invariants based on criterion (3.14) and the application of this criterion requires the specimen thickness to be less than a defined extinction distance,  $\xi_{3\text{-beam}}$  (when  $z = \xi_{3\text{-beam}}$ , the difference of the intensities at their respective three-beam conditions is zero, i.e.,  $I_g(\zeta_g = 0, \zeta_h = 0, z = \xi_{3\text{-beam}}) - I_{\bar{g}}(\zeta_{\bar{g}} = 0, \zeta_{\bar{h}} = 0, z = \xi_{3\text{-beam}}) = 0$ ). Whether the specimen thickness is less than the three-beam extinction distance,  $\xi_{3\text{-beam}}$ , can be decided by inspection of three-beam CBED patterns too: if two criteria, criterion I and II (derived in Section 3.5), are not satisfied simultaneously, the CBED patterns should be rejected as unsuitable for the determination of the sign (of sine three-phase invariants) by observation. Unlike the determination of sine three-phase invariants, the determination of a cosine three-phase invariant requires only one three-beam CBED pattern and does not restrict the use of thick specimens.

Since we can decide if sine and cosine three-phase invariants are plus, minus or zero and there are eight ways to combine “ $\sin\phi >, =, \text{ or } < 0$ ” with “ $\cos\phi >, =, \text{ or } < 0$ ”, we are able to determine the three-phase invariants to within an octant, i.e., with a mean error of  $\pm 22.5^\circ$ . Although not all of the three-phase invariants that exist in a crystal structure can be measured, a small number of measured three-phase invariants in conjunction with direct methods can greatly enhance the success rate of *ab initio* phasing [3, 99]. The possibility of measuring three-phase invariants from structures with large unit cells has also been discussed. A few examples of three-beam CBED patterns are given for structures with certain complexities that are not trivial to solve, which encourages the application/development of three-beam CBED to the measurement of three-phase invariants in complex structures.

A flow chart of the procedure for qualitative phase measurement is given on the next page.

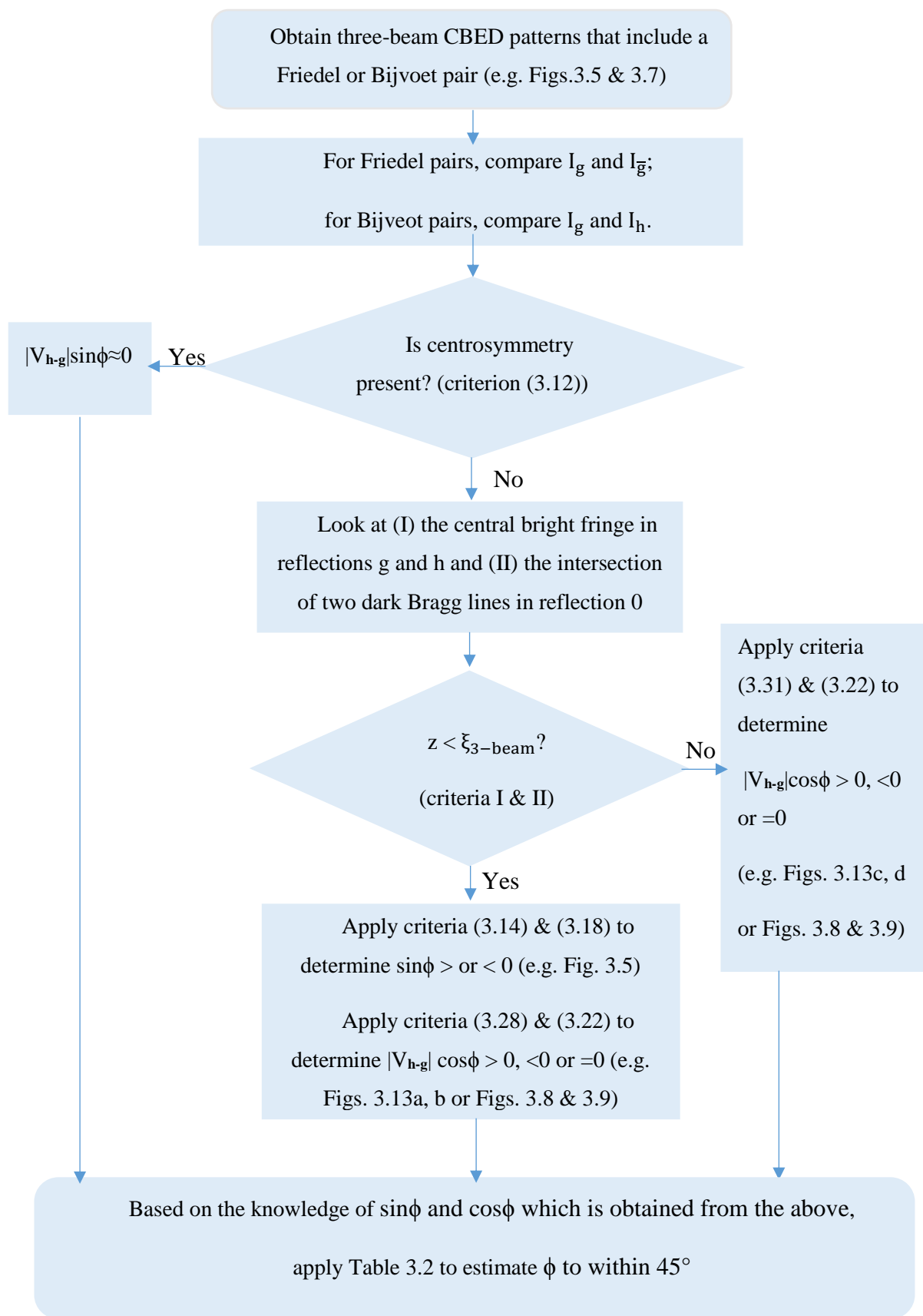


**Figure 3.19.** A flow chart for the determination of the three-phase invariant,  $\phi$ , by direct observations of three-beam CBED patterns.



## Chapter 4. Determination of three-phase invariants by observation: experiment

Chapter 4 presents experimental implementations of the new method in Chapter 3. As a proof of concept, electron diffraction experiments are carried out on a centrosymmetric crystal, Si, and a noncentrosymmetric crystal, GaAs, to demonstrate the feasibility of direct measurement of three-phase invariants. A new diffraction technique, large-angle rocking beam electron diffraction (LARBED) [23], has been applied to measure three-phase invariants for the first time. Through software-controlled data collection and post processing of data, a large-angle convergent-beam electron diffraction (LACBED) pattern can be obtained from a local volume of the specimen. Usually, the reconstructed LACBED pattern can cover several three-beam diffraction conditions, among which, pairs of centrosymmetrically related ones ( $0 / g / h$  and  $0 / \bar{g} / \bar{h}$ ) can be found. This significantly improves the ease of interpretation and widens the applicability of three-beam electron diffraction. In addition to LARBED, the possibility of using lower electron dose with other diffraction techniques are also discussed.

### 4.1 Large-angle rocking beam electron diffraction (LARBED)

#### 4.1.1 Introduction

In traditional CBED, the convergence angle (the size of discs in the pattern) is restricted by the lengths of the basis vectors in the projection of reciprocal lattice to avoid overlap between neighbouring discs. For crystals with large unit cells, the reciprocal lattice can be very dense and convergence angles need to be small (e.g., Fig. 3.18). This makes it very difficult to search for three-beam diffraction conditions and difficult to interpret the data where the angular range is too limited.

Additionally, to determine the sign of three-phase invariants for reflections with distinct structure factor magnitudes ( $|V_g| \neq |V_h|$ ), it is necessary to compare a Friedel pair,  $g$  and  $\bar{g}$ , from a centrosymmetrically related pair of three-beam diffraction conditions,  $0 / g / h$  and  $0 / \bar{g} / \bar{h}$ , at the same thickness. To satisfy this requirement, traditional CBED would have to involve manual control of specimen tilt or beam tilt, which is labour intensive and exceptionally

difficult. Traditional LACBED, which uses a defocused probe (mentioned in Section 2.3), has poor spatial resolution and is limited to specimens with very little variation in thickness.

The techniques that may facilitate data collection and interpretation are large-angle rocking beam electron diffraction (LARBED) [23] and digital LACBED [94], which tilt the electron beam about a point on the specimen to achieve the large angular variation and good spatial resolution simultaneously (i.e. LACBED obtained from a local volume). The work by this PhD candidate has applied LARBED, which is commercially available from the Quantitative Electron Diffraction (QED) software [106] as a plug-in for DigitalMicrograph (Gatan Inc., Pleasanton, CA). The software has been set up on a JEOL 2100F TEM with a field emission gun at the Monash Centre for Electron Microscopy (MCEM). The LARBED function in the software consists of three parts: 1) calibration of the deflection system and compensation of aberrations of the illumination system (which are executed in preparation for data collection), 2) data collection and 3) data processing.

LARBED is originally designed for using a parallel beam of illumination in nanodiffraction mode. By tilting the parallel beam off the optic axis up to 90 mrad, a series of spot patterns are recorded from different incident beam directions sequentially. A CBED-like (or LACBED-like) pattern can be reconstructed from the spot patterns. However, a huge data set of spot patterns needs to be recorded to reveal details of the intensity oscillations as a function of incident beam directions. To reduce the size of the data sets, this work has used a convergent beam of illumination to perform LARBED experiments and has written a code for LACBED reconstructions from CBED patterns which are collected with special experimental setups<sup>10</sup>.

#### 4.1.2 Method

First, standard alignments for CBED was performed using a convergence angle that avoids overlap between adjacent discs. Then, the deflection system was calibrated and the aberration-induced beam shifts were compensated in CBED mode by using the QED software. Without this preparation work, the electron probe would wander to different regions of the sample during beam tilting due to the imperfect beam tilt/beam shift separation and aberrations of the lenses. Third, the data collection was initiated.

---

<sup>10</sup> After the work in this chapter was finished, a new version of QED software (version 1.4) was released. The new version included a function of LACBED reconstruction from data sets of CBED patterns, which is called “LARCBEED reconstruction”. To demonstrate a part of the PhD work, the LACBED patterns that are reconstructed by the code written by this PhD candidate are presented in this chapter.



As shown in Fig. 4.1, the electron beam is tilted off the optic axis to different directions (Fig. 4.1a) while a data stack of CBED patterns are recorded in the sequence of the beam tilts (Fig. 4.1b). Special combinations of the tilt amplitude (which is the largest angle of beam tilt) and number of tilts (which is an integer number) were used in this work to maximize the step size <sup>11</sup> of beam tilt ( $= \frac{\text{tilt amplitude}}{\text{number of tilts}}$ ), which was made equal to the  $\sqrt{2}$  times of the semi-convergence angle (Fig. 4.1c). These settings facilitated coding of LACBED reconstruction as explained in Fig. 4.2 and also reduced the total exposure time required for data acquisition. Schematics in Fig. 4.1 has only shown three beam tilts. In reality, there are often hundreds of beam tilts and the beam is tilted in a fashion that rasters in a square array in reciprocal space along a zigzag trajectory.

When the data collection was finished, a data stack of CBED patterns was obtained. This was then followed by LACBED reconstruction.

Reconstruction of LACBED patterns is depicted in Fig. 4.2. The reconstructed LACBED pattern for a reflection (say  $h$ ) in Fig. 4.2 is a montage of the largest squares inside a CBED disc ( $h$ ) recorded at different tilts or moments ( $t_1, t_2, t_3 \dots$ ) in Fig. 4.1b where the squares are stitched together in the sequence of the beam tilt.

---

<sup>11</sup> Smaller step sizes of the beam tilt need to be used if LACBED reconstruction in the new version of QED (version 1.4) is executed. With smaller step sizes, the total exposure time will be longer.

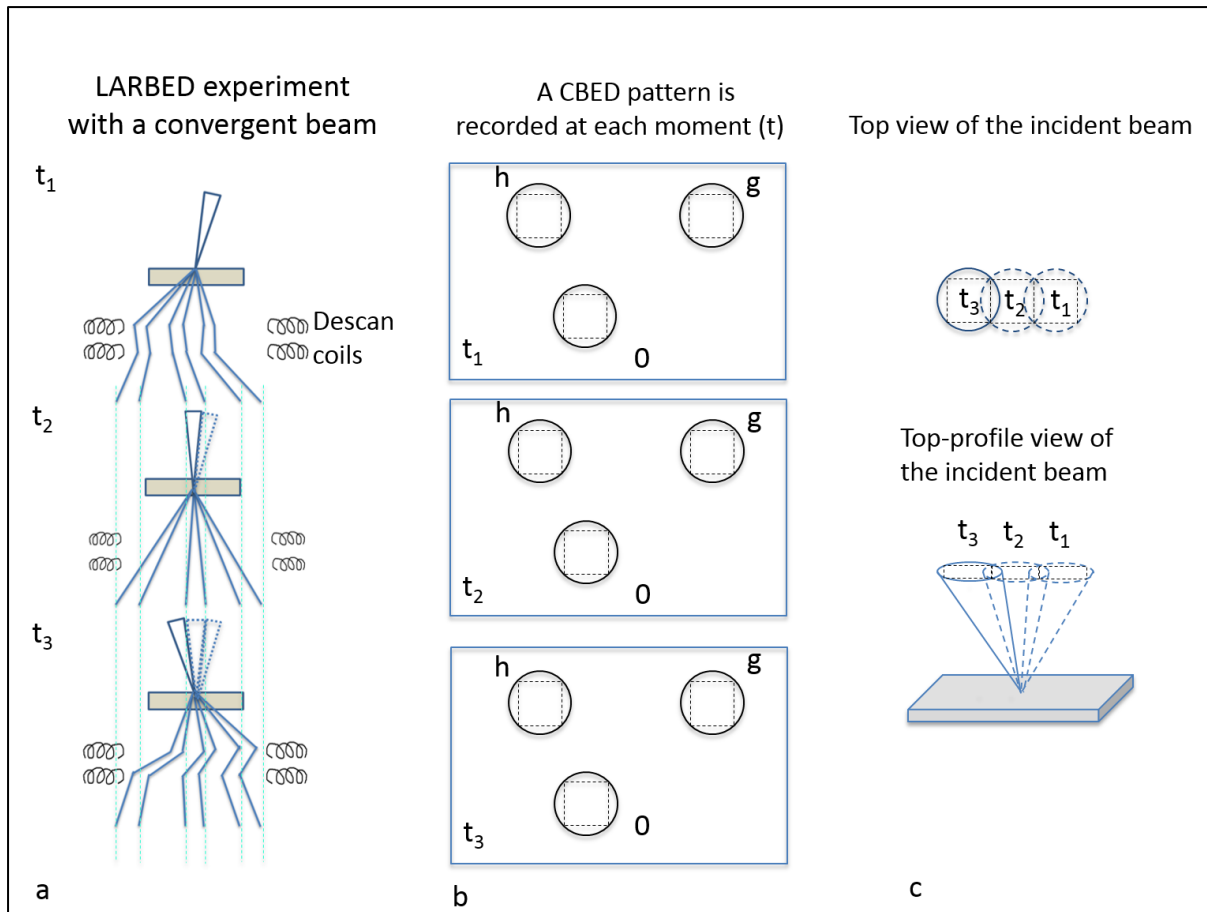


**Figure 4.1. A schematic illustration of LARBED with a convergent beam under the special experimental setup.** The incident beam is tilted about a spot on the specimen and a data stack of CBED patterns are recorded in the sequence of the beam tilts. (a) A complete descscan is applied: no matter which direction the incident beam is tilted in, the descscan coils (diffraction shift coils) in the deflection system bring the diffraction discs to the same positions as in the untilted condition (as at the moment  $t_2$ ). (b) A data stack of CBED patterns is recorded for different tilts. If they are piled up on top of each other, all the reflections (0, g, h ...) lie in the same positions as a consequence of the complete descscan. The largest squares inside the discs are drawn with dashed lines. (c) Using a convergent beam requires much fewer tilting steps than using a nearly parallel beam to cover the same range of reciprocal space. Also, the largest step size of beam tilt is related to the size of the largest square within each disc.

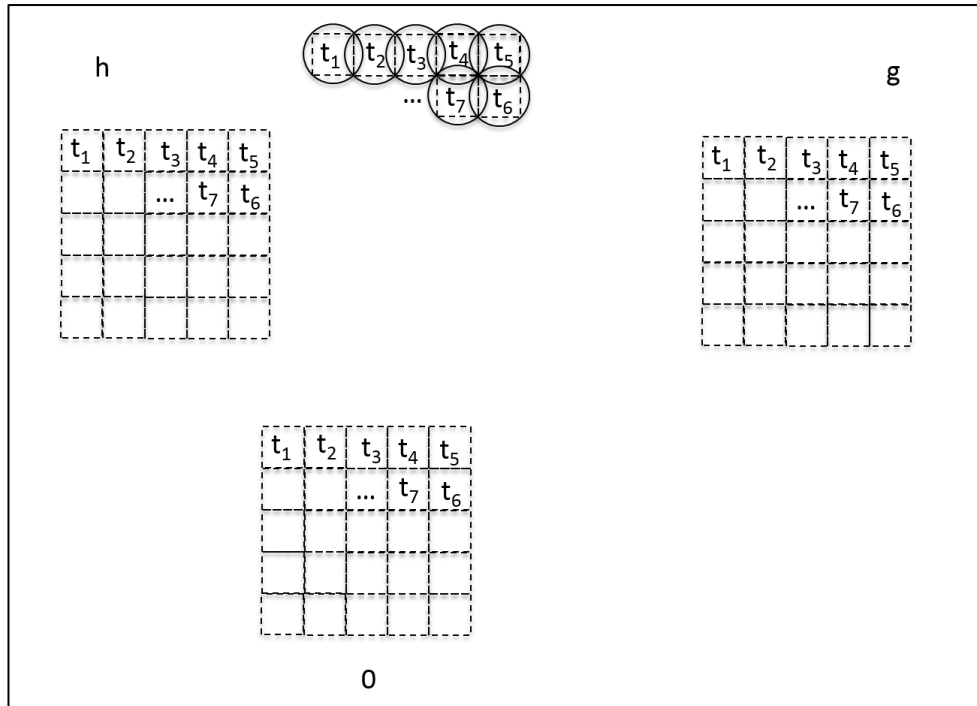


**Figure 4.2.** A schematic illustration of LACBED reconstruction by using the code developed in this PhD work. The code is written in the Digital Micrograph scripting language (which facilitates viewing the results on site in a TEM session). The beam tilt in reciprocal space follows a zigzag trajectory, which rasters a square array. The regions within the largest squares inside each CBED disc (i.e., the regions within the dashed squares in Fig. 4.1b) are copied and stitched together for each reflection in the sequence of data collection (which is the sequence of beam tilts). Therefore, the reconstructed LACBED pattern for each reflection is displayed as a square.

### 4.1.3 Results

As a proof of concept, the experimental implementations of the theories in Chapter 3 have been carried out on two commonly used materials, Si (which is centrosymmetric) and GaAs (which is noncentrosymmetric), to demonstrate direct measurement of three-phase invariants in both centrosymmetric and noncentrosymmetric crystals with LARBED.

In the current experimental setup, a data stack of 121 CBED patterns was recorded from 121 beam tilts (11 x 11). The tilt amplitude was 33 mrad along both horizontal and vertical directions of the CCD detector with a step size of 6.6 mrad (which is exactly  $\sqrt{2}$  times of the semi-convergence angle of incident beam).

#### 4.1.3.1. Si

Once a data set was collected, the stack of CBED patterns were displayed as an integrated pattern in Digital Micrograph (shown in Fig. 4.3a). The reflections could be indexed based on their distances to the central beam and the angles between the reciprocal lattice vectors. Then, the LACBED patterns of the selected reflections were reconstructed (shown in Fig. 4.3b).

The reconstructed central beam is useful for searching for three-beam conditions: three-beam conditions can be found at intersections of two Bragg lines (usually two dark lines at low thicknesses) where no other Bragg lines for strong reflections lie in the neighbourhood.

In Fig. 4.3b, a centrosymmetrically related pair of three-beam conditions,  $0\ 0\ 0 / \bar{5}\ \bar{3}\ 1 / \bar{3}\ \bar{5}\ 1$  and  $0\ 0\ 0 / 5\ 3\ \bar{1} / 3\ 5\ \bar{1}$ , are found in the reconstructed central beam and labelled with circles in different colours. It should be reminded from Section 2.3.1 that the same coordinate in each reconstructed reflection corresponds to the same incident beam direction. For example, the green circles in the discs of  $0\ 0\ 0$ ,  $\bar{5}\ \bar{3}\ 1$  and  $\bar{3}\ \bar{5}\ 1$  correspond to the same three-beam condition (and its neighbourhood). The oscillation fringes in the central beam show that the thickness is even for different incident beam directions. The intensity distributions within the green circle in the  $\bar{5}\ \bar{3}\ 1$  disc and within the red circle in the  $5\ 3\ \bar{1}$  disc have a centre of inversion at somewhere outside the circles. According to criterion (3.12), the presence of centre of inversion between the two reflections of a Friedel pair is the evidence of  $\sin(\varphi_{\bar{5},\ \bar{3},\ 1} + \varphi_{2,\ \bar{2},\ 0} - \varphi_{\bar{3},\ \bar{5},\ 1}) = 0$ . According to the criterion (3.28), intensity asymmetry about the three-beam conditions reveals that  $\cos(\varphi_{\bar{5},\ \bar{3},\ 1} + \varphi_{2,\ \bar{2},\ 0} - \varphi_{\bar{3},\ \bar{5},\ 1}) > 0$ . Therefore, according to Table 3.2,  $\varphi_{\bar{5},\ \bar{3},\ 1} + \varphi_{2,\ \bar{2},\ 0} - \varphi_{\bar{3},\ \bar{5},\ 1} \approx 0$ . This agrees with the value calculated from the isolated atom model (IAM) [107] without considering inelastic scattering.

A careful comparison of the integrated intensities within the green circle in the  $\bar{5}\ \bar{3}\ 1$  disc and the integrated intensities within the red circle in the  $5\ 3\ \bar{1}$  disc reveals that

$$\frac{I_{\bar{5}\ \bar{3}\ 1} - I_{5\ 3\ \bar{1}}}{(I_{\bar{5}\ \bar{3}\ 1} + I_{5\ 3\ \bar{1}})/2} = 2.0\% .$$

For the other Friedel pair,  $\bar{3}\ \bar{5}\ 1$  and  $3\ 5\ \bar{1}$ ,

$$\frac{I_{\bar{3}\ \bar{5}\ 1} - I_{3\ 5\ \bar{1}}}{(I_{\bar{3}\ \bar{5}\ 1} + I_{3\ 5\ \bar{1}})/2} = -4.4\% .$$

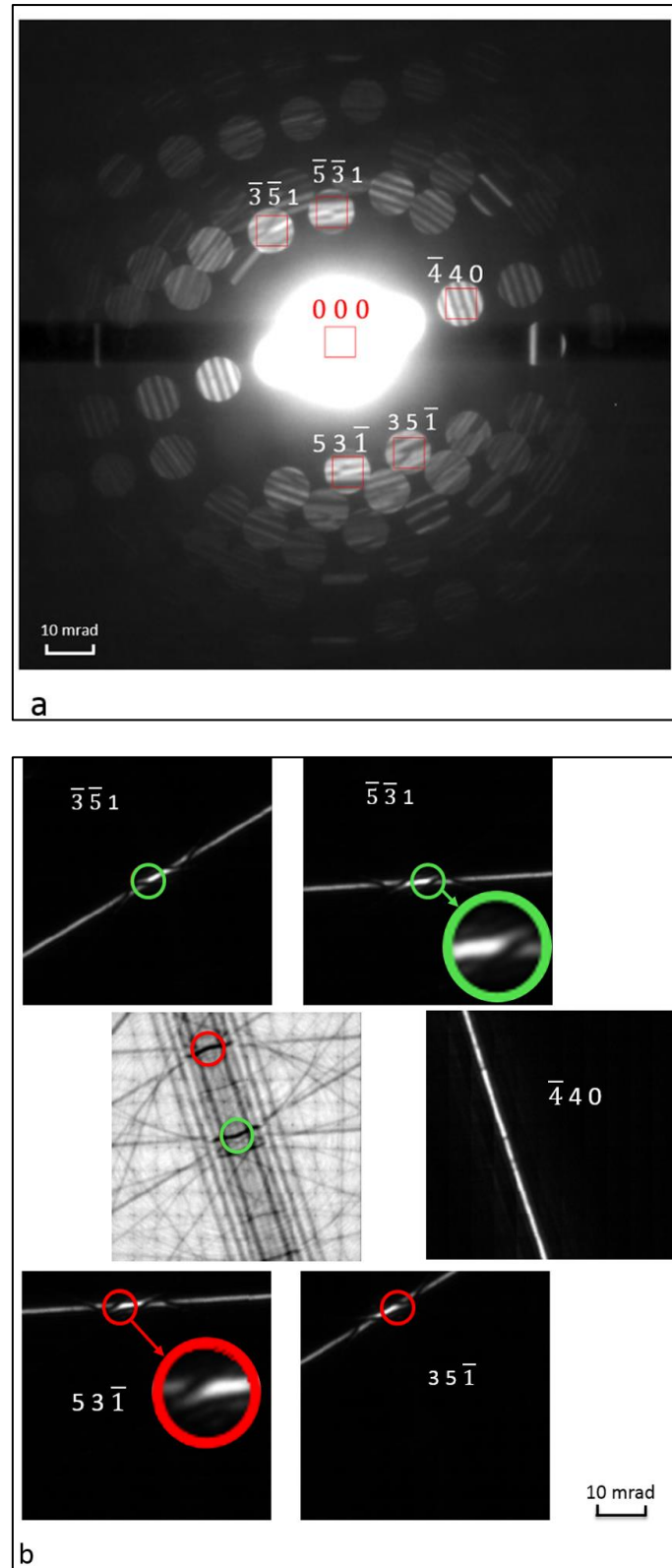


**Figure 4.3.** An integrated CBED pattern (a) and reconstructed LACBED patterns (b), both from a data stack of 121 CBED patterns from Si near  $[1\ 1\ 8]$  at 200kV. (a) The pattern is created by integrating all the 121 CBED patterns on top of one another. This pattern can be used for indexation, measurement of the convergence angle, and allocation of the largest

internal squares. The largest squares inside the selected discs are labelled in red. (b) Reconstructed LACBED patterns of the selected reflections in (a). A pair of centrosymmetrically related three-beam conditions for  $0\ 0\ 0 / \bar{5}\ \bar{3}\ 1 / \bar{3}\ \bar{5}\ 1$  and  $0\ 0\ 0 / 5\ 3\ \bar{1} / 3\ 5\ \bar{1}$  are found in the reconstructed central beam and labelled with circles in green and red, respectively. The intensity distributions near the three-beam conditions in a Friedel pair,  $\bar{5}\ \bar{3}\ 1$  and  $5\ 3\ \bar{1}$ , are magnified for a better view for visual comparisons. The intensity distributions of within the two circles have a centre of inversion at somewhere outside the circles. The symmetry reveals that the sine three-phase invariant is zero. The intensity distribution within each circled region shows significant asymmetry, which is the evidence of positive cosine three-phase invariant.

By combining the two Friedel pairs, an intensity difference can be defined as

$$\frac{(I_g + I_{\bar{h}}) - (I_{\bar{g}} + I_h)}{[(I_g + I_{\bar{h}}) + (I_{\bar{g}} + I_h)]/2} .$$

Substituting the values from the current case, the intensity difference is

$$\frac{I_{\bar{5}\ \bar{3}\ 1} - I_{5\ 3\ \bar{1}} + I_{\bar{3}\ \bar{5}\ 1} - I_{3\ 5\ \bar{1}}}{(I_{\bar{5}\ \bar{3}\ 1} + I_{5\ 3\ \bar{1}} + I_{\bar{3}\ \bar{5}\ 1} + I_{3\ 5\ \bar{1}})/2} = -3.3\% .$$

If three-beam diffraction of elastically scattered electrons is assumed, the difference above should be zero. The small deviation may be due to the influence of many beam diffraction and experimental errors which may origin from the astigmatism in the focused probe at large-angle tilts. Nevertheless, such an error is tolerable for the estimation of three-phase invariants. To take into account such an error in the interpretation, we may state an empirical rule based on the result of the intensity difference above that the intensity difference between the Friedel pair can be ignored:

|      |   |
|------|---|
| If   | $\left  \frac{(I_g + I_{\bar{h}}) - (I_{\bar{g}} + I_h)}{[(I_g + I_{\bar{h}}) + (I_{\bar{g}} + I_h)]/2} \right  \leq 5\% ,$ |
| then | $I_g(\zeta_g, \zeta_h, z) \approx I_{\bar{g}}(\zeta_{\bar{g}}, \zeta_{\bar{h}}, z) ,$                                       |
| and  | $ V_{h-g}  \sin\phi \approx 0 . \quad (4.1)$  |

Otherwise, the effect of the sign of  $\sin\phi$  is responsible for the intensity difference that is larger than 5% (or smaller than -5%).

#### 4.1.3.2. GaAs

A TEM specimen was made from a GaAs [1 0 0] wafer by tripod polishing with a MULTIPREP™ POLISHING SYSTEM - 12" (ALLIED High Tech Products. Inc., Rancho Dominguez, CA) and low energy ion milling with a Gentle Mill 2 (Technoorg Linda LTD. CO., Hungary).

The specimen was tilted to [5 1 0] and data collection was commenced.

LACBED patterns for five selected reflections were reconstructed and are shown in Fig. 4.4. According to the two criteria discussed in Section 3.5, one can conclude from inspection of the Bragg lines that the thickness is within the validity range for the sign determination by direction observation (i.e.,  $z < \xi$ ). Therefore, the sign of the three-phase invariant can be determined by a direct comparison of a Friedel pair. In Fig. 4.4, a centrosymmetrically related pair of three-beam conditions,  $0\ 0\ 0 / 1\ \bar{5}\ 1 / 1\ \bar{5}\ \bar{1}$  and  $0\ 0\ 0 / \bar{1}\ 5\ \bar{1} / \bar{1}\ 5\ 1$ , are labelled with circles in red and green. The intensity within the red circle in  $1\ \bar{5}\ 1$  is much brighter than that within the green circle in  $\bar{1}\ 5\ \bar{1}$  and the intensity within the red circle in  $1\ \bar{5}\ \bar{1}$  is much darker than that within the green circle in  $\bar{1}\ 5\ 1$ . According to criterion (3.14),  $\sin(\varphi_{1, \bar{5}, 1} + \varphi_{0, 0, \bar{2}} - \varphi_{1, \bar{5}, \bar{1}}) > 0$ . Within the four circles, each intensity distribution has a centre of inversion at its three-beam condition. According to criterion (3.28),  $\cos(\varphi_{1, \bar{5}, 1} + \varphi_{0, 0, \bar{2}} - \varphi_{1, \bar{5}, \bar{1}}) \approx 0$ . Therefore,  $(\varphi_{1, \bar{5}, 1} + \varphi_{0, 0, \bar{2}} - \varphi_{1, \bar{5}, \bar{1}}) \approx +90^\circ$ . The result of this qualitative measurement agrees with the calculated value based on the IAM [107], which gives  $+96^\circ$ . It should be noted that  $1\ \bar{5}\ 1$  and  $1\ \bar{5}\ \bar{1}$  are a Bijvoet pair. According to equation (3.15) and criterion (3.14), the sign of  $\varphi_{1, \bar{5}, 1} + \varphi_{0, 0, \bar{2}} - \varphi_{1, \bar{5}, \bar{1}}$  can also be determined by comparing the intensity difference between a Bijvoet pair.

This example demonstrates the application of LARBED to the determination of three-phase invariants in a noncentrosymmetric crystal based on the theories in Chapter 3.

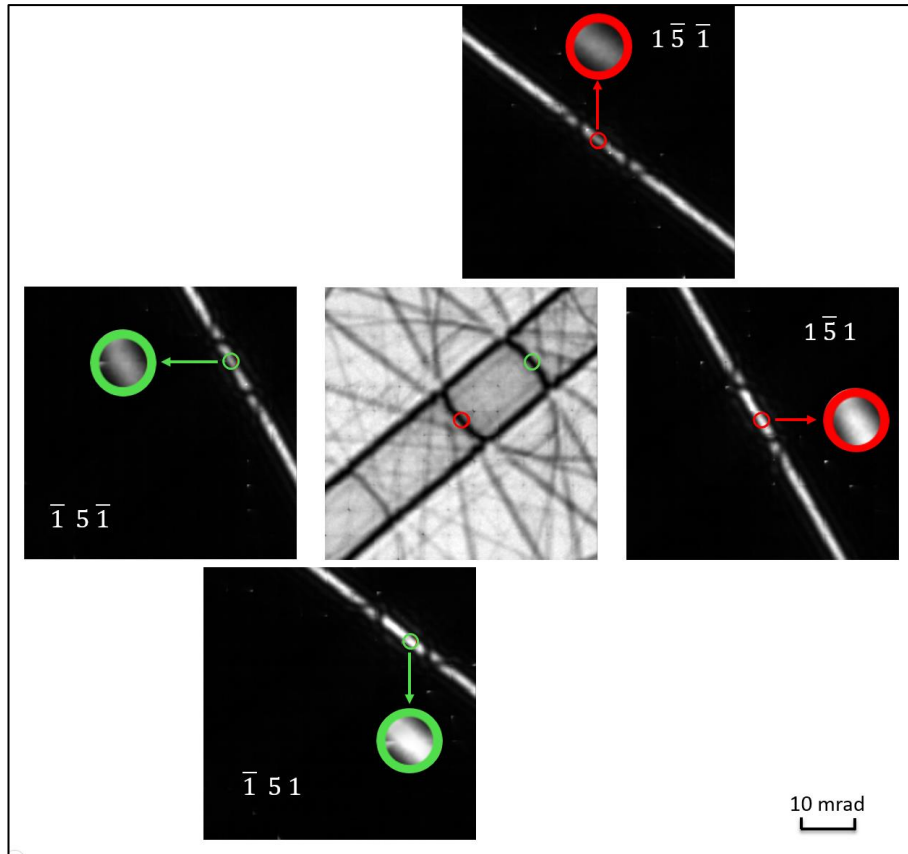


**Figure 4.4. Reconstructed LACBED patterns from GaAs [5 1 0] at 200 kV.** The same experimental setup for data acquisition as in Fig. 4.3 has been used. A centrosymmetrically related pair of three-beam conditions,  $0\ 0\ 0 / 1\ \bar{5}\ 1 / 1\ \bar{5}\ \bar{1}$  and  $0\ 0\ 0 / \bar{1}\ 5\ \bar{1} / \bar{1}\ 5\ 1$ , are highlighted with red and green circles, respectively. The intensities of the four diffracted beams at the three-beam conditions are magnified for a better view for visual comparisons. Significant contrast between the green-circled and the red-circled regions reveal the sign of the three-phase invariants. The intensity distribution within each circled region has a centre of inversion at their respective three-beam conditions, which reveals that cosine three-phase invariants is close to zero.

As stated earlier, three-beam conditions can be found in places where only two Bragg lines (dark lines in the central beam) intersect each other without contacting any other Bragg lines for strong reflections (which appear to be dark and broad in thin specimens) near the intersection. Near the zone axis [5 1 0], many Bragg lines intersect at the same places and only a few three-beam conditions can be found, which is not optimal for measuring a number of



three-phase invariants. A more favourable zone axis should include multiple three-beam conditions in the reconstructed LACBED patterns, which is now demonstrated as follows.

The specimen was tilted to a minor zone axis,  $[9\ 1\ \bar{2}]$ , where the reciprocal lattice points are sparsely spaced. Multiple three-beam conditions (intersections of only two Bragg lines) can be found in the reconstructed LACBED pattern of the central beam in Fig.4.5a. Eight of them are circled and numbered in the figure. Among the numbered three-beam conditions, 1 and 1', are centrosymmetrically related and can be used to determine a unique three-phase invariant  $\phi_1 = \varphi_{1\ 1\ 5} + \varphi_{0\ \bar{4}\ \bar{2}} - \varphi_{1\ \bar{3}\ 3}$  (since  $\phi_{1'} = -\phi_1$ ) as follows:

- 1) the intensity distribution near the three-beam condition in a Bragg reflection has a centre of inversion at the exact three-beam condition, and according to the criterion (3.28),  $|V_{0\ \bar{4}\ \bar{2}}| \cos\phi_1 \approx 0$ .

- 2) Calculation of the intensity difference defined in (4.1) gives

$$\frac{(I_{1\ 1\ 5} + I_{\bar{1}\ 3\ \bar{3}}) - (I_{\bar{1}\ \bar{1}\ \bar{5}} + I_{1\ \bar{3}\ 3})}{[(I_{1\ 1\ 5} + I_{\bar{1}\ 3\ \bar{3}}) + (I_{\bar{1}\ \bar{1}\ \bar{5}} + I_{1\ \bar{3}\ 3})]/2} = -8.7\% ,$$

which has exceeded the 5 % error that may origin from the experiment and the effect of many-beam diffraction. And according to criterion (3.14),  $|V_{0\ \bar{4}\ \bar{2}}| \sin\phi_1 < 0$ .

Combining  $|V_{0\ \bar{4}\ \bar{2}}| \cos\phi_1 \approx 0$  and  $|V_{0\ \bar{4}\ \bar{2}}| \sin\phi_1 < 0$ , it can be estimated that  $\phi_1 \approx -90^\circ$  according to Table 3.2. This result of qualitative measurement is consistent with the calculated value based on IAM [107], which is  $-92^\circ$ .

It may have been also noticed that the intensity differences between the Friedel pairs in this case are very small. This suggests that the value of  $|V_{0\ \bar{4}\ \bar{2}}|$  is very small, which is consistent with the calculated value based on IAM [107], which gives  $|V_{0\ \bar{4}\ \bar{2}}| = 0.1\ \text{V}$ .

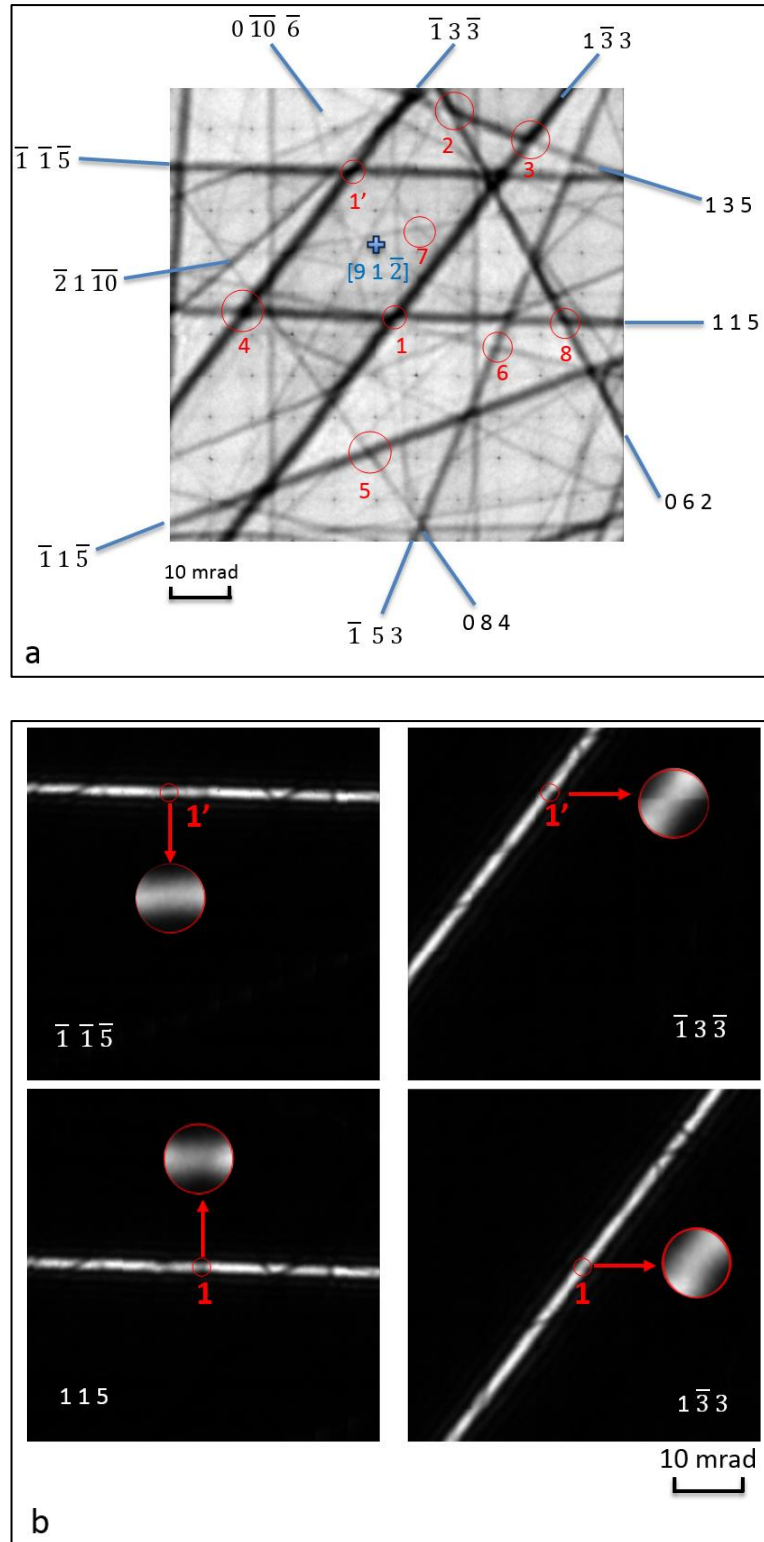


**Figure 4.5. Reconstructed LACBED patterns of GaAs  $[9\ 1\ \bar{2}]$  at 200 kV.** (a) The reconstructed LACBED pattern of the central beam serves to search for three-beam conditions. Three-beam conditions are circled and numbered. A centro-symmetrically related pair of three-beam conditions,  $0\ 0\ 0 / 1\ 1\ 5 / 1\ \bar{3}\ \bar{3}$  and  $0\ 0\ 0 / \bar{1}\ \bar{1}\ \bar{5} / \bar{1}\ \bar{3}\ \bar{3}$ , are circled and numbered with

1 and 1', respectively. (b) The reconstructed LACBED patterns of four diffracted beams that satisfy the three-beam conditions 1 and 1'. The intensity distributions near the three-beam conditions are magnified to facilitate observation. A shear between two parts in the circle in reflection  $\bar{1} \ 3 \ \bar{3}$  is caused by the misalignment of the cropped CBED discs in the LACBED reconstruction (which may be compensated by applying the “LARCBED reconstruction” function in the newly released version of QED software).

For other three-beam conditions in Fig. 4.5a, 2 to 8, the signs of  $\cos\phi_2, \cos\phi_3 \dots \cos\phi_8$  can be determined and according to criterion (3.28) and they are all positive. The signs of  $\sin\phi$  cannot be directly determined by observation of the reconstructed patterns since no Friedel or Bijvoet pair is available within the angular range of the reconstructed patterns in Fig. 4.5. However, the signs of  $\sin\phi$  can be determined from a visual comparison with a series of simulated three-beam CBED patterns at different thicknesses given that the structure factor magnitudes are measured by other techniques such as precession electron diffraction (PED) [27] (which can be done in the same QED software [23]) or X-ray diffraction. Alternatively, the current angular range, which is 33 mrad, can be expanded by increasing the tilt amplitude (up to 90 mrad) and the tilt number.

**Table 4.1 Summary of the main results in Section 4.1.3**

| The three-phase invariants  | Specimens & zones     | The estimated values of $\phi$ from inspection of the experimental patterns | The calculated values of $\phi$ from IAM [107] |
|---|-----------------------|---|--|
| $\varphi_{\bar{5}, \bar{3}, 1} + \varphi_{2, \bar{2}, 0} - \varphi_{\bar{3}, \bar{5}, 1}$ | Si [1 1 8]            | 0°  | 0°   |
| $\varphi_{1, \bar{5}, 1} + \varphi_{0, 0, \bar{2}} - \varphi_{1, \bar{5}, \bar{1}}$       | GaAs [5 1 0]          | +90°  | +96°   |
| $\varphi_{1, 1, 5} + \varphi_{0, \bar{4}, \bar{2}} - \varphi_{1, \bar{3}, 3}$             | GaAs [9 1 $\bar{2}$ ] | -90°  | -92°   |

#### 4.1.4 Discussions

As a proof of concept, the results demonstrate the possibility of using the reconstructed LACBED patterns from LARBED experiments to measure three-phase invariants in both centrosymmetric and noncentrosymmetric crystals. The same procedures should be transferrable to measure the three-phase invariants in complicated structures with unknown

atom positions. As discussed in Section 3.6, the measured three-phase invariants in conjunction with direct methods can greatly improve crystal structure determination so that structure solutions can be found more easily in the early stage of the structure determination.

In addition, the measured three-phase invariants measured from reconstructed LACBED patterns can be used to identify chirality of chiral crystal structures.

Inversion transformation of the coordinates of a chiral structure,  $V(\mathbf{r})$ , will give its enantiomorphic structure,  $V(-\mathbf{r})$ , which cannot be superimposed onto  $V(\mathbf{r})$  by pure rotation, which is the same as the symmetry between the left and right hand. If we label the original structure  $V(\mathbf{r})$  as the left-hand structure  $V^L(\mathbf{r})$ , and its inverted image as the right-hand structure  $V^R(\mathbf{r})$ , where  $V^L(\mathbf{r}) = V(\mathbf{r})$  and  $V^R(\mathbf{r}) = V(-\mathbf{r})$ . Then, the Fourier expansion of the right-hand structure is:

$$V^R(\mathbf{r}) = \sum_{\mathbf{g}} |V_{\mathbf{g}}| \exp(i\varphi_{\mathbf{g}}^R) \exp(+2\pi i \mathbf{g} \cdot \mathbf{r}) , \quad (4.2)$$

which is the same as the Fourier expansion of the inverted left-hand structure

$$V^L(-\mathbf{r}) = \sum_{\mathbf{g}} |V_{\mathbf{g}}| \exp(i\varphi_{\mathbf{g}}^L) \exp(-2\pi i \mathbf{g} \cdot \mathbf{r}) . \quad (4.3)$$

Instead of summing over  $\mathbf{g}$ , we can rewrite equation (4.3) as a summation over  $-\mathbf{g}$ :

$$V^L(-\mathbf{r}) = \sum_{-\mathbf{g}} |V_{-\mathbf{g}}| \exp(i\varphi_{-\mathbf{g}}^L) \exp\{+2\pi i (-\mathbf{g}) \cdot \mathbf{r}\} . \quad (4.4)$$

For elastic scattering,  $|V_{\mathbf{g}}| = |V_{-\mathbf{g}}|$ . By equating equations (4.2) and (4.4), we have

$$\varphi_{\mathbf{g}}^R = \varphi_{-\mathbf{g}}^L = -\varphi_{\mathbf{g}}^L . \quad (4.5)$$

Thus, the three-phase invariants in a pair of chiral structures are connected as:

$$\phi_{0/\mathbf{g}/\mathbf{h}}^R = \phi_{0/\bar{\mathbf{g}}/\bar{\mathbf{h}}}^L = -\phi_{0/\mathbf{g}/\mathbf{h}}^L \quad (4.6)$$

From equation (4.6), it can be concluded that for a pair of enantiomorphically related structures: the same three-phase invariant have the opposite signs ( $\phi_{0/\mathbf{g}/\mathbf{h}}^R = -\phi_{0/\mathbf{g}/\mathbf{h}}^L$ ); the three-phase invariants for the opposite three-beam conditions have the same sign ( $\phi_{0/\mathbf{g}/\mathbf{h}}^R = \phi_{0/\bar{\mathbf{g}}/\bar{\mathbf{h}}}^L$ ). Therefore, to identify chirality of a structure, both the signs for indexes of reflections  $\mathbf{g}$  and  $\mathbf{h}$ , and the sign for the three-phase invariant,  $\phi_{0/\mathbf{g}/\mathbf{h}}$ , have to be determined consistently.

Since three-beam diffraction alone involves three reciprocal vectors that are coplanar, it is impossible to identify chirality, which is three-dimensional information, unless a fourth beam that is not in the same zone axis (non-coplanar) is present in the field of view [108]. Therefore, at least one three-beam condition and one HOLZ reflection should be present in the same diffraction pattern.

In traditional CBED techniques, a Bijvoet pair in the ZOLZ together with HOLZ reflections in the dark field are compared with simulated patterns of known crystal structures to identify the chirality [56, 109, 110]. This may require careful manual operations of aligning the crystal due to the limited angular range of traditional CBED. Within the bright field pattern of a reconstructed LACBED pattern, a centrosymmetrically related pair of three-beam conditions and deficiency HOLZ lines can be found simultaneously. Based on the positions of the deficiency HOLZ lines relative to the three-beam conditions in the reconstructed central beam, a Friedel pair can be indexed without ambiguity. Three-phase invariants can be determined from direct observation of the reconstructed diffracted beams. Therefore, chirality can be clearly identified from just a single reconstructed LACBED pattern (with both central beam and diffracted beams) where a Friedel or Bijvoet pair is present.

## **4.2 Three-beam electron diffraction in selected area diffraction**

As discussed in the last section, the reconstructed LACBED can be used to determine the three-phase invariants for unknown crystal structures and to identify chirality of chiral structures. Chirality identification using three-beam electron diffraction (not limited to LARBED or CBED experiments) may find application in pharmaceutical development where a new drug crystal with mixed forms of handedness is not desired [111]. Chirality identification for a pharmaceutical crystal has been demonstrated using three-beam X-ray diffraction [112]. The limitation of three-beam X-ray diffraction is that a large single crystal (on the scale of 10 $\mu$ m in length [112]) with little imperfection is required. That is not a limitation for three-beam electron diffraction since significant dynamic diffraction is present in electron diffraction by crystals of a few dozen nanometres. However, the issues of beam damage in electron diffraction is critical. In particular, LARBED can cause beam damage problems for more beam-sensitive materials due to the long exposure time that results from:

- 1) a focused electron probe staying in one place over the lengthy period of data collection;
- 2) the current software requires certain numbers of counts on the detector to start running.

To reduce the beam damage, selected area diffraction (SAD) can be applied to direct measurement of three-phase invariants.

Selected area electron diffraction uses a parallel beam and selected area aperture in the image plane to form a spot diffraction pattern in the back focal plane of the objective lens. By using a nearly parallel beam with a very small convergence angle, the contrast of Kikuchi lines can be clearly observed for the specimens that are not very thin. Guided by the Kikuchi pattern, the specimen can be tilted to a three-beam condition where two Bragg spots sit on the two intersecting excess Kikuchi lines. The contrast of the two Kikuchi lines is enhanced only when the crystal orientation is close to the three-beam condition. By tilting the crystal slightly off the three-beam condition, the Bragg spots  $g$  and  $h$  can be separated from the Kikuchi lines of the same reflections  $g$  and  $h$ . The effect of  $\sin\phi$  is present in the contrast between the two Kikuchi lines of a Bijvoet pair as well as in the contrast between the two Bragg spots that are near the exact three-beam condition.

Here, an example demonstrates the determination of the sign of  $\sin\phi$  with a SAD pattern which was recorded from GaAs  $[11\ 0\ 1]$  (shown in Fig. 4.6). Guided by the Kikuchi band of  $0\ 4\ 0$  and  $0\ \bar{4}\ 0$ , the three-beam condition for  $0\ 0\ 0 / 1\ \bar{1}\ \bar{1}\bar{1} / 1\ 1\ \bar{1}\bar{1}$  could be located. The contrast between two excess Kikuchi lines qualitatively mimics the contrast between the two Bragg reflections in a CBED pattern that is recorded in the same orientation. The Bragg spots in the SAD pattern can be viewed as spots from CBED discs (although the spatial resolution is quite different). Therefore, the same criteria for the determination of three-phase invariants that have been applied to three-beam CBED patterns in Chapter 3 can be applied to the spots and Kikuchi lines in SAD patterns. In Fig. 4.6, at the three-beam conditions (where the arrows point to), Kikuchi line of  $1\ \bar{1}\ \bar{1}\bar{1}$  is brighter than that of  $1\ 1\ \bar{1}\bar{1}$ . Also, the spot of  $1\ \bar{1}\ \bar{1}\bar{1}$  is also brighter than the spot of  $1\ 1\ \bar{1}\bar{1}$ . Therefore, according to criterion (3.14) and equation (3.15),  $\sin(\varphi_{1, \bar{1}, \bar{1}\bar{1}} + \varphi_{0, 2, 0} - \varphi_{1, 1, \bar{1}\bar{1}}) > 0$ . Determination of the sign of  $\cos\phi$  from Kikuchi patterns has been discussed in previous works [8, 9].

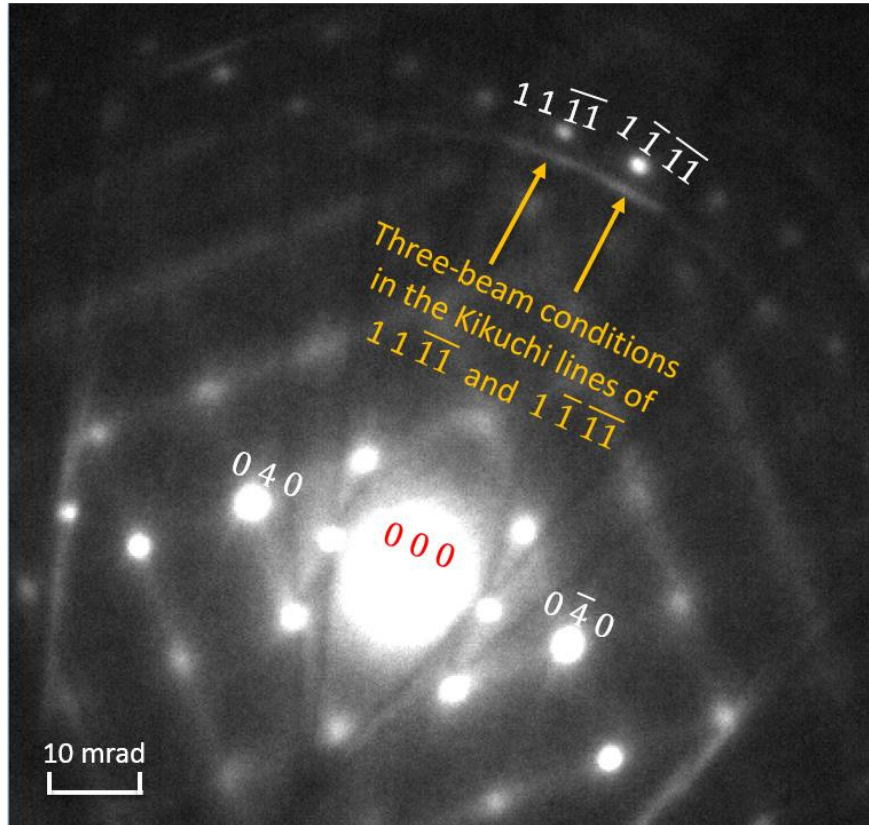


**Figure. 4.6.** A selected area diffraction pattern of GaAs [11 0 1] taken from a FEI Tecnai G<sup>2</sup> T20 with LaB<sub>6</sub> gun at 200 kV. The pattern was recorded on an Orius SCD200D wide-angle CCD camera with an exposure time of 1s. According to the nominal dose rate stated by the Tecnai Imaging & Analysis (TIA) software, the total dose during the exposure was estimated to be 200 e/Å<sup>2</sup>. Collective vibration of the crystal lattice causes the diffuse scattering of electrons that results in the bright lines between Bragg spots along {0 1 1} directions.

### 4.3 On automatic collection of diffraction patterns with low doses

Based on the previous discussions in this chapter, LARBED can automatically collect diffraction information from a wide angular range but may encounter the issues of beam damage for beam-sensitive materials. On the other hand, SAD may reduce the dose level but requires manual tilting of specimens, which is less experimentally efficient. New experiments of three-beam electron diffraction are needed to tackle the phase problem for beam-sensitive materials.

In three-beam X-ray diffraction, an established experimental technique called “reference-beam diffraction (RBD)” enables fast collection of multiple three-beam diffraction conditions

from a wide range of orientations [113]. In a parallel beam of illumination, the crystal is first rotated to a two-beam condition for reflection  $g$  and then data collection is initiated. By tilting the crystal about the reciprocal vector  $g$ , a series of three-beam conditions,  $0 / g / h_1$ ,  $0 / g / h_2$ ,  $0 / g / h_3 \dots$  can be satisfied sequentially. The intensities of  $g$ ,  $h_1$ ,  $h_2$ ,  $h_3 \dots$  will oscillate rapidly near their respective three-beam conditions. The spot diffraction patterns can be reconstructed to give intensity profiles across the three-beam conditions, providing information for phase measurement. Geometrically, the reconstructed profiles are equivalent to the profiles along a certain locus across LACBED discs. Such an experiment should be transferrable to electron microscopes. With the use of a parallel beam, the electron dose can be reduced dramatically.

There is an existing method in TEM called “rotation electron diffraction (RED)” which combines electron beam tilts with goniometer tilts around a common tilt axis [101]. With some modifications of RED, RBD may be practicable in electron microscopes. Alternatively, LARBED with a parallel beam, which carefully prevents the probe from shifting to different regions during beam tilting, could be modified to adopt such an experimental scheme.



## Chapter 5. A three-beam CBED approach for local composition measurement in $\text{In}_x\text{Ga}_{1-x}\text{As}$

Semiconductor materials with zinc blende crystals structures such as  $\text{In}_x\text{Ga}_{1-x}\text{As}$ ,  $\text{Al}_x\text{Ga}_{1-x}\text{As}$  and  $\text{Cd}_x\text{Zn}_{1-x}\text{Se}$  have been widely used in daily life applications such as transistors in mobile phone power amplifiers and diodes in laser emitters. Recent progress in InGaAs n-channel metal–oxide–semiconductor field-effect transistors (MOSFETs) have shown promises as a replacement for Si in complementary metal–oxide–semiconductors (CMOS) [114]. Engineering the indium composition in the InGaAs nanolayers may improve the performance of such devices [115]. Therefore, accurate local composition measurement at the nanoscale (or even at the atomic scale) is important for the development of these new technologies.

This chapter introduces a three-beam CBED approach to measure local composition in ternary semiconductors with a zinc blende structure such as  $\text{In}_x\text{Ga}_{1-x}\text{As}$ . The crystal is tilted away from  $[0\ 0\ 1]$  to a three-beam diffraction condition where a Bijvoet pair, reflections  $\bar{1}\ 11\ 1$  and  $1\ \bar{1}1\ \bar{1}$ , are set to their Bragg conditions simultaneously. The two reflections are coupled by the vector  $2, 0, 0$ , and  $V_{2, 0, 0}$  dramatically changes with composition in  $\text{In}_x\text{Ga}_{1-x}\text{As}$ .

According to equation (3.15), the intensity difference between the two reflections,  $I_{\bar{1}\ 11\ 1} - I_{1\ \bar{1}1\ \bar{1}}$ , is proportional to the structure factor magnitude  $|V_{2, 0, 0}|$ . Therefore, the composition can be measured by comparing the intensities of the two Bragg reflections. From the same CBED pattern, the thickness can be measured from the fringes in the  $4\ 0\ 0$  disc and lattice constants can be measured from the deficiency HOLZ lines in the central beam by following the well-established CBED methods of strain measurement [116]. Therefore, composition, thickness and lattice constants can be measured simultaneously from three separate parts of a single CBED pattern that is derived from the same local volume of the specimen.

Bloch wave calculations and some preliminary experiments suggest that the composition can be measured to high accuracy. Furthermore, the current work investigated the influence of strain in a cross-sectional specimen of an  $\text{In}_x\text{Ga}_{1-x}\text{As}/\text{GaAs}$  quantum well (QW) on the composition measurement by means of simulations. With an assumed indium concentration profile, the strain distribution in the QW specimen was first calculated by the finite element

method. The atom positions in the specimen were then extrapolated from the strains and were input to a multislice [43] code [117] for simulations of CBED patterns. The composition measurement from the simulated CBED patterns showed that the strains had weak influence on the composition measurement. Therefore, the current approach may be applicable to map composition in cross-sectional specimens of  $\text{In}_x\text{Ga}_{1-x}\text{As}/\text{GaAs}$  QWs for practical applications.

Section 5.1 will review the existing TEM methods currently available for local composition measurements. Section 5.2 will explain the experimental conditions and the theoretical basis for the current method. Section 5.3 will illustrate the procedures for the composition measurement. Section 5.4 will demonstrate the independence of the measurements of compositions, local thicknesses, and lattice constants. Section 5.5 will examine the effect of strain on composition measurement in cross-sectional specimens of  $\text{In}_x\text{Ga}_{1-x}\text{As}/\text{GaAs}$  QWs.

## **5.1 Compositional characterisation in TEM**

There are several existing techniques for composition measurement using TEM. The three most commonly used techniques are summarised and discussed below.

### **5.1.1 Energy dispersive spectroscopy (EDS)**

EDS is based on counting characteristic X-rays produced by inner-shell excitations. However, the number of X-rays received by an EDS detector also depend on many instrumental and geometrical factors other than composition, which are challenging to quantify. For example, in EDS analysis of  $\text{GaAs}_{1-x}\text{Sb}_x$  nanowires, if the exact crystal orientations relative to the incident beam or to the EDS detector are uncertain, the measured composition can vary by 15% [118].

### **5.1.2 High-angle annular dark-field scanning transmission electron microscopy (HAADF-STEM)**

A HAADF-STEM image is formed by scanning a focused probe over the specimen in a raster and, at each probe position, collecting the electrons scattered to high angles using an annular detector. In an atomic resolution HAADF-STEM image, the contrast depends on the composition, the specimen thickness and the strain, as well as several instrumental parameters, the most significant of which are the spatial coherence function and detector response [119-124]. Compositional measurements from HAADF images therefore require knowledge of these parameters (especially the detector response).

The specimen thickness of an  $\text{In}_x\text{Ga}_{1-x}\text{As}$  layer, where the composition  $x$  is unknown, is typically deduced from measurements of the thickness of adjacent regions of GaAs. This can be done by comparing experimental CBED, PACBED or normalised HAADF image intensities of GaAs with simulations at different thicknesses. In other words, the thickness at an  $\text{In}_x\text{Ga}_{1-x}\text{As}$  layer is not measured locally but is deduced from adjacent regions [125]. In the case of HAADF images, the quantitative measurement of normalised intensities requires knowledge of many instrumental parameters. Alternatively, the thickness can be estimated by taking an electron-energy loss spectroscopy (EELS) spectrum [126] (this will incorporate the thickness of any amorphous surface layers).

Besides, HAADF-STEM intensities are sensitive to strains, which will modify the compositional contrasts in HAADF-STEM image [127].

Other parameters influencing HAADF image contrast, such as detector response, must also be measured and there are well-established techniques for doing this [119-124].

Then, to quantify the composition, the ratio of the intensities from the regions of  $\text{In}_x\text{Ga}_{1-x}\text{As}$  and GaAs,  $I_{\text{In}_x\text{Ga}_{1-x}\text{As}}/I_{\text{GaAs}}$ , is compared with simulated data for different compositions at the evaluated thickness. However, imperfections in the alignment of the crystal orientation (i.e., tilting off the zone axis) can cause an error in the composition measurement.

In summary, HAADF-STEM image contrast depends on many factors and quantification of the composition measurement requires careful and labour intensive measurement of a variety of instrumental parameters [119-124], so that the only free parameter is the composition.

### 5.1.3 Composition evaluation by lattice fringe (CELFA)

This technique makes use of the fact that the structure factor  $V_{2, 0, 0}$  in zinc blende structures is sensitive to its composition and changes linearly with the composition, which can be seen from the calculation of the structure factor:

for pure GaAs, according to equation (2.1),  $V_{2, 0, 0} = 4 f_{\text{Ga}} - 4 f_{\text{As}}$  ( $V_{2, 0, 0} < 0$ );

for  $\text{In}_x\text{Ga}_{1-x}\text{As}$ ,  $V_{2, 0, 0} = 4 x f_{\text{In}} + 4 (1 - x) f_{\text{Ga}} - 4 f_{\text{As}}$ , which changes linearly with the composition  $x$  ( $V_{2, 0, 0} > 0$  when  $x > 0.225$ ).

For the reciprocal vector  $2, 0, 0$ , the scattering angle is low scattering angle and at this scattering angle,  $f_{\text{In}}$ ,  $f_{\text{Ga}}$  and  $f_{\text{As}}$  are significantly different from each other. Thus,  $V_{2, 0, 0}$  is sensitive to composition.

To set up the experimental condition, the crystal is first tilted to an orientation near  $[0\ 0\ 1]$  where reflection  $4\ 0\ 0$  is set to the Bragg condition. The beam is then tilted to place reflection  $2\ 0\ 0$  at the optic axis. Third, the objective aperture is inserted to include reflection  $2\ 0\ 0$  and a series of dark field images are taken with varying defocus of the objective lens. The resulting high resolution TEM images show lattice fringes that run parallel to the  $\text{In}_x\text{Ga}_{1-x}\text{As}/\text{GaAs}$  interface. To quantify the composition, the ratio of the intensity in the  $\text{In}_x\text{Ga}_{1-x}\text{As}$  region to the intensity that is interpolated from the adjacent regions of pure GaAs is compared to simulated data with the corresponding thickness and defocus. Such an intensity ratio is weakly affected by thickness when the value of  $|V_{2,0,0}|$  is small. However, the lens aberration, uncertainties in defocus, uncertainties in specimen thickness and noises can complicate the analysis, which requires more careful treatment [128].

#### **5.1.4 Limitations of existing TEM techniques**

The TEM techniques mentioned above allow measurements of local compositions with high spatial resolution. However, there are some limitations to these techniques:

- 1) EDS and EELS may require using high electron doses, which could damage the specimen before getting any meaningful results.
- 2) The measurement of the specimen thickness in regions with unknown composition are based on deduction from neighbouring regions with known composition, possible thickness fluctuation across the interfaces is ignored. Accurate measurement of local thickness is hard to achieve.
- 3) Instrumental parameters can have significant influences on the images or EDS spectra, making it complicated to decouple the contribution from compositions. The simulations need to consider the instrumental conditions and these may vary for different TEM sessions, requiring measurement with each experiment.

#### **5.1.5. The current method**

The current method uses CBED patterns recorded in a specific three-beam diffraction condition. The local composition, local thickness, and possibly the lattice constants (if the experiment is performed at a low temperature like 100 K) can be measured from three different parts of a single CBED pattern. As will be discussed later, the three parts have distinct sensitivity to composition, thickness and lattice constants, which makes the composition measurements more independent and potentially more accurate than the traditional TEM techniques. In addition, few precisely-measured instrumental parameters are needed.

## 5.2 The diffraction condition and the theoretical basis

### 5.2.1 The diffraction condition

The crystal is tilted  $3.8^\circ$  away from the zone axis  $[0\ 0\ 1]$  along the  $4\ 0\ 0$  Kikuchi lines to a three-beam condition where two reflections of a Bijvoet pair,  $\bar{1}\ 1\ 1$  and  $1\ 1\ 1$ , satisfy their Bragg conditions simultaneously. The two Bragg reflections are coupled by the vector,  $2, 0, 0$ , and  $V_{2, 0, 0}$  is sensitive to composition in  $\text{In}_x\text{Ga}_{1-x}\text{As}$ . The diffraction condition is sketched in Fig. 5.1a and a simulated CBED pattern of GaAs is shown in Fig. 5.1b. The CBED pattern was simulated for GaAs with a specimen thickness of  $1000\ \text{\AA}$  ( $100\ \text{nm}$ ) by using Bloch wave in JEMS [58]. The calculation included more than 1000 beams, the atomic scattering factors with absorptive potential which has accounted for thermal diffuse scattering [129] and core excitation [130] (so-called “WKc” in JEMS), and Debye-Waller factors [131] at 100K.

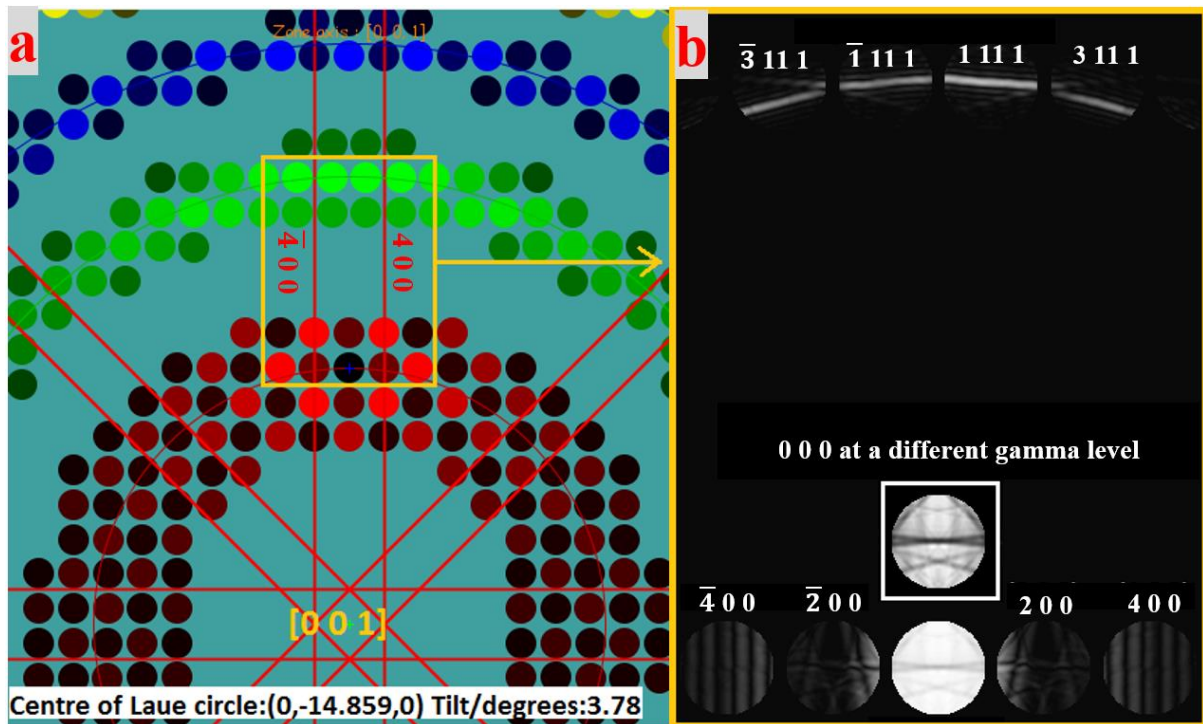


**Figure 5.1. Illustration for the diffraction condition.** (a) The crystal is tilted  $3.78^\circ$  away from the zone axis  $[0\ 0\ 1]$  along the  $4\ 0\ 0$  and  $\bar{4}\ 0\ 0$  Kikuchi lines. At this tilt angle, the centre of the Laue circle (CLC) is placed at  $(0, -14.859, 0)$ . The yellow rectangle labels the region where the CBED pattern of interest is from. An example of the CBED pattern is shown in (b): the intensity in reflections  $\bar{1}\ 1\ 1$  and  $1\ 1\ 1$  are significantly different. The central beam captured

in the box is displayed at a different contrast level to optimise the view of the deficiency HOLZ lines.

## 5.2.2 The theoretical basis for the current method

### 5.2.2.1 A qualitative perspective

The intensity distribution near the three-beam condition for  $0\ 0\ 0 / \bar{1}\ 11\ 1 / 1\ 11\ 1$ , can be qualitatively explained by the theory of three-beam dynamic diffraction. According to equation (3.15),

$$I_{1\ 11\ 1}(\zeta_g, \zeta_h, z) - I_{\bar{1}\ 11\ 1}(\zeta_g, \zeta_h, z) = 16\sigma^3 |V_{1\ 11\ 1}| |V_{\bar{1}\ 11\ 1}| |V_{2\ 0\ 0}| \sin\phi \prod_{i=1}^3 \frac{\sin\left(\frac{\mu_i z}{2}\right)}{\mu_i}, \quad (5.1)$$

where  $\zeta_g, \zeta_h$  are the excitation errors, which refer to a spot inside the CBED discs.  $z$  is the specimen thickness,  $\sigma$  is the interaction constant, and  $\mu_i$  is the difference between two eigenvalues of three-beam diffraction (where there are three eigenvalues in total).  $\phi = \varphi_{1\ 11\ 1} - \varphi_{\bar{1}\ 11\ 1} - \varphi_{2\ 0\ 0}$ , is the three-phase invariant, and

for  $\text{In}_x\text{Ga}_{1-x}\text{As}$  where  $x < 0.225$ ,  $\varphi_{1\ 11\ 1} \approx -45^\circ$ ,  $\varphi_{\bar{1}\ 11\ 1} \approx 45^\circ$  and  $\varphi_{2\ 0\ 0} = 180^\circ$ , we have  $\phi \approx +90^\circ$ ;

for  $\text{In}_x\text{Ga}_{1-x}\text{As}$  where  $x > 0.225$ ,  $\varphi_{1\ 11\ 1} \approx -45^\circ$ ,  $\varphi_{\bar{1}\ 11\ 1} \approx 45^\circ$  and  $\varphi_{2\ 0\ 0} = 0^\circ$ , we have  $\phi \approx -90^\circ$ .

As discussed in criterion (3.14), if the thickness is not too large (smaller than the three-beam extinction distance), the intensity difference between the Bijvoet pair can be observed such that:

for  $x < 0.225$ ,  $I_{1\ 11\ 1}(\zeta_g = 0, \zeta_h = 0, z) > I_{\bar{1}\ 11\ 1}(\zeta_g = 0, \zeta_h = 0, z)$  (as shown in Fig.5.1 b);

for  $x > 0.225$ ,  $I_{1\ 11\ 1}(\zeta_g = 0, \zeta_h = 0, z) < I_{\bar{1}\ 11\ 1}(\zeta_g = 0, \zeta_h = 0, z)$ .

From equation (5.1), the contrast between the Bijvoet pair reflections is proportional to  $|V_{2\ 0\ 0}| \sin\phi$ , and  $|V_{2\ 0\ 0}| \sin\phi$  is proportional to the composition in  $\text{In}_x\text{Ga}_{1-x}\text{As}$  as  $V_{2\ 0\ 0}$  is proportional to composition (since  $\sin\phi \approx 1$  when  $V_{2\ 0\ 0} < 0$  and  $\sin\phi \approx -1$  when

$V_{2, 0, 0} > 0$  ). Furthermore,  $|V_{1, 11, 1}|$  and  $|V_{\bar{1}, 11, 1}|$  are insensitive to composition. For example, when the  $x$  increases from 0.00 to 0.10,  $|V_{2, 0, 0}|$  decreases from 0.568 V to 0.348 V while  $|V_{1, 11, 1}|$  decreases from 0.492 V to 0.490 V.

Therefore, the intensity difference between reflections  $\bar{1} 11 1$  and  $1 11 1$  is proportional and sensitive to the composition in  $\text{In}_x\text{Ga}_{1-x}\text{As}$ .

#### 5.2.2.2 A quantitative perspective

To quantify compositions, a ratio of two integrated intensities inside discs of reflection  $\bar{1} 11 1$  and  $1 11 1$  can be used. The integrated intensities are defined as follows: two squares with a size of  $2 \times 2$  mrad are placed inside the discs of  $\bar{1} 11 1$  and  $1 11 1$ , centred at the three-beam condition (shown in Fig. 5.2a); then, the intensities within the squares are summed to give the integrated intensities. It is the ratio of these two integrated intensities that is considered for measuring the composition.

It should be noted that the squares are placed relative to the three-beam condition in each disc rather than the centre of the disc (although these two happen to be in the same place in Fig. 5.2a). Therefore, whether the three-beam condition is centred in the disc does not matter the ratio. In other words, the crystal does not need to be perfectly aligned to a specific orientation (as long as the three-beam condition is within each disc) to carry out this composition measurement.

In order to assess the applicability of using the ratio for composition measurement in real situations, calculations of the intensity ratio at different compositions and thicknesses have been performed by using the Bloch wave method in JEMS [58]. The simulation has included more than 1000 reflections (to ensure the convergence of the Bloch wave calculations), atomic scattering factors with absorptive potential (so-called “WKc”) which has accounted for thermal diffuse scattering [129] and core excitation [130], and Debye-Waller factors that are deduced from generalized phonon densities of states which are derived from first principles [131] at 294 K.

The ratio-thickness curves have been calculated for several ranges of compositions (with a step size of  $\Delta x = 0.05$  or  $0.02$ ):  $0 < x < 0.25$  (Fig. 5.2b),  $0.50 < x < 0.60$  (Fig. 5.2c) and  $0.64 < x < 0.74$  (Fig. 5.2d). These ranges of compositions correspond to different ranges of  $V_{2, 0, 0}$

(only its real part): from - 0.57 V to 0.07 V, from 0.49 V to 0.67 V, and from 0.74 V to 0.93 V. In summary, these calculations have covered a range of  $|V_{2, 0, 0}|$  from 0 V to 0.93 V.

Note: for the range  $0.25 < x < 0.50$  (which is not plotted here),  $V_{2, 0, 0}$  varies from 0.07 V to 0.49 V, and one does not need to plot the ratio-thickness curves to just see the trend of the ratio, which can be explained as follows:

For both of the ranges,  $0.25 < x < 0.50$  (not plotted) and  $0.05 < x < 0.25$  (plotted in Fig 5.2b),  $|V_{2, 0, 0}|$  ranges from 0.07 V to  $\sim 0.5$  V. If the values of  $|V_{2, 0, 0}|$  and  $|V_{1, 11, 1}|$  are approximately equal, according to equation (5.1), the intensity differences,  $I_{1, 11, 1} - I_{\bar{1}, 11, 1}$ , will have approximately the same magnitudes but the opposite signs (as the signs of  $\sin\phi$  are opposite). Therefore, trend of the ratios with thickness for  $0.25 < x < 0.50$  can be obtained from the reciprocal of the ratios for  $0.05 < x < 0.25$  (Fig. 5.2b).

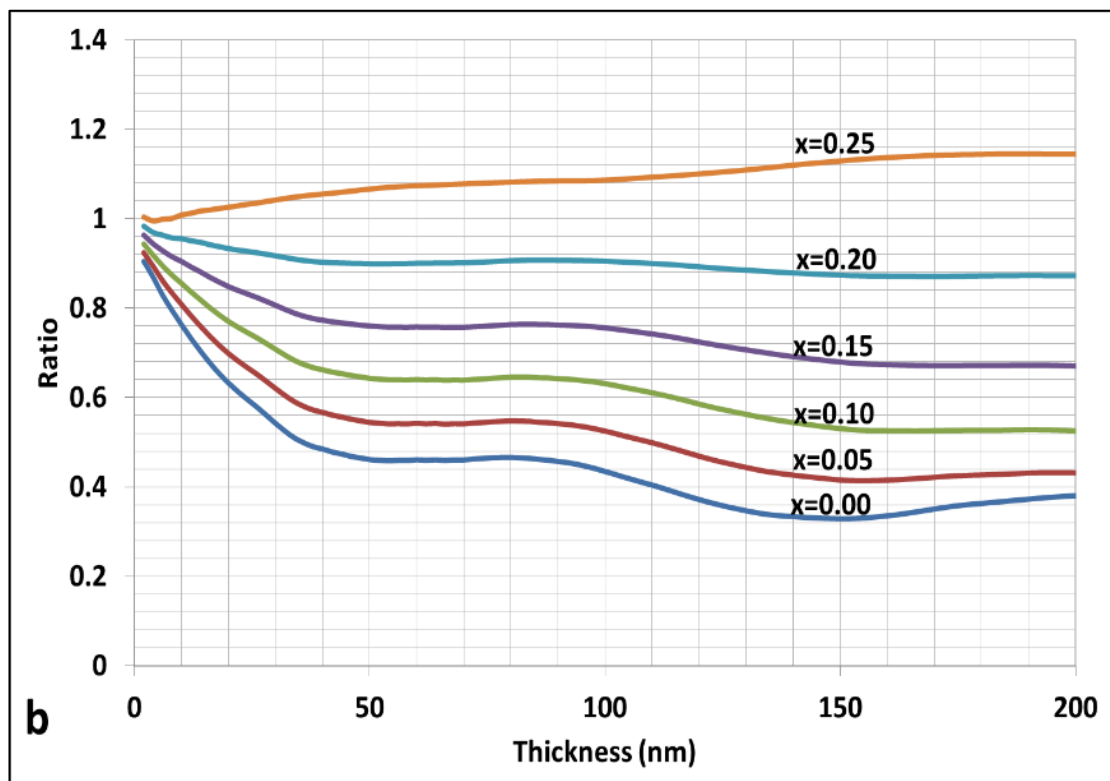
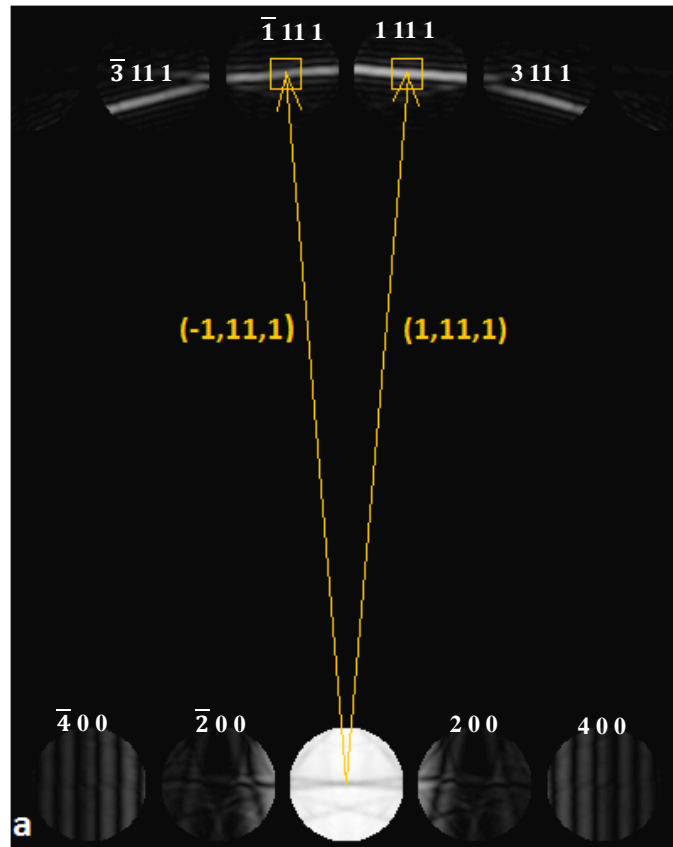
According to the plots for the ranges of indium concentration levels,  $x < 0.25$  (Fig. 5.2b),  $0.5 < x < 0.6$  (Fig. 5.2c) and  $0.64 < x < 0.74$  (Fig. 5.2d), the ratio increases monotonically with composition for a wide range of thicknesses: from 0 to at least 200 nm (calculations above 200 nm were not undertaken), from 0 to 130 nm, and from 0 to 80 nm, respectively. Therefore, the ratio may be used for measuring the indium content for a wide range of specimen thicknesses until a high indium concentration level ( $x = \sim 0.8$ ) is encountered.

The thickness can be determined from the intensity oscillations (or “fringes”) in disc  $4\ 0\ 0$  or  $\bar{4}\ 0\ 0$  (in Fig 5.2a). Unlike  $V_{2, 0, 0}$ ,  $V_{4, 0, 0}$  is fairly insensitive to composition. For example, as  $x$  increases from 0.00 to 0.10,  $|V_{4, 0, 0}|$  increases from 4.35 V to 4.40 V, which has an increment of 0.05 V or 1.1 %. By contrast,  $|V_{2, 0, 0}|$  decreases from 0.568 V to 0.348 V, which has an increment of -0.22 V or -38.7%. However, the fringes in the  $4\ 0\ 0$  disc are very sensitive to thickness because the  $4\ 0\ 0$  reflection has a short extinction distance and is far from its Bragg condition. The sensitivity to thickness and insensitivity to composition of the  $4\ 0\ 0$  reflections is powerful, enabling thickness to be measured from the CBED pattern, largely independent of the specimen composition.

Furthermore, the lattice constants can be measured from the deficiency HOLZ lines in the central disc if the temperature is sufficiently low (e.g. at  $\sim 100$  K, such as in Fig. 5.1) so that the deficiency HOLZ lines are not blurred by thermally-induced atomic vibrations. At room temperature, as both experiments and simulations (at 294 K) suggest, most of the deficiency



HOLZ lines become invisible even at a large thickness (e.g.  $\sim 200$  nm) due to the significant vibration of the atoms, which makes it extremely difficult to use the HOLZ pattern in the current diffraction condition for lattice parameter measurement at room temperature.



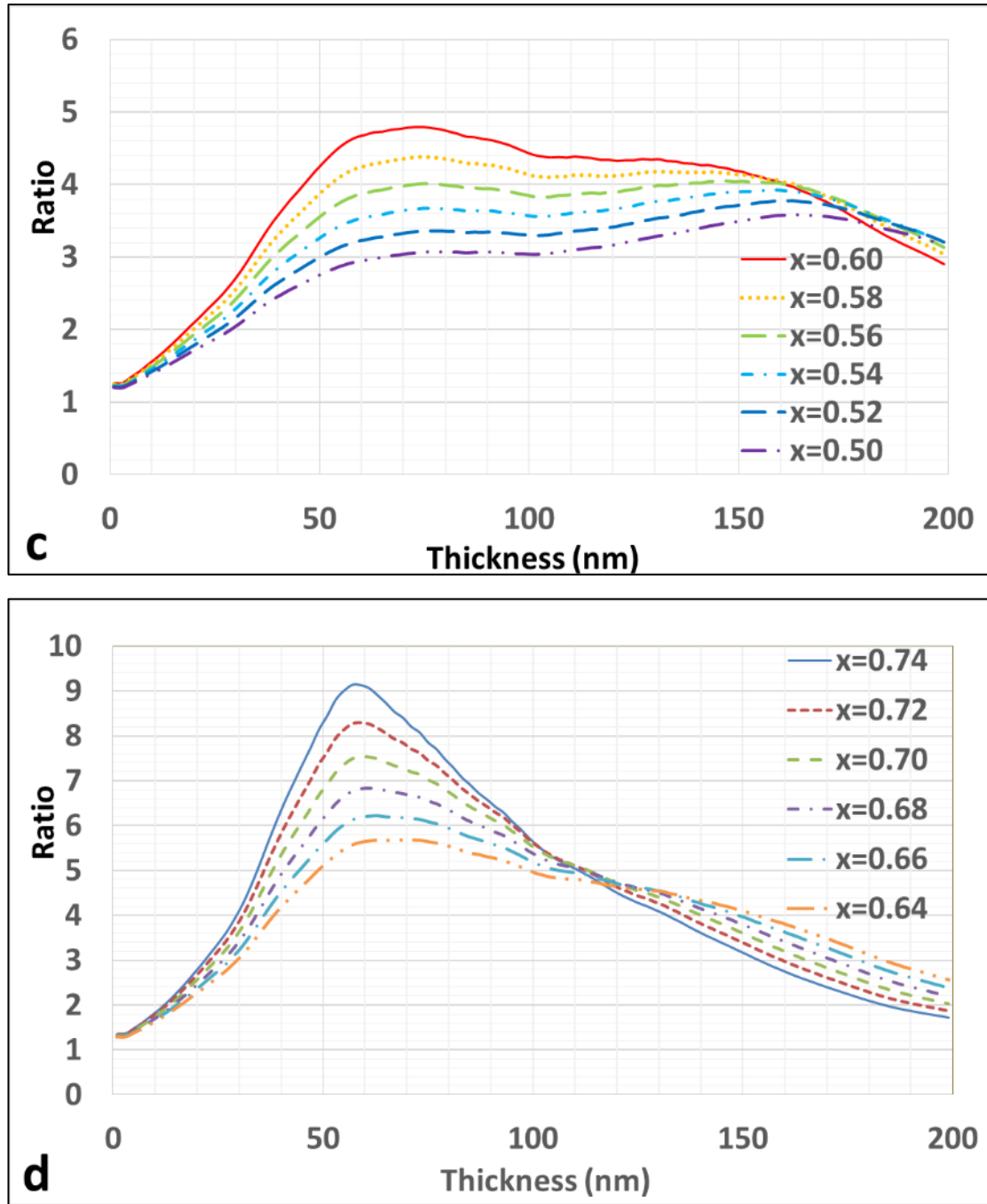


**Figure 5.2.** The intensity ratio for the composition measurement is defined in (a) and calculated for different compositions (b-d) as a function of thickness. (a) A pair of 2 x 2 mrad squares (in orange) defines the regions from which the two integrated intensities are acquired. The squares are centred at the three-beam condition in the  $\bar{1} 11 1$  and  $1 11 1$  discs, which are conjugated to the three-beam condition in the  $0 0 0$  disc by the reciprocal vectors,  $\bar{1}, 11, 1$  and  $1, 11, 1$ , respectively. The ratios of the integrated intensities versus the thickness at 200 kV are calculated for different composition ranges: (b)  $x = 0.00$ -0.25, (c)  $x = 0.50$ -0.60,

and (d)  $x = 0.64-0.74$ . JEMS [58] has been used for producing the CBED pattern in (a) and the calculations in (b-d).

## 5.3 Experimental demonstration of the composition measurement

As discussed in the last section, the composition can be determined from two quantities that can be measured independently from the same CBED pattern: 1) the ratio of the two integrated intensities and 2) the specimen thickness. This section will demonstrate how these values can be measured from an experimental CBED pattern.

### 5.3.1 Measurement of the intensity ratio

**Step 1.** Locate the coordinates of the three-beam condition inside each disc of the Bijvoet pair:

In thick specimens, the intersection of the deficiency Bragg lines of reflections  $\bar{1} 11 1$  and  $1 11 1$  in the central disc is sharp and is easy to locate, and the three-beam conditions in discs  $\bar{1} 11 1$  and  $1 11 1$  are connected to this intersection by the reciprocal vectors  $\bar{1}, 11, 1$  or  $1, 11, 1$  as shown in Fig. 5.2a. Therefore, it is straightforward to locate the coordinates of the three-beam condition in the Bijvoet pair in the case of thick specimens.

In thin specimens where the same intersection is broadened, the following procedure allows accurate location of the three-beam condition (the procedures also work for thick specimens):

- 1) Once the CBED pattern is recorded, the pattern is rotated so that the  $4, 0, 0$  vector lies in the horizontal direction. A line profile with an integration width of about the diameter of a CBED disc is drawn in the horizontal direction (shown in Fig. 5.3a). From this line profile (Fig. 5.3b), edges of the Kikuchi band formed by  $4 0 0$  and  $\bar{4} 0 0$  can be located. A small amount of disc overlap is allowed.
- 2) The coordinates of the three-beam condition must be identified along both the horizontal (x) and the vertical (y) axes. Location of the x-coordinates is guided by the Kikuchi band formed by  $4 0 0$  and  $\bar{4} 0 0$ . The x-coordinates of the three-beam condition in two reflections are inside the Kikuchi band and away from the two edges of the band by a distance that is equal to  $1/4$  of the width of the band (shown in Fig. 5.3c).
- 3) Once the x-coordinates of the two three-beam conditions have been determined, two line profiles with an integration width of 2 mrad are drawn in the vertical direction (shown in Fig. 5.3d). One of the line profiles is shown in Fig. 5.3e. The y-coordinate is

just at the peak of the line profile (shown in Fig. 5.3f). This is because when  $\cos\phi \approx 0$ , the intensity distribution around the three-beam condition has a centre of inversion at the three-beam condition according to the theory given in equation (3.22).

**Step 2.** Subtract the background and acquire the integrated intensities:

In the line profile shown in Fig. 5.3f, the diffuse background intensities need to be subtracted from the peak for quantitative comparisons to simulations. It is assumed that the background intensity distribution across each reflection (and parallel to the Kikuchi lines) changes linearly. Such an approximation has been made in a previous work of quantitative CBED [132].

To subtract the linear background intensities from integrated peak intensity (shown in the red rectangle in Fig. 5.3f), an easy approach is to subtract the average of two integrated background intensities (in the green and blue rectangles in Fig. 5.3f) on each side of the three-beam condition. Then, the ratio of two integrated peak intensities with linear background subtracted is obtained and ready for comparison with simulations.

A preliminary code for the above procedures has been written here using the DigitalMicrograph scripting language.

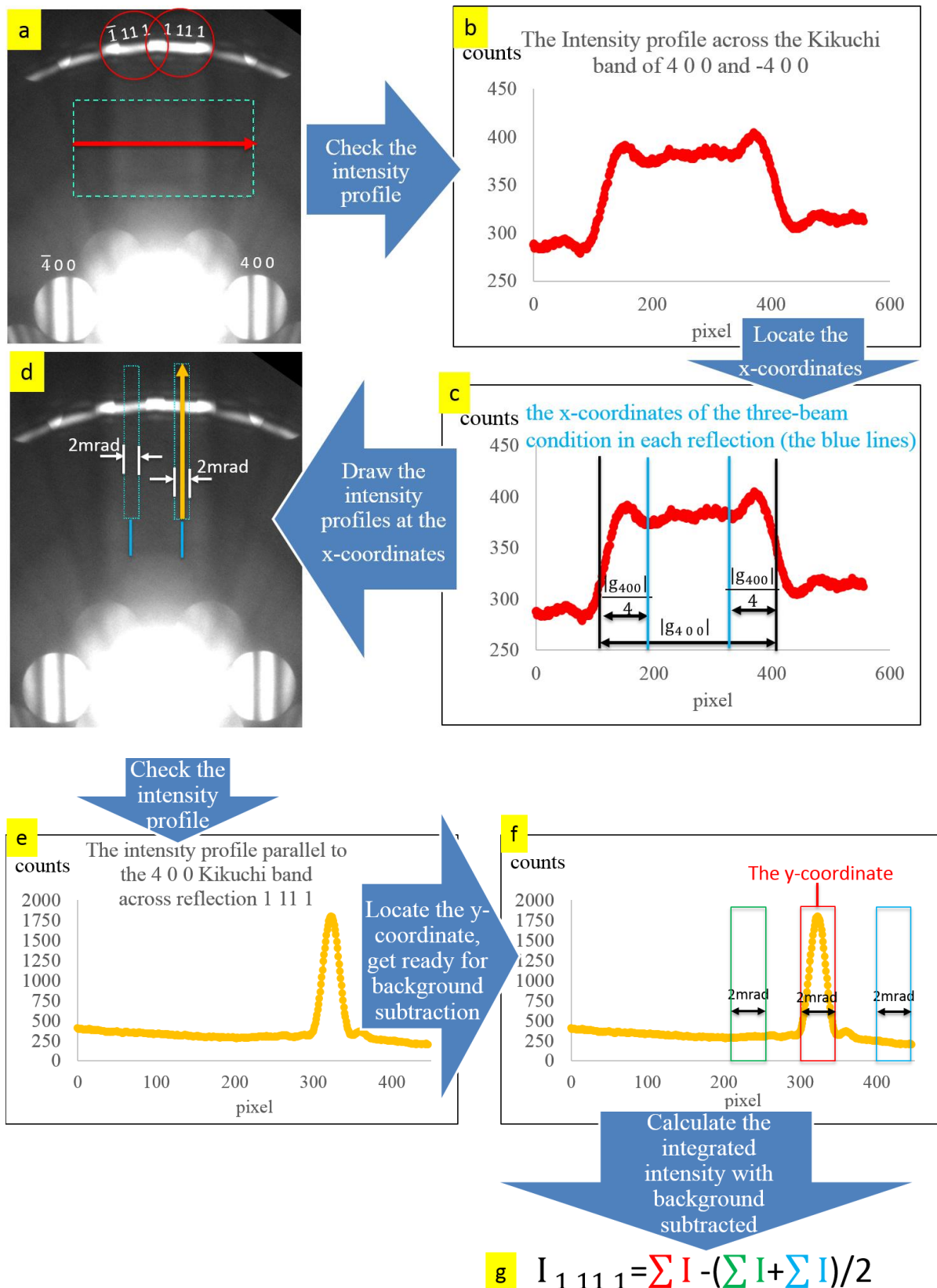


**Figure 5.3. Illustration of locating the three-beam condition inside each reflection of the Bijvoet pair and subtracting the linear background from the integrated peak intensities.**

The CBED pattern of GaAs in (a) was taken from FEI Tecnai G<sup>2</sup> T20 TEM at 200 kV at room

temperature. No energy-filtering device was installed on this TEM. The CBED pattern was recorded on Orius SCD200D wide-angle CCD camera with an exposure time of 0.6 s and is not energy-filtered.

### 5.3.2 Thickness measurement and composition determination

To measure the thickness from the 4 0 0 disc, a simulated CBED pattern of GaAs (or  $\text{In}_x\text{Ga}_{1-x}\text{As}$  with the nominal composition and lattice constants) is needed for a comparison with the experimental pattern. Two parameters are needed from the experimental pattern to set up the simulation:

- 1) the x-coordinate of the three-beam condition in the central disc, which is the average of the two x-coordinates in the Bijvoet pair reflections (the y-coordinate is not critical as the fringes are parallel to the y-axis).
- 2) The convergence angle.

The thickness can be determined within 1 nm just by a visual comparison between the experimental pattern and simulated patterns at different thicknesses. A thickness measurement with higher accuracy is not necessary for a wide range of thicknesses where the ratio-thickness curves (in Figs 5.2b-d) are separated far apart.

Once the ratio and the thickness are determined, they can be found on a ratio-thickness curve which has been calculated for a certain composition. The corresponding composition is the measured value of the composition (show in Fig. 5.4).

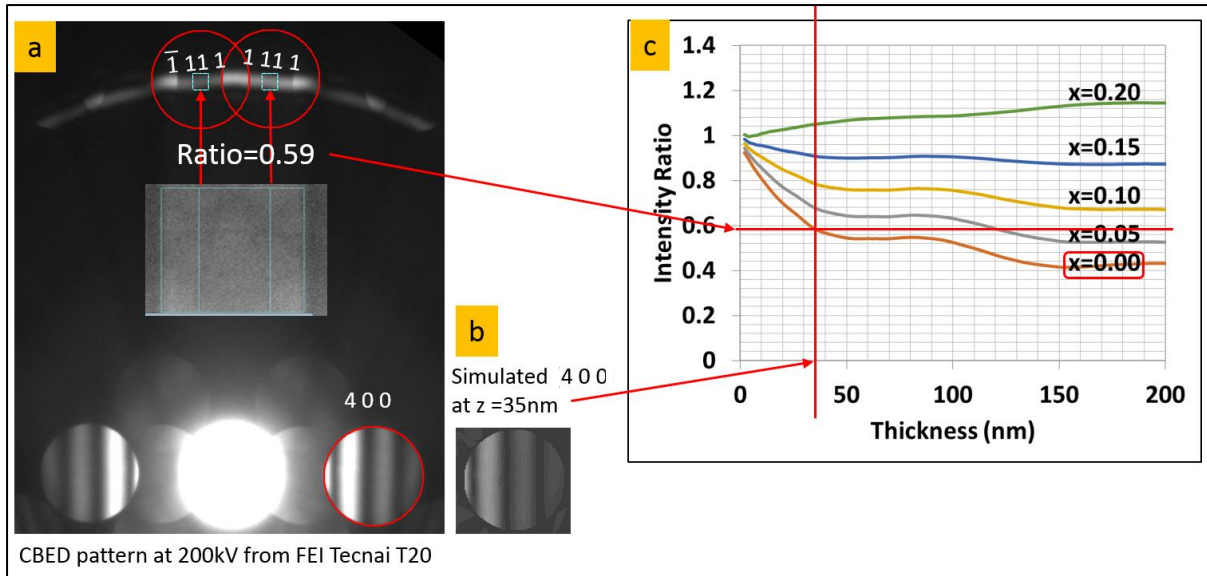


**Figure 5.4. Illustration of composition measurement from an experimental CBED pattern:** (a) the ratio of the two integrated intensities is acquired by following the procedures described in Section 5.3.1, and the thickness is measured by comparing the fringes in 4 0 0 with (b) simulations. Then, the measured values of the ratio = 0.59 and the thickness = 35 nm can be found on a ratio-thickness curve in (c), which has been calculated for a composition of  $x = 0.00$ . This means composition in the structure which the CBED pattern in (a) is obtained from is  $x = 0.00$  (i.e. pure GaAs).

### 5.3.3 Quantitative calculations of the look-up tables

It should be noted that in producing the look-up table for composition determination, the effect of the chemical bonds and static atomic displacements<sup>12</sup> on the value of  $V_{2,0,0}$  must be included because isolated atom model (IAM) (e.g. [129]) for the atomic scattering factors (which has been used in producing the calculations in Figs. 5.2b-d) can underestimate the value of  $V_{2,0,0}$  [133]. Here, we label the  $V_{2,0,0}$  from independent atom model as  $V_{2,0,0}^{\text{IAM}}$  and the  $V_{2,0,0}$  from the more accurate model, which has included the effects of chemical bonds and static atomic displacements, as  $V_{2,0,0}^{\text{B}}$ . From the calculations in [133], one can derive a relation between  $V_{2,0,0}^{\text{IAM}}$  and  $V_{2,0,0}^{\text{B}}$ , such that

<sup>12</sup> Static atomic displacements: the atoms (ions) in an alloy like  $\text{In}_x\text{Ga}_{1-x}\text{As}$  are actually displaced from their average crystalline sites due to their distinct atomic or covalent radii.

$$V_{2, 0, 0}^{\text{IAM}}(x - 0.05) \approx V_{2, 0, 0}^{\text{B}}(x) ,$$

where both  $V_{2, 0, 0}^{\text{IAM}}(x)$  and  $V_{2, 0, 0}^{\text{B}}(x)$  show approximately linear relationships with the composition,  $x$ . Therefore, if the look-up table for composition determination is calculated based on  $V_{2, 0, 0}^{\text{IAM}}(x)$  rather than  $V_{2, 0, 0}^{\text{B}}(x)$ , the composition can be overestimated by an systematic error of about +0.05.

Since other structure factors which also play significant roles in the dynamic diffraction in this nominal three-beam diffraction condition are associated with high scattering angles and are only weakly influenced by the chemical bonds (e.g.  $V_{1, 11, 1}^{\text{IAM}}(x) \approx V_{1, 11, 1}^{\text{B}}(x)$ ). Furthermore, they are insensitive to composition in  $\text{In}_x\text{Ga}_{1-x}\text{As}$  (e.g.  $V_{4, 0, 0}$  is not sensitive to composition). Therefore, to a good approximation (and to enable a time-efficient initial assessment of the potential of this approach), the look-up tables in Fig 5.2b-d which are based on  $V_{2, 0, 0}^{\text{IAM}}(x)$  can still be used after a calibration of the compositions by subtracting 0.05 from each labelled composition. In this way, the compositions in Fig 5.2b has been calibrated, which gives the look-up table in Fig. 5.4c (preliminary experiments on GaAs show that such an approximate calibration works well at least for  $x = 0$ ). To produce more accurate look-up tables, one should take the values of  $V_{2, 0, 0}$  from the first-principle calculations [133] for different compositions and the values of other structure factors from isolated atom model [129] for the corresponding compositions.

Once the look-up table has been made for a certain accelerating voltage (usually 200 kV or 300 kV), it can be re-used for different TEM sessions as long as the corresponding accelerating voltage is used.

## 5.4. Testing the independence of the measurements

The measurement of composition is not only feasible but potentially accurate as well because the three parts in the CBED patterns have very distinct sensitivities to composition, thickness and lattice constants. This section will study the influences of the uncertainties in the measurements of thickness and lattice constants on the composition measurements.



#### 5.4.1. The influence of the uncertainties in composition and lattice constants on the thickness measurement

In the thickness measurement, the simulated 4 0 0 disc for GaAs or  $\text{In}_x\text{Ga}_{1-x}\text{As}$  with the nominal composition is compared with the experimental pattern. The uncertainties in composition and lattice constants may influence the measurement of the thickness.

To study how significant these uncertainties are on thickness measurement, two crystal structures with distinct compositions and lattice constants have been input to CBED simulations using the Bloch wave method in JEMS [58]. The simulation included more than 1000 reflections, and treated inelastic scattering by the absorptive potential which has accounted for thermal diffuse scattering [129] and core excitation [130]. The Debye-Waller factors at 294 K [131] were used.

The normalised intensity (relative to the intensity of the incident beam) at the three-beam condition point inside the 4 0 0 disc oscillates rapidly with varying thickness, which is shown in Fig. 5.5. An increment of indium concentration by 20 and 25%, with respect to an increment of lattice constants by 1.4 and 1.8%, has only led to a shift of the pendollosung along the thickness axis by less than 2 nm when the thickness is close to 100 nm. Thus, the uncertainties in thickness measurement caused by uncertainties in composition and lattice constants are usually less than 2 nm (and less than 1 nm if the thickness is 60 nm or below). This level of uncertainties in the thickness has negligible effect on the composition measurement for low and medium indium content levels (which can be seen from Fig. 5.2 b, c) and is sufficient for resolving a compositional difference of  $\Delta x = 0.02$  at high indium concentration levels (which can be seen from Fig. 5.2 d). Therefore, the uncertainties in the thickness measurement have a very small influence on the result of the composition measurement.

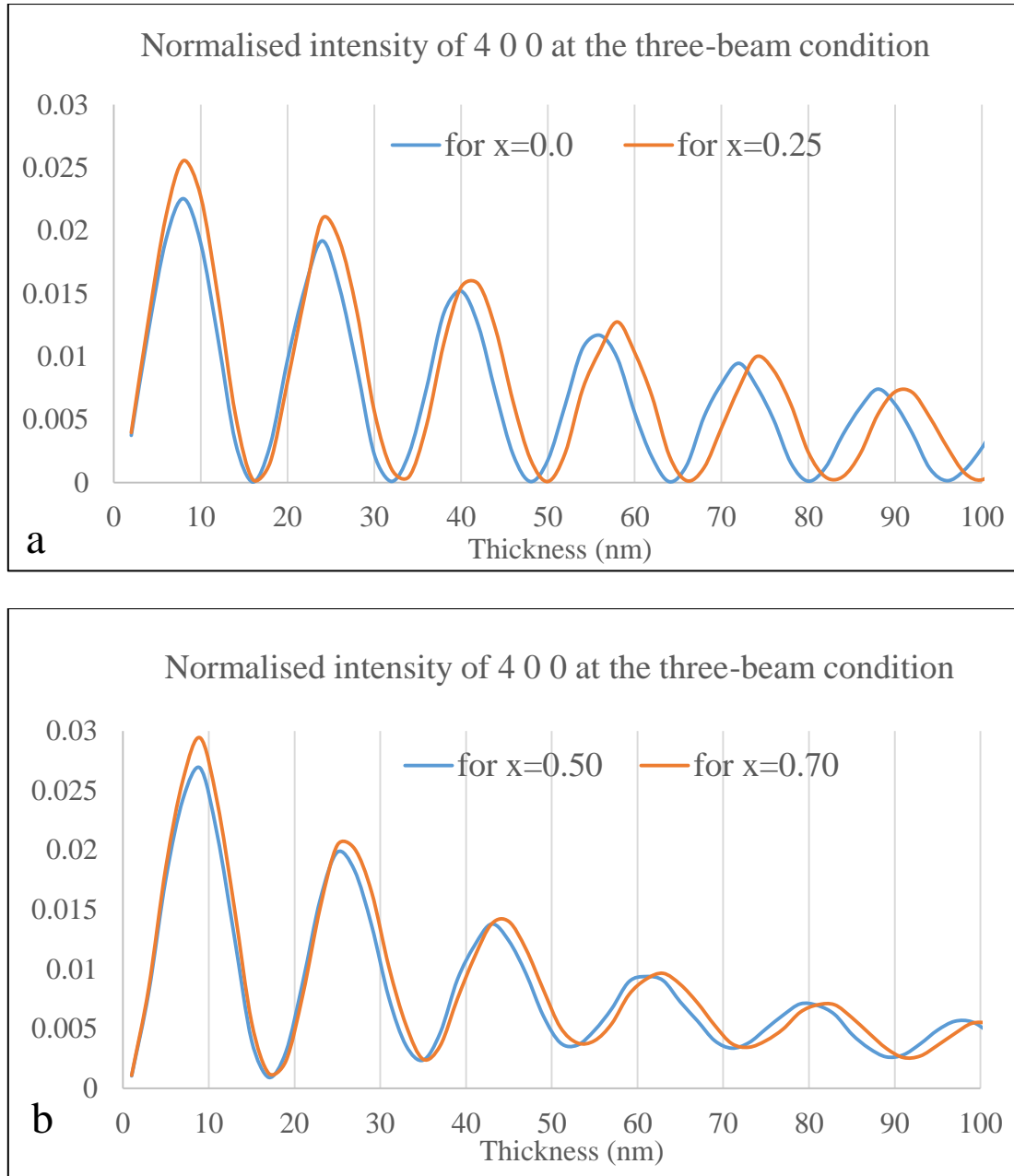


**Figure 5.5. The influence of the uncertainties in compositions and lattice constants on the thickness measurements.** The thickness dependence of the normalised intensities (relative to the intensity of the incident beam) at the three-beam condition inside the 4 0 0 disc are plotted for four different compositions: (a)  $x = 0.0$  and  $x = 0.25$ ; (b)  $x = 0.50$  and  $x = 0.70$ . The lattice constants for different compositions are derived from Vegard's law.

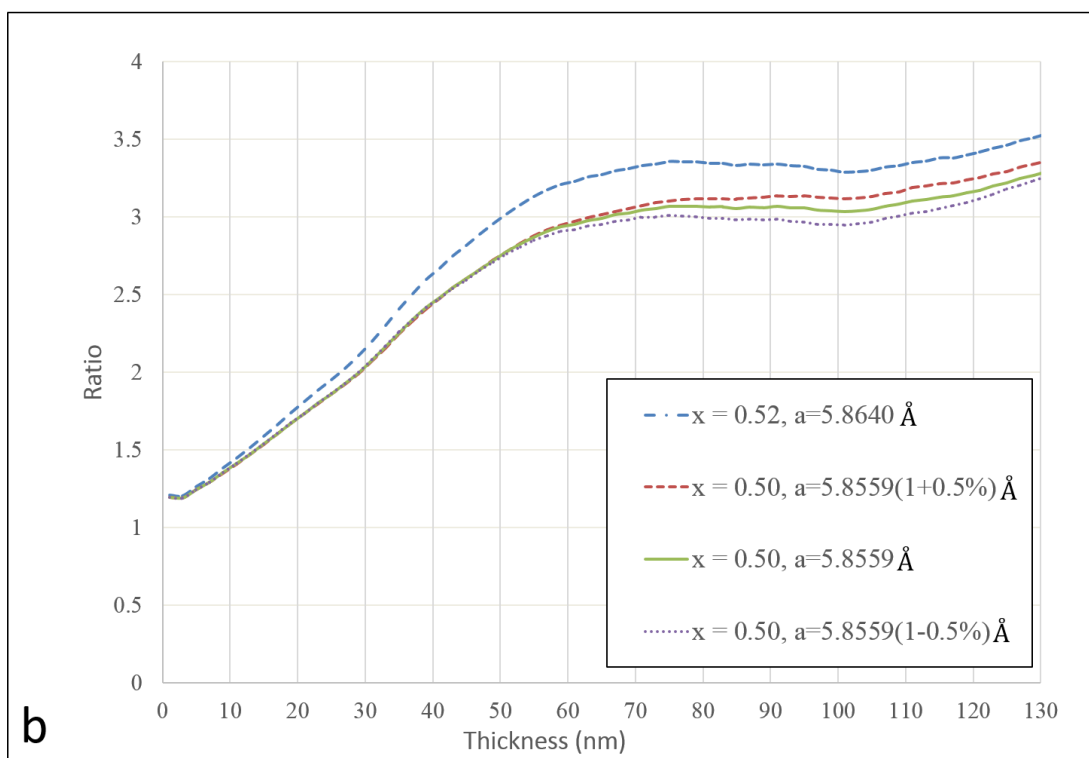
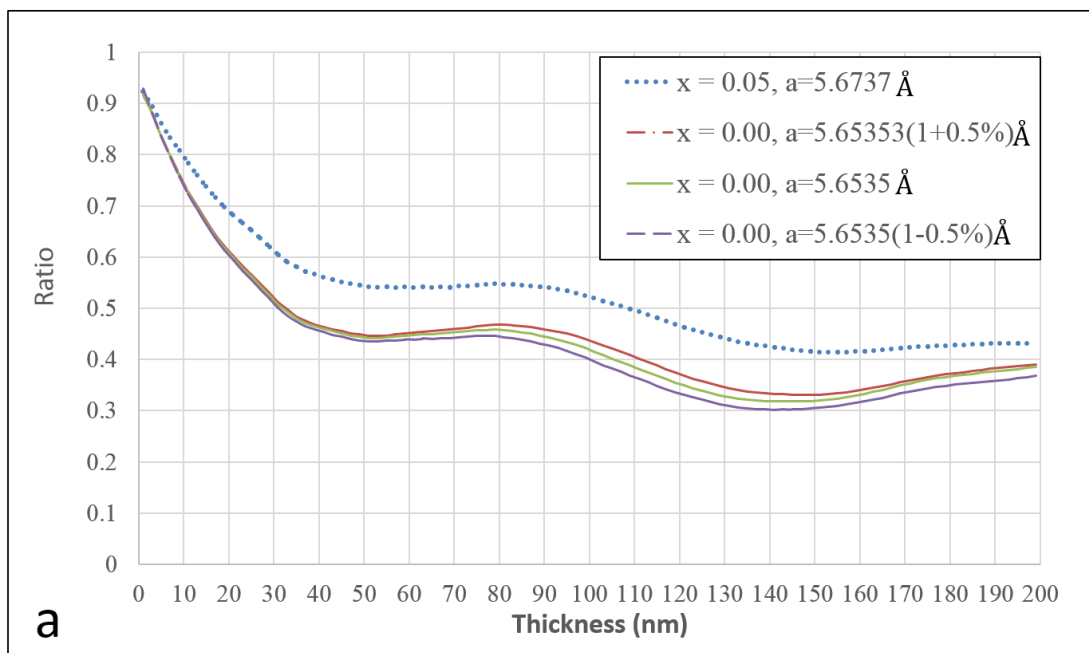
#### 5.4.2. The influence of the uncertainties in lattice constants on the composition measurement

To calculate the lattice constants of  $\text{In}_x\text{Ga}_{1-x}\text{As}$ , Vegard's law is commonly applied:

$$a_{\text{In}_x\text{Ga}_{1-x}\text{As}} = x a_{\text{InAs}} + (1 - x) a_{\text{GaAs}} .$$

This is an approximation. The deviation of lattice constants from Vegard's law in  $\text{In}_x\text{Ga}_{1-x}\text{As}$  has been reported in [134], where a deviation of about 6% towards a higher indium concentration has been found in the  $\text{InGaAs}$  layers that are lattice matched with  $\text{InP}$ . The deviation of lattice constants from Vegard's law at other indium concentration levels have not been studied. Therefore, the uncertainties in lattice constants may result in uncertainties in the simulations in the look-up table of the intensity ratio-thickness curves, which may further influence the composition measurements.

To study the influence of the lattice constants, some of the ratio-thickness curves in Fig 5.2 are re-calculated with modified lattice constants which are  $(1 \pm 0.5\%)$  times the lattice constants derived from Vegard's law. The results (in Fig 5.6) show that when lattice constants of the cubic unit cell are changed by  $\pm 0.5\%$ , the ratio is almost unchanged up to a thickness of 60 nm for all indium concentration levels (Fig. 5.6 a-c) and is only slightly changed at a higher thickness for high indium concentration levels (Fig. 5.6c). Therefore, the composition measurement is robust with respect to uncertainties in lattice parameters, so Vegard's law can be assumed in producing the look-up table for the composition measurements.



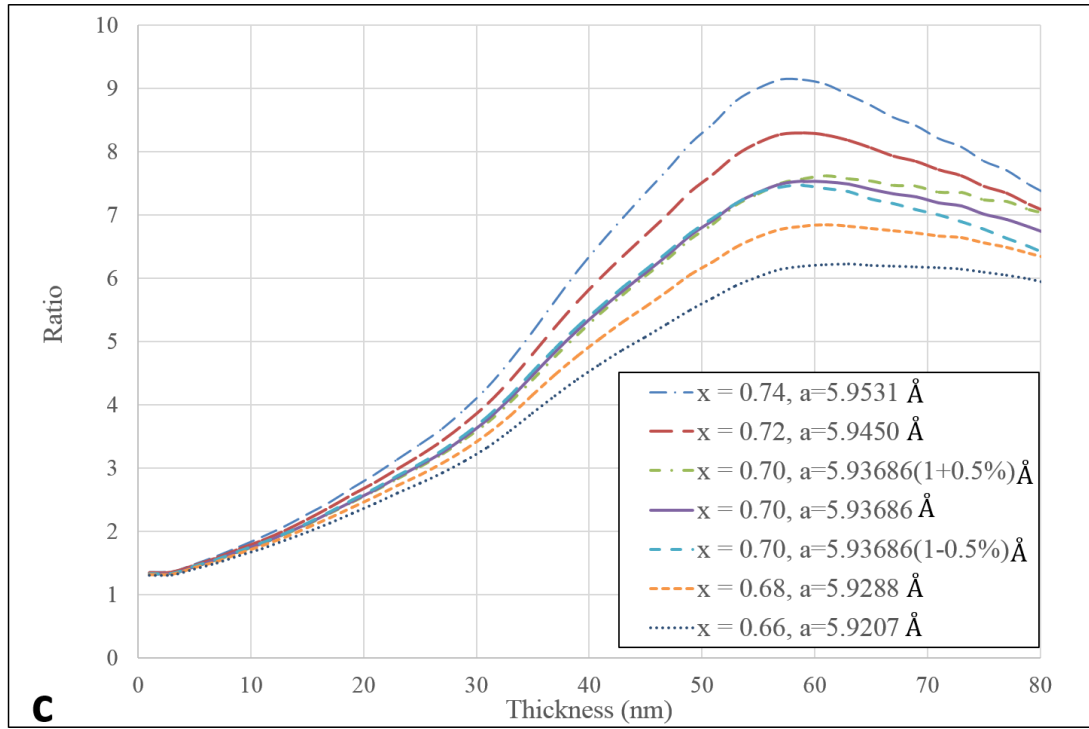


**Figure 5.6. The influence of the uncertainties in lattice constants on the composition measurement.** The ratio-thickness curves are plotted for bulk  $\text{In}_x\text{Ga}_{1-x}\text{As}$  (which has a cubic unit cell) with modified lattice constants. The lattice constants for three compositions, (a)  $x = 0.0$ , (b)  $x = 0.50$ , (c)  $x = 0.70$ , are changed by  $\pm 0.5\%$  relative to the lattice constants derived from the Vegard's law. The ratio-thickness curves for neighbouring compositions ( $+5\%$  In in (a),  $+2\%$  In in (b), and  $\pm 2\%$  In in (c)) are also plotted for reference. The plots show the influence of uncertainties in lattice constants on the composition measurement at different composition levels. The most significant influence is found in (c) at thicknesses higher than 60 nm, where the uncertainties in lattice constants by  $\pm 0.5\%$  may result in an uncertainty of  $\Delta x = 0.02$  in composition determination.

#### 5.4.3. The influence of the uncertainties in composition on the measurement of lattice constants

The lattice parameters can be measured from the positions of the deficiency HOLZ lines in the central beam by following the well-established procedures in [65, 116, 135, 136, 137, 138]. In order to study the feasibility of using the HOLZ pattern in the current orientation to measure the lattice constants, a simulation based on Bloch wave in JEMS [58] was carried out for an accelerating voltage of 200 kV. The CBED simulation included more than 300 reflections, and inelastic scattering was accounted for by absorptive potential from [129] and Debye-Waller

factors at 100 K from [131]. To include larger view of the HOLZ pattern in the central disc, a semi-convergence angle of 7 mrad was used. The results are shown in Fig. 5.7.

Although the diffraction condition in the current method may not be optimal for setting up a HOLZ pattern for the measurement of the lattice constants, there are still several deficiency HOLZ lines visible at 100 K and they are sensitive to the lattice constants. For example, the  $19\ 3\ 1$  and  $\overline{19}\ 3\ 1$  deficiency HOLZ lines intersect with several other deficiency HOLZ lines such as  $14\ \overline{10}\ 0$  and  $9\ 9\ 1$ , and the positions of these intersections are quite sensitive to lattice parameters.

Comparisons between Fig. 5.7a and Fig. 5.7b, and between Fig. 5.7a and Fig. 5.7d, can reveal that the positions of the deficiency HOLZ lines in this orientation are sensitive to lattice parameters but insensitive to compositions. Fig. 5.7c shows the HOLZ pattern for a GaAs structure that is distorted into a tetragonal structure, which is significantly different from the HOLZ pattern in Fig. 5.7a. This suggests that the lattice constants for a tetragonal unit cell (which can be found in a plan-view specimen of  $\text{In}_x\text{Ga}_{1-x}\text{As}/\text{GaAs}$  quantum wells) should also be measurable from the HOLZ patterns in the current orientation.

By contrast, when the Debye-Waller factors at 294 K were included in the Bloch wave calculation, the strain sensitive HOLZ lines like  $19\ 3\ 1$  become non-distinguishable from the rest of the bright field pattern. This suggests the necessity of doing experiment with a cooling stage if the deficiency HOLZ lines are of interest.

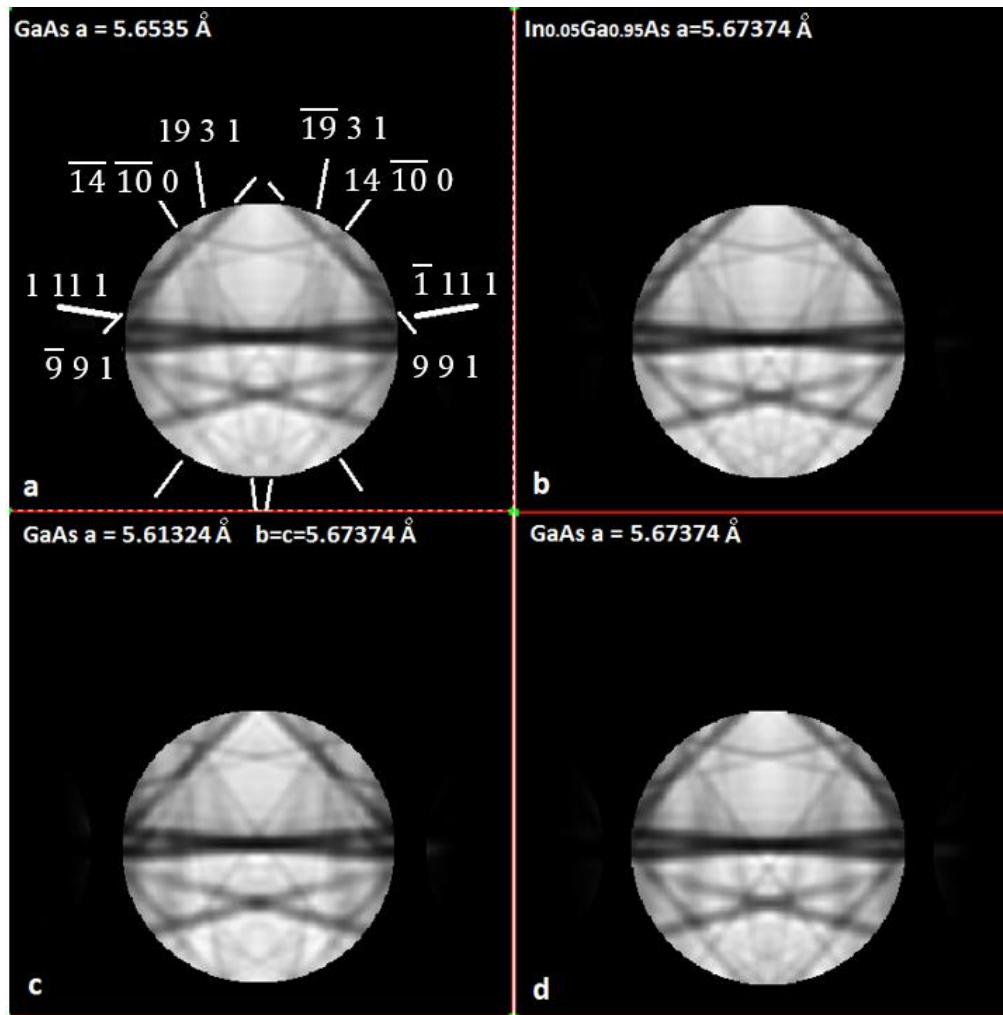


**Figure 5.7. The influence of the composition on the measurement of lattice constants by using HOLZ patterns.** Simulated HOLZ patterns of (a) GaAs (b)  $\text{In}_{0.05}\text{Ga}_{0.95}\text{As}$  (c) GaAs with a tetragonal unit cell and (d) GaAs with the lattice constants of  $\text{In}_{0.05}\text{Ga}_{0.95}\text{As}$ , at a common thickness of 113 nm. A semi-convergence angle of 7 mrad, an accelerating voltage of 200 kV and Debye-Waller factors [131] at 100 K are used in the simulations by Bloch wave in JEMS [58]. The deficiency HOLZ lines are labelled in (a). The positions of these deficiency HOLZ lines are governed by the lattice constants rather than compositions, which can be seen by visual comparisons between (b) and (d), and between (a) and (d). A visual comparison between (a) and (c) suggests that the HOLZ pattern is also sensitive to anisotropic variation of lattice constants.

### 5.4.3. Summary of the section

To summarize this section, the uncertainties in either the measured thickness or the lattice constants derived from Vegard's law result in small uncertainties in the measured composition. For example, in the worst case examined, an uncertainty of less than  $\Delta x = 0.02$  in measured compositions was found at a specimen thickness that is close to 100 nm. This uncertainty in composition is greatly reduced if the thickness is below 60 nm. Furthermore, if a cooling stage is used, the deficiency HOLZ lines in the central disc can be used to measure lattice constants independent of composition.

## 5.5 The effect of strain relaxation on the composition measurement

### 5.5.1 Strain relaxation

The embedded nanometre-thick layers of  $\text{In}_x\text{Ga}_{1-x}\text{As}$  in GaAs can form quantum wells (QWs) which confine the motion of electrons and holes in the dimension that is perpendicular to the  $\text{In}_x\text{Ga}_{1-x}\text{As}/\text{GaAs}$  interface. The QWs are usually grown on GaAs wafers by molecular beam epitaxy (MBE) or chemical vapour deposition (CVD). The mismatch between the lattice constants of  $\text{In}_x\text{Ga}_{1-x}\text{As}$  and GaAs cause biaxial contraction of  $\text{In}_x\text{Ga}_{1-x}\text{As}$  and biaxial extension of GaAs in the plane that is parallel with the interfaces and extension of  $\text{In}_x\text{Ga}_{1-x}\text{As}$  and contraction of GaAs in the direction that is perpendicular to the interface. Therefore, the cubic unit cells of GaAs and  $\text{In}_x\text{Ga}_{1-x}\text{As}$  are strained, effectively generating a tetragonal distortion, in the multilayered structures.

After the strained  $\text{In}_x\text{Ga}_{1-x}\text{As}/\text{GaAs}$  QW is thinned to electron transparency in the cross-sectional view, the interfaces of  $\text{In}_x\text{Ga}_{1-x}\text{As}/\text{GaAs}$  are exposed to the surfaces. The material at the surface relaxes and has very different local strain profiles from the interior of the multilayer structure, which results in a non-uniform strain distributions in the direction perpendicular to the interface and the direction perpendicular to the surfaces. This is referred to as “(elastic) strain relaxation.”

Strain relaxation can have a great influence on electron scattering [139] especially at high scattering angles, as has been studied, for example, in HAADF-STEM images [127] and HOLZ patterns [140, 141, 142]. The effect of the strain relaxation on HOLZ patterns has been studied in cross-sectional specimens of  $\text{In}_x\text{Ga}_{1-x}\text{As}/\text{GaAs}$  QWs, where splitting of deficiency HOLZ lines is found in an  $\text{In}_{0.03}\text{Ga}_{0.97}\text{As}/\text{GaAs}$  QW and fully blurred HOLZ patterns are found in an



$\text{In}_{0.14}\text{Ga}_{0.86}\text{As}/\text{GaAs}$  QW when the focused electron probe is placed adjacent to or within the  $\text{In}_x\text{Ga}_{1-x}\text{As}$  layers [142]. In the latter case where the effect of strain relaxation is more significant (due to the larger lattice mismatch at a higher indium concentration level), the local strain measurements in  $\text{In}_x\text{Ga}_{1-x}\text{As}$  nanometre-thick layers become very complicated or even impossible. The traditional CBED method of composition measurement which deduces compositions from the strains measured by HOLZ patterns [65] also becomes unavailable.

However, the strain relaxation may not limit the use of the current three-beam CBED method for local composition measurement, since the underpinning scattering mechanism is different. Analogous to CELFA, the three-beam CBED method makes use of the compositional sensitive reflection 2 0 0 that is more sensitive to composition, than it is to strain [133]. To investigate the effect of strain relaxation on the current composition measurement, CBED patterns are simulated for a model of cross-sectional specimens of an  $\text{In}_x\text{Ga}_{1-x}\text{As}/\text{GaAs}$  QW with an assumed composition profile which can induce a fairly large amount of strain relaxation.

### 5.5.2 The model for a strained QW specimen

The strain field in the model with an assumed composition profile was first simulated by the finite element method (FEM) using Abaqus version 6.14 [143] (see Fig. 5.8). Then, the atom positions were extrapolated from the nodal displacements. The details of the FEM simulations are described as follows.

A model of an  $\text{In}_x\text{Ga}_{1-x}\text{As}/\text{GaAs}$  QW with assumed composition profile was constructed. The QW specimen consisted of nine alternating layers of  $\text{In}_{0.2}\text{Ga}_{0.8}\text{As}$  and GaAs of 6-unit-cell ( $\sim 3.4$  nm) wide<sup>13</sup>, which were sandwiched by GaAs bases of 30 unit-cell wide. The interface of  $\text{In}_{0.2}\text{Ga}_{0.8}\text{As}/\text{GaAs}$  was assumed to have an abrupt change in composition for simplicity of treatment (which followed the practice in [128]). In the specimen thickness direction, there were 100 unit cells ( $\sim 57$  nm thick). For a pseudomorphically grown QW with such a lattice mismatch (1.4%), no misfit dislocations exist in the epitaxial layers up to 8 nm thick [144]. Thus, the lattice of  $\text{In}_{0.2}\text{Ga}_{0.8}\text{As}$  should be strained elastically to fit the lattice of GaAs. To simulate such a system, the FEM applied a virtual thermal expansion coefficient,  $\alpha_{\text{thermal}}$ , that fulfils the relation

---

<sup>13</sup> In the cross-sectional specimen, the “width” refers to the thickness of the epitaxial layer in the original QW structure before TEM specimen preparation, and the “specimen thickness” refers to the thickness of the TEM specimen.

$$a_{\text{GaAs}}(1 + \alpha_{\text{thermal}}\Delta T) = a_{\text{In}_{0.2}\text{Ga}_{0.8}\text{As}},$$

where the temperature step  $\Delta T=1$  was for  $\text{In}_{0.2}\text{Ga}_{0.8}\text{As}$  layers, and  $\Delta T=0$  was for GaAs layers. This treatment followed [128]. The elastic constants and lattice parameters used in the simulation are listed in Table 5.1.

**Table 5.1. Elastic constants and lattice constants used for the simulation by finite element method**

|                          | GaAs   | InAs   | $\text{In}_{0.2}\text{Ga}_{0.8}\text{As}$<br>(linearly interpolated) |
|--------------------------|--------|--------|--|
| Lattice constant $a$ (Å) | 5.6535 | 6.0583 | 5.7335   |
| $C_{11}$ (GPa)           | 118.1  | 83.3   | 111.14   |
| $C_{12}$ (GPa)           | 53.2   | 45.3   | 51.62  |
| $C_{13}$ (GPa)           | 59.4   | 39.6   | 55.44  |

The length of the mesh was chosen to be a half of the lattice constant of GaAs,  $\frac{1}{2}a_{\text{GaAs}}$ . The following boundary conditions were applied: the four surface planes perpendicular to  $[1\ 0\ 0]$  and  $[0\ 1\ 0]$  directions were constrained while the two surface planes perpendicular to  $[0\ 0\ 1]$  (which are the surfaces of the TEM specimen) were set free to move. In addition, an extra plane in the middle that was perpendicular to  $[1\ 0\ 0]$  and a point within the plane were fixed to prevent the object to be strained from the moving or rotating.

The FEM simulation was then initiated. Once the FEM simulation was finished, a field of the nodal displacements was acquired together with the fields of strains and stresses. The distribution of a normal strain component in  $[1\ 0\ 0]$  direction,  $e_{11} = \frac{a_{[1\ 0\ 0]} - a_{\text{GaAs}}}{a_{\text{GaAs}}}$ , is shown in Fig. 5.8.

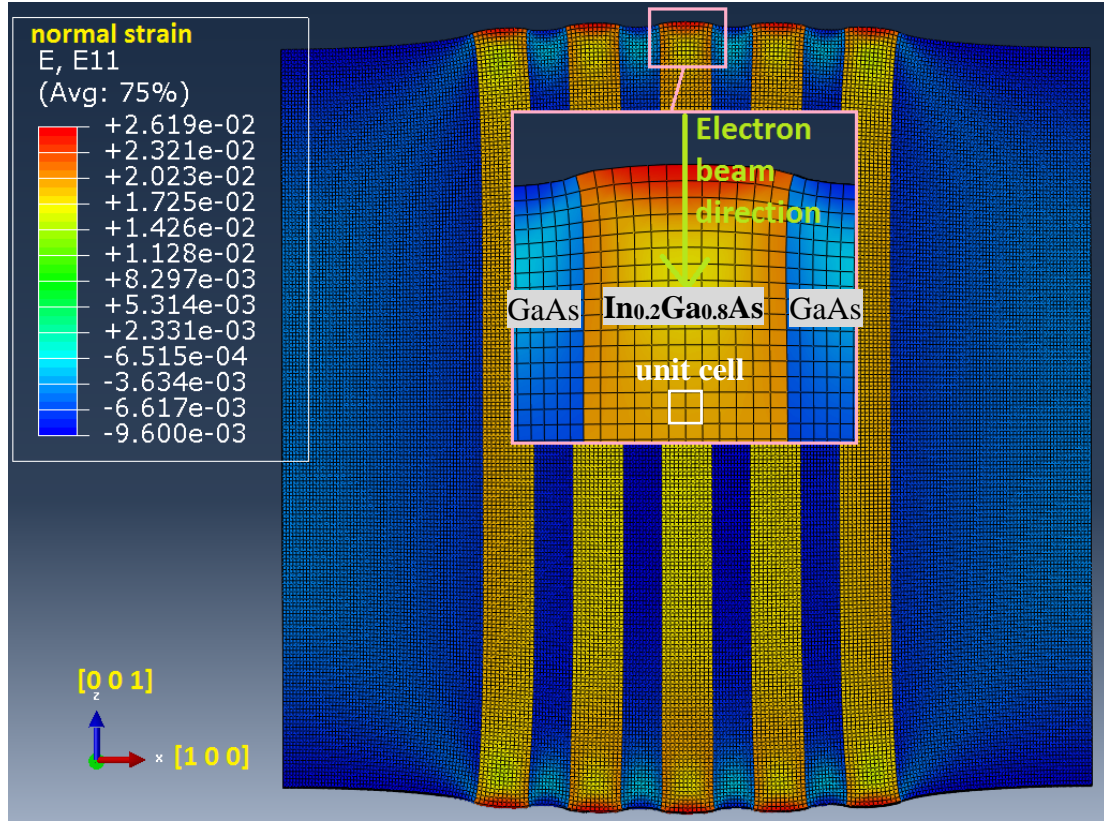


**Figure 5.8. Distribution of the normal strain component in the  $[1\ 0\ 0]$  direction,  $e_{11} = \frac{a_{[1\ 0\ 0]} - a_{\text{GaAs}}}{a_{\text{GaAs}}}$ , which is calculated by the finite element method.** The five layers of  $\text{In}_{0.2}\text{Ga}_{0.8}\text{As}$  (coloured in yellow, orange and red) are extended along  $[1\ 0\ 0]$  (as  $e_{11} > 0$ ) while the GaAs layers (coloured in light and dark blue) are contracted along  $[1\ 0\ 0]$  (as  $e_{11} < 0$ ). Bulges exist at the surfaces of the specimen due to the elastic relaxation. The size of the mesh is chosen to be equal to  $\frac{1}{2} a_{\text{GaAs}}$ .

Then, the positions for gallium and arsenic atom sites were extrapolated bilinearly<sup>14</sup> from the nodal displacements using a code written here in Matlab R2014a [145]. The atomic structures in the nanolayers of  $\text{In}_{0.2}\text{Ga}_{0.8}\text{As}$  were created by filling the gallium atom sites with indium and gallium atoms that are weighted by the site occupancies, i.e. 0.20 for indium and 0.80 for gallium.

<sup>14</sup> The nodal displacements along  $[0\ 1\ 0]$  direction are zero, so only a bilinear interpolation was needed.

### 5.5.3. Simulations of the CBED patterns and the composition measurements

#### 5.5.3.1 The multislice simulations

The atomic structure of the central part of the strained QW specimen was input to the structure file for CBED simulations in the multislice [43] programme, computem [117]. The atomic structure in the structure file consisted of  $24 \times 1 \times 100$  strained unit cells. The supercell for multislice calculation had a size of  $136.87 \times 137.04 \times 571.47 \text{ \AA}$  ( $24 \times 24 \times 100$  strained unit cells). A numerical real space grid of  $4096 \times 4096$  pixels was used, which corresponded to a real space sampling resolution of  $\Delta x = 0.033 \text{ \AA/pixel}$  and a reciprocal space sampling resolution of  $\Delta K = 0.00365 \text{ \AA}^{-1}/\text{pixel}$ . The supercell was sliced along  $[0\ 0\ 1]$  direction with a slice thickness of  $0.36 \text{ \AA}$ . A specimen tilt of  $66.3 \text{ mrad}$  ( $= 3.8^\circ$ ) about the  $[1\ 0\ 0]$  axis was applied to satisfy the diffraction condition (the tilt is in the plane that is parallel with the interfaces). The convergence angle was  $4 \text{ mrad}$ . The final normalisation value was  $0.988$ . When the electron probe was placed in the middle of the third  $\text{In}_{0.2}\text{Ga}_{0.8}\text{As}$  layer as shown in Fig. 5.8, a CBED pattern was calculated and the result is shown in Fig. 5.9a.

Note: Computem can include small amounts of specimen tilt by a modification to the propagation function. This is an approximation that is valid for limited range of thicknesses up to a few hundred  $\text{\AA}$  at a tilt angle of a few degrees [146]. To verify the validity of using this approximation for the current diffraction condition, multislice and Blochwave (using the same atomic scattering factors from Kirkland [117]) calculations on bulk materials of GaAs and  $\text{In}_{0.2}\text{Ga}_{0.8}\text{As}$  were compared. The comparison showed that the application of a specimen tilt of  $3.8^\circ$  to a specimen of  $571 \text{ \AA}$  thick using this approximation in the Computem multislice did not affect the value of the intensity ratio by more than  $+1\%$  relative to that calculated using the Bloch wave approach in JEMS [58], which approved the use of this approximation (in computem) for the current research purpose.

Another multislice simulation for a CBED pattern of bulk material of  $\text{In}_{0.2}\text{Ga}_{0.8}\text{As}$  was carried out as a reference. The result is shown in Fig. 5.9b. The supercell had a size of  $137.124 \times 137.124 \times 571.35 \text{ \AA}$  ( $24 \times 24 \times 100$  cubic unit cells). A numerical real space grid of  $4096 \times 4096$  pixels, a slice thickness of  $0.36 \text{ \AA}$ , a convergence angle of  $4 \text{ mrad}$  and a specimen tilt of  $66.3 \text{ mrad}$  were used. The final renormalisation value was  $0.993$ .

For a testing purpose, no inelastic scattering has been included in the current multislice simulations.

### 5.5.3.2 Results of the multislice simulations

A comparison of the thickness fringes in the discs  $\bar{4}00$  and  $400$  in Fig. 5.9a and Fig. 5.9b can reveal that the thickness measurement is not affected by the strain relaxation. However, the strain relaxation has caused the blurring of the deficiency HOLZ lines in the central beam in Fig. 5.9a, which is consistent with a previous experimental finding [142]. To be more specific, the deficiency HOLZ lines of  $1931$  and  $\bar{19}31$  almost disappear and the edges of the central disc are shifted along the  $h, 0, 0$  direction because the electrons that travel through the specimen have been scattered by  $(h\ 0\ 0)$  planes with varying spacing (which varying the length of the vector  $h, 0, 0$  in reciprocal space). The blurred HOLZ pattern makes the strain measurement complicated or even impossible.

To evaluate the influence of strain relaxation on the composition measurement in the QW specimen, the intensity ratio measured from the CBED pattern in Fig. 5.9a is compared with that in Fig. 5.9b, giving 0.967 versus 0.930. These intensity ratios correspond to compositions  $x=0.21$  and  $x=0.20$  in the look-up table produced by the Bloch wave calculations which do not include inelastic scattering (so that the comparison with the multislice simulations are consistent). Therefore, in this example, the indium concentration will be overestimated by 1% if the influence of strain relaxation is ignored in this case.

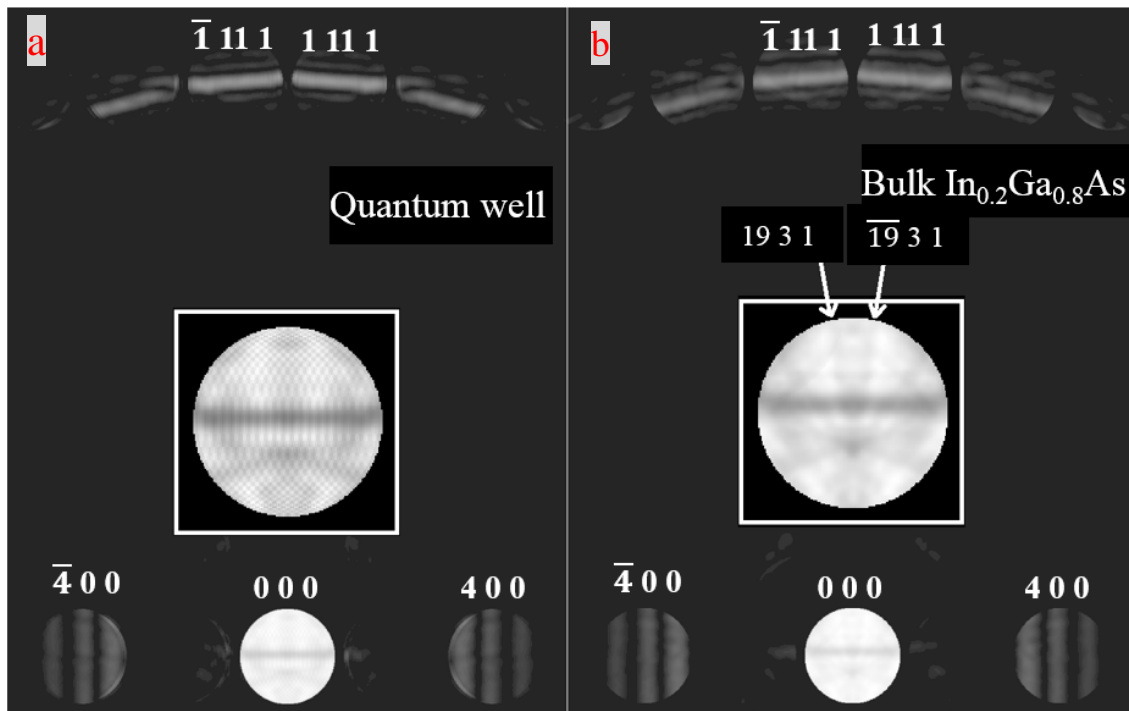


**Figure 5.9.** Simulated CBED patterns for (a) the strained QW specimen (the probe position is shown in Figure 5.8) and (b) bulk, unstrained  $\text{In}_{0.2}\text{Ga}_{0.8}\text{As}$ . Both specimens are

100 unit cells thick (about 57 nm). The magnified views of the central discs (captured in the white squares) are displayed at a different contrast level to optimise the HOLZ pattern in each case. The  $19\ 3\ 1$  and  $\overline{19}\ 3\ 1$  deficiency HOLZ lines that are evident in (b) are not distinguishable in (a), and the edges of the discs in (a) are shifted along the  $h, 0, 0$  direction because the spacings between the  $(h\ 0\ 0)$  planes vary in the thickness direction and all of the reflections are displaced in the direction of the  $h, 0, 0$  vectors. However, the intensity distributions (the bright and dark fringes) in the discs  $\overline{4}\ 0\ 0$  and  $4\ 0\ 0$  in (a) appear to be the same as those in (b). This suggests that the thickness measurement is not affected by the strain relaxation.

### 5.5.3.3 The simulation of scanning CBED and the composition mapping

To acquire a map of composition, the probe was shifted across two  $\text{In}_{0.20}\text{Ga}_{0.80}\text{As}/\text{GaAs}$  interfaces in the middle of the QW specimen and a series of CBED patterns were calculated (i.e. a ‘scanning CBED’ experiment was simulated). The step size of the scanning probe is set to be as small as the length of a unit cell. To examine the effect of “cross talk” (electrons propagate in two types of materials and the information in the CBED pattern comes from different regions), even smaller step size was used when the probe was placed close to the interfaces.

A composition profile (red dots in Fig. 5.10) was evaluated from these CBED patterns by comparing the intensity ratios to those from the bulk  $\text{In}_x\text{Ga}_{1-x}\text{As}$  at the same thickness. To have a time-efficient evaluation of the compositions, the compositions were interpolated from the intensity ratios for the bulk  $\text{In}_x\text{Ga}_{1-x}\text{As}$  with  $x = 0, 0.05, 0.15, 0.20$ , and  $0.25$ . This gives the red dots in Fig. 5.10.

In Fig. 5.10, the evaluated composition profile is compared with the originally assumed composition profile (so-called “true composition profile”). The results are presented in Fig. 5.10. The evaluated composition profile shows a transition region near the  $\text{In}_x\text{Ga}_{1-x}\text{As}/\text{GaAs}$  interfaces due to the electron propagation in both regions with different compositions. An error of less than  $\pm 2\%$  of indium concentration can be found in the evaluated composition profile due to the strain relaxation, which indicates that fairly accurate measurements of compositions could be achieved with the current method, *even* if the strain field brought by the lattice misfit and strain relaxation is unknown or assumed to be absent. Once a composition profile is evaluated together with the specimen thicknesses, a model for FEM can be constructed to



compute the strain field. With the computed strain field, the compositions can be further refined and the strains can be deduced iteratively.

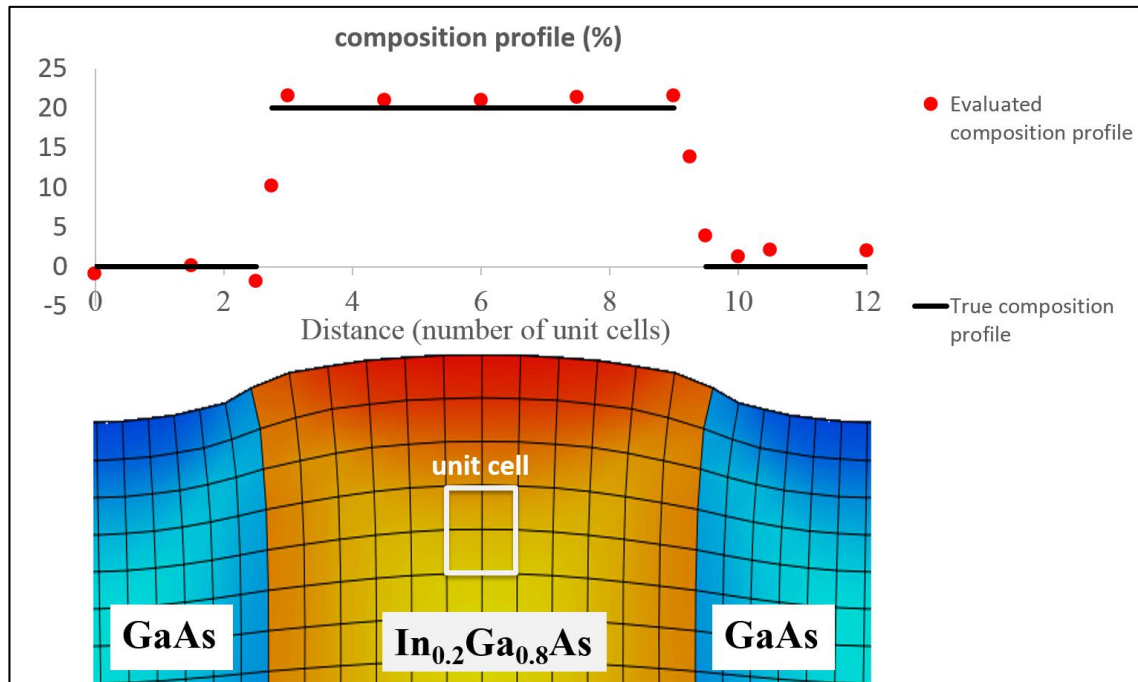


**Figure 5.10. Composition profiles across two In<sub>0.2</sub>Ga<sub>0.8</sub>As/GaAs interfaces in the middle of the QW specimen shown in Fig. 5.8.** The red dots are the evaluated compositions from the simulated CBED patterns and the black lines are the true compositions which have been assumed in the first place. The step size of the scanning probe is set to be as small as the length of a unit cell (even smaller when the probe gets close to interfaces).

#### 5.5.3.4 The meaning of the current simulations

The current simulations did not include the effect of inelastic scattering, bonding, and static atomic displacement. A more complete study of the strain relaxation effect on the composition measurements should compare experimental data with a carefully prepared look-up table for composition measurements in bulk In<sub>x</sub>Ga<sub>1-x</sub>As which has considered inelastic scattering, bonding, and static atomic displacement. Nevertheless, the current test gives some hints on how small the influence of strain relaxation could be on the current composition measurements, which lends weight to the applicability of the current method for composition measurements in real quantum wells.

## 5.6 Discussions

### 5.6.1 The selection of the current diffraction condition

The inclusion of reflection  $2\ 0\ 0$  (or reflections for the  $\{2\ 0\ 0\}$  type crystal planes) in setting CBED patterns for composition measurements in III-V semiconductors has been attempted or mentioned in previous work in different diffraction conditions [147] [148]. The diffraction condition in the current method is selected based on the theory stated by the equation (3.15). Particularly, the Bijvoet pair  $\bar{1}\ 11\ 1$  and  $1\ 11\ 1$  are selected rather than  $\bar{1}\ 9\ 1$  and  $1\ 9\ 1$  or  $\bar{1}\ 13\ 1$  and  $1\ 13\ 1$  because of the following considerations:

- 1) The extinction distances of the Bragg reflections should be long so that a wide range of thicknesses can be available. Thus,  $\bar{1}\ 9\ 1$  and  $1\ 9\ 1$  are excluded.
- 2) The peak intensities of Bragg reflections should be much higher than the Kikuchi background intensities, thus,  $\bar{1}\ 13\ 1$  and  $1\ 13\ 1$  are excluded.
- 3) The selection of a Bijvoet pair rather (than two reflections with different reciprocal-vector lengths) can also reduce the influence of the uncertainties in Debye-Waller factors.

Besides, the integrated intensities are used for the ratio because they can minimize the errors due to mis-locations of the three-beam points in the experiments and reduce the strain relaxation effect on the intensity ratio.

### 5.6.2 Comparison with other methods

A key feature of the current CBED method is that three different parts of the same pattern have distinct sensitivities to composition, thickness and lattice constants and can be used to measure the three pieces of information simultaneously but effectively independently. In other methods, these three parameters have a complex interdependence, meaning that uncertainty in one parameter impacts on the measurement of the others. An important application of this feature in future work would be the experimental determination of the lattice constants-composition relations (or deviation from Vegard's law) for bulk  $\text{In}_x\text{Ga}_{1-x}\text{As}$

In analogy with CELFA, the current method is most suited to zinc blende structures with a small value of  $|V_{2,0,0}|$  so that the compositional sensitive features are not strongly dependent on the variation of the specimen thickness for a wide range of thicknesses. To be more specific, the ratio (which is the gauge for composition measurement) increases monotonically with composition up to a specimen thickness of 80 nm for structures with  $|V_{2,0,0}| < 1\ \text{\AA}$ , such as



$\text{In}_x\text{Ga}_{1-x}\text{As}$  with  $0 < x < 0.76$ ,  $\text{Al}_x\text{Ga}_{1-x}\text{As}$  with  $0 < x < 0.3$  and  $\text{Al}_x\text{In}_{1-x}\text{As}$  with  $0.15 < x < 0.8$ . Furthermore, the current CBED method has the potential measure compositions in cross-sectional specimens of  $\text{In}_x\text{Ga}_{1-x}\text{As}$  /GaAs quantum wells to high accuracy because the composition measurement is not strongly affected by the strain relaxation.

In CELFA and HAADF-STEM, a region of pure GaAs next to  $\text{In}_x\text{Ga}_{1-x}\text{As}$  is often preferred for interpolation of the specimen thickness and normalisation of the intensities. However, such a neighbouring region of GaAs may not be available in certain applications where a thick pseudomorphic layer ( $\sim 1\mu\text{m}$ ) of  $\text{In}_x\text{Ga}_{1-x}\text{As}$  is grown [149]. The current method is capable of measuring composition in such a homogeneous material of  $\text{In}_x\text{Ga}_{1-x}\text{As}$  without any reference regions of pure GaAs.

Apart from the three most commonly used techniques (i.e. EDS, HAADF-STEM and CELFA), there are also existing CBED methods for compositional analysis of zinc-blende semiconductors [147, 150]. One of those methods is based on the compositional dependence of the wave vectors for certain dominant Bloch states in the [100] zone axis of  $\text{Al}_x\text{Ga}_{1-x}\text{As}$ , which causes the shifts of the split excess HOLZ lines with composition [150]. By measuring the separation of the split excess lines in HOLZ discs, the composition can be determined through comparison with Bloch wave calculations. Since the positions of the HOLZ lines used in this method have high index numbers, such as (15 9 1), and are also sensitive to lattice constants, such a method may have limited accuracy when applied to structures where the lattice constants are strongly dependent on composition [151], for example  $\text{In}_x\text{Ga}_{1-x}\text{As}$ . By contrast, the current method is much less influenced by the uncertainties in lattice constants as mentioned before. Also, the influence of the noises may be less significant for the current method as ratios of the integrated intensities are used.



## Chapter 6. Conclusions

This thesis has introduced new methods of three-beam electron diffraction for structural investigations at the nanometre scale. The study has resulted in two new methods for different applications: (1) a method for determining three-phase invariants in noncentrosymmetric crystals and (2) a method for measuring compositions in  $\text{In}_x\text{Ga}_{1-x}\text{As}$ . The former is related to crystal structure determination and is especially for improving phasing in structure solutions. The latter is related to composition measurements in zinc-blende type semiconductors. Although these applications are related to different fields of research, the basic principles behind them are the same, which come from the newly developed theories of three-beam electron diffraction (which have been introduced in Chapter 3).

### 6.1 Determination of three-phase invariants by observation: theory

1) When the crystal is tilted to a minor zone axis, one can decide if an intersection of two deficiency Bragg lines can be regarded as a three-beam condition or not by inspection of the central disc. If the intersection is a three-beam condition, then the determination of three-phase invariants can be continued by following the flow chart given in Section 3.7.

2) The three-phase invariants can be determined to within  $45^\circ$  simply by inspecting the intensities near three-beam conditions in CBED or LACBED patterns, if the following conditions are satisfied:

- a. In the diffraction pattern, there is a centrosymmetrically related pair of three-beam conditions,  $0/g/h$  and  $0/\bar{g}/\bar{h}$ , or a single three-beam condition where the two reflections,  $g$  and  $h$ , have similar structure factor magnitudes, i.e.  $|V_g| \approx |V_h|$ .
- b. The thickness is less than the three-beam extinction distance, which can also be confirmed by inspection of the CBED or reconstructed LACBED patterns following the two criteria discussed in Section 3.5.

## 6.2 Determination of three-phase invariants by observation: experiment

1) Some preliminary experiments for implementing the newly developed method for phase determination have been carried out with large-angle rocking beam electron diffraction (LARBED) [23]. Instead of using parallel beams of illumination, this work has applied convergent beam illumination at each beam tilt. A script for stitching the CBED patterns to reconstruct a LACBED pattern has been written.

2) As a proof of concept, the measurements of three-phase invariants have been demonstrated for a centrosymmetric crystal structure, Si, and a noncentrosymmetric crystal, GaAs.

3) It is possible to develop methods of three-beam electron diffraction at fairly low dose. It should be kept in mind that the current method of measuring three-phase invariants only requires a qualitative observation of the pattern, which may imply that such a method does not require CBED patterns of high signal to noise.

## 6.3 Composition measurement in $\text{In}_x\text{Ga}_{1-x}\text{As}$

1) It has been found that the CBED patterns recorded at a particular three-beam condition,  $0\ 0\ 0 / \bar{1}\ 1\ 1 / 1\ 1\ 1$ , can be used for measuring compositions in  $\text{In}_x\text{Ga}_{1-x}\text{As}$  because the intensity difference between reflections  $\bar{1}\ 1\ 1$  and  $1\ 1\ 1$  is proportional to the structure factor of the coupling vector,  $2, 0, 0$ , which is sensitive and proportional to the composition,  $x$ . Meanwhile, the fringes in the  $4\ 0\ 0$  disc can be used for determining the thickness, and the deficiency HOLZ lines in the central disc can be used for measuring the lattice constants if a cooling stage is used.

2) Bloch wave simulations show that the measurements of compositions, thicknesses and lattice constants are quite independent of each other, which suggests the composition measurement can potentially be very accurate.

3) The current work has also investigated the influence of strain, in a cross-sectional specimen of an  $\text{In}_x\text{Ga}_{1-x}\text{As}/\text{GaAs}$  quantum well (QW), on the composition measurement by means of simulations. With an assumed indium concentration profile, the strain distribution in the QW specimen was first calculated by the finite element method [143]. The atom positions in the specimen were then extrapolated from the strains and were entered into to a multislice

[43] programme [117] for simulations of CBED patterns. The composition measurement from the simulated CBED patterns showed that the strains had only a weak influence on the composition measurement. Therefore, the current approach may be applicable in mapping composition in cross-sectional specimens of  $\text{In}_x\text{Ga}_{1-x}\text{As}$ /GaAs QWs in real devices.

## 6.4 Recommended future work

It can be anticipated that the combination of three-beam electron diffraction with precession electron diffraction (PED) [27] will result in more reliable structure solutions. The LARBED technique can be applied to determine three-phase invariants in more complex crystals structures, with much larger unit cells, than those examples presented in Chapter 4. The challenges in performing LARBED on beam-sensitive materials may not be easily negated. However, new TEM experiments (yet to be developed) that follow the scheme of “reference-beam diffraction” [113] in three-beam dynamic X-ray diffraction may be useful for the acquisition of intensity profiles that contain three-phase invariants at a low electron dose level.

In terms of the method for composition measurements in  $\text{In}_x\text{Ga}_{1-x}\text{As}$ , more experiments need to be done to confirm its applicability in  $\text{In}_x\text{Ga}_{1-x}\text{As}$  quantum wells. The method could also be tested with other nanostructures such as quantum dots and nanowires.



## References

- [1] J. M. Zuo and J. L. Rouvière, *IUCrJ* **2**, 7 (2015).
- [2] H. A. Hauptman, *Rep. Prog. Phys.* **54**, 1427 (1991).
- [3] F. Mo, R. H. Mathiesen, B. C. Hauback, and E. T. Adman, *Acta Crystallogr. Sect. D* **52**, 893 (1996).
- [4] K. Shinohara, *Sci. Pap. Inst. Phys. Chem. Res.* **20**, 39 (1932).
- [5] E. Fues, *Z. Physik.* **125**, 531 (1949).
- [6] K. Kambe, *J. Phys. Soc. Jpn.* **12**, 13 (1957).
- [7] K. Kambe, *J. Phys. Soc. Jpn.* **12**, 25 (1957).
- [8] J. Gjønnes and R. Høier, *Acta Crystallogr. Sect. A* **25**, 595 (1969).
- [9] J. Gjønnes and R. Høier, *Acta Crystallogr. Sect. A* **27**, 313 (1971).
- [10] A. F. Moodie, *Chem. Scr.* **14**, 21 (1978-79).
- [11] A. C. Hurley and A. F. Moodie, *Acta Crystallogr. Sect. A* **36**, 737 (1980).
- [12] J. Taftø and J. C. H. Spence, *J. Appl. Crystallogr.* **15**, 60 (1982).
- [13] K. Marthinsen and R. Høier, *Acta Crystallogr. Sect. A* **42**, 484 (1986).
- [14] D. M. Bird, R. James, and A. R. Preston, *Phys. Rev. Lett.* **59**, 1216 (1987).
- [15] J. M. Zuo, R. Høier, and J. C. H. Spence, *Acta Crystallogr. Sect. A* **45**, 839 (1989).
- [16] K. Marthinsen, *Acta Crystallogr. Sect. A* **49**, 324 (1993).

- [17] P. N. H. Nakashima, A. F. Moodie, and J. Etheridge, *Acta Crystallogr. Sect. A* **63**, 387 (2007).
- [18] P. N. H. Nakashima, A. F. Moodie, and J. Etheridge, *Ultramicroscopy* **108**, 901 (2008).
- [19] P. Goodman, *Z. Naturforsch. A* **28**, 580 (1973).
- [20] A. F. Moodie, J. Etheridge, and C. J. Humphreys, *Acta Crystallogr. Sect. A* **52**, 596 (1996).
- [21] P. N. H. Nakashima, A. F. Moodie, and J. Etheridge, *Proc. Natl. Acad. Sci. USA* **110**, 14144 (2013).
- [22] H. Bethe, *Ann. Phys. (Berlin)* **87**, 55 (1928).
- [23] C. T. Koch, *Ultramicroscopy* **111**, 828 (2011).
- [24] A. C. Hurley, A. F. Moodie, A. W. S. Johnson, and P. C. Abbott, *Acta Crystallogr. Sect. A* **55**, 216 (1999).
- [25] H. A. Hauptman, *Crystal structure determination: the role of the cosine seminvariants* (Plenum Press, New York, 1972).
- [26] C. J. Humphreys, *Rep. Prog. Phys.* **42**, 1825 (1979).
- [27] P. A. Midgley and A. S. Eggeman, *IUCrJ* **2**, 126 (2015).
- [28] G. N. Ramachandran and R. Srinivasan, *Fourier methods in crystallography* (Wiley-Interscience, New York, 1970).
- [29] The Cambridge Crystallographic Database Centre,  
<http://www.ccdc.cam.ac.uk/Solutions/CSD-System/Components/CSD/>.
- [30] A. J. C. Wilson, *Nature* **150**, 151 (1942).
- [31] W. Cochran, *Acta Crystallogr.* **8**, 473 (1955).
- [32] G. Oszlányi and A. Sütő, *Acta Crystallogr. Sect. A* **60**, 134 (2004).



- [33] W. A. Hendrickson, *Q. Rev. Biophys.* **47**, 49 (2014).
- [34] M. Vijayan and S. Ramaseshan, in: *International Tables for Crystallography Vol. B: Reciprocal space*, edited by U. Shmueli (Springer, Dordrecht, Netherlands 2006), pp. 264-275.
- [35] Online Dictionary of Crystallography: Mosaic crystals,  
[http://reference.iucr.org/dictionary/Mosaic\\_crystal](http://reference.iucr.org/dictionary/Mosaic_crystal)
- [36] E. Weckert and K. Hummer, *Acta Crystallogr. Sect. A* **53**, 108 (1997).
- [37] Q. Shen, *Adv. Imag. Elect. Phys.*, **134**, 69 (2005).
- [38] S.-L. Chang, *X-ray multiple-wave diffraction : theory and application* (Springer, Heidelberg, 2004).
- [39] D. Sayre, *Struct. Chem.* **13**, 81 (2002).
- [40] K. Fujiwara, *J. Phys. Soc. Jpn.* **16**, 2226 (1961).
- [41] K. Watanabe, S. Hara, and I. Hashimoto, *Acta Crystallogr. Sect. A* **52**, 379 (1996).
- [42] C. Dwyer, *Phys. Rev. B* **72**, 144102 (2005).
- [43] J. M. Cowley and A. F. Moodie, *Acta Crystallogr.* **10**, 609 (1957).
- [44] Z. L. Wang, *Elastic and inelastic scattering in electron diffraction and imaging* (Plenum Press, New York, 1995).
- [45] K. Ishizuka, *Acta Crystallogr. Sect. A* **38**, 773 (1982).
- [46] K. Ishizuka and N. Uyeda, *Acta Crystallogr. Sect. A* **33**, 740 (1977).
- [47] L. Sturkey, *Acta Crystallogr.* **10**, 858 (1957).
- [48] F. Fujimoto, *J. Phys. Soc. Jpn.* **14**, 1558 (1959).

- [49] A. F. Moodie, J. M. Cowley, and P. Goodman, in: *International Tables for Crystallography, Vol. B: Reciprocal Space*, edited by U. Shmueli (Springer, Dordrecht, Netherlands 2006), pp. 552-556
- [50] A. C. Hurley, A. W. S. Johnson, A. F. Moodie, and J. R. Sellar, in: *Inst. Phys. Conf. Ser. No. 41*(1978), pp. 34.
- [51] J. M. Cowley and A. F. Moodie, *J. Phys. Soc. Jpn.* **17**, 86 (1962).
- [52] J. M. Cowley, *Diffraction physics*, Third Revised Edition (Elsevier Science B.V., Amsterdam & New York, 1995).
- [53] K. Fujiwara, *J. Phys. Soc. Jpn.* **14**, 1513 (1959).
- [54] J. Gjønnes and A. F. Moodie, *Acta Crystallogr.* **19**, 65 (1965).
- [55] A. F. Moodie and H. J. Whitfield, *Acta Crystallogr. Sect. A* **51**, 198 (1995).
- [56] A. W. S. Johnson, *Acta Crystallogr. Sect. B* **63**, 511 (2007).
- [57] D. B. Williams and C. B. Carter, *Transmission electron microscopy: a textbook for materials science*, Second Edition (Springer, New York & London, 2009).
- [58] P. A. Stadelmann, Computer Program JEMS - EMS java version Version 4.0,(JEMS - SAAS,Switzerland, 2004).
- [59] B. F. Buxton, J. A. Eades, J. W. Steeds, and G. M. Rackham, *Phil. Trans. R. Soc. A* **281**, 171 (1976).
- [60] M. Tanaka, R. Saito, and H. Sekii, *Acta Crystallogr. Sect. A* **39**, 357 (1983).
- [61] M. Tanaka, H. Sekii, and T. Nagasawa, *Acta Crystallogr. Sect. A* **39**, 825 (1983).
- [62] K. Tsuda, A. Yasuhara, and M. Tanaka, *Appl. Phys. Lett.* **103**, 082908 (2013).
- [63] K. H. Kim and J. M. Zuo, *Acta Crystallogr. Sect. A* **70**, 583 (2014).
- [64] K. H. Kim, D. A. Payne, and J. M. Zuo, *Appl. Phys. Lett.* **107**, 162902 (2015).

- [65] J. C. H. Spence and J. M. Zuo, *Electron microdiffraction* (Plenum Press, New York, 1992).
- [66] T. Akaogi, K. Tsuda, M. Terauchi, and M. Tanaka, *J. Electron Microsc.* **53**, 593 (2004).
- [67] T. Akaogi, K. Tsuda, M. Terauchi, and W. Tanaka, *J. Electron Microsc.* **53**, 11 (2004).
- [68] R. Vincent, D. M. Bird, and J. W. Steeds, *Philos. Mag. A* **50**, 745 (1984).
- [69] R. Vincent, D. M. Bird, and J. W. Steeds, *Philos. Mag. A* **50**, 765 (1984).
- [70] K. Tsuda and M. Tanaka, *Acta Crystallogr. Sect. A* **51**, 7 (1995).
- [71] P. A. Midgley, M. E. Sleight, and R. Vincent, *J. Solid State Electrochem.* **124**, 132 (1996).
- [72] C. J. Rossouw, M. A. Gibson, and C. T. Forwood, *Ultramicroscopy* **66**, 193 (1996).
- [73] J. M. Zuo and J. C. H. Spence, *Ultramicroscopy* **35**, 185 (1991).
- [74] J. M. Zuo, M. Kim, M. O'Keeffe, and J. C. H. Spence, *Nature* **401**, 49 (1999).
- [75] K. Tsuda, Y. Ogata, K. Takagi, T. Hashimoto, and M. Tanaka, *Acta Crystallogr. Sect. A* **58**, 514 (2002).
- [76] P. N. H. Nakashima, A. E. Smith, J. Etheridge, and B. C. Muddle, *Science* **331**, 1583 (2011).
- [77] M. Tanaka, R. Saito, K. Ueno, and Y. Harada, *J. Electron Microsc.* **29**, 408 (1980).
- [78] D. Cherns and A.R. Preston, in: *11<sup>th</sup> International Congress on Electron Microscopy*, edited by T. Imura et al. (Japanese Society of Electron Microscopy, Kyoto, 1986), pp.721-722.
- [79] M. Tanaka, M. Terauchi, and T. Kaneyama, *J. Electron Microsc.* **40**, 211 (1991).
- [80] J. P. Morniroli, *J. Microsc. (Oxf)* **223**, 240 (2006).

- [81] L. J. Allen, H. M. L. Faulkner, and H. Leeb, *Acta Crystallogr. Sect. A* **56**, 119 (2000).
- [82] L. J. Allen, C. Koch, M. P. Oxley, and J. C. H. Spence, *Acta Crystallogr. Sect. A* **57**, 473 (2001).
- [83] L. J. Allen and A. V. Martin, *Mod. Phys. Lett. B* **22**, 2123 (2008).
- [84] C. T. Koch, *Acta Crystallogr. Sect. A* **61**, 231 (2005).
- [85] J. C. H. Spence, *J. Microsc. (Oxf)* **190**, 214 (1998).
- [86] S.-L. Chang, H. E. King, M. T. Huang, and Y. Gao, *Phys. Rev. Lett.* **67**, 3113 (1991).
- [87] K. Hummer, W. Schwegle, and E. Weckert, *Acta Crystallogr. Sect. A* **47**, 60 (1991).
- [88] Q. Shen, *Acta Crystallogr. Sect. A* **42**, 525 (1986).
- [89] D. M. Bird and R. James, *Ultramicroscopy* **26**, 31 (1988).
- [90] K. Hummer and H. W. Billy, *Acta Crystallogr. Sect. A* **38**, 841 (1982).
- [91] A. F. Moodie, J. Etheridge, and C. J. Humphreys, in: *The Electron*, edited by A. Kirkland & P. Brown, (IOM Communications Ltd, London, 1998) pp. 235–246.
- [92] A. Howie and M. J. Whelan, *Proc. R. Soc. A* **263**, 217 (1961).
- [93] Wolfram Research, Inc., *Mathematica*, Version 10.0, (Wolfram Research, Inc., Champaign, IL, 2014).
- [94] R. Beanland, P. J. Thomas, D. I. Woodward, P. A. Thomas, and R. A. Roemer, *Acta Crystallogr. Set. A* **69**, 427 (2013).
- [95] P. P. Ewald and Y. Heno, *Acta Crystallogr. Sect. A* **24**, 5 (1968).
- [96] M. A. Spackman, B. Jiang, T. L. Groy, H. He, A. E. Whitten, and J. C. H. Spence, *Phys. Rev. Lett.* **95**, 085502 (2005).
- [97] R. Høier, C. R. Birkeland, R. Holmestad, and K. Marthinsen, *Acta Crystallogr. Sect. A* **55**, 188 (1999).

- [98] M. M. Woolfson and H.-F. Fan, *Physical and Non-Physical Methods of Solving Crystal Structures* (Cambridge University Press, Cambridge, England, 2005).
- [99] C. M. Weeks, H. L. Xu, H. A. Hauptman, and Q. Shen, *Acta Crystallogr. Sect. A* **56**, 280 (2000).
- [100] R. Vincent and P. A. Midgley, *Ultramicroscopy* **53**, 271 (1994).
- [101] W. Wan, J. L. Sun, J. Su, S. Hövmøller, and X. D. Zou, *J. Appl. Crystallogr.* **46**, 1863 (2013).
- [102] E. Weckert, W. Schwegle, and K. Hummer, *Proc. R. Soc. A* **442**, 33 (1993).
- [103] A. S. Soares et al., *Acta Crystallogr. Sect. D* **59**, 1716 (2003).
- [104] J. S. Wu and J. C. H. Spence, *Microsc. Microanal.* **9**, 428 (2003).
- [105] L. G. Sillen, *Arkiv för Kemi, Mineralogi och Geologi. A* **12**, 1 (1938).
- [106] C. T. Koch, Computer Program Quantitative Electron Diffraction version 1.3, (HREM Research Inc, 2010.)
- [107] P. A. Doyle and P. S. Turner, *Acta Crystallogr. Sect. A* **24**, 390 (1968).
- [108] J. C. H. Spence, J. M. Zuo, M. O’Keeffe, K. Marthinsen, and R. Høier, *Acta Crystallogr. Sect. A* **50**, 647 (1994).
- [109] H. Inui, A. Fujii, K. Tanaka, H. Sakamoto, and K. Ishizuka, *Acta Crystallogr. Sect. B* **59**, 802 (2003).
- [110] A. W. S. Johnson and A. R. Preston, *Ultramicroscopy* **55**, 348 (1994).
- [111] E. J. Ariens, *Eur. J. Clin. Pharmacol.* **26**, 663 (1984).
- [112] A. Meents, C. Ketterer, E. Weckert, and B. Wünsch, HASYLAB at DESY, Determination of the Absolute Configuration of C<sub>12</sub>H<sub>13</sub>O<sub>2</sub> by Three-Beam Diffraction, 2004.
- [113] Q. Shen, *Phys. Rev. Lett.* **80**, 3268 (1998).

- [114] M. J. Rodwell, C. Y. Huang, S. Lee, V. Chobpattana, B. Thibeault, W. Mitchell, S. Stemmer, and A. Gossard, *ECS Trans.* **66**, 135 (2015).
- [115] J. Lin, D. A. Antoniadis, and J. A. del Alamo, *IEEE Trans. Electron Devices* **62**, 11 (2015).
- [116] J. M. Zuo, *Ultramicroscopy* **41**, 211 (1992).
- [117] E. J. Kirkland, *Advanced computing in electron microscopy*, 2<sup>nd</sup> edition (Springer, New York, 2010).
- [118] H. Kauko, B. O. Fimland, T. Grieb, A. M. Munshi, K. Muller, A. Rosenauer, and A. T. J. van Helvoort, *J. Appl. Phys.* **116**, 144303 (2014).
- [119] J. M. LeBeau, S. D. Findlay, L. J. Allen, and S. Stemmer, *Phys. Rev. Lett.* **100**, 206101 (2008).
- [120] J. M. LeBeau and S. Stemmer, *Ultramicroscopy* **108**, 1653 (2008).
- [121] C. Maunders, C. Dwyer, P. C. Tiemeijer, and J. Etheridge, *Ultramicroscopy* **111**, 1437 (2011).
- [122] C. Dwyer, C. Maunders, C. L. Zheng, M. Weyland, P. C. Tiemeijer, and J. Etheridge, *Appl Phys Lett* **100**, 191915 (2012).
- [123] H. Katz-Boon, C. J. Rossouw, C. Dwyer, and J. Etheridge, *Ultramicroscopy* **124**, 61 (2013).
- [124] C. L. Zheng and J. Etheridge, *Ultramicroscopy* **125**, 49 (2013).
- [125] T. Mehrtens, K. Muller, M. Schowalter, D. Z. Hu, D. M. Schaadt, and A. Rosenauer, *Ultramicroscopy* **131**, 1 (2013).
- [126] R. F. Egerton, *Electron energy-loss spectroscopy in the electron microscope*, 2nd edition (Plenum Press, New York, 1996).
- [127] V. Grillo, *Ultramicroscopy* **109**, 1453 (2009).
- [128] A. Rosenauer, *Transmission Electron Microscopy of Semiconductor Nanostructures: An Analysis of Composition and Strain State* (Springer-Verlag, Berlin, 2003).

- [129] A. Weickenmeier and H. Kohl, *Acta Crystallogr. Set. A* **47**, 590 (1991).
- [130] A. Weickenmeier and H. Kohl, *Philos. Mag. B* **60**, 467 (1989).
- [131] M. Schowalter, A. Rosenauer, J. T. Titantah, and D. Lamoen, *Acta Crystallogr. Set. A* **65**, 5 (2009).
- [132] K. Tsuda and M. Tanaka, *Acta Crystallogr. Set. A* **55**, 939 (1999).
- [133] A. Rosenauer, M. Schowalter, F. Glas, and D. Lamoen, *Phys. Rev. B* **72**, 085326 (2005).
- [134] E. Villaggi, C. Bocchi, N. Armani, G. Carta, G. Rossetto, and C. Ferrari, *Japan. J. Appl. Sci.* **41**, 1000 (2002).
- [135] A. Toda, N. Ikarashi, and H. Ono, *J. Crys. Growth* **20**, 341 (2000).
- [136] P. Zhang, A. A. Istratov, E. R. Weber, C. Kisielowski, H. He, C. Nelson, and J. C. H. Spence, *Appl. Phys. Lett.* **89**, 161907 (2006).
- [137] A. Morawiec, *Ultramicroscopy* **107**, 390 (2007).
- [138] S. J. Rozeveld, J. M. Howe, and S. Schmauder, *Acta Metall. Mater.* **40**, S173 (1992).
- [139] M. M. J. Treacy and J. M. Gibson, *J. Vac. Sci. Technol. B* **4**, 1458 (1986).
- [140] A. Chuvilin, U. Kaiser, Q. de Robillard, and H. J. Engelmann, *J. Electron Microsc.* **54**, 515 (2005).
- [141] F. Houdellier, C. Roucau, L. Clement, J. L. Rouviere, and M. J. Casanove, *Ultramicroscopy* **106**, 951 (2006).
- [142] F. Houdellier, C. Roucau, and M. J. Casanove, *Microelectron. Eng.* **84**, 464 (2007).
- [143] Computer Program Abaqus Version 6.14, (Dassault Systèmes Simulia Corp., 2014).
- [144] R. H. Dixon and P. J. Goodhew, *J Appl Phys* **68**, 3163 (1990).
- [145] MATLAB Version R2014a, (The MathWorks, Inc., 2014).

- [146] J. H. Chen, D. Van Dyck, and M. Op de Beeck, *Acta Crystallogr. Set. A* **53**, 576 (1997).
- [147] Z. Liliental and K. Ishizuka, in: *Fortieth Annual Electron Microscopy Society of America Meeting*, edited by G. W. Bailey (Claitor's Publishing Division, Baton Rouge, 1982), pp. 448-449.
- [148] B. Jiang, J. M. Zuo, D. Holec, C. J. Humphreys, M. Spackman, and J. C. H. Spence, *Acta Crystallogr. Set. A* **66**, 446 (2010).
- [149] D. Saito, H. Yonezu, T. Kawai, M. Yokozeki, and K. Pak, *Jpn. J. Appl. Phys. Part 2* **33**, L1205 (1994).
- [150] D. J. Eaglesham and C. J. Humphreys, in: *XIth Int. Congress on Electron Microsc.*(1986), pp.209.
- [151] C. J. D. Hetherington, D. J. Eaglesham, C. J. Humphreys, and G. J. Tatlock, in: *Inst. Phys. Conf. Ser. No. 87*(1987), pp. 655.